Strength, structure and stability of polyelectrolyte complex coacervates

Thesis committee

Thesis supervisor
Prof. dr. M. A. Cohen Stuart
Professor of Physical Chemistry and Colloid Science
Wageningen University

Thesis co-supervisor
Dr. ir. J. van der Gucht
Associate professor, Laboratory of Physical Chemistry and Colloid Science
Wageningen University

Other members
Prof. dr. J. Baschnagel, Institut Charles Sadron, Strassbourg, France
Prof. dr. H.-J. Butt, Max Planck Institute for Polymer Research, Mainz, Germany
Prof. dr. W. K. Kegel, Utrecht University
Prof. dr. E. van der Linden, Wageningen University

This research was conducted under the auspices of Graduate School VLAG.

Strength, structure and stability of polyelectrolyte complex coacervates

Evan Spruijt

Thesis
submitted in fulfillment of the requirements for the degree of doctor
at Wageningen University,
by the authority of the Rector Magnificus,
prof. dr. M. J. Kropff,
in the presence of the
Thesis Committee appointed by the Academic Board,
to be defended in public
on Friday 12 October 2012
at 4 p.m. in the Aula.

Evan Spruijt
Strength, structure and stability of polyelectrolyte complex coacervates
304 pages

PhD thesis, Wageningen University, Wageningen, The Netherlands (2012)
with references, with summaries in English and Dutch.

ISBN: 978-94-6173-354-5

Contents

Chapter 1

Introduction: from liquid phases to ionic bonds

This thesis deals with complex coacervates of flexible polyelectrolytes. The first Chapter serves as an introduction to the field of physical chemistry and colloid science in general and to the subject of this thesis in particular. We briefly introduce the concepts that are key to the subject of this thesis: complex coacervation, polyelectrolytes and ionic bonds. We discuss what interactions are relevant in the liquid complex coacervate phases, which properties they have in common and what questions remain unanswered. Polyelectrolytes offer a well-defined and versatile model system for experiments aimed at answering these questions. We introduce the polyelectrolytes that play an important role as model systems in the research described in this thesis. The motivation for this research is based on both academic interest and potential applications: it originates from the lack of understanding of complex coacervation as a fundamental phenomenon and is catalysed by the benefits of insights into the strength, structure and stability of complex coacervates for many applications. Following these three aspects of the characteristics of complex coacervates, we give an outline of this thesis at the end of this Chapter.

1.1 Lyophobic and lyophilic colloids

In everyday life we often rely on the stability of colloidal systems without noticing. We expect a stable colloidal dispersion whenever we drink a glass of milk or wine, when we use soap to wash the dishes, when we brush our teeth, when we sign a letter with a fountain pen, when we paint a wall or a door and when we prepare sauces or gravy in our kitchens. Instabilities in these colloidal systems often have adverse effects. Milk coagulates, unclarified wine flocculates and paint may sediment or gel when the particles in the paint start to aggregate. Similarly, the blood in our body and the fluid content of our cells are dense colloidal dispersions that must remain stable for us to stay healthy. All these colloidal systems have in common that they contain particles with sizes between those of small molecules and microscopic objects: colloids.[1] The particles can be anything from long and flexible thread-like molecules to rigid hard spheres, but they are all subject to a delicate balance of thermal motion and external and interparticle forces.[2] The nature of the particles is however important when we consider their stability. In general, colloidal systems are divided into two classes: *lyophobic colloids* and *lyophilic colloids*.[3,4]

Lyophobic colloids, such as pigments in ink and tannins in red wine, have little or no affinity for the solvent surrounding them, and a considerable amount of work is needed to disperse them. They are essentially thermodynamically unstable and are also called irreversible colloids. Lyophobic colloids are often stabilised by charges and their interactions can be described effectively by a potential energy profile shown in Figure 1.2a. When they become unstable, for instance upon addition of salt, they often flocculate or coagulate into solid-like aggregates.[5] Flocculated colloids can sometimes be repeptised by strong shaking or stirring.

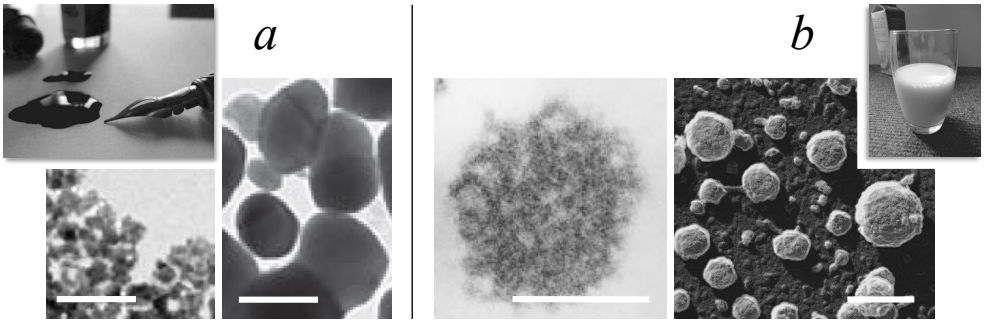

Figure 1.1: (a) Lyophobic colloids: pigments in ink visualised by transmission electron microscopy. Reprinted with permission: Wiley-Blackwell.[6] (b) Lyophilic colloids: casein micelles in milk visualised by transmission (left) and scanning (right) electron microscopy. Reprinted with permission: M. Kaláb,[7] Elsevier.[8] All scale bars represent 200 nm.

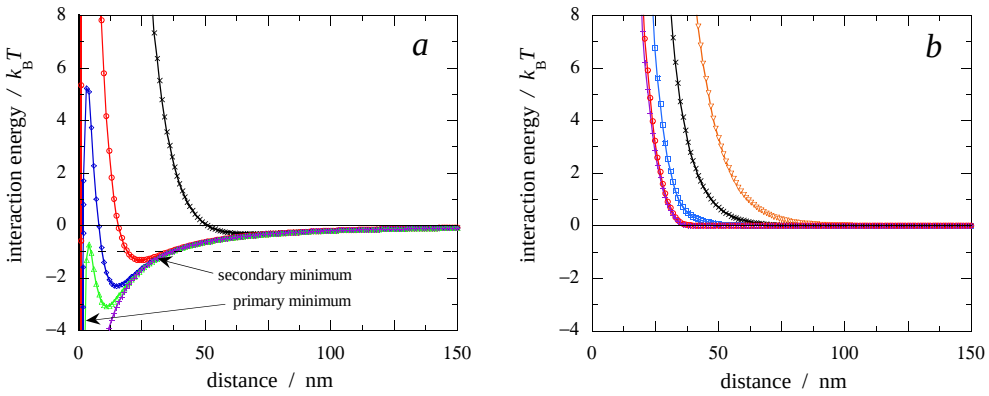

Figure 1.2: Schematic pair potentials for (a) lyophobic and (b) lyophilic colloids. Negative interaction energies imply a tendency to aggregate. The curves in (a) are calculated from a Derjaguin-Landau-Verwey-Overbeek (DLVO) potential,[3] with salt concentration increasing towards the left. Both primary and secondary minima are indicated. The curves in (b) are calculated from the pair potential of a charged star-shaped polymer,[14] with salt concentrations increasing towards the left.

Lyophilic colloids on the other hand, have a strong affinity for the solvent surrounding them. When water is the solvent, we usually call them hydrophilic. Examples of lyophilic colloids are the casein micelles in milk and many polymers.[9] They dissolve spontaneously and are entirely open to the solvent, implying that every link or atom of these colloids is in contact with the solvent molecules.[3] These colloidal dispersions are thermodynamically stable and are called reversible colloids. Their pair interactions are sketched in Figure 1.2b. When lyophilic colloids are destabilised, for instance by addition of a co-solvent, we find another striking difference with lyophobic colloids. Although aggregation into solid-like agglomerates may occur, this is not a general phenomenon for lyophilic colloids. Instead, Tiebackx, Bungenberg-de Jong and Kruyt found that these colloids often aggregate into liquid droplets that retain a large amount of the original solvent (see for example Figure 1.3).[10–13] They called these dense, colloid-rich droplets *coacervates* and the type of aggregation *coacervation*, both derived from the prefix *co* and the Latin word *acervus*, meaning 'heap', which relates to the dense liquid droplets.[12] Coacervation is thus loosely translated as 'to come together in a heap'.

1.2 Complex coacervates

One type of colloidal system that often forms coacervates is a mixture of positively and negatively charged macromolecules in water. These macromolecules have a strong

affinity for each other and tend to form a complex of interacting charges (see Figure 1.4). Under the right conditions the complexed macromolecules phase separate from the original dispersion into liquid coacervate droplets or layers (see Figure 1.3). In this case, the coacervates contain both positively and negatively charged macromolecules and water of hydration. They are therefore called *complex coacervates.*[12]

Complex coacervates are thus dense phases of oppositely charged hydrophilic colloids that contain a significant amount of 'hydration' water. They differ from the solid-like aggregates formed in lyophobic colloidal systems in their liquid appearance: they are "tropfbare Flüssigkeiten" (Figure 1.3).[12] Usually, complex coacervates are formed from dilute dispersions of hydrophilic colloids, as shown in Figure 1.4. The dense complex coacervate will not take up the total volume of the mixed solutions. Excess water is expelled and remains in contact with the complex coacervate phase. Eventually, two liquid phases will emerge, similar to the phase separation of oil and water mixtures into two liquid phases: one containing mostly oil, the other mostly water. In the case of complex coacervation however, both phases contain large amounts of water, but the complex coacervate phase contains most or all of the charged macromolecules, as shown in Figure 1.4.

Based on the description above, complex coacervation is considered to be a liquid-liquid phase separation that is driven by the association of two oppositely charged macromolecules. It is therefore sometimes referred to as associative phase separation.[15] Nonetheless, the same driving forces do not lead to complete liquid-liquid phase separation in all cases. Sometimes, aggregation of the charged macromolecules stops at a few tens of macromolecules, with a typical aggregate size of ten nanometre,[16–18] or at tiny droplets with a typical size of ten micrometre.[19–21] In other cases, different, purposefully introduced molecular interactions prevent the aggregation from continuing.[15,22] This may lead to well-defined and often dynamic colloidal structures, as we will discuss hereafter in Section 1.2.4. On a macroscopic scale, we observe in both cases no liquid-liquid phase separation and the colloids in the mixture remain dispersed. Confusingly, the term complex coacervates has been used to refer to these dispersions as a whole, instead of the dense liquid in a phase separated system only.[23] Alternatively, the term microcoacervates is used for microscopic droplets that form prior to macroscopic phase separation.[12] In this thesis we will keep the original terminology and use complex coacervates to refer to the dense phase only.

So far, we have considered the charged macromolecules that aggregate into coacervates only in a general way. In fact, many different types of macromolecules may form complex coacervates. In their original research, Bungenberg-de Jong and Kruyt investigated gelatin and gum arabic, a protein and a polysaccharide, respectively.[10–12] Both are natural macromolecules, derived from plants and animals. Since then, numerous other proteins and polysaccharides have been shown to form complex

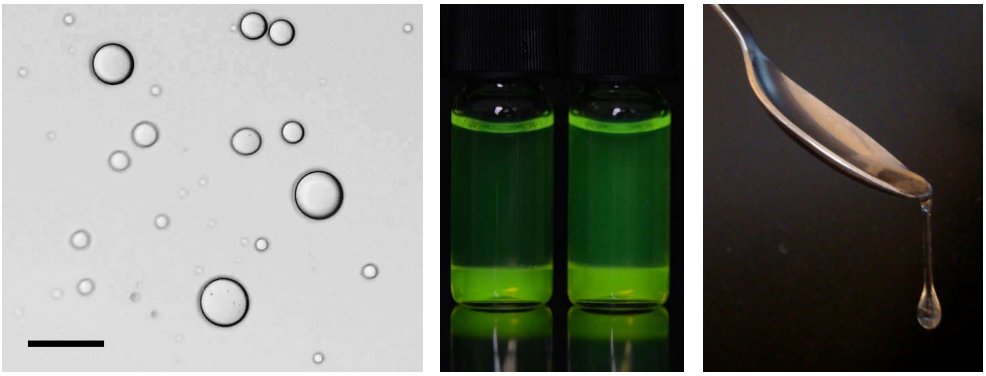

Figure 1.3: Examples of complex coacervates: droplets in dilute aqueous solutions, separated phases and a drop of complex coacervate trickling from a spoon. See Chapters 3 and 4 for more details.

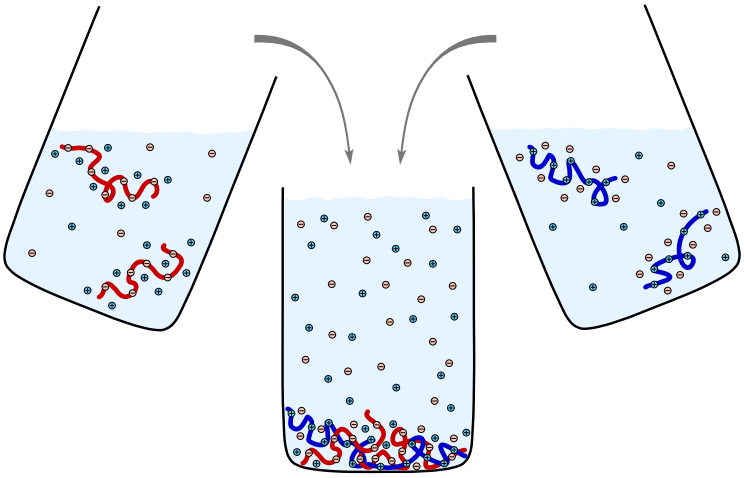

Figure 1.4: Schematic drawing of the process of mixing solutions of two oppositely charged polymers. After mixing, phase separation occurs and a dense complex coacervate forms at the bottom. The released counterions are distributed over the available volume.

coacervates.[24,25] More recently, also synthetic polyelectrolytes were found to form complex coacervates,[26,27] and we will introduce these polyelectrolytes in the next Section.

Finally, complex coacervation seems not to be limited to the flexible macromolecules we have mentioned thus far. Rigid laponite disks,[28] hard nanoparticles,[29] stiff rod-like virus particles,[30,31] self-assembling surfactant micelles[32] and small multivalent ions[33] all have the potential to aggregate into dense liquid phases that

are tentatively called complex coacervates. Complex coacervation seems not to discriminate against charged macromolecules, colloids or micelles.[34] The versatility of components and the fact that charges are ubiquitous in the world of molecules and particles in water are two main reasons why complex coacervates and the underlying aggregation by association are present in so many natural systems and applications and why they are explored intensively in search for new materials.

1.2.1 Complex coacervates in nature

In nature, complex coacervation occurs in many places. At the cellular level, our DNA is compacted by positively charged histon proteins into complex-coacervate-like agglomerates that fold into chromatin fibers.[35–39] In bacteria and eukaryotic mitochondria, DNA is condensed into a dense liquid phase by a combination of multivalent cations, such as spermine and spermidine, DNA-binding proteins and other crowding agents.[40–42] The dense phase of condensed DNA is called the nucleoid and is very similar to a complex coacervate.[35] In the process of blood clotting, charge-charge complexation is thought to play an important role as well. Near an injury, clotting factors become anchored to cell membranes, mainly driven by a complex of negatively charged phospholipids and the positively charged calcium-rich GLA domain of clotting proteins.[43] After anchoring, they initiate the cascade of reactions that should ultimately lead to repair of the injury.

At the level of organisms, complex coacervates are used as a natural underwater glue. The sandcastle worm builds highly robust tubular shells near the sea shore to protect itself, by glueing together small mineral particles one by one (see Figure 1.5). The glue is secreted as a mixture of oppositely charged proteins and some additional curing agents.[44] The pH change between the worm's secretory system and the sea water probably triggers the complexation and within tens of seconds, the glue has cured sufficiently to keep a newly added particle firmly in position. Caddisfly larvae have a similar strategy to build composite retreats out of rocks and sticks, using a sticky underwater silk protein complex that is considered a natural complex coacervate.[44]

1.2.2 Complex coacervates in food, coatings and enhanced oil recovery

Yogurt drinks and milk fruit drinks are stabilised by methyl esterified pectins.[45,46] Without stabilisation, the low pH in such drinks would cause flocculation of the casein and formation of whey. These pectins are positively charged and form complex-coacervate-like aggregates with the negatively charged casein micelles in the milk, thereby preventing their flocculation at low pH.[45,47] On a more macroscopic scale

Figure 1.5: The sandcastle worm (*Phragmatopoma californica*) builds tubular shells from mineral particles, such as zirconium oxide (left, diameter: 500 µm) or glass (middle, right, diameter: 550 µm). The beads are glued together with a complex-coacervate-like glue, as visualised by scanning electron microscopy (right). Reprinted with permission: R. Stewart.

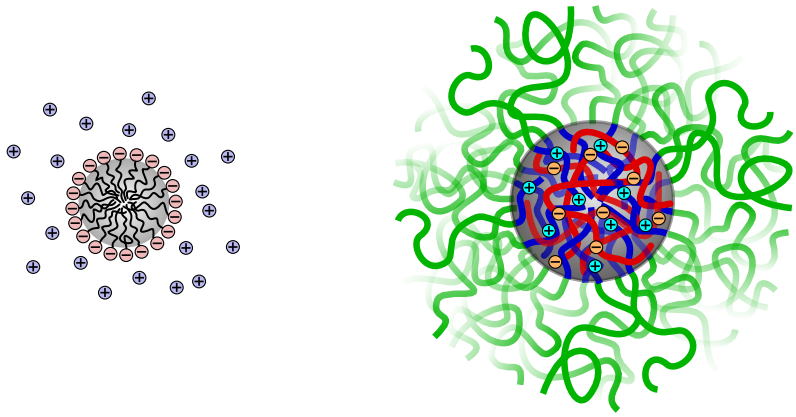

Figure 1.6: Schematic drawing of (a) amphiphilic micelles, such as sodium dodecyl sulphate and (b) complex coacervate core micelles.

in foods, we can make use of the immiscibility of complex coacervates and water. Droplets of complex coacervates made from edible components could replace fat globules in fatty snacks to help reduce overweight.[48–50]

The immiscibility of complex coacervates and water, combined with the potential of complex coacervates to take up remarkable amounts of solid particles and oil, is interesting for applications in enhanced oil recovery as well.[12,51–53] However, many issues related to adsorption of the complex coacervates to surfaces and the extraction of the recovered compounds from the coacervates still have to be addressed before complex coacervates can be applied in this field.

Adsorption to surfaces is an advantage in another field of applications: coatings. Complexes of oppositely charged macromolecules provide versatile, self-healing coatings for many surfaces.[54–56] By carefully choosing the types of charged macro-

molecules and additives, and by controlling the order in which they are applied to the surface, the coatings can be made anything from tough to soft and from water-repellent to protein-repellent. In most cases the complexes are arranged in layers on the surface and they are not in the same state as a complex coacervate,[54,55] but for some applications a true complex coacervate layer is preferred.[56,57]

1.2.3 The origin of life

There is a strong resemblance between some protein complex coacervates and the intracellular fluid of many cells. Both contain high concentrations of proteins without any sign of protein aggregation or unfolding and both can maintain an ion concentration different from their surroundings.[58,59] In addition, when a cell membrane is locally disrupted, the intracellular fluid usually does not mix with the surrounding fluid,[60,61] as if it is phase separated from its surroundings. These observations led to the hypothesis that life may well have originated from complex coacervates.[62–64] According to this hypothesis, small droplets of a complex coacervate phase accumulated small molecules, proteins and nucleic acid precursors and kept them well separated from the surroundings.[20] Locally, sufficiently high concentrations could be reached for small molecules to evolve into more complex cellular components, structures and mechanisms. A cell membrane may have adsorbed at the complex coacervate droplet's interface in a later stage to create the first protocells.[65] This view on the origin of life has been strikingly called the 'garbage-bag world'. One of its deficiencies is the lack of a mechanism by which loaded complex coacervate droplets can reproduce other than statistically. In 1980 it was therefore succeeded by the then more popular hypothesis of the 'RNA world' as the origin of life.[65] However, some aspects of the garbage-bag world are still compelling. Renewed interest in complex coacervates has also led to new ideas on how they might play a role in cells and biochemical pathways.[66–68]

1.2.4 Designing new functional materials and structures

Nature's approaches to use complex coacervation as a way to assemble charged macromolecules into biological structures and materials have been mimicked in many laboratories using synthetic building blocks. By changing the architecture of the macromolecules, a variety of new structures and materials has been designed.

Combinations of charged macromolecules and diblock copolymers (see Section 1.3) that consist of two separate blocks, one charged and one neutral, form small complex coacervates in solution. The size of these complexes is limited by the repulsion between the neutral polymer blocks at the periphery of the complexes. This situation is very similar to that of amphiphilic surfactants in water, as shown in Figure 1.6, and the complexes are therefore called complex coacervate core micelles (C3Ms).[22,69] Complex coacervate core micelles have a typical core radius of 5 nm and an overall

hydrodynamic radius of 20 nm.[70] They can be used as packaging capsules for a variety of small molecules, metal ions[71] and macromolecules, such as proteins[72] and DNA.[73]

C3Ms are colloidal particles themselves. Their stability depends on the balance between attractive and repulsive forces between the polymer blocks. We started off by dividing colloidal particles into lyophilic and lyophobic colloids, because this division has important consequences for their stability. It turns out that C3Ms are not simple colloids, as they cannot be classified as typical lyophobic or lyophilic colloids. The polymers they consist of are almost always hydrophilic colloids. The C3Ms are however biphasic systems, with a core that is separated from the surrounding dispersion medium by an interface (see Figure 1.6). This is characteristic of lyophobic colloids. On the other hand, both the core and the surrounding medium consist mostly of water. The colloidal assemblies are considered thermodynamically stable and in most cases their assembly is reversible,[70,72] which is characteristic of lyophilic colloids. Moreover, the comparable amphiphilic micelles shown in Figure 1.6 are usually classified as lyophilic colloids. Perhaps classification of these types of colloids into an additional class, consisting of molecular assemblies, such as micelles, microemulsions and C3Ms, would be more appropriate.[2]

By slightly changing the architecture of the macromolecules (see Figure 1.8) and the preparation procedure, but keeping the attractive interactions between positively and negatively charged molecules in place, alternative structures to C3Ms can be formed. Examples include hollow capsules,[74] long thin ribbons[75] and flat membranes that can be used to enclose micrometre-sized droplets.[76] Finally, changing diblock copolymers into triblock copolymers allows interconnecting C3Ms into physical gels.[77] These gels have viscoelastic properties that can be tuned by many different parameters, the most important one being the salt concentration.

1.3 Polyelectrolytes and copolymers

Polymers are long molecules built from a large number of repeating units (*monomers*) linked by covalent or physical bonds, as shown in Figure 1.7. Many natural materials we still use today, such as rubber, silk and cellulose, consist of polymers. Other natural polymers, such as DNA, RNA and proteins, are essential for life as we know it. Synthetic polymers have become an integral part of our everyday life as well: all plastic bags, nylon and polyester clothing are made from polymers.

The number of repeating units in a polymer can be quite large. When only two monomers are connected, the molecule is called a *dimer*. Up to roughly ten monomers compose an *oligomer*. All molecules with more than roughly ten monomers are called *polymers*. Some polymers consist of more than a million monomers.[78]

Most polymers consist of only one type of monomer (*homopolymers*). In a good solvent for this monomer, a linear homopolymer will also dissolve and its shape is termed a 'random coil', which is a continuously changing random arrangement of connected monomers. The coil is entirely open to the solvent, as is the case for lyophilic colloids.

Some polymers consist of more than one type of monomer (*copolymers*). The number of different monomers and the order in which they are located along the polymer chain can strongly influence the random coil conformation. Especially if one or more types of monomers have a strong affinity for each other, a much more compact structure will be formed. Proteins, for instance, have twenty types of monomers (amino acids), some of which have affinity for each other. As a result, almost all proteins fold into dense globular structures, allowing them to perform specific functions. In the more simple case of two types of monomers, they can be arranged in blocks (Figure 1.8a, *block copolymers*) or at random (Figure 1.8b, *statistical* or *random copolymers*).

Finally, branching of the polymer chain leads to even more different types of polymers. These polymers are no longer linear, but their shape in solution is usually still close to a random coil if the monomers have no strong affinity for each other. If the branches are short compared to the main polymer chain, the polymer is called a *graft copolymer* (Figure 1.8c). If the branches become as long as the ends of the main polymer chain, or if several polymer chains are connected by a central moiety, the polymer is called a *star copolymer* (Figure 1.8d).

Polyelectrolytes are polymers that contain charged monomers. Charged monomers bear acidic or basic chemical groups or salts thereof that can dissociate in water. The charge of these groups depends on the pH of the solution and the dissociation or protonation constant of the acidic or basic groups. If the dissociation or protonation constant falls roughly in the range $0 < \mathrm{p}K < 14$, the groups can be charged and discharged in aqueous solution in practice by changing the pH. These polyelectrolytes are called *weak* or *annealed polyelectrolytes*. If the dissociation or protonation constant is so large that the groups are essentially always charged in aqueous solutions, the polyelectrolytes are called *strong* or *quenched polyelectrolytes*. Examples of weak polyelectrolytes are poly(acrylic acid) and poly(N,N-dimethylaminoethyl methacrylate). Examples of strong polyelectrolytes are poly(styrene sulphonate) and poly(N,N,N-trimethylaminoethyl methacrylate) (see Figure 1.9). Most natural polyelectrolytes, such as chitosan and hyaluronic acid, are weak polyelectrolytes. DNA and RNA are strong natural polyelectrolytes.

Because electric charges come in two classes, polyelectrolytes are either positively charged, negatively charged or neutral (equal amounts of positive and negative charges). Positively charged polyelectrolytes are called *polycations*, negatively charged polyelectrolytes are called *polyanions*. Polyelectrolytes that contain equal numbers of

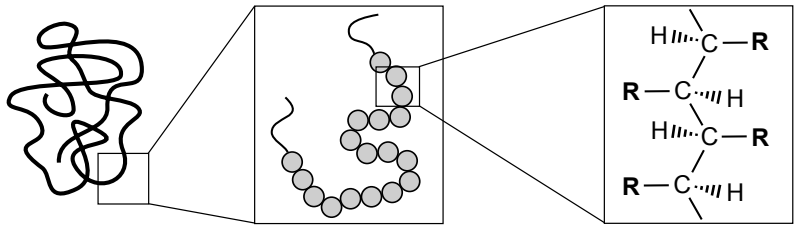

Figure 1.7: Schematic drawing of a polymer: the random coil consists of segments of repeating units, which are covalently linked together.

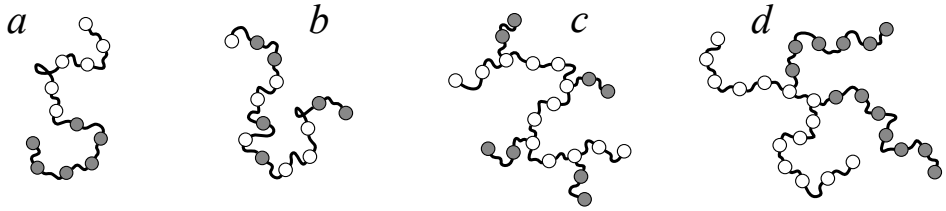

Figure 1.8: Schematic drawing of various types of copolymers: (a) block, (b) statistical or random, (c) graft and (d) star copolymers.

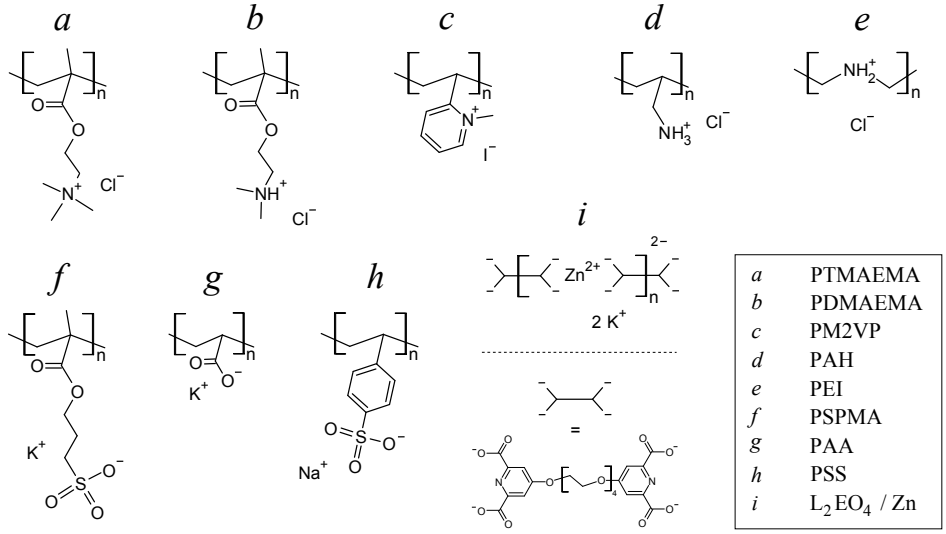

Figure 1.9: Structure of various synthetic polyelectrolytes that are used in this thesis. Abbreviations: PTMAEMA = PMETAC = PMADQUAT = poly(N,N,N-trimethylaminoethyl methacrylate), PDMAEMA = poly(N,N-dimethylaminoethyl methacrylate), PM2VP = poly(N-methyl-2-vinylpyridinium), PAH = poly(allylamine), PEI = poly(ethylene imine), PSPMA = poly(3-sulphopropyl methacrylate), PAA = poly(acrylic acid), PSS = poly(styrene sulphonate), L_2EO_4 / Zn = 'living' metal-ligand coordination polymer.[79]

positively and negatively charged groups are called *polyampholytes* or *zwitterionic polyelectrolytes*.

Synthetic polyelectrolytes provide a well-defined and versatile model system for studying fundamental aspects of complex coacervates. They can be not only synthesised with high reliability, but also adjusted easily to different lengths and types of charged monomeric groups. In addition, many of their properties in dilute aqueous solutions are now well understood.[80,81] We have selected a number of linear, flexible polyelectrolytes with different charged monomeric groups to study complex coacervates. Their chemical structures are shown in Figure 1.9.

1.4 Thermodynamics of complex coacervation

Following the rules of electrostatics, like charges repel each other, whereas opposites attract. Coulomb's law gives the precise value of the repulsive interaction between two like charges and the attractive interaction between two unlike charges for ions in a vacuum. The interaction energy U is given by

$$U_{12}(r_{12}) = \frac{q_1 q_2}{4\pi\epsilon_0 r_{12}} \tag{1.1}$$

where q_1 and q_2 are the signed charges, r_{12} is the distance between them and ϵ_0 is the vacuum permittivity. According to Coulomb's law, bringing two oppositely charged ions in closer proximity is always energetically favourable.

For interactions between molecules with an arbitrary charge distribution, such as dipoles and higher order multipoles, the molecular charge densities $\rho(\vec{r})$ can be expanded as a collection of point charges and integrated to yield the electrostatic interaction energy:[1]

$$U_{12}(r_{12}) = \int \rho_1(\vec{r})\psi_2(\vec{r})\,\mathrm{d}^3\vec{r} = \frac{1}{4\pi\epsilon_0}\iint \frac{\rho_1(\vec{r})\,\rho_2(\vec{r}\,')}{|\vec{r}-\vec{r}\,'|}\,\mathrm{d}^3\vec{r}\,\mathrm{d}^3\vec{r}\,' \tag{1.2}$$

where $\psi_i(\vec{r})$ is the electrostatic potential and $\rho_i(\vec{r})$ is the signed charge density around species i. Integration is over volume elements $\mathrm{d}^3\vec{r}$ and $\mathrm{d}^3\vec{r}\,'$. U_{el} can be split into a contribution from repulsive interactions between like charges and a contribution from attractive interactions between opposite charges for reasons of clarity.

In aqueous solutions the situation is more complicated. First of all, evaluating the electrostatic interactions between all multipole water molecules, ions and polyelectrolytes would be an enormous amount of work. Therefore, the presence of a dielectric medium is usually taken into account in first approximation by replacing the vacuum permittivity ϵ_0 by an effective permittivity $\epsilon_{\mathrm{r}}\epsilon_0$. The solvent response, represented by ϵ_{r}, involves both energy and entropy contributions and as a consequence, the electrostatic energy is actually a free energy of solvated ions.[1]

This approximation no longer holds for small separations between charges in water, where hydration effects and specific ion interactions beyond generic electrostatics start to play a role. Disregarding these limitations, the electrostatic energy can be calculated for any charged molecule, polymer, particle or combination thereof in water, using an effective permittivity:[1]

$$U_{\mathrm{el}} = \frac{1}{2} \int_V \rho(\vec{r})\, \psi(\vec{r})\, \mathrm{d}V = \frac{\epsilon_{\mathrm{r}} \epsilon_0}{2} \int_V (\vec{\nabla}\psi)^2\, \mathrm{d}V \tag{1.3}$$

where $\vec{\nabla}\psi$ is the gradient of the electrostatic potential and $\rho(\vec{r})$ is the overall signed charge density. Whether or not this electrostatic energy will favour complexation and complex coacervation of a specific combination of charged species, depends on the gradient of the electrostatic potential before and after complexation, and will vary with salt concentration.

Secondly, charged polymers and particles (macroions) in aqueous solutions are surrounded by an electrical double layer. In the double layer, counterions are accumulated and co-ions are depleted. This state has a lower entropy compared to one in which all counterions are randomly mixed. When two oppositely charged macroions form a complex, their double layers cancel out to a certain extent and the counterions are released in the form of an ordinary salt solution, as shown schematically in Figure 1.4. This leads to an increase in entropy and hence a decrease in free energy.

The free energy of complexation includes both the effect of electrostatic energy (Equation 1.3) and the effect of counterion entropy. In a typical experimental system where the number of molecules and the temperature are constant, and assuming that the volume does not change upon complexation, the Helmholtz free energy F is the characteristic thermodynamic quantity:

$$\Delta F_{\mathrm{el}} = \Delta U_{\mathrm{el}} - T\Delta S_{\mathrm{el}}\,. \tag{1.4}$$

If the volume is affected, the Gibbs free energy ΔG is the required quantity and a small $P\Delta V$ term has to be taken into account.[82] In aqueous solutions at room temperature, the difference between changes in the Helmholtz free energy and the Gibbs free are usually minor.[4] If the bulk concentrations rather than the total number of ions are the fundamental variables (open isothermal system), the total number of ions is fixed only by the choice of a detailed statistical mechanical model, such as the Boltzmann equation, and the combination of the electric field energy and the entropy yields a *grand* potential Ω.[83] In the research described in this thesis we mainly consider experimental systems with a fixed number of molecules and assume that the volume is not affected by rearrangements of counterions, hence, we usually take the Helmholtz free energy as characteristic thermodynamic quantity.

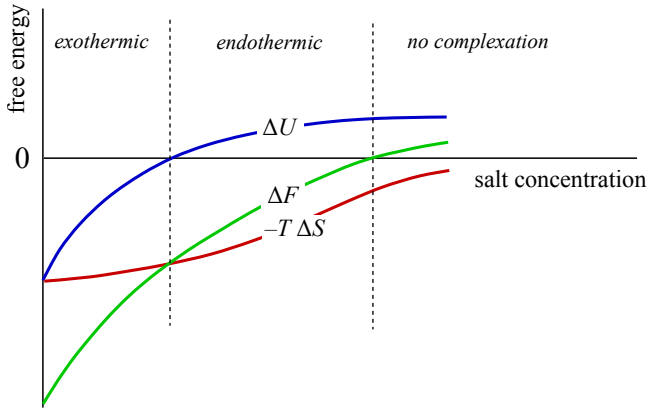

Figure 1.10: Schematic picture showing the hypothesised effect of salt on the total free energy of complexation (ΔF), and the separate contributions of the electrostatic energy (ΔU) and the ion release entropy ($-T\Delta S$).[15]

Whether complexation between two oppositely charged macromolecules in aqueous solution is favoured by a decrease in energy, an increase in entropy, or both, will depend on the chemical details of the macroions and the salt concentration (ionic strength). In Chapter 2 we give an extensive analysis of this problem for various charged objects, ranging from planar surfaces to cylindrical polyelectrolytes and spherical particles. Here, we give a qualitative argument to account for the effect of salt on the free energy of complexation.[15]

The entropy change associated with complex formation is dominated by the release of counterions that were initially confined to a double layer, and hence likely to be positive. At low ionic strength, the counterion concentrations inside the double layer are significantly higher than in the bulk solution and the entropy increase upon complexation is large. As the ionic strength increases, the entropy gain of counterion release becomes smaller, approaching zero in the limit of very high ionic strength.

The energetic contribution to complexation may be either negative or positive (exothermic or endothermic, assuming a constant volume), depending on the ionic strength. At low ionic strength, the electrical double layers are thick and dilute and the average distance between opposite charges is large, whereas the polyelectrolyte complexes are dense, often having tight ion pairing between oppositely charged groups. As a result, the average distance between opposite charges decreases upon complexation and the electrostatic energy will decrease. If, on the other hand, the ionic strength is high, the electrical double layers are compact and the decrease in electrostatic energy due to the released counterions is not compensated by a decrease in electrostatic energy due to newly formed macroion complexes. The overall

energy change is positive and the complexation is endothermic. Naturally, various parameters, such as polyelectrolyte charge density and chain length, will affect this qualitative picture, and we discuss this in more detail in Chapters 2 and 3. Figure 1.10 summarises the argument above and shows that, in general, macroion complexation changes from exothermic to endothermic with increasing ionic strength before it becomes thermodynamically unfavourable at high ionic strength.

Complex coacervation involves more contributions to the free energy of the entire system than outlined above. In the much denser complex coacervates, macroions will have a reduced translational entropy compared to a randomly mixed solution, for example. One of the simplest theoretical treatments of complex coacervation that takes into account these mixing entropy terms, together with a simplified estimate of the electrostatic free energy F_{el}, was developed by Voorn and Overbeek.[84,85] Their model predicts associative phase separation in solutions of oppositely charged macroions under certain conditions, similar to the experimental observations of complex coacervation. We discuss this in detail in Chapter 3.

1.5 Aim of this research

Despite the biological, industrial and fundamental scientific importance of complex coacervates, many questions about their formation, structure and stability remain unanswered. To what extent is complex coacervation similar to the classical phase separation of an oil-water mixture? How does the formation of complex coacervates depend on the salt concentration, temperature and the chemical and physical properties of the charged macromolecules? What is the microscopic structure of a complex coacervate? How strong is the attraction between the oppositely charged macromolecules and how is this strength related to the characteristics of the macroscopic complex coacervate materials? What are the properties of the interface between the complex coacervate phase and the dilute aqueous phase?

Many of these questions are both crucial for practical applications of complex coacervates and interesting from an academic point of view. The aim of the research described in this thesis is to investigate model systems for complex coacervation and to answer the above questions about the strength, structure and stability of complex coacervates.

1.6 Outline of this thesis

This thesis is divided into three main parts. Each part focusses on a different aspect of complex coacervates, as is also reflected in the title of this thesis: strength, structure and stability. We chose to arrange the parts in a way that agrees with a

top-down approach of studying complex coacervates, the opposite of what the title suggests. We start from macroscopic stability of complex coacervates and end with the microscopic interaction strength of the bonds between oppositely charged groups inside the complex coacervates.

Part I is called 'Stability'. In this part we focus mainly on macroscopic complex coacervate phases. In Chapter 2 we consider the thermodynamic driving forces for complexation of oppositely charged colloids. We solve the Poisson-Boltzmann equation for oppositely charged plates, polymeric cylinders and spherical particles and explicitly evaluate the contributions of the field energy, entropy and chemical energy to the total free energy of interaction.

In Chapter 3 we investigate how these driving forces are translated experimentally into the phase behaviour of mixture of oppositely charged polyelectrolytes. We construct an experimental salt-polymer phase diagram of complex coacervation for flexible polyelectrolytes with varying length. We study the effect of salt and polymer chain length on the stability of the complex coacervate phases in detail and derive a relation for the critical salt concentration as a function of chain length.

In Chapter 4 we investigate to what extent this phase behaviour is general for any combination of oppositely charged flexible polyelectrolytes. We combine polyelectrolytes of similar length and backbone structure, but with different charged groups and measure their critical salt concentration, water content and composition. For two combinations of polyelectrolytes we investigate whether different types of monovalent salts affect the complex coacervate stability in a different way. In addition, we describe the effect of temperature on the stability of complex coacervates in terms of the phase diagram we reported in Chapter 3.

In Chapter 5 we focus on the micelles with complex coacervate cores (C3Ms), formed from the flexible polyelectrolytes we have studied in Chapter 4. We investigate the stability of these C3Ms as a function of salt concentration and chain length. There are striking differences between the stability of C3Ms and the stability of macroscopic coacervates, but also interesting similarities. We show that the polyelectrolyte chain lengths can be used not only to change the stability of C3Ms against addition of salt, but also to change their morphology from spherical star-like to crew-cut to worm-like micelles.

In Chapter 6 we apply complex coacervation to assemble microscopic colloidal particles into fractal gels. We create 'hairy', spherical colloids with oppositely charged polyelectrolyte brushes grafted to their surfaces. Complex coacervation serves as a driving force for their assembly, but also leaves the formed aggregates completely reversible in water. Following our findings from the previous Chapters, we can simply increasing the salt concentration beyond the critical point to trigger disassembly, which is favoured by the gain in entropy of the colloidal particles. We study the

interparticle interactions as a function of salt concentration by atomic force microscopy, light scattering and laser scanning confocal microscopy and relate the observed assembly kinetics to the time-dependent interactions between these hairy colloidal particles.

Part II is called 'Structure'. In this part we focus on the microscopic structure of complex coacervates. In Chapter 7 we use scattering of neutrons, X-rays and light to investigate the static structure of the complex coacervates we studied in Chapter 3. We measure the conformation of single polycations and polyanions in the complex coacervates and find that they have a nearly Gaussian conformation. Together they form a semidilute polymer solution of overlapping chains with a characteristic mesh size that increases with decreasing salt concentration. At length scales larger than the mesh size, we find density fluctuations that give rise to a power law in scattering intensity in neutron scattering, X-ray scattering and light scattering. In dynamic light scattering we observe the related structural relaxations on two separate length scales: one corresponding to the mesh size and one to the size of the density fluctuations. The overall static structure of the complex coacervates hardly depends on salt concentration.

In Chapters 8 and 9 we study the dynamic structure of complex coacervates in more detail using rheology. In contrast to the static structure, we find that salt does have a very pronounced effect on the dynamics of complex coacervates, changing them from mostly elastic gels, to highly viscous fluids and eventually causing the complex coacervate phase to become unstable and completely miscible with the dilute phase. The role of salt in this process is very generic. In Chapter 8 we describe how this finding leads to the proposition of a time-salt superposition principle for complex coacervates and other charge-driven materials.

In Chapter 9 we apply this time-salt superposition to study the relaxation processes in complex coacervates in more detail. We reconstruct the relaxation time spectra for complex coacervates of different chain lengths and salt concentrations. By analysing the effect of salt and polymer chain length on these relaxation spectra we obtain insight into the structural rearrangements of the polyelectrolytes in a complex coacervate. We find that ionic bonds between oppositely charged groups act as sticky points that slow down relaxation of an applied stress or strain. Relaxation eventually occurs via Rouse modes of the polymer chains.

Part III is called 'Strength'. In this part we focus on the interactions between oppositely charged macromolecules on a molecular scale. Two oppositely charged chemical moieties can form an ionic bond when they are close enough together. These ionic bonds were introduced in Chapters 8 and 9 and in this Part we focus on their

strength against rupture and the link between this strength to the stability of complex coacervate phases discussed in Part I.

In Chapter 10 we study the interfacial tension between the complex coacervate and its coexisting dilute aqueous phase. The interfacial tension is a macroscopic property, but results from the microscopic interactions between molecules across the interface. In the complex coacervate, charged macromolecules are able to form ionic bonds among themselves, but the macromolecules at the interface cannot form ionic bonds in all directions. The result is a net attractive force towards the bulk complex coacervate, normal to the interface. Like for any liquid-liquid interface, the interfacial tension favours minimisation of the interfacial area of the complex coacervates. This explains why two complex coacervate droplets have a tendency to fuse and is related to the work needed to separate a macroscopic complex coacervate phase into small droplets. This process of separation will probably not directly cause rupture of ionic bonds between the oppositely charged polyelectrolytes, but rearrangements at the interface do lead to fewer possibilities for ion pairing for some polyelectrolytes. Using colloidal probe atomic force microscopy, we can measure the interfacial tension of a complex coacervate phase that forms by capillary condensation in the confined space between the colloidal probe and the facing bare surface. From the ease with which complex coacervate droplets can be generated from macroscopic complex coacervates, we expect low interfacial tensions. We study how the interfacial tension depends on the salt concentration and use concepts from classical polymer physics to derive an expression for this dependence.

In Chapter 11 we use atomic force microscopy to directly measure the strength of single ionic bonds. By covalently grafting the oppositely charged polyelectrolytes to two different surfaces, we can force the rupture of ionic bonds instead of the disruption into two net neutral microcoacervates like in Chapter 10. We find two modes of rupture, which we relate to the two ways in which the oppositely charged polyelectrolyte can bind each other. The 'zipper' mode corresponds to the rupture of ionic bonds, one at a time. The 'snapper' mode corresponds to rupture of a complex of multiple ionic bonds at once. By studying the effect of salt and loading rate on both rupture modes, we are able to calculate the energy barrier of single ionic bonds as a function of salt concentration. These bond strengths directly relate to the dynamics of polymers inside complex coacervates (Chapters 8 and 9) and to the stability of macroscopic complex coacervates (Chapter 3), C3Ms (Chapter 5) and colloidal particle assemblies (Chapter 6).

In Chapter 12 we take the previous approach one step further and investigate the rupture force of many ionic bonds between two oppositely charged polyelectrolyte brushes using atomic force microscopy. These rupture forces are related to the interactions between the oppositely charged hairy colloids in Chapter 6. As expected from Chapter 11, we find a strongly salt-dependent rupture force and no attractive

interactions between the brushes beyond a critical salt concentration. We investigate the kinetics of complex formation by varying the loading rate and compression time of the brushes. The formation of these complexes is a rather slow process that does not reach equilibrium in our atomic force microscopy measurements.

General discussion. In the final Chapter of this thesis we return to where we started: the stability of lyophilic colloids. We discuss how our findings in the previous Chapters have contributed to understanding complex coacervates from a fundamental point of view. We will discuss the questions we formulated in the previous section and ask ourselves if our answers are general for all complex coacervates or specific to some. Furthermore, we emphasise what questions are still partly unanswered and what additional questions have come up during our investigation. Based on these questions, we speculate what direction future fundamental research on complex coacervates should take.

References

[1] D. F. Evans and H. Wennerström, *The colloidal domain*, Wiley-VCH, 2nd edn., 1999.

[2] W. B. Russell, D. A. Saville, and W. R. Schowalter, *Colloidal dispersions*, Cambridge University Press, 1989.

[3] E. J. W. Verwey and J. Th. G. Overbeek, *Theory of the stability of lyophobic colloids*, Elsevier Publishing Co., 1948.

[4] J. Lyklema, *Fundamentals of Interface and Colloid Science I*, Academic Press London, 1991.

[5] T. Cosgrove, *Colloid science*, Blackwell Publishing, 2005.

[6] T. Høgsberg, K. Loeschner, D. Löf, and J. Serup, *British J. Dermatol.*, 2011, **165**, 1210–1218.

[7] M. Kaláb, *In focus*, 2010, **18**, 4–37.

[8] D. J. McMahon and W. R. McManus, *J. Dairy Sci.*, 1998, **81**, 2985–2993.

[9] P. Walstra, J. T. M. Wouters, and T. J. Geurts, *Dairy science and technology*, CRC Press, 2005.

[10] F. W. Tiebackx, *Koll. Z.*, 1911, **8**, 198–201.

[11] F. W. Tiebackx, *Koll. Z.*, 1911, **9**, 61–65.

[12] H. G. Bungenberg-de Jong and H. R. Kruyt, *Proc. KNAW*, 1929, **32**, 849–856.

[13] H. R. Kruyt, *Colloid Science*, Elsevier Publishing Co., 1949.

[14] S. T. Milner, T. A. Witten, and M. E. Cates, *Macromolecules*, 1988, **21**, 2610–2619.

[15] J. van der Gucht, E. Spruijt, M. Lemmers, and M. A. Cohen Stuart, *J. Coll. Int. Sci.*, 2011, **361**, 407–422.

[16] W. A. Bowman, M. Rubinstein, and J. S. Tan, *Macromolecules*, 1997, **30**, 3262–3270.

[17] O. Nikolaeva, T. Budtova, Yu. Brestkin, Z. Zoolshoev, and S. Frenkel, *J. Appl. Pol. Sci.*, 1999, **72**, 1523–1528.

[18] J. H. E. Hone, A. M. Howe, and T. Cosgrove, *Macromolecules*, 2000, **33**, 1199–1205.

[19] H. Sato and A. Nakajima, *Coll. Pol. Sci.*, 1974, **252**, 944–948.

[20] H. Okihana and C. Ponnamperuma, *Origins of Life*, 1982, **12**, 347–353.

[21] C. Thomasin, H. P. Merkle, and B. Gander, *J. Pharmaceut. Sci.*, 1998, **87**, 269–275.

[22] M. A. Cohen Stuart, N. A. M. Besseling, and R. G. Fokkink, *Langmuir*, 1998, **14**, 6846–6849.

[23] H. G. Bungenberg-de Jong and J. Bonner, *Protoplasma*, 1935, **24**, 198–218.

[24] C. G. de Kruif, F. Weinbreck, and R. de Vries, *Curr. Opin. Coll. Int. Sci.*, 2004, **9**, 340–349.

[25] S. L. Turgeon, C. Schmitt, and C. Sanchez, *Curr. Opin. Coll. Int. Sci.*, 2007, **12**, 166–178.

[26] R. Chollakup, W. Smitthipong, C. D. Eisenbach, and M. Tirrell, *Macromolecules*, 2010, **43**, 2518–2528.

[27] E. Spruijt, A. H. Westphal, J. W. Borst, M. A. Cohen Stuart, and J. van der Gucht, *Macromolecules*, 2010, **43**, 6476–6484.

[28] N. Pawar and H. B. Bohidar, *Adv. Coll. Int. Sci.*, 2011, **167**, 12–23.

[29] J.-F. Berret, *Macromolecules*, 2007, **40**, 4260–4266.

[30] W. C. Burger and M. A. Stahmann, *J. Biol. Chem.*, 1951, **193**, 13–22.

[31] H. Katakura, A. Harada, K. Kataoka, M. Furusho, F. Tanaka, H. Wada, and K. Ikenaka, *J. Gene Medicine*, 2004, **6**, 471–477.

[32] Y. Wang, K. Kimura, Q. Huang, P. L. Dubin, and W. Jaeger, *Macromolecules*, 1999, **32**, 7128–7134.

[33] C. Gerardin, N. Sanson, F. Bouyer, F. Fajula, J.-L. Putaux, M. Joanicot, and T. Chopin, *Angew. Chem. Int. Ed.*, 2003, **42**, 3681–3685.

[34] P. L. Dubin, *Adv. Coll. Int. Sci.*, 2011, **167**, 1.

[35] J. Th. G. Overbeek, in *Jaarboek KNAW*, Amsterdam, 1977, ch. Levensbericht H.G. Bungenberg-de Jong, pp. 158–163.

[36] D. J. Clark and T. Kimura, *J. Mol. Biol.*, 1990, **211**, 883–896.

[37] J. Widom, *Ann. Rev. Biophys. Biomol. Struct.*, 1998, **27**, 285–327.

[38] A. Perico, G. La Penna, and L. Arcesi, *Biopolymers*, 2006, **81**, 20–28.

[39] J. Clausell, N. Happel, T.K. Hale, D. Doenecke, and M. Beato, *PLoS ONE*, 2009, **4**, e0007243.

[40] I. Miyakawa, S. Fumoto, T. Kuroiwa, and N. Sando, *Plant Cell Phys.*, 1995, **36**, 1179–1188.

[41] S. Cunha, C. L. Woldringh, and T. Odijk, *J. Struct. Biol.*, 2001, **136**, 53–66.

[42] R. de Vries, *Biochimie*, 2010, **92**, 1715–1721.

[43] N. Tavoosi, R. L. Davis-Harrison, T. V. Pogorelov, Y. Z. Ohkubo, M. J. Arcario, M. C. Clay, C. M. Rienstra, E. Tajkhorshid, and J. H. Morrissey, *J. Biol. Chem.*, 2011, **286**, 23247–23253.

[44] R. J. Stewart, C. S. Wang, and Hui Shao, *Adv. Coll. Int. Sci.*, 2011, **167**, 85–93.

[45] R. H. Tromp, C. G. de Kruif, M. van Eijk, and C. Rolin, *Food Hydrocolloids*, 2004, **18**, 565–572.

[46] Herbstreith & Fox, *Acidified Milk Products and Protein Stabilisation*, 2011.

[47] R. Tuinier, C. Rolin, and C. G. de Kruif, *Biomacromolecules*, 2002, **3**, 632–638.

[48] M. A. E. Bakker, M. M. G. Konig, and J. Visser, *World Patent Application*, 1994, WO94/14334.

[49] S. I. Laneuville and S. L. Paquin, P.and Turgeon, *J. Food Sci.*, 2005, **70**, s513–519.

[50] C. Schmitt and S. L. Turgeon, *Adv. Coll. Int. Sci.*, 2011, **167**, 63–70.

[51] Q. Wang, Y. Dan, and X. G. Wang, *J. Macromol. Sci. – Pure & Appl. Chem.*, 1997, **34**, 1155–1169.

[52] K. S. Mayya, A. Bhattacharyya, and J.-F. Argillier, *Pol. Int.*, 2003, **52**, 644–647.

[53] F. Weinbreck, M. Minor, and C. G. de Kruif, *J. Microencapsulation*, 2004, **21**, 667–679.

[54] G. Decher, *Science*, 1997, **277**, 1232–1237.

[55] J. L. Lutkenhaus and P. T. Hammond, *Soft Matter*, 2007, **3**, 804–806.

[56] W. M. de Vos, J. M. Kleijn, A. de Keizer, and M. A. Cohen Stuart, *Angew. Chem. Int. Ed.*, 2009, **48**, 5369–5371.

[57] A. M. Brzozowska, B. Hofs, A. de Keizer, R. Fokkink, M. A. Cohen Stuart, and W. Norde, *Colloids and Surfaces A*, 2004, **242**, 146–155.

[58] J. Xia, K. Mattison, V. Romano, P. L. Dubin, and B. B. Muhoberac, *Biopolymers*, 1997, **41**, 359–365.

[59] Y. Xu, M. Mazzawi, K. Chen, L. Sun, and P. L. Dubin, *Biomacromolecules*, 2011, **12**, 1512–1522.

[60] J. A. Galbraith and M. Terasaki, *Mol. Biol. Cell*, 2002, **14**, 1808–1817.

[61] C. Palm-Apergi, A. Lorents, K. Padari, M. Pooga, and M. Hällbrink, *J. Fed. Am. Soc. Exp. Biol.*, 2009, **23**, 214–223.

[62] A. I. Oparin, *The Origin of Life*, Dover Publications, 1953.

[63] J. D. Bernal, *The Origin of Life*, Weidenfeld and Nicholson, London, 1967.

[64] T. N. Evreinova, T. W. Mamontova, V. N. Karnauhov, S. B. Stephanov, and U. R. Hrust, *Origin of Life*, 1974, **5**, 201–205.

[65] F. Dyson, *Origins of Life*, Cambridge University Press, 1999.

[66] H. Walter and D. E. Brooks, *FEBS Lett.*, 1995, **361**, 135–139.

[67] P. Li, S. Banjade, H.-C. Cheng, S. Kim, B. Chen, L. Guo, M. Llaguno, J. V. Hollingsworth, D. S. King, S. F. Banani, P. S. Russo, Q.-X. Jiang, B. T. Nixon, and M. K. Rosen, *Nature*, 2012, **483**, 336–340.

[68] A. A. Hyman and K. Simons, *Science*, 2012, **337**, 1047–1049.

[69] I. K. Voets, A. de Keizer, and M. A. Cohen Stuart, *Adv. Coll. Int. Sci.*, 2009, **147–148**, 300–318.

[70] I. K. Voets, *Ph.D. thesis*, Wageningen University, 2008.

[71] Y. Yan, A. de Keizer, M. A. Cohen Stuart, M. Drechsler, and N. A. M. Besseling, *J. Phys. Chem. B*, 2008, **112**, 10908–10914.

[72] S. Lindhoud, *Ph.D. thesis*, Wageningen University, 2009.

[73] J. F. Tan, H. P. Too, T. A. Hatton, and K. C. Tam, *Langmuir*, 2006, **22**, 3744–3750.

[74] K. Köhler, P. M. Biesheuvel, R. Weinkamer, H. Möhwald, and G. B. Sukhorukov, *Phys. Rev. Lett.*, 2006, **97**, 188301.

[75] Y. Yan, A. A. Martens, N. A. M. Besseling, F. A. de Wolf, A. de Keizer, M. Drechsler, and M. A. Cohen Stuart, *Angew. Chem. Int. Ed.*, 2008, **47**, 4192–4195.

[76] R. M. Capito, H. S. Azevedo, Y. S. Velichko, A. Mata, and S. I. Stupp, *Science*, 2008, **319**, 1812–1816.

[77] M. Lemmers, J. Sprakel, I. K. Voets, J. van der Gucht, and M. A. Cohen Stuart, *Angew. Chem. Int. Ed.*, 2010, **49**, 708–711.

[78] S. C. Gregory *et al.*, *Nature*, 2006, **441**, 315–321.

[79] T. Vermonden, J. van der Gucht, P. de Waard, Marcelis A. T. M., N. A. M. Besseling, E. J. R. Sudhölter, G. J. Fleer, and M. A. Cohen Stuart, *Macromolecules*, 2003, **36**, 7035–7044.

[80] F. Oosawa, *Polyelectrolytes*, Marcel Dekker Inc., 1971.

[81] H. Dautzenberg and B. Philipp, *Polyelectrolytes*, Hanser Publishers, 1994.

[82] J. Th. G. Overbeek, *Colloids and Surfaces*, 1990, **51**, 61–75.

[83] E. S. Reiner and C. J. Radke, *Adv. Coll. Int. Sci.*, 1993, **47**, 59–147.

[84] J. Th. G. Overbeek and M. J. Voorn, *J. Cell. Comp. Phys.*, 1957, **49**, 7–26.

[85] M. J. Voorn, *Ph.D. thesis*, University Utrecht, 1956.

Part I

Stability

Chapter 2

Energy and entropy of interaction between oppositely charged polymers, particles and planar surfaces

In this Chapter we consider the thermodynamic driving forces for interactions of oppositely charged colloids. We solve the Poisson-Boltzmann equation for oppositely charged plates, cylindrical polymers and spherical particles and explicitly evaluate the contributions of the electric field energy and the ion entropy to the free energy of interaction. We mainly focus on interactions at constant surface charge, but we derive equivalent expressions for interactions at constant surface potential and interactions between surfaces with ionisable groups that are subject to charge regulation. For planar surfaces at low surface charge, the contributions of the field energy and the ion entropy to the interaction free energy are equal, when two surfaces are in sufficiently close contact. However, at high surface charge the interaction free energy is dominated by entropic terms. These classical results change significantly for curved electrical double layers. For highly curved, convex, double layers at low surface charge, the interaction free energy is strongly dominated by the electric field energy. When the surface charge increases, a cross-over to entropy-dominated interactions is found. Our approach can be extended to any combination of surfaces with like or opposite charges, at constant charge, constant potential or subject to charge regulation. Comparison to complexation in practical situations reveals that, in general, complexation is driven by a combination of energetic and entropic terms, and neither can be neglected.

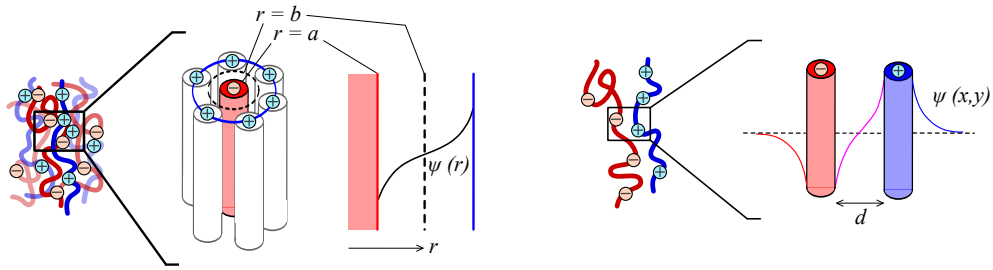

2.1 Introduction

Complexation between oppositely charged macromolecules, proteins or colloidal particles in aqueous solutions is a common phenomenon in nature and in man-made systems. It is driven by a decrease of the free energy of the interacting electrical double layers. Complexation can manifest itself as flocculation or coagulation of particles,[1–3] proteins[4–6] or polymers,[7,8] or as complex coacervation into dense liquid-like phases.[7–10]

The free energy of a single electrical double layer or a set of interacting double layers can be written as a sum of electric field energy, ion entropy and a term that accounts for the chemical preference of charge-determining ions for the surface over the bulk.[11] Which of these contributions dominates the interaction depends on the experimental system and conditions under consideration. Hence, it comes to no surprise that this issue has given rise to much debate,[7,12,13] in some cases leading to strongly opinionated conclusions that complexation is entirely entropy-driven.[7,14–17]

In applying the theory of interacting double layers to real systems, several aspects have to be considered. First of all, the measurement technique applied most often in studies on polyelectrolyte complexation, isothermal titration calorimetry (ITC), gives an overall enthalpy change, including besides electrostatic energy, also hydrogen bonding energy and solvation energy. The overall free energy change then follows from fits to a binding model. However, classical binding models are usually insufficient to describe charge-driven complexation, since it is often very strong at low salt concentrations and may follow a complicated mechanism.[12] As a result, uncertainties in the free energy of complexation are usually large. Another point of consideration is the fact that for heterointeraction, the interacting species are usually not identical in shape, flexibility and hydrophobicity. Nevertheless, these aspects give rise to varying contributions of electrical energy and entropy to the free energy of interaction, as we will show here.

In Poisson-Boltzmann theory of interacting double layers, explicit separation of the complexation free energy into energetic and entropic terms is straightforward. For a single plate with an electrical double layer Overbeek showed that electrical energy and ion entropy contribute equally to the free energy of the electrical double layer in the limit of small surface potentials ($\psi^{\mathrm{s}} < k_{\mathrm{B}}T/e$).[11] Bringing two such planar surfaces with opposite charges in contact, is driven by both a decrease of the electric field energy and an increase in entropy due to the release of ions from the respective electrical double layers. However, in the limit of high surface potentials, the electrical energy of a single electrical double layer is much smaller than the loss of entropy of the ions in the double layer. Hence, interactions between two highly charged, planar surfaces are driven mainly by the entropy increase due to electrolyte release.

McCormack et al. elaborated this for the free energy of an electrical double layer near a planar surface with ionisable groups.[18] They combined their final expressions for energy and entropy and report only overall free energy changes. Biesheuvel et al. followed a slightly different approach by writing the free energy as a sum of surface and volume terms for cylindrical surfaces with ionisable groups,[19] and spherical surfaces without[4] and with ionisable groups.[20] They used the overall free energy to construct phase diagrams for polyelectrolyte and protein complexation. Finally, Ou and Muthukumar explicitly evaluated energetic and entropic contributions to the free energy in a Langevin dynamics simulation of flexible polyelectrolytes in good solvent.[21] They showed that complexation is driven by a strong decrease in electrical energy for weakly charged polyelectrolytes, with ion entropy playing only a minor role. For highly charged polyelectrolytes, the complexation changes from energy-dominated to entropy-dominated.

In this Chapter we consider the energy and entropy of interaction between various oppositely charged surfaces. The surfaces may be planar, cylindrical or spherical. The charge density on the two colloidal surfaces (particles) is always considered to be of opposite sign in the calculations, but the theory we present is of general validity, irrespective of the charge and the exact nature of the surface charging process.

The planar geometry is of use for colloidal particles that are large relative to the Debye screening length. It can, for instance, be used to describe the internal swelling of clay particles. In addition, combined with the Derjaguin approximation, it can be used to predict force-distance and energy-distance curves between curved interfaces from the pressure-distance curves between planar surfaces. Cylindrical rods may be representative for many linear polyelectrolytes, such as hyaluronic acid, DNA, which are both natural polyelectrolytes, and poly(styrene sulphonate), a synthetic polyelectrolyte. Charged spherical particles are often used to approximate proteins, nanoparticles or colloidal particles in low dielectric media.

We distinguish two approaches to evaluate the free energy of complexation (see Figure 2.1 and Section 2.2.3). In the first approach, we consider the complexation of many oppositely charged particles or polyelectrolytes into large aggregates or complex coacervates. We approximate these interactions using the heterogeneous cell model developed by Biesheuvel et al.[4,19,20] The heterogeneous cell model is considered to be a good approximation both for homogeneous dilute phases, and for dense liquid-like complex coacervate phases, while it is possibly less suited in phases of intermediate density and in flocculated systems.[22]

In the second approach, we consider the classical problem of interactions between pairs of oppositely charged particles. We solve the Poisson-Boltzmann equation for such pairs using the finite element method.[23] For planar surfaces there is no difference between these approaches. In general, complexation can be driven by changes in either electrical energy, or ion entropy, or by changes in both. As we will show, not only the

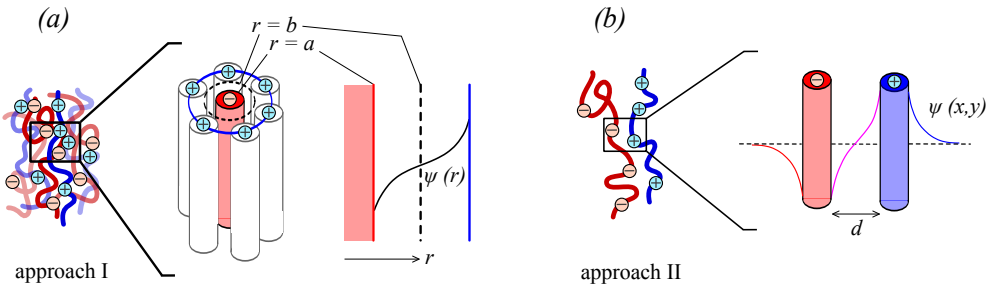

Figure 2.1: Schematic illustration of the two approaches we distinguish to study the free energy of interaction between plates, cylinders and spheres. (a) In approach I, we consider complex coacervates, for which we approximate the interactions using the heterogeneous cell model. In this illustration only one cell for the polyanions is shown. The boundary condition is assumed homogeneous, and the electrostatic potential is a function of the radial coordinate r only. The polycations are likewise described by a cylindrical cell with a polycation at its centre and with the interactions with surrounding polyanions smeared out at the edge. (b) In approach II, we consider pairs of oppositely charged cylinders and spheres, for which we evaluate the interactions using the finite element method. The electrostatic potential is a function of two coordinates x and y.

surface charge density, but also the salt concentration and the shape of the interacting particles has a strong influence on which of these driving forces prevails.

2.2 Theory

2.2.1 The Poisson-Boltzmann equation

We consider an open isothermal system with volume V, containing ions of type i, valency z_i and bulk number density n_i^{b} (in m^{-3}). The volume contains a number of charged surfaces (of type j). These surfaces can be planar, cylindrical or spherical. We write the electrostatic potentials as ψ, with dimensionless form $y = e\psi/k_{\mathrm{B}}T$, for which we assume the Poisson-Boltzmann equation (PB) to hold. For each surface, we only consider the diffuse part of the electrical double layer (EDL), and we do not explicitly include Stern layers.

We assume that the volume and temperature are not affected by a complexation between the charged objects. The combination of energy and entropy terms for this volume yields a grand potential Ω.[24,25] In most experiments the total number of ions, instead of the bulk number density, is a fixed quantity. However, the total volume that is considered is often large and at sufficiently high ion concentrations, the changes in bulk number densities of the ions upon complexation are negligible.[20] Also in the case of complex coacervation, the dense complex coacervate is in equilibrium with

a large volume of a dilute aqueous phase with an effectively constant bulk number density of ions (see Chapter 3).[9,26] Given these assumptions, we can simply consider the Helmholtz free energy F of the system, as outlined below in detail.

For our description of the electrostatic potential near a charged surface, we start from the Poisson equation,

$$\vec{\nabla}^2\psi = -\frac{\rho(\vec{r})}{\epsilon_\mathrm{r}\epsilon_0} \tag{2.1}$$

where ρ is the volume charge density in the electrolyte solution. The distribution of ions in an electric field, which constitutes the charge density profile ρ, is – in the mean-field approximation for ions as point charges – given by the Boltzmann equation,

$$\rho(\vec{r}) = \sum_i z_i e n_i = \sum_i z_i e n_i^\mathrm{b} \exp\left(-\frac{z_i e\psi}{k_\mathrm{B}T}\right) . \tag{2.2}$$

Combining Equations 2.1 and 2.2 leads to the Poisson-Boltzmann (PB) equation for the electrostatic potential in electrolyte solutions,

$$\vec{\nabla}^2\psi = -\sum_i \frac{z_i e n_i^\mathrm{b}}{\epsilon_\mathrm{r}\epsilon_0 k_\mathrm{B}T} \exp\left(-\frac{z_i e\psi}{k_\mathrm{B}T}\right) . \tag{2.3}$$

For a $z\!:\!z$ electrolyte and using dimensionless potentials, we can write the PB equation as

$$\vec{\nabla}^2 y = \kappa^2 \sinh(y) \tag{2.4}$$

where κ^{-1} is the Debye screening length, defined by

$$\kappa^2 = \frac{\sum_i z_i^2 e^2 n_i^\mathrm{b}}{\epsilon_\mathrm{r}\epsilon_0 k_\mathrm{B}T} \tag{2.5}$$

which for a $1\!:\!1$ electrolyte reduces to

$$\kappa^2 = \frac{2N_\mathrm{Av}\, e^2 {c_\mathrm{s}}^\mathrm{b}}{\epsilon_\mathrm{r}\epsilon_0 k_\mathrm{B}T} = 8\pi\ell_\mathrm{B} N_\mathrm{Av} {c_\mathrm{s}}^\mathrm{b} \tag{2.6}$$

where ${c_\mathrm{s}}^\mathrm{b}$ is the bulk concentration of the $1\!:\!1$ electrolyte in mM and $\ell_\mathrm{B} = e^2/4\pi\epsilon_\mathrm{r}\epsilon_0 k_\mathrm{B}T$ is the Bjerrum length, which is 0.71 nm in pure water at room temperature.

Equation 2.3 or 2.4 can be solved either analytically or numerically. Analytical solutions exist for many geometries in the limit of small potentials ($y \ll 1$) or far away from the charged surface ($\kappa x \gg 1$). We discuss our approaches to solve the PB equation numerically in Section 2.2.3.

2.2.2 Free energy of complexation

The free energy of interaction between charged surfaces with an EDL can be written as a sum of electrical energies $U_{\rm el}$, entropic contributions $-TS_{\rm el}$ for free, diffuse ions in solution, and contributions that account for the chemical preference of charge-determining ions ($F_{\rm ch}$), which include both energetic and entropic terms,

$$F = U_{\rm el} - TS_{\rm el} + F_{\rm ch} \,. \tag{2.7}$$

The process of complexation involves bringing two or more charged species from large separation distances to a finite separation d. The *interaction* free energy ΔF is therefore the difference between these two cases: $\Delta F = F(d) - F(\infty)$. For the calculation of these interaction free energies the nature of the surface charging process is important. We distinguish surfaces with a constant surface charge σ, with a constant surface potential ψ^0 and with a constant density of ionisable groups N^0 (charge regulation). For reasons of clarity, we restrict ourselves in the main text to surfaces at constant surface charge. We give the expressions for surfaces at constant surface potential and at charge regulation in the Appendix to this Chapter.

For surfaces with a constant surface charge, such as strong synthetic polyelectrolytes, DNA, sulphonate-coated nanoparticles and the colloidal particles we use in Chapter 6, the chemical component $F_{\rm ch}$ is independent of the separation d between two surfaces. This term will therefore not contribute to the *interaction* free energy ΔF^σ. The interaction free energy for surfaces at constant surface charge thus follows from $\Delta F^\sigma = \Delta U_{\rm el} - T\Delta S_{\rm el}$.[11] The electric field energy is given by[11]

$$U_{\rm el} = \frac{\epsilon_{\rm r}\epsilon_0}{2} \int\limits_V (\vec{\nabla}\psi)^2 \, {\rm d}V \tag{2.8}$$

which for a 1:1 electrolyte reduces to

$$\frac{U_{\rm el}}{k_{\rm B}T} = \frac{n^b}{\kappa^2} \int\limits_V (\vec{\nabla}y)^2 \, {\rm d}V \,. \tag{2.9}$$

As this expression contains the effective permittivity $\epsilon_{\rm r}\epsilon_0$, $U_{\rm el}$ is actually a free energy, including entropic contributions from solvent molecules that respond to the electric field, as we have discussed in Chapter 1. To distinguish this contribution, due to the electric field energy, from the translational entropy associated with the ions in the double layer, we denoted it $U_{\rm el}$.

The entropy contribution to the free energy, associated with the ions in the EDL, is the difference between the translational entropy of the ions that are confined to the EDL and the translational entropy that the same ions would have in a fully mixed solution at $\psi = 0$. This entropy can be written as[11,18]

$$-T\Delta S_{\mathrm{el}} = -k_{\mathrm{B}}T \int_V \sum_i n_i^b \left\{ \left(\frac{z_i e\psi}{k_{\mathrm{B}}T} + 1 \right) \exp\left(-\frac{z_i e\psi}{k_{\mathrm{B}}T} \right) - 1 \right\} \mathrm{d}V \tag{2.10}$$

which for a 1:1 electrolyte reduces to

$$-\frac{T\Delta S_{\mathrm{el}}}{k_{\mathrm{B}}T} = 2n^{\mathrm{b}} \int_V \left(y\sinh(y) - \cosh(y) + 1 \right) \mathrm{d}V \,. \tag{2.11}$$

A combination of Equations 2.9 and 2.11 gives the following expression for the free energy of the electrical double layers surrounding surfaces at constant surface charge in a 1:1 electrolyte:

$$\frac{F^\sigma}{k_{\mathrm{B}}T} = \frac{n^{\mathrm{b}}}{\kappa^2} \int_V (\vec{\nabla} y)^2 \, \mathrm{d}V + 2n^{\mathrm{b}} \int_V \left(y\sinh(y) - \cosh(y) + 1 \right) \mathrm{d}V \,. \tag{2.12}$$

Using this Equation, the interaction free energy follows from $\Delta F^\sigma = F^\sigma(d) - F^\sigma(\infty)$. This equation is often simplified by partial integration of $y\sinh(y)$, because U^{el} and $-T\Delta S^{\mathrm{el}}$ contain partially cancelling terms,[18,19]

$$\frac{F^\sigma}{k_{\mathrm{B}}T} = -n^{\mathrm{b}} \int_V \left(\frac{1}{\kappa^2} (\vec{\nabla} y)^2 + 2\left(\cosh(y) - 1 \right) \right) \mathrm{d}V + \sigma \int_{A_j} \psi_j^{\mathrm{s}} \, \mathrm{d}A \tag{2.13}$$

where the last term contains an integration over all surfaces. We will use the full Equation 2.12 because it distinguishes clearly between energetic and entropic terms and thus allows comparing the energetic and entropic contributions to the free energy of complexation. For interactions at constant surface charge, Equations 2.8-2.12 suffice, as no additional chemical terms need to be considered for the *interaction* free energy. For interactions at constant surface potential or subject to charge regulation, an additional chemical term contributes to the interaction free energy, as described in the Appendix to this Chapter.

Finally, we note that minimisation of the free energy as expressed in Equation 2.12 with respect to $n_\pm$ and with respect to ψ yields the Poisson-Boltzmann equation (Equation 2.3), which thus corresponds to the thermodynamic equilibrium state.[27]

2.2.3 Solving the Poisson-Boltzmann equation numerically

After solving the Poisson-Boltzmann equation (Equation 2.4), we can evaluate the free energy of complexation, following the strategy outlined above. We distinguish two approaches to study the free energy of complexation (see Figure 2.1).

In the first approach (I), we consider the complexation of many oppositely charged particles or polyelectrolytes into large aggregates or complex coacervates. We approximate these interactions using the heterogeneous cell model developed by Biesheuvel et al. [4,19,20]

Briefly, each polymer chain or spherical particle occupies a (cylindrical or spherical) cell in which the electrostatic potential in the diffuse part of the EDL is given by the PB equation in cylindrical or spherical coordinates, respectively, and the boundary conditions at the inner cell radius $r = a$, which corresponds to the surface of the cylindrical polymer or spherical particle, and the outer cell radius $r = b$ (see Figure 2.1). In theory, an unlimited number of different polyelectrolytes or particles with like and opposite charges can be included, as well as electrolytes other than a 1 : 1 electrolyte. In this Chapter, we focus on symmetric mixtures of oppositely charged polyelectrolytes and particles in a 1:1 electrolyte.

For instance, for cylinders with a constant surface charge, the boundary condition at $r = a$ is given by

$$\left.\frac{\mathrm{d}y}{\mathrm{d}r}\right|_{r=a} = -\frac{2\lambda\ell_\mathrm{B}}{a} \tag{2.14}$$

where λ is the linear line charge density in m^{-1}. The boundary condition at $r = b$ is assumed homogeneous along the outer cell radius and is given by

$$\sum_j f_j \left.\frac{\mathrm{d}y_j}{\mathrm{d}r}\right|_{r=b_j} = 0 \tag{2.15}$$

where f_j is the fraction of cylindrical cells of type j. The values of the outer cell radii b_j of the various cells are chosen such that the total free energy goes through a minimum as a function of the positions b_j, while making sure that all cells together are space-filling. Equation 2.15 ensures overall electroneutrality via the field strength at the outer edges of the various cells. Therefore, all cells are considered simultaneously in the calculations.

We solve the PB equation for complexes of oppositely charged cylindrical polymers and spherical particles using a finite difference scheme and numerically evaluate the integrals in Equation 2.12. The interaction free energy follows from the difference between the free energy at infinite separation and at finite separation d, corresponding to a density $\phi = a^2/b^2$ for complexes of cylinders or $\phi = a^3/b^3$ for complexes of spherical particles, when both types of particles have the same inner and outer cell radii a and b.

In the second approach (II), we consider the interactions between pairs of oppositely charged particles or cylinders (see Figure 2.1). These pair interactions have been considered, for instance, in modifications of the DLVO theory, and are at play

in Molecular Dynamics (MD) and Monte Carlo (MC) simulations of two oppositely charged polyelectrolytes.[21,28] In these cases, the PB equation no longer reduces to a one-dimensional problem, but the solution becomes radially asymmetric. We approximate these interactions by pairs of parallel cylinders and spheres in a 2-dimensional plane, where the electrostatic potential follows the 2-D Poisson-Boltzmann equation (Equation 2.3). We solve the PB equation for such pairs using the finite element method (FEM).[23] Similar to approach I, we calculate the interaction free energy by numeric integration. To accommodate the solution of the PB equation by the finite element method, we write its weak form[29]

$$\int_V \vec{\nabla} y \cdot \vec{\nabla} v + \kappa^2 \sinh(y) \cdot v \; \mathrm{d}V = 0 \tag{2.16}$$

where v is a test function. A detailed overview of the FEM for solving the PB equation is given elsewhere.[30,31]

2.3 Results and discussion

The theory outlined in the previous Section and the two approaches we distinguished to study the interaction free energy are generally valid for all kinds of interacting particles, both of like and opposite charge. In this Chapter, we focus on the interactions of particles with a constant, fixed surface charge. The values of the surface charges on the interacting particles are exactly opposite to each other and the mixture of oppositely charged particles is symmetric. To begin with, we will analyse the free energy of a *single* electrical double layer (EDL) of a planar, cylindrical and spherical surface (Section 2.3.1). We will use the expressions from the previous Section to separate energetic and entropic contributions to the free energy of the EDL. In Section 2.3.2 we will discuss the interaction free energy of mixtures of oppositely charged particles in a heterogeneous cell model, following approach I. Finally, in Section 2.3.3 we will discuss pair interactions between oppositely charged particles, calculated using approach II.

2.3.1 Single electrical double layers

The free energy associated with a single electrical double layer near a charged surface is expressed by Equation 2.12. For planar surfaces, both terms in this expression can be integrated analytically, to[11,32]

$$\frac{e\,U_{\mathrm{el}}}{\sigma k_{\mathrm{B}} T} = \frac{1}{s}\left(\sqrt{s^2+1}-1\right) \tag{2.17}$$

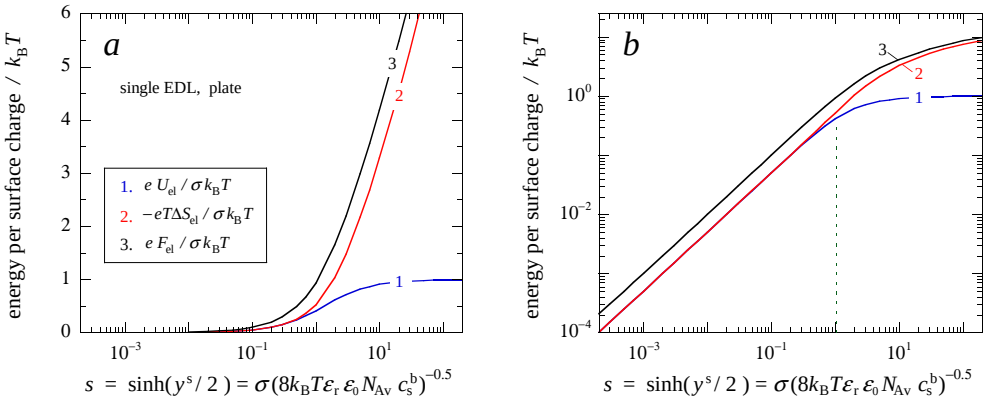

Figure 2.2: Free energy of the electrical double layer of a charged planar surface on (a) a linear-logarithmic and (b) a double-logarithmic scale as a function of the dimensionless surface charge s. The contributions from the electric field energy (U_{el}) and the ion entropy ($-T\Delta S_{\mathrm{el}}$) to the free energy (F_{el}) are both shown.

$$-\frac{e\,T\Delta S_{\mathrm{el}}}{\sigma k_{\mathrm{B}}T} \;=\; 2\ln\left(s+\sqrt{s^2+1}\right)-\frac{3}{s}\left(\sqrt{s^2+1}-1\right) \tag{2.18}$$

where $s = \sigma/\sqrt{8k_{\mathrm{B}}T\epsilon_{\mathrm{r}}\epsilon_0 N_{\mathrm{Av}}{c_{\mathrm{s}}}^{\mathrm{b}}} = \sinh(e\psi^0/2k_{\mathrm{B}}T)$ is the dimensionless surface charge, and ${c_{\mathrm{s}}}^{\mathrm{b}}$ is the bulk concentration of 1:1 electrolyte in mM.

We show both contributions and their sum as a function of s in Figure 2.2. In the limit of small surface charge, the electric field energy and ion entropy associated with the EDL are exactly equal.[11] At high surface charge, the electrical energy per surface charge (eU_{el}/σ) levels off to 1 $k_{\mathrm{B}}T$, whereas the entropic term keeps increasing. As a result, the total free energy of a single EDL near a planar surface is dominated by the entropy of the counterions that are confined to the double layer. We note that surface charges as high as $s = 10$ ($\sigma = 0.1$ C/m^2 for ${c_{\mathrm{s}}}^{\mathrm{b}} = 10$ mM) are seldom reached in practice.

For electrical double layers near a cylindrical or a spherical surface, the situation is different. Analytical expressions for U_{el} and $-T\Delta S_{\mathrm{el}}$ are not available, but we can solve the PB equation for a single cylinder or sphere with $\mathrm{d}y/\mathrm{d}r|_{r\to\infty} = 0$ and evaluate the integrals in Equation 2.12 numerically. In Figure 2.3 and 2.4 we show both contributions for a single EDL near a cylindrical and a spherical surface, respectively. In both cases we display the results for different values of the curvature of the electrical double layer κa, as a function of a dimensionless surface charge. For cylinders the dimensionless surface charge is given by $\lambda\ell_{\mathrm{B}}$ with λ the line charge density (m^{-1}) and ℓ_{B} the Bjerrum length. For spheres the dimensionless, normalised surface charge is

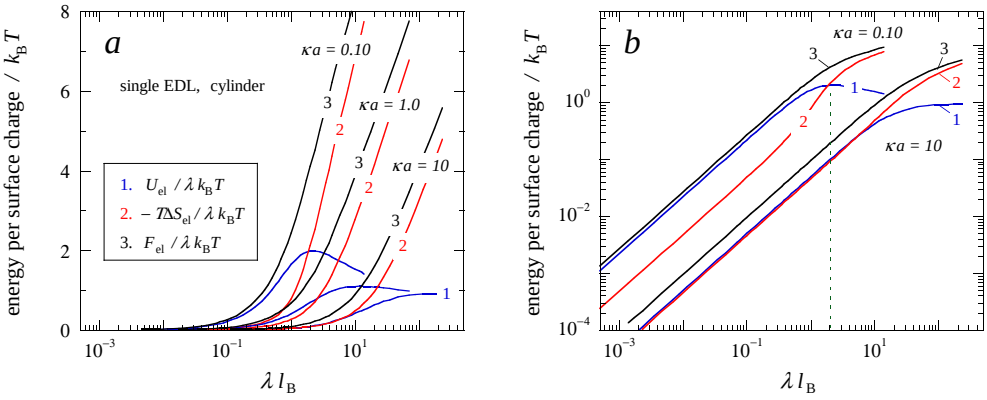

Figure 2.3: Same plots as in Figure 2.2, for the EDL of a cylinder with varying κa, as indicated by the labels.

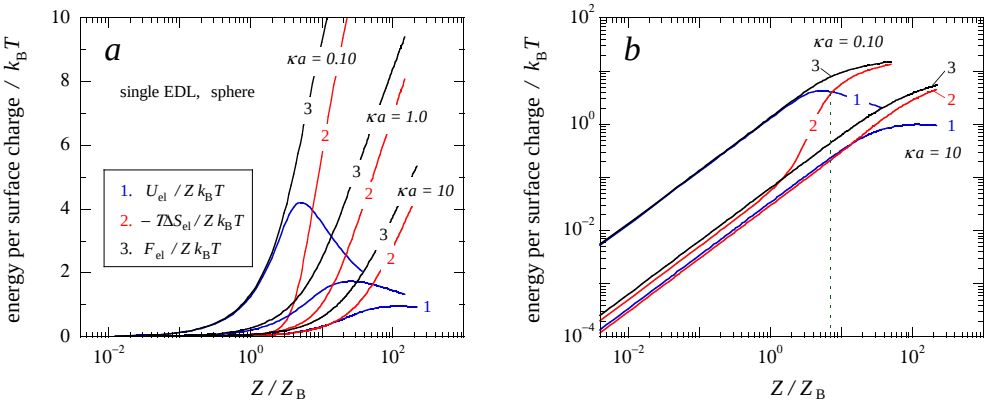

Figure 2.4: Same plots as in Figure 2.2, for the EDL of a sphere with varying κa, as indicated by the labels.

given by Z/Z_B with Z the charge number and Z_B the charge number of a sphere of the same size for which the total free energy F of the EDL equals 1 $k_B T$.

For cylinders with $\kappa a \ll 1$, the energetic and entropic contributions to the interaction free energy are no longer equal at low surface charges, as we found for planar surfaces. Instead, the electrical energy dominates the total free energy of the EDL at low surface charge, with the effect becoming larger for a stronger curvature of the EDL. At high surface charge, the electrical energy per surface charge (U_{el}/λ) starts levelling off again to about 1 $k_B T$, and we find a cross-over around $\lambda \ell_B = 2$ for $\kappa a = 0.10$ to a regime where the entropy dominates the free energy of a single EDL

again, analogous to the situation for planar surfaces.

As κa increases, the curvature of the EDL decreases and the surface resembles a planar surface again. Consequently, we find that U_{el}/λ and $-T\Delta S_{\mathrm{el}}/\lambda$ are approximately equal for $\kappa a = 10$ at low surface charge and $-T\Delta S_{\mathrm{el}}/\lambda \gg U_{\mathrm{el}}/\lambda$ at high surface charge.

For spherical surfaces, the effects described above become even more pronounced, as shown in Figure 2.4. Nevertheless, we recover the results for planar surfaces in the limit of high κa and at high surface charge.

2.3.2 Complexation involving many particles

In the case that two or more oppositely charged surfaces are brought into contact, part of the free energy F in Figures 2.2–2.4 is gained. In general, the total decrease of free energy and the relative contributions of the electric field energy and ion entropy to this decrease will depend on the number of interacting species, their charges and the final separation distance d.

For planar surfaces, we can evaluate the free energy of interaction of *two* oppositely charged plates as a function of their separation d by solving the PB equation and calculating the integrals in Equation 2.12 for various d. We note that the integrals remain finite in the limit $d \to 0$ for surfaces at constant, opposite charge, such that the contact free energy ($\Delta F^{\sigma}_{d\to 0} = F^{\sigma,(2)}(0) - F^{\sigma\,(2)}(\infty) = -2F^{\sigma,(1)}(\infty)$) can be evaluated.

Figure 2.5a shows the contributions of the electric field energy (ΔU_{el}) and of the ion entropy ($-T\Delta S_{\mathrm{el}}$) to the free energy of interaction for various surface charges. The interaction free energy of surfaces at constant surface charge is the sum of these two contributions and decreases monotonically with decreasing separation distance d. As the double layers of the two surfaces start overlapping, the entropy term decreases continuously. The energy term on the other hand, exhibits a 'barrier' that increases with increasing surface charge. The separation d of the maximum in ΔU_{el} corresponds to the condition that the potential gradient has become almost constant between the plates.

When two oppositely charged surfaces with a low surface charge are brought into contact ($d = 0$), the change in free energy ΔF contains exactly equal contributions from the electric field energy and the ion entropy, as can be seen in Figure 2.5a. This also follows from Figure 2.2, where the electric field energy and ion entropy of a single EDL were found to be equal in the limit of low surface charge. As the surface charge increases, the entropic term starts dominating the contact free energy, similar to our findings in Figure 2.2. In general, the contact free energy of two interacting, oppositely charged plates with equal charge densities can be calculated from Figure 2.2

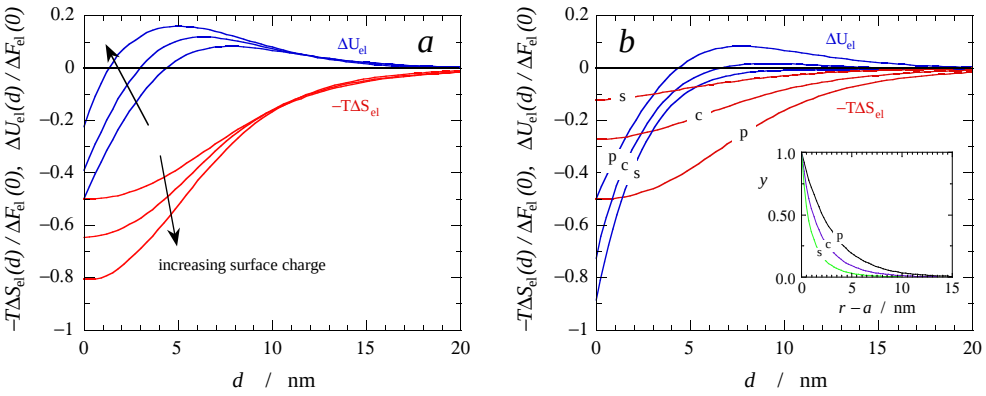

Figure 2.5: (a) Profile of the normalised energy and entropy of interaction between two oppositely charged planar surfaces as a function of their separation d, at a constant surface charge, in 10 mM 1 : 1 electrolyte, for various surface charge densities, increasing in the direction of the arrows. (b) Profiles of the normalised energy and entropy of interaction of oppositely charged planar surfaces (p), cylinders (c) and spherical (s) particles, as a function of their separation d, calculated using the heterogeneous cell model, following approach I. All surfaces have a surface potentials at infinite separation of $y^0 = 1$. The inset shows the electrostatic potential profile of a single plate (p), cylinder (c) and sphere (s) at the same surface charge.

according to $\Delta F^{\sigma}_{d\to 0} = -2F^{\sigma\,(1)}(\infty) = -2U^{(1)}_{\rm el}(\infty) + 2T\Delta S^{(1)}_{\rm el}(\infty)$, where $F^{\sigma\,(1)}(\infty)$ is the electrical free energy of a single EDL.

For cylindrical and spherical surfaces, we evaluate the free energy of interaction in dense complexes of many particles, using the heterogeneous cell model, following approach I (see Figure 2.1). In Figure 2.5b we show the same interaction profiles as in Figure 2.5a for planar surfaces, and cylindrical and spherical surfaces with equal charge densities. These profiles were calculated for surfaces with a relatively low surface charge, corresponding to $y^0_j(\infty) = 1$. We find that the decrease in field energy upon bringing the oppositely charged surfaces together, becomes larger when the surfaces are cylindrical or spherical. At the same time, the entropic contribution to the interaction free energy becomes relatively smaller. These findings are similar to our findings in Figures 2.3 and 2.4 for a single EDL surrounding a cylinder and a sphere, respectively. We can explain these findings from the electrostatic potential near these surfaces (inset in Figure 2.5b). The electrostatic potentials decay more rapidly close to highly curves surfaces. Consequently, the electric field is stronger there and the decrease in field energy due to overlap of parts of the double layer, especially close to the curved surfaces, is larger. At the same time, the magnitude of the electrostatic potential is not larger than in the case of planar surfaces. At equal distances from the surface, it is even lower. Consequently, the accumulation of

counterions in a curved double layer is not much larger than in a planar double layer, after correction for the increase in volume with increasing distance. Therefore, the increase in translational entropy due to release of ions upon overlap of the electrical double layers is not larger.

To calculate the free energy of complexation for cylinders and spheres, we must choose the density ϕ of the complex coacervate, and consequently, the average distance between the cells d. We note that in the limit of $d \to 0$, the complexation free energy of cylinders and spheres is simply given by $\Delta F^{\sigma}_{d\to 0} = -2F^{\sigma\,(1)}(\infty) = -2U^{(1)}_{\mathrm{el}}(\infty) + 2T\Delta S^{(1)}_{\mathrm{el}}(\infty)$, analogous to the interaction between planar surfaces. Hence, the free energy of complexation is simply given by the values in Figures 2.3 and 2.4, taking into account a factor -2. We note that the integrals in this limit $d \to 0$ remain finite only for surfaces at constant surface charge or subject to charge regulation, but not for surfaces at constant potential.

The complexation free energy in the limit $d \to 0$ would correspond to a polymer volume fraction of unity ($\phi \to 1$), which is never realised in practice. Nonetheless, this limit does allow for a simple comparison of the relative importance of contributions of the electric field energy and ion entropy to the free energy of complexation. We will therefore apply it in Section 2.4, where we compare our results for approach I and II to some experimental examples of complexation. In reality, complex coacervates have a lower density than the fully packed limit of $\phi \to 1$. As shown in Figure 2.5b, when assuming $\phi \to 1$, we overestimate the ratio $\Delta U_{\mathrm{el}}/T\Delta S_{\mathrm{el}}$. However, typical polymer densities in a complex coacervate can easily reach $\phi = 0.3$ (see Chapter 3). As a result, the average distance between nearest neighbours in polyelectrolyte complex coacervates ($a = 0.25$ nm) is 0.7 – 0.9 nm. Therefore, the actual interaction energies and entropies will not differ significantly from the values in the limit $\phi \to 1$.

2.3.3 Pair interactions

In the case that only two oppositely charged cylindrical polymers or spherical particles are interacting, we find many similarities with the complexation involving many particles, which we discussed above. Numerically, we evaluate the interaction free energy of pairs of oppositely charged (parallel) cylinders and spheres using the finite element method, following approach II. For planar surfaces, the pair interaction has already been discussed in the previous Section. For cylinders and spheres, we take the interaction free energy as the difference in free energy between an infinite separation and a separation $d = 0.01\kappa^{-1}$.

We show these interaction free energies and the contributions of the electric field energy and the ion entropy in Figures 2.6 and 2.7. As in Figures 2.3 and 2.4, we display the results for different values of κa, as a function of a dimensionless surface charge.

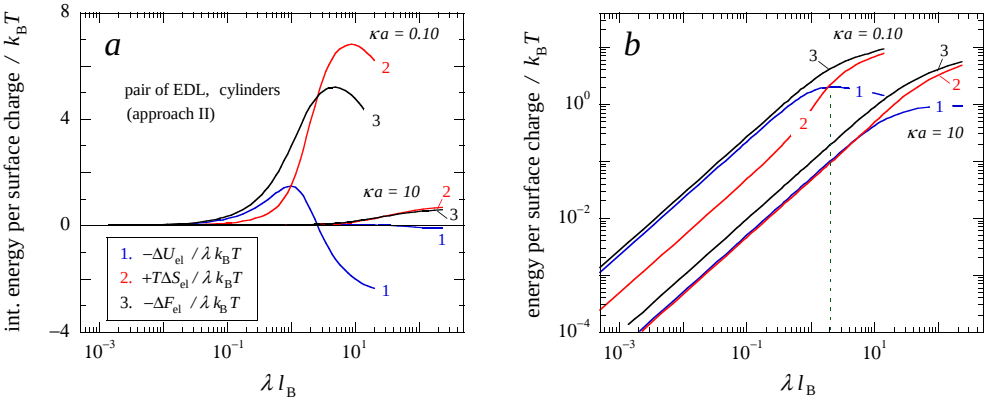

Figure 2.6: Free energy of interaction between pairs of oppositely charged (parallel) cylinders, calculated using the finite element method, following approach II, as a function of the dimensionless line charge density $\lambda\ell_{\mathrm{B}}$. The results for two limiting values of κa are shown on (a) a linear-logarithmic and (b) a double-logarithmic scale. The contributions from the electric field energy ($-\Delta U_{\mathrm{el}}$) and the ion entropy ($T\Delta S_{\mathrm{el}}$) to the negative free energy of interaction ($-\Delta F_{\mathrm{el}}^{\sigma}$) are both shown.

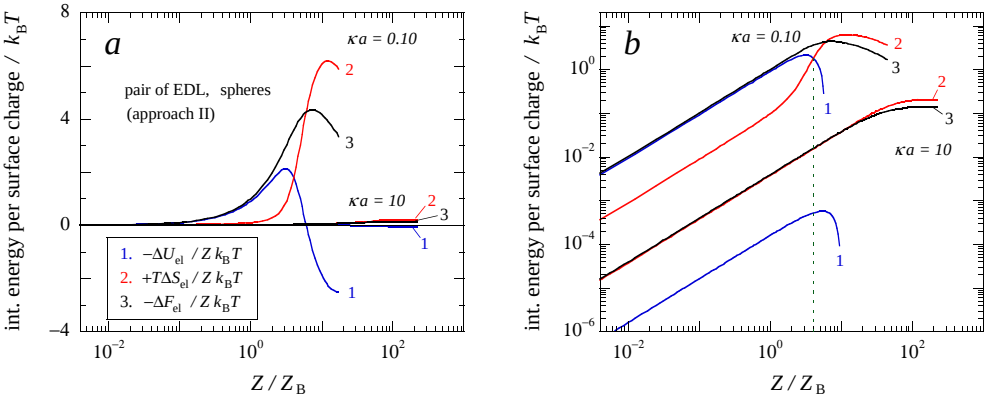

Figure 2.7: Same plots as in Figure 2.7, for pairs of oppositely charged spheres for two limiting values of κa.

For pairs of parallel cylinders at low κa, the electrical energy still dominates the total free energy at low surface charge. Following our discussion in the previous Section, we recognise the process of complexation as driven predominantly by a decrease in electric field energy. At high surface charge, we find again a cross-over to a regime where the entropic term dominates. The cross-over is shifted to slightly lower $\lambda \ell_B$ (cross-over at $\lambda \ell_B \approx 1$ for $\kappa a = 0.10$), compared to the cross-over in interactions between many cylinders, calculated following approach I (see Figure 2.3). Interestingly, the cross-over in Figure 2.6 for $\kappa a = 0.10$ exactly matches the cross-over between energy and entropy found by Ou and Muthukumar in their Langevin dynamics calculations of complexation between two oppositely charged linear polyelectrolytes with $\kappa a \approx 0.10$.[21] At even higher surface charges, we find that the contribution of the electric field energy to the complexation free energy decreases again and even becomes positive (note that the vertical axis in Figure 2.6 denotes $-\Delta F^{\sigma}$). In other words, we find endothermic complexation, similar to the findings of Ou and Muthukumar.[21] This change is caused by the fact that the integral in Equation 2.9 only vanishes in between the two cylinders when they are brought into contact. The contribution of the potential gradients just off the centre of the midplane between the cylinders to U_{el} increases with increasing charge density, and at a certain point this contribution outweighs the favourable decrease in electric field energy upon complexation in between the cylinders.

For weakly curved cylindrical double layers ($\kappa a \gg 1$), we no longer retrieve the same results as for two planar surfaces, because the electrical potentials only cancel out at the plane exactly in between the two cylinders. Instead, the contribution of ΔU_{el} to the free energy becomes smaller than $-T\Delta S_{el}$, even at low surface charge. At high surface charge, again ΔU_{el} becomes positive, but now a cross-over between ΔU_{el} and $-T\Delta S_{el}$ no longer exists.

For pairs of spheres, we find the same effects as described above (see Figure 2.7), but more pronounced, because the EDL surrounding the spheres is more strongly curved than the EDL surrounding a cylinder of identical radius a.

2.4 Comparison with experiments

Our calculations have shown that the question what drives the complexation of oppositely charged colloids can only be answered accurately if the surface charge, the number of interacting colloids, and, most importantly, the geometry and curvature of the interacting colloids is known. We summarise our findings of the effect of curvature of the EDL surrounding the colloids on the relative importance of the energetic and entropic contributions to the interaction free energy at low surface charge in Figure 2.8. The curvature of the EDL is expressed by κa and the relative importance of the

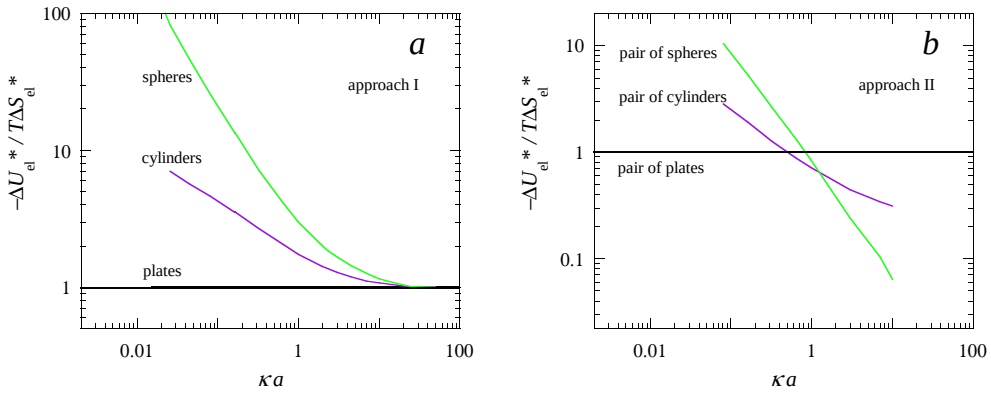

Figure 2.8: (a) Ratio of the energetic and entropic contribution to the interaction free energy of planar, cylindrical and spherical surfaces, calculated from approach I for $d \to 0$, in the limit of low surface charge (indicated by asterisk), as a function of κa. (b) The same ratio for the interaction between pairs of oppositely charged planar surfaces, cylinders and spherical particles, calculated from approach II.

energetic and entropic contributions to the interaction free energy is expressed as a ratio $-\Delta U_{\rm el}/T\Delta S_{\rm el}$.

In Figure 2.8a we show this ratio as a function of κa for the complexation of many particles (approach I), in the limit $d \to 0$. As shown in Figures 2.2 – 2.7, the ratio $-\Delta U_{\rm el}/T\Delta S_{\rm el}$ remains constant up to charge densities of $s \approx 1$ for planar surfaces, $\lambda \ell_{\rm B} \approx 0.5$ for cylinders and $Z/Z_{\rm B} \approx 1$ for spheres. For planar surfaces, the ratio is unity, irrespective of κ, which follows from Equations 2.17 and 2.18. For cylinders and spheres, the ratio is always larger than unity for low surface charges, and becomes larger with decreasing κa. In the limit of high κa, the ratio approaches unity, which is the value we expect for planar surfaces. As discussed above, the limit $d \to 0$ is physically not realistic. Nonetheless, the general dependence of the ratio depicted in Figure 2.8a on κa will remain unchanged when the values at a different d are taken.

In Figure 2.8b we show the same ratio as a function of κa for the interaction between pairs of oppositely charged parallel cylinders and spheres (approach II). For highly curved double layers (small κa), we find that the ratio $-\Delta U_{\rm el}/T\Delta S_{\rm el}$ is larger than unity, similar to Figure 2.8a. For $\kappa a > 1$ however, the ratio becomes smaller than unity, as we discussed in the previous Section, because the integral in Equation 2.9 only vanishes exactly in between the two cylinders. However, when three or more cylinders or spheres form a complex, the situation gradually changes into the situation depicted in Figure 2.8a, where the ratio approaches unity for high κa.

It is informative to compare these ratios and the charge densities where we find a cross-over between the energy and entropy in Figures 2.3, 2.4, 2.6 and 2.7 for various

degrees of curvature of the electrical double layers, to some practical situations.

The B-form of the DNA double helix is a cylinder with a diameter of approximately 2.0 nm ($a \approx 1$ nm). It contains two negative charges per base pair along the strand, and therefore $\lambda\ell_B \approx 4$.[33] Both in dilute aqueous solutions with little salt (e.g., c_s = 10 mM, $\kappa a = 0.3$) and in conditions mimicking the cytosol (c_s = 150 mM, κa = 1.3) complexation involving DNA is likely to be strongly entropy-driven, because in both cases the DNA charge density is much larger than the cross-over charge density in Figures 2.3 and 2.6. Naturally, the actual balance will also depend on the surface charge of the oppositely charged species.

In low dielectric media, charged colloidal particles (a = 1 – 4 μm) may form ionic colloidal crystals.[34] The Debye screening length is typically large, such that $\kappa a \approx$ 0.7 – 3. The surface charge of these colloidal particles is rather low, $Z \approx \pm 100$, corresponding to 1 μC/ m^2. The ratio of energy to entropy contributions to the interaction free energy of these colloids can therefore be estimated from Figure 2.8. As this ratio is much larger than unity for spherical particles with small κa, the complexation into (dense) crystalline phases is likely dominated by contributions from the electric field energy.

Many oppositely charged polyelectrolytes and proteins can form complex coacervates in aqueous solutions (see also Chapters 3 and 4). Many polysaccharides, such as gum arabic,[35] alginate,[36] murein,[37] pectins[38] and chitosan[39] are cylindrical strands with an effective radius a = 0.25 – 0.50 nm. Their charge densities vary from weakly charged ($\lambda\ell_B \approx 0.01$ for gum arabic and gelatin at pH 4, for instance[26]) to rather strongly charged ($\lambda\ell_B \approx 1$ for some highly esterified pectins[38]). For the weakly charged polyelectrolytes, the ratio of energy to entropy contributions to the interactions free energy can be estimated from Figure 2.8. Since this ratio is much larger than unity for cylinders at low κa (e.g., c_s = 30 mM, $\kappa a \approx 0.5$[40]), complex coacervation of weakly charged polysaccharides is likely dominated by a decrease of the electric field energy. On the other hand, many synthetic polyelectrolytes, such as poly(acrylic acid), poly(styrene sulphonate) and poly(N, N-dimethylaminoethyl methacrylate) have a small effective radius (a = 0.25 nm), but a high charge density ($\lambda\ell_B$ = 1 – 2). As can be seen in Figure 2.3, this charge density is close to the point where we find a cross-over between ΔU_{el} and $-T\Delta S_{el}$. At high salt concentrations κa will be large (e.g., c_s = 1.0 M, $\kappa a \approx 3$) and complex coacervation is probably driven by a significant increase in translational entropy of the ions. Nevertheless, the decrease in electric field energy cannot be neglected close to the cross-over point.

As a final example, we consider the complexation of oppositely charged nanoparticles of poly(styrene) and silica in water.[1] These particles have a radius a of 10 – 100 nm. They bear a varying number of surface charges, corresponding to a typical surface charge density of 1 mC/ m^2. The ratio of energy to entropy contributions to the interactions free energy can still be estimated from Figure 2.8. Typical salt

concentrations vary in the experiments, as will κa. For a typical experimental mixture $c_s = 0.1$ mM and $\kappa a \approx 1$. Hence, the effects of the curved electrical double layer play an important role (see Figure 2.8). Complexation is expected to be driven mainly by a decrease of the electric field energy.

2.5 Concluding remarks

Complexation between oppositely charged polymers, particles or planar surfaces with purely electrostatic interactions can be driven by either a decrease of the electric field energy or by an increase in the translational entropy of the ions upon release from the overlapping electrical double layer. Which of these contributions dominates depends strongly on the charge of the surfaces and, less well-known, depends on the curvature of the electrical double layer. For highly charged surfaces and weakly curved double layers, complexation is entropy-driven. However, if the surfaces are weakly or intermediately charged and they have strongly curved double layers, because of small particle radii or large Debye screening lengths, complexation is driven predominantly by a decrease of the electric field energy. In conclusion, in most practical situations complexation is likely to be driven by a combination of energetic and entropic terms, and neither can be neglected.

Appendix.
Interaction free energy for surfaces at constant surface potential and charge regulating surfaces

To analyse how to evaluate the contributions of U_{el} and $-T\Delta S_{el}$ and F_{ch} to the interaction free energy of surfaces at constant surface potential and charge regulating surfaces, we start from the free energy of a charged surface j with a surrounding electrical double layer, as calculated from a charging process,[18]

$$F = \int_{A_j} \sum_i \int_0^{\Gamma_j} (\mu_i^s(\psi_j^s) - \mu_i^b)\, \mathrm{d}\Gamma_i\, \mathrm{d}A \tag{2.19}$$

where μ_i^s and μ_i^b are the chemical potentials of ion type i at the surface and in the bulk, respectively, and ψ_j^s is the surface potential of surface j. The summation is over all ions that adsorb on the surface. The chemical potential of an ion at a charged surface is written as

$$\mu_i^s = \hat{\mu}_i^s + z_i e \psi^0 \tag{2.20}$$

where $\hat{\mu}_i^{\mathrm{s}}$ represents the chemical potential of ion i at the surface at zero potential. The free energy can be separated into an electrical component and a chemical component, as was done in Equation 2.7:

$$F = F_{\mathrm{el}} + F_{\mathrm{ch}} = \int_{A_j} \int_0^{\sigma_j} \psi_j^{\mathrm{s}}(\sigma)\, \mathrm{d}\sigma\, \mathrm{d}A + \int_{A_j} \sum_i \int_0^{\Gamma_i} (\hat{\mu}_i^{\mathrm{s}} - \mu_i^{\mathrm{b}})\, \mathrm{d}\Gamma_i\, \mathrm{d}A\,. \tag{2.21}$$

The electrical contribution to the free energy is given by Equations 2.8–2.12 for all types of surfaces.

The expression for the chemical contribution F_{ch} depends on the nature of the surface charging process. For surfaces with a **constant surface potential**, such as some metallic colloids, sparingly soluble oxides or salts,[11] the charge-determining ions at the surface are in equilibrium with these ions in solution at all separations by adsorption or dissociation ($\mu_i^{\mathrm{b}} = \mu_i^{\mathrm{s}}$). Therefore, $\hat{\mu}_i^{\mathrm{s}} - \mu_i^{\mathrm{b}} = -z_i e \psi_j^{\mathrm{s}}$, and[18]

$$F_{\mathrm{ch}}^{\psi} = \int_{A_j} \sum_i \int_0^{\Gamma_i} (\hat{\mu}_i^{\mathrm{s}} - \mu_i^{\mathrm{b}})\, \mathrm{d}\Gamma_i\, \mathrm{d}A = -\int_{A_j} \sigma \psi_j^{\mathrm{s}}\, \mathrm{d}A \tag{2.22}$$

where $\sigma_j = \sum z_j e \Gamma_j$ with the summation over all charge charge-determining ions for surface j. The total free energy of surfaces at constant surface potential follows from $F^{\psi} = U_{\mathrm{el}} - T\Delta S_{\mathrm{el}} + F_{\mathrm{ch}}^{\psi}$. For a 1:1 electrolyte in units $k_{\mathrm{B}}T$:

$$\frac{F^{\psi}}{k_{\mathrm{B}}T} = \frac{n^{\mathrm{b}}}{\kappa^2} \int_V (\vec{\nabla} y)^2\, \mathrm{d}V + 2n^{\mathrm{b}} \int_V (y \sinh(y) - \cosh(y) + 1)\, \mathrm{d}V - \int_{A_j} \sigma_j \psi_j^{\mathrm{s}}\, \mathrm{d}A\,. \tag{2.23}$$

For **charge-regulating surfaces**, such as weak polyelectrolytes, proteins, carboxy-coated nanoparticles and colloids, the actual surface charge σ is not only related to the surface potential via the PB equation, but also via a chemical adsorption or dissociation equilibrium. Explicit expressions for the chemical component of the free energy in Equation 2.21 have been derived for surfaces with a single pK_{a} or pK_{b} dissociation equilibrium,[41,42] surfaces with amphoteric groups[18,42] and surfaces with zwitterionic groups.[18] We derive F_{ch} here for surfaces with a single type of acid or base groups.

In that case, the charge-potential relation follows from the equilibria $\mathrm{HA} \rightleftarrows \mathrm{H}^+ + \mathrm{A}^-$ (K_{a}) and $\mathrm{BH}^+ \rightleftarrows \mathrm{B} + \mathrm{H}^+$ (K_{b}). The ionisation degree α is related to the surface potential by

$$\alpha_j = \frac{1}{1 + \exp(z_j(y_j^0 - y^{\mathrm{N}}))} \tag{2.24}$$

where z_j is the valency of the chargeable surface groups on surface j (in our examples -1 for surfaces with acidic groups and $+1$ for surfaces with basic groups), y^0 is the dimensionless surface potential and y^{N} can be called the Nernst potential, which is the potential at which 50% of the surface groups is dissociated

$$y^{\mathrm{N}} = \ln(10) \cdot (\mathrm{p}K - \mathrm{pH}) \tag{2.25}$$

The surface charge can be written as

$$\sigma_j = z_j e \alpha_j N_j^0 = \frac{z_j e N_j^0}{1 + \exp(z_j(y_j^0 - y^{\mathrm{N}}))} \tag{2.26}$$

where N_j^0 is the surface charge density of ionisable groups on surface j.

To find the chemical contribution to the free energy for charge regulating surfaces $F_{\mathrm{ch}}^{\mathrm{cr}}$, we expand $\sum_i \mu$ in Equation 2.21 for the equilibria above and we assume that the entropy terms are ideal, following Payens,[42]

$$\sum_i \hat{\mu}_i^{\mathrm{s}} = \sum_i \hat{\mu}_i^{\mathrm{s},0} + k_{\mathrm{B}}T \ln\left(\frac{\alpha\, c_{\mathrm{H}^+}}{1-\alpha}\right) \tag{2.27}$$

where $\sum_i \hat{\mu}_i^{\mathrm{s},0} = \hat{\mu}_{\mathrm{H}^+}^{\mathrm{s},0} + \hat{\mu}_{\mathrm{A}^-}^{\mathrm{s},0} - \hat{\mu}_{\mathrm{HA}}^{\mathrm{s},0} = -k_{\mathrm{B}}T\ln(10)\cdot \mathrm{p}K_{\mathrm{a}}$ with c_{H^+} the actual proton concentration, for surfaces with acidic groups, and equivalently, $\sum_i \hat{\mu}^{\mathrm{s},0} = -k_{\mathrm{B}}T\ln(10)\cdot \mathrm{p}K_{\mathrm{b}}$ for surfaces with basic groups. We substitute Equation 2.27 in 2.21 and find, after integration[41,42]

$$\begin{aligned}\frac{F_{\mathrm{ch}}^{\mathrm{cr}}}{k_{\mathrm{B}}T} &= \int_{A_j} N_j^0 \left\{ \alpha_j \frac{\sum_i \hat{\mu}_i^{\mathrm{s},0}}{k_{\mathrm{B}}T} + \left[\alpha_j \ln(\alpha_j) + (1-\alpha_j)\ln(1-\alpha_j) + \alpha_j \ln(c_{\mathrm{H}^+})\right] \right\} \mathrm{d}A \\ &= -\int_{A_j} \sigma_j \psi_j^{\mathrm{s}} - N_j^0 \ln(1-\alpha_j)\, \mathrm{d}A\,. \end{aligned} \tag{2.28}$$

In this expression the bulk part of the chemical potential (Equation 2.21) has been omitted, as we assume that the bulk concentrations of ions do not change. Consequently, the bulk part of the chemical potential does not contribute to the *interaction* free energy.

The chemical contribution to the interaction free energy of charge regulating surfaces (Equation 2.28) clearly contains an energetic (first term, $\Delta U_{\mathrm{ch}}^{\mathrm{cr}}$) and an entropic (second term, $-T\Delta S_{\mathrm{ch}}^{\mathrm{cr}}$) component. $\Delta U_{\mathrm{ch}}^{\mathrm{cr}}$ represents the chemical adsorption energy of the charge-determining ions and $-T\Delta S_{\mathrm{ch}}^{\mathrm{cr}}$ represents the entropy of the charges on the surface. At $\alpha_j = 0.5$ the entropy is at a maximum.

The total free energy of charge regulating surfaces follows from $F^{\mathrm{cr}} = U_{\mathrm{el}} - T\Delta S_{\mathrm{el}} + F^{\mathrm{cr}}_{\mathrm{ch}}$. For a 1:1 electrolyte in units $k_{\mathrm{B}}T$:

$$\frac{F^{\mathrm{cr}}}{k_{\mathrm{B}}T} = \frac{n^{\mathrm{b}}}{\kappa^2}\int_V (\vec{\nabla}y)^2\,\mathrm{d}V + 2n^{\mathrm{b}}\int_V (y\sinh(y) - \cosh(y) + 1)\,\mathrm{d}V \qquad (2.29)$$
$$-\int_{A_j}\Big(\sigma_j\psi_j^{\mathrm{s}} - N_j^0\ln(1-\alpha_j)\Big)\,\mathrm{d}A\,,$$

$$\frac{U^{\mathrm{cr}}}{k_{\mathrm{B}}T} = \frac{n^{\mathrm{b}}}{\kappa^2}\int_V (\vec{\nabla}y)^2\,\mathrm{d}V + \int_{A_j} N_j^0\alpha_j\sum_i \hat{\mu}_i^{\mathrm{s},0}\,\mathrm{d}A\,, \qquad (2.30)$$

$$-\frac{T\Delta S^{\mathrm{cr}}}{k_{\mathrm{B}}T} = 2n^{\mathrm{b}}\int_V (y\sinh(y) - \cosh(y) + 1)\,\mathrm{d}V$$
$$+\int_{A_j} N_j^0\big[\alpha_j\ln(\alpha_j) + (1-\alpha_j)\ln(1-\alpha_j) + \alpha_j\ln(c_{\mathrm{H}^+})\big]\,\mathrm{d}A\,. \qquad (2.31)$$

References

[1] P. Luckham and B. Vincent, *Colloids and Surfaces*, 1980, **1**, 281–293.

[2] A. Y. Kim and J. C. Berg, *J. Coll. Int. Sci.*, 2000, **229**, 607–614.

[3] M. Rasa, A. P. Philipse, and J. D. Meeldijk, *J. Coll. Int. Sci.*, 2004, **278**, 115–125.

[4] P. M. Biesheuvel, S. Lindhoud, R. de Vries, and M. A. Cohen Stuart, *Langmuir*, 2006, **22**, 1291–1300.

[5] G. J. Piazza and R. A. Garcia, *Bioresource Tech.*, 2010, **101**, 5759–5766.

[6] Y. Desfougères, T. Croguennec, V. Lechevalier, S. Bouhallab, and F. Nau, *J. Phys. Chem. B*, 2010, **114**, 4138–4144.

[7] C. G. de Kruif, F. Weinbreck, and R. de Vries, *Curr. Opin. Coll. Int. Sci.*, 2004, **9**, 340–349.

[8] R. Chollakup, W. Smitthipong, C. D. Eisenbach, and M. Tirrell, *Macromolecules*, 2010, **43**, 2518–2528.

[9] E. Spruijt, A. H. Westphal, J. W. Borst, M. A. Cohen Stuart, and J. van der Gucht, *Macromolecules*, 2010, **43**, 6476–6484.

[10] E. Kizilay, A. B. Kayitmazer, and P. L. Dubin, *Adv. Coll. Int. Sci.*, 2011, **167**, 24–37.

[11] J. Th. G. Overbeek, *Colloids and Surfaces*, 1990, **51**, 61–75.

[12] S. L. Turgeon, C. Schmitt, and C. Sanchez, *Curr. Opin. Coll. Int. Sci.*, 2007, **12**, 166–178.

[13] W. M. de Vos, F. A. M. Leermakers, A. de Keizer, M. A. Cohen Stuart, and J. M. Kleijn, *Langmuir*, 2010, **26**, 249–259.

[14] V. Ball, M. Winterhalter, P. Schwinte, P. Lavalla, J.C. Voegel, and P. Schaaf, *J. Phys. Chem.*, 2002, **106**, 2357–2364.

[15] J. B. Schlenoff, A. H. Rmaile, and C. B. Bucur, *J. Am. Chem. Soc.*, 2008, **130**, 13589–13597.

[16] S. Bharadwaj, R. Montazeri, and D. T. Haynie, *Langmuir*, 2006, **22**, 6093–6101.

[17] X. Feng, R. Pelton, M. Leduc, and S. Champ, *Langmuir*, 2007, **23**, 2970–2976.

[18] D. McCormack, S. L. Carnie, and D. Y. C. Chan, *J. Coll. Int. Sci.*, 1995, **169**, 177–196.

[19] P. M. Biesheuvel and M. A. Cohen Stuart, *Langmuir*, 2004, **20**, 4764–4770.

[20] P. M. Biesheuvel, S. Lindhoud, M. A. Cohen Stuart, and R. de Vries, *Phys. Rev. E*, 2006, **73**, 014108.

[21] Z. Ou and M. Muthukumar, *J. Chem. Phys.*, 2006, **124**, 154902.

[22] R. de Vries and M. A. Cohen Stuart, *Curr. Opin. Coll. Int. Sci.*, 2006, **11**, 295–301.

[23] K.-J. Bathe, *Finite element procedures*, Prentice Hall, 1996.

[24] J. Lyklema, *Fundamentals of Interface and Colloid Science I*, Academic Press London, 1991.

[25] E. S. Reiner and C. J. Radke, *Adv. Coll. Int. Sci.*, 1993, **47**, 59–147.

[26] M. J. Voorn, *Ph.D. thesis*, University Utrecht, 1956.

[27] D. Ben-Yaakov, D. Andelman, D. Harries, and R. Podgornik, *J. Phys. Cond. Mat.*, 2009, **21**, 424106.

[28] M. A. Trejo-Ramos, F. Tristán, J.-L. Menchaca, E. Pérez, and M. Chávez-Páez, *J. Chem. Phys.*, 2007, **126**, 014901.

[29] N. Baker, M. Holst, and F. Wang, *J. Comp. Chem.*, 2000, **21**, 1343–1352.

[30] L. Chen, M. Holst, and J. Xu, *Siam. J. Numer. Anal.*, 2007, **45**, 2298–2320.

[31] M. Holst, J. A. McCammon, Z. Yu, Y. Zhou, and Y. Zhu, *Commun. Comp. Phys.*, 2012, **11**, 179–214.

[32] D. F. Evans and H. Wennerström, *The colloidal domain*, Wiley-VCH, 2nd edn., 1999.

[33] J. Vesenka, T. Marsh, E. Henderson, and C. Vellandi, *Scanning Micros.*, 1998, **12**, 329–342.

[34] M. E. Leunissen, C. G. Gristova, A.-P. Hynninen, C. P. Royall, A . I. Campbell, A. Imhof, M. Dijkstra, R. van Roij, and A. van Blaaderen, *Nature*, 2005, **437**, 235–240.

[35] W. Qi, C. Fong, and D. Lamport, *Plant Physiol.*, 1991, **96**, 848–855.

[36] G. O. Phillips and P. A. Williams, *Handbook of hydrocolloids*, Woodhead Publishing, 2001.

[37] B. Leps, H. Labischinski, and H. Bradaczek, *Biopolymers*, 1987, **26**, 1391–1406.

[38] K. Kamburova, V. Milkova, I. Petkanchin, and T. Radeva, *Biomacromolecules*, 2008, **9**, 1242–1247.

[39] P. L. Ma, M. Lavertu, F. M. Winnik, and M. D. Buschmann, *Biomacromolecules*, 2009, **10**, 1490–1499.

[40] L. de Ruiter and H. G. Bungenberg-de Jong, *Proc. KNAW*, 1947, **50**, 836–848.

[41] P. M. Biesheuvel, *J. Coll. Int. Sci.*, 2004, **275**, 514–522.

[42] Th. A. J. Payens, *Philips Res. Rep.*, 1955, **10**, 425–481.

Chapter 3

Phase behaviour of complex coacervates

In this Chapter we determine the experimental polymer-salt phase diagram of a model system of polyelectrolyte complex coacervates. This model system consists of combinations of fluorescein-labelled poly(acrylic acid) (PAA) and poly(N,N-dimethylaminoethyl methacrylate) (PDMAEMA) of four different, but equal chain lengths. The complex coacervates they form have a water content of about 70%, practically independent of chain length, which increases with increasing salt concentration. We further analyse our results using the mean-field theory for complex coacervation developed by Voorn and Overbeek. We find strong similarities between these complex coacervates and classical segregative demixing.

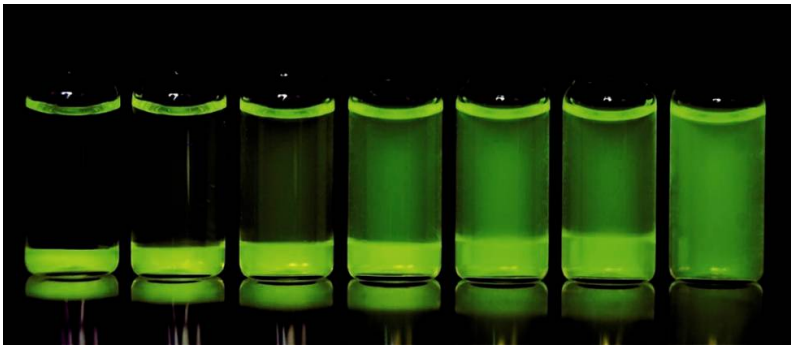

This Chapter is based on:
E. Spruijt, A. H. Westphal, J. W. Borst, M. A. Cohen Stuart and J. van der Gucht, *Binodal compositions of polyelectrolyte complexes*, Macromolecules **43** (2010), 6476–6484, doi 10.1021/ma101031t.

3.1 Introduction

Segregative phase separation is a common phenomenon in polymer solutions and mixed polymer melts: many polymers have unfavourable mixing enthalpies. If the polymers become long enough, translational entropy, favouring overall mixing, no longer dominates, and separation into two phases, each rich in at least one of the polymers from the original mixture, occurs. Knowledge of phase compositions and compatibility criteria is of great value for polymer processing, pharmaceutics and food industry, where (bio)polymer mixtures often need to be stabilised. For mixtures of two polymers in a single solvent, binodal compositions can be plotted in a simple phase diagram, as is schematically shown in Figure 3.1a.[1]

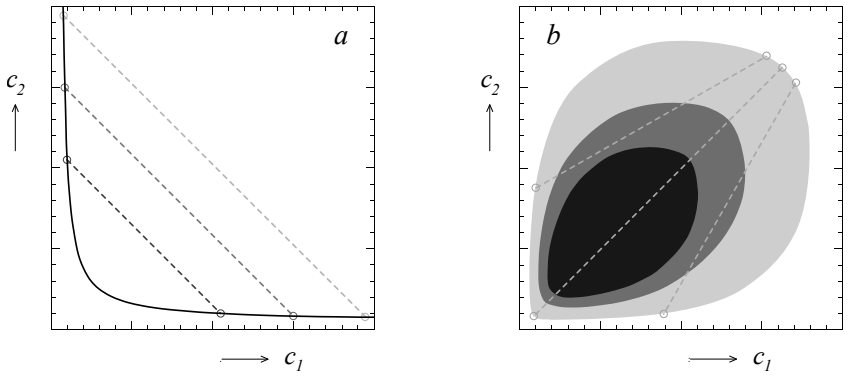

Figure 3.1: Schematic two-component phase diagrams showing binodal compositions of coexisting phases for (a) segregative and (b) associative phase separation. Dashed lines are possible tie lines. The different shades in (b) represent different relative strengths of association between the components.

Oppositely charged polymers are one of the few examples of polymers with strongly favourable mixing enthalpies, caused by electrostatic attraction between their opposite charges. These polymers can also undergo phase separation, but both polymers will now end up in the same phase, while the coexisting phase contains a low concentration of both polymers (see Figure 3.1b). This *associative* phase separation results in the formation of a complex coacervate, which is essentially a macroscopic polyelectrolyte complex.[1]

Associative phase separation can not only be used to create macroscopic complex coacervates, it can also be applied on a microscopic scale to drive the co-assembly of micelles,[2,3] create micro-emulsions[4] or vesicles,[5–7] which can be used, for example, as drug carriers[8,9] or packaging materials for enzymes.[10] In general, any of these nanostructures can be designed and engineered by choosing the correct balance of attractive forces between the oppositely charged polymers and competing

repulsive forces. In more macroscopic applications, polyelectrolyte complexation can be used to reversibly coat surfaces with polymer brushes at grafting densities well above 1 nm^{-2},[11] to make multiresponsive, reversible transient gels,[12] to serve as potential fat replacers in food,[13,14] and to prepare microgels with an upper critical solution temperature (UCST) near human body temperature that can release charged molecules, such as DNA, upon heating.[15]

All these examples of polyelectrolyte complexation would benefit from a quantitative understanding of the underlying associative phase separation. However, the many factors that influence the formation of polyelectrolyte complexes complicate such a description. Important experimental factors are polymer chain length, charge density, polymer concentration, mixing ratio, salt concentration, temperature and pH. In general, the strongest tendency for polyelectrolyte complex formation is found for long polymers, high charge densities, a polymer mixing ratio at which polymer charges are present at a 1:1 ratio and low salt concentrations.[16]

Several attempts have been made to construct a theoretical model to predict the influence of all these parameters on polyelectrolyte complexation quantitatively, but with only little experimental data. The first theoretical description of complex coacervation was given by Voorn and Overbeek and treats weakly charged polymers.[17] Their model estimates the total free energy of mixing as a sum of mixing entropy terms and mean-field electrostatic interactions in a Debye-Hückel approximation. Parameters that are explicitly included in this model are chain length, charge density and concentrations of polymer and salt. The mean-field approximation neglects correlation effects and the Debye-Hückel approximation is thought to limit the applicability of the model to low charge densities and low salt concentrations. Only much later, Borue et al.,[18] Castelnovo and Joanny[19,20] and Ermoshkin, Kudlay and Olvera de la Cruz[21,22] derived relations for polyelectrolyte complexation based on a random phase approximation, which allows correcting for higher charge densities and for connectivity of the polymer segments. Finally, Biesheuvel et al. developed another off-lattice approach to describe complexation of proteins and polyelectrolytes with pH-dependent charges.[23,24] They used the framework of Voorn and Overbeek, but treat polymeric charges separately and include their pH-dependence, using a chemical dissociation equilibrium. Monovalent ions are part of the diffuse layer around the polyelectrolytes in a cylindrical geometry and they solve the Poisson-Boltzmann equation to calculate ion distributions (see also Chapter 2). The approach of these authors is the first to take into account the effect of charge regulation on polyelectrolyte complexation, which is very important in many biopolymer complex coacervates.

After the first experimental observation of complex coacervation by Bungenberg-de Jong and Kruyt,[25] only a few experimental studies followed. Recently, complex coacervates of mainly biological macromolecules are receiving renewed interest.[26–36]

Most of these reports describe complex coacervation on a phenomenological basis. Chollakup et al. constructed an extensive phase diagram for poly(allylamine)/ poly(acrylic acid) complexation, including the effects of pH, temperature, mixing ratio and salt.[33] However, they did not measure the concentrations of polyelectrolytes in both phases directly, but determined phase boundaries between miscibility, coacervation and precipitation using microscopy and turbidity measurements.

In this Chapter we aim at bridging the gap between experimental reports on polyelectrolyte complexation and theoretical models. We measure binodal compositions of complex coacervates of highly charged poly(N,N-dimethylaminoethyl methacrylate) (PDMAEMA) and poly(acrylic acid) (PAA) directly using fluorescently labelled polymers. We focus on the effect of chain length and salt concentration on phase behaviour, but our approach can easily be extended to measure phase behaviour as a function of composition, pH and temperature, for example. We further analyse our experimental phase diagrams using a mean-field theoretical model for polyelectrolyte complexation with two adjustable parameters. The insights of this quantitative description lead to a better understanding of polyelectrolyte complex coacervation in general and the effect of chain length and salt concentration on similar complex coacervates between other strongly charged flexible polyelectrolytes in particular (see also Chapter 4).

3.2 Experimental details

3.2.1 Materials

We used poly(N,N-dimethylaminoethyl methacrylate) (PDMAEMA), a cationic polyelectrolyte with pH-dependent charges, and poly(acrylic acid) (PAA), an anionic polyelectrolyte with pH-dependent charges, to form complex coacervates in aqueous solutions. For both PDMAEMA and PAA we used different chain lengths, in the range $17 < N < 1728$. The specifications of the polymers we used are given in Table 3.1. Figure 3.2 shows elution profiles from size-exclusion chromatography (SEC) of all polymers, confirming their relative size differences.

For labelling of poly(acrylic acid) we used anhydrous N-methylpyrrolidone (NMP), triethylamine (TEA), N,N'-dicyclohexylcarbodiimide (DCC), and fluorescein amine (isomer II). These chemicals were all purchased from Sigma-Aldrich.

For preparation of the complex coacervates we used stock solutions of 3.0 M KCl, 1.0 M HCl and 1.0 M KOH in Milli-Q water (resistance > 18.2 M$\Omega \cdot$cm).

Table 3.1: Specifications of the PDMAEMA and PAA polymers used in this Chapter. N is the number-averaged degree of polymerisation, calculated from M_n.

Polymer	Supplier	M_n (kg/mol)	N	M_w/M_n
PAA_{20}	Polymer Source	1.5	20	1.32
PAA_{47}	Polymer Source	3.4	47	1.30
PAA_{139}	Polymer Source	10.0	139	1.15
PAA_{500}	Polymer Source	36.0	500	1.10
PAA_{1728}	Polymer Source	124.5	1728	1.25
$PDMAEMA_{17}$	Polymer Source	2.7	17	1.18
$PDMAEMA_{51}$	Polymer Source	8.0	51	1.40
$PDMAEMA_{150}$	Polymer Source	23.5	150	1.04
$PDMAEMA_{527}$	Polymer Source	82.7	527	1.09

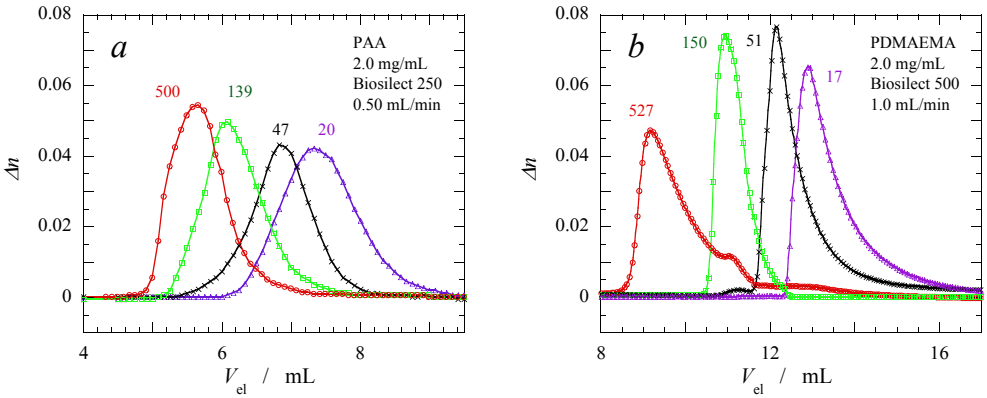

Figure 3.2: (a) Elution profiles of PAA (a) and PDMAEMA (b) from SEC.

3.2.2 Charged groups on PAA and PDMAEMA as a function of pH

Figure 3.3a shows a pH titration of PAA_{20}, starting from a fully protonated (acidic) form, and $PDMAEMA_{527}$, starting from a deprotonated (basic) form, at different salt concentrations. We approximate these protonation equilibria of PAA and PDMAEMA by a single effective pK_a, which is taken as the pH halfway of the equivalence point. The effective pK_a of PAA_{20} is 5.5 at 0.10 M KCl, almost independent of chain length, but decreases with increasing salt concentration to about 5.0 at 1.0 M KCl.

For PDMAEMA we find similar behaviour, but now protonation occurs as the pH is lowered. We find an effective pK_b of 7.5 at 0.10 M KCl, increasing with increasing salt concentration to about 7.9 at 1.0 M KCl.

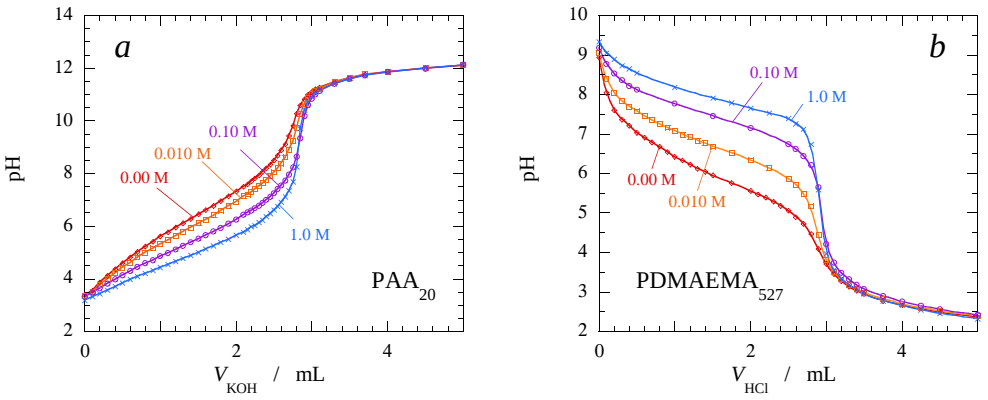

Figure 3.3: (a) pH titrations of a 250 mL 1.0 g/L solution of PAA_{20}, acidic form, with a 1.0 M KOH solution. (b) pH titrations of a 250 mL 2.0 g/L solution of $PDMAEMA_{527}$, basic form, with a 1.0 M HCl solution. 0.00 M indicates no added salt.

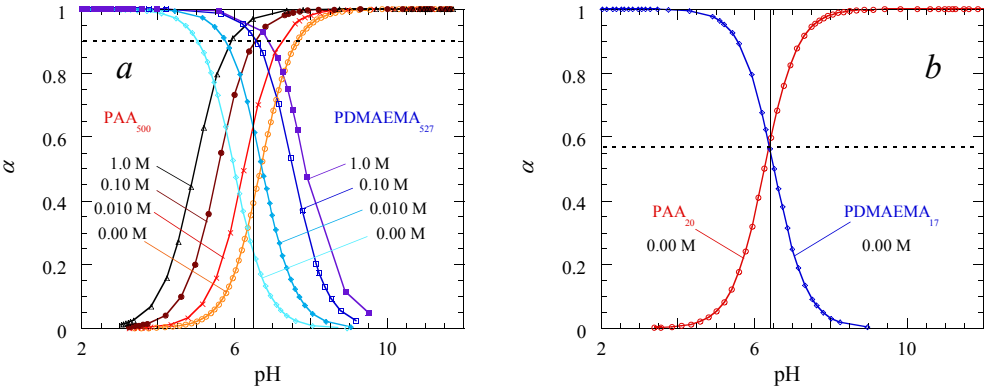

Figure 3.4: (a) Degree of ionisation α, for PAA_{500} and $PDMAEMA_{527}$ as a function of pH. (b) Idem for PAA_{20} and $PDMAEMA_{17}$.

Figure 3.3b shows the calculated degree of ionisation as a function of pH for PAA and PDMAEMA of two different chain lengths at four different salt concentrations. The degree of ionisation is approximated by

$$\alpha_- = \frac{10^{\,\mathrm{pH}-\mathrm{p}K_{\mathrm{a,eff}}}}{1+10^{\,\mathrm{pH}-\mathrm{p}K_{\mathrm{a,eff}}}} \tag{3.1}$$

$$\alpha_+ = \frac{10^{\,\mathrm{p}K_{\mathrm{b,eff}}-\mathrm{pH}}}{1+10^{\,\mathrm{p}K_{\mathrm{b,eff}}-\mathrm{pH}}}\,. \tag{3.2}$$

All our complex coacervates were prepared from PDMAEMA and PAA stock solutions at pH 6.5, where both polyelectrolytes have equal charge densities at all salt concentrations between 1.0 mM and 1.0 M KCl (see Figure 3.3).

3.2.3 Fluorescent labelling of poly(acrylic acid)

PAA (N = 20, 47, 139 and 500) was labelled with fluorescein amine, following a procedure of Anghel et al.[37] Briefly, 0.50 g of PAA, acid form, was dissolved in 25 mL N-methylpyrrolidone (NMP) at 60 °C. We added a solution of 13 mg TEA and 34 mg DCC in 2.5 mL NMP and a solution of 36 mg fluorescein amine in 2.5 mL NMP to this mixture. The resulting mixture was clear and had a pale yellow color. This mixture was stirred in the dark at 60 °C for 24 hours. The mixture was then cooled to room temperature and PAA was precipitated by drop-wise addition of a 1.0 M KOH solution (7 mL).

The orange precipitate was collected by filtration and washed three to five times with NMP. Uv/Vis spectroscopy was used to quantify the remaining amount of free label. After washing, the precipitate was dissolved in water and dialysed three times against 1 L of water in a 1,000 or 3,500 M_w cut-off membrane, depending on the polymer length. The solution inside the membrane was then freeze-dried, yielding the potassium salt of labelled PAA as a pale orange powder.

The total loss of polymer was low during this labelling procedure. Typically, 90% of the polymer was regained after freeze-drying. The labelling efficiency for this fluorescein label, however, was low, in contrast to the labelling efficiency reported by Anghel et al. We determined labelling efficiencies by dissolving a known amount of labelled polymer in water, adjusting the pH to 12 and recording the absorption spectrum using a Varian Uv/Vis spectrometer. The molar extinction coefficient of free fluorescein was measured to be 8.09×10^4 M^{-1} cm^{-1} at 489 nm. The labelling ratios of the four PAA polymers are 1 : 8400, 1 : 1250, 1 : 9350 and 1 : 4480 for PAA_{20}, PAA_{47}, PAA_{139} and PAA_{500}, respectively. This means that on average 1 per 10 to 20 polymer chains contains a label and the probability of having more than one label per polymer chain is low.

The reason for the low labelling efficiency is probably the location of the amino group, which is directly attached to an aromatic ring in isomer II of fluorescein amine. Nonetheless, for our present purpose of measuring polymer concentrations of the order of 10 mg/L, this labelling ratio suffices. Because of the small amount of labels per polymer we assume that the labels do not influence the phase behaviour of the polyelectrolytes we use. This assumption was verified by determining the critical salt concentration of labelled $PDMAEMA_{17}$ and PAA_{20} and comparing it to the critical salt concentration of their unlabelled counterparts.

Labelled PAA was further quantified by Fluorescence Correlation Spectroscopy (FCS) (see Section 3.2.4). We corrected all our measurements for the presence of free label.

3.2.4 Fluorescence correlation spectoscopy

Fluorescence correlation spectroscopy (FCS) measurements of fluorescein-labelled, free PAA and dilute phases of the phase separated mixtures of PDMAEMA and PAA were carried out on a Zeiss LSM510 setup, using a C-Apochromat 40× 1.2 water immersion objective, an Ar ion laser (488 nm excitation), an emission filter of 505 – 550 nm and a pinhole size of 90 µm. This setup resulted in a confocal volume of approximately 0.2 fL, with an aspect ratio A_v of 6 – 8.

The solutions of labelled, free PAA were prepared in 0.50 M KCl at pH 6.5, with a total concentration of fluorescent labels of 1 µM and a total polymer concentration of 0.50 g/L. Just before the measurement, all solutions were diluted 10× in 0.50 M KCl with a pH of 12, to obtain a better fluorescence signal from the fluorescein labels. The final label concentration was therefore fixed at 100 nM, which resulted in an average of 1 – 5 fluorescent molecules in the confocal volume. Rhodamine-6G was used to calibrate the confocal volume at the beginning of every series of measurements.

The FCS correlation data were fitted to a standard autocorrelation function of 3-D diffusion of one or two components with a triplet state correction:

$$g(t) = g(\infty) + \frac{1}{\langle n \rangle} \frac{1 - f_t + f_t e^{-t/\tau_t}}{1 - f_t} \sum_i \left(\frac{f_i}{(1 + t/\tau_i)\sqrt{1 + t/{A_v}^2 \tau_i}} \right) \tag{3.3}$$

where A_v is the aspect ratio of the confocal volume (ω_z/ω_{xy}), $\langle n \rangle$ is the average number of fluorescent molecules in the confocal volume, τ_i is the diffusion time of species i, which is derived from the diffusion coefficient: $D_i = {\omega_{xy}}^2/4\tau_i$, and f_i the fraction of species i. The triplet lifetime and fraction are given by τ_t and f_t.

The fitting of FCS autocorrelation functions was done using FFS data processor. We have summarised the fit parameters in Table 3.2. PAA_{20}, PAA_{47} and PAA_{139} all consist of a single diffusing species, with diffusion coefficients decreasing with increasing chain length. Only PAA_{500} consist of two components with different diffusion coefficients. The largest diffusion coefficient corresponds to free fluorescein, which has a slightly smaller diffusion coefficient than Rhodamine-6G. The smallest diffusion coefficient is attributed to diffusion of labelled PAA_{500}.

We also measured FCS autocorrelation functions for three different dilute phases of phase separated mixtures between PDMAEMA and PAA: $N_{cat}/N_{an} = 17/20$ and c_s =0.40 M, $N_{cat}/N_{an} = 150/139$ and $c_s = 1.0$ M and $N_{cat}/N_{an} = 527/500$ and $c_s = 0.50$ M. We did not observe any difference in the FCS autocorrelation functions between

Table 3.2: FCS fit parameters for fluorescein-labelled, free PAA chains in aqueous solution. f_1 corresponds to free label, f_2 corresponds to labelled polymer chains.

Sample	A_v	$\langle N \rangle$	f_t	τ_t (µs)	f_1	f_2	D_1 (10^{-10} m^2s^{-1})	D_2	$g(\infty)$
Rhodamine-6G	5.96	1.04	0.20	2.36	1.00		4.30		1.000
Fluorescein	5.96	2.37	0.40	1.67	1.00		3.83		1.000
PAA_{20}-Fl	7.80	2.26	0.50	1.68		1.00		1.88	1.001
PAA_{47}-Fl	5.96	4.01	0.46	1.68		1.00		1.42	1.000
PAA_{139}-Fl	5.96	2.62	0.39	1.67		1.00		0.759	1.000
PAA_{500}-Fl	7.80	1.86	0.47	1.22	0.49	0.51	3.73	0.303	1.000

labelled, free PAA and the labelled PAA in the dilute phase of a phase separated mixture of PDMAEMA and PAA. This indicates that the labelled PAA chains in the dilute phase of a phase separated mixture of PDMAEMA and PAA are neither smaller nor larger than free chains.

3.2.5 Polyelectrolyte complex formation

Mixtures of the two oppositely charged polyelectrolytes were prepared at an overall monomer concentration of 0.11 M (PDMAEMA 17.3 g/L, PAA 7.9 g/L) in a total volume of 4 mL. In this Chapter all mixtures have an overall 1:1 ratio of chargeable groups, since all mixtures were prepared at pH 6.5 ± 0.2, where both polyelectrolytes have equal charge densities (see Figure 3.4). The fraction of charged groups (i.e., protonated for PDMAEMA and deprotonated for PAA) ranges from $\alpha = 0.93$ at 0.10 M KCl to $\alpha = 0.97$ at 1.0 M KCl for both polyelectrolytes. Finally, we focused on mixtures of PDMAEMA and PAA with similar chain lengths. This means we have made four combinations for which we measured the binodal compositions as a function of salt concentration: $N_{cat}/N_{an} = 17/20$, 51/47, 150/139 and 527/500.

The procedure we followed to prepare our mixtures was as follows. First of all, we prepared stock solutions of both PDMAEMA and PAA of the desired chain length at pH 6.5 with a concentration of 50 g/L. The stock solutions of PAA contained about 20% labelled polymer by weight. Secondly, 1.38 mL of the PDMAEMA solution was mixed with a calculated amount of 3.0 M KCl solution and water in a plastic vial ($V_{max} = 6$ mL) of known weight to give 3.37 mL total solution at pH 6.5. Finally, 0.63 mL of PAA solution was added to give a mixture with a total volume of 4.0 mL, an overall monomer concentration of 0.11 M and a 1 : 1 ratio of DMAEMA to AA monomers. In our calculation of the overall salt concentration, we corrected for the ions present in the stock solutions of PDMAEMA and PAA.

Complexation took place immediately upon addition of the PAA if the salt concentration was low enough. The complex appeared as a pale white, gel-like substance that initially floated through the mixture. At this point all mixtures were shaken vigorously and left to equilibrate for five days in total at room temperature. After about one hour, the phase separated mixtures became transparent and the polyelectrolyte complex had sedimented. Two days after mixing all samples were centrifuged gently at $1{,}000 \times g$ for five minutes. At this point all phase separated mixtures had two clearly separated phases, which were both transparent (see Figure 3.6). The mixtures were then left for the remaining three days before they were analysed.

3.2.6 Analysis of the separated phases

The mixtures were separated into the two phases and the volume of the dilute (top) phase was measured using a graduated pipette. The concentrated (bottom) phase was weighed and then dried in an oven at 110 °C until the dry weight no longer changed. The density and water content of the coacervate phase were calculated using the measured weight and calculated volume of this phase. The density of the dilute phase was measured using a densiometer, which was calibrated using air and Milli-Q water. The error in the calculation of the water content of the coacervate phase was estimated based on a 10 mg uncertainty in the weight of the coacervate before drying, due to a small amount of the dilute phase that was not separated from the coacervate phase.

The concentration of fluorescein labels in the dilute phase was measured using a Varian Uv/Vis spectrometer and Hellma quartz cuvets with an optical path length of 1.0 cm. All absorption measurements were carried out at pH 12, where all fluorescein labels are in a dissociated form. Samples were brought to pH 12 by dropwise addition of a 1.0 M KOH solution for mixtures with an overall salt concentration below 1.0 M, or by diluting first with a 3.0 M KCl solution and subsequent addition of a 1.0 M KOH solution for mixtures with an overall salt concentration above approximately 1.0 M, because PDMAEMA would otherwise become unsoluble at this high pH and salt concentration. An absorption spectrum was recorded for all samples in the range 200 – 600 nm, using a scan rate of 1 nm/s. A maximum absorbance was found at 489 nm for all samples. This maximum is unique for the dissociated fluorescein label and it was used in all further calculations.

We calculated the concentrations of PAA (expressed as mol/L of AA monomers) both in the dilute and in the concentrated phase from the measured volumes of both phases, the labelling ratio of the PAA, the mixing ratio of labelled and unlabelled PAA and the concentration of the fluorescein label in the dilute phase. We assumed that the salt concentration is equal in both phases, as we will discuss hereafter. We estimated the relative uncertainty in the concentrations we calculated by summation over the relative uncertainties in the volume (absolute error ±50 µL), the labelling

ratio (0.05), the mixing ratio of labelled and unlabelled PAA (0.02), the molar extinction coefficient of fluorescein (0.001), the measured absorbance (absolute error ±0.002) and the dilution in the cuvet (0.02). We verified for one pair of polymers ($N_{\mathrm{cat}}/N_{\mathrm{an}} = 17/20$) that a separate measurement of the concentration of fluorescein label in the concentrated phase results in the same concentration of AA monomers in the concentrated phase as our calculation, within the given accuracy. For this measurement, we dissolved the concentrated phase in a known volume of 3.0 M KCl solution and adjusted to pH 12 using 1.0 M KOH.

3.2.7 Calculation of the theoretical phase behaviour

We used the mean-field lattice model of Voorn and Overbeek to describe our experimental binodal compositions of PDMAEMA/PAA complex coacervates.[16,17] We start from the general expression for the free energy of a mixture of polyelectrolyte solutions with a Debye-Hückel approximation for the electrostatic interactions and a Flory-Huggins approximation for the mixing entropy:

$$\frac{l^3 F}{V k_{\mathrm{B}} T} = -A \left(\sum_i \alpha_i \phi_i \right)^{3/2} + \sum_i \frac{\phi_i}{N_i} \ln \phi_i + \sum_i \sum_{j<i} \chi_{ij} \phi_i \phi_j \tag{3.4}$$

where l is the lattice size, corresponding to the size of a monomer, V is the total volume, α_i is the charge density, ϕ_i the volume fraction and N_i the chain length of component i. Additional nonionic interactions between two or more components can be included using a nonelectrostatic χ parameter.[38] A is the electrostatic interaction parameter:

$$A = \frac{\sqrt{4\pi}}{3} \left(\frac{\ell_{\mathrm{B}}}{l} \right)^{3/2} \tag{3.5}$$

where $\ell_{\mathrm{B}} = e^2/4\pi\epsilon_{\mathrm{r}}\epsilon_0 k_{\mathrm{B}} T$ is the Bjerrum length, which is 7.1 Å in pure water.

The mixtures we are interested in consist of three components: (1) a polymer salt PQ, composed of two equally long polyelectrolytes (P^{z+} and Q^{z-}) of length N and charge density $\alpha = z/N \leq 1$, (2) a microsalt KCl, composed of two monovalent ions (K^+ and Cl^-), with $N = 1$ and $\alpha = 1$, and (3) water. Volume fractions of the polymer salt, microsalt and water are ϕ_{p}, ϕ_{s} and $(1 - \phi_{\mathrm{p}} - \phi_{\mathrm{s}})$, respectively.

A two-phase equilibrium is found when the two coexisting phases have a lower free energy than a homogeneous mixture of all components: $\Delta F = F^{\mathrm{I}} + F^{\mathrm{II}} - F^{\mathrm{mix}} < 0$. The compositions of the coexisting phases can be derived from the condition that the electrochemical potentials of all components have to be equal in both phases: $[\hat{\mu}_i \pm z_i e\psi]^{\mathrm{I}} = [\hat{\mu}_i \pm z_i e\psi]^{\mathrm{II}}$. For equal lengths and charge densities of both polymers, the electrostatic potential difference between both phases must be zero: $\Delta\psi = 0$.[16]

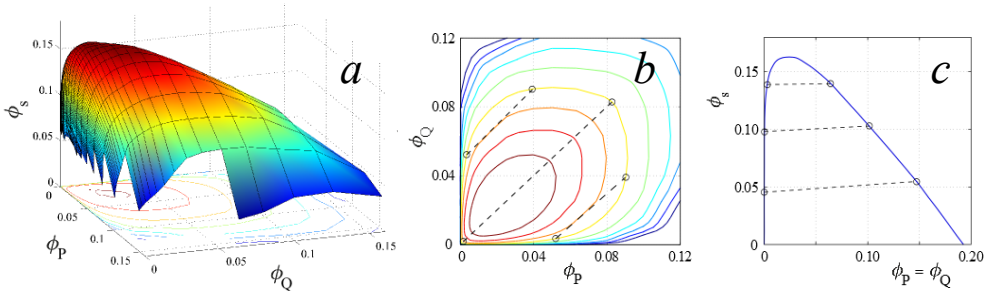

Figure 3.5: Theoretical phase diagram for polyelectrolyte complexation between polycation P and polyanion Q using the mean-field lattice theory of Voorn and Overbeek, using $N_P = N_Q = 100$, $A = 0.9$ and $\alpha_P = \alpha_Q = 0.95$. (a) 3-D representation showing volume fractions ϕ of polycation, polyanion and salt. (b) 2-D contour representation of the same phase diagram. The binodal lines for different salt concentrations are shown, as well as three (dashed) tie lines connecting coexisting phases. (c) Binodal line for a stoichiometric mixture of polyelectrolytes, with three (dashed) tie lines.

Numerically, we solve this problem using a simulated annealing procedure, to obtain the polymer concentrations and salt concentrations in both phases.[39,40] A typical phase diagram of associative phase separation, based on the mean-field lattice model of Voorn and Overbeek is shown in Figure 3.5.

The problem above can be simplified by assuming that the salt concentrations in both phases are (almost) equal. In that case, the binodal compositions can be found from a common tangent construction in the graph of the free energy versus the polymer volume fraction. Numerically, this simplified problem can be solved by first calculating the spinodal points, for which $\partial^2 F/\partial\phi^2 = 0$. Then, the binodal points can be found close to the spinodal points from the condition of equal tangents using the first derivative of the free energy. Finally, the critical point can be derived from the conditions $\partial^2 F/\partial\phi^2 = 0$ and $\partial^3 F/\partial\phi^3 = 0$.

The assumption of equal salt concentrations in both phases is based on both experimental measurements of the salt concentration in complex coacervates and their coexisting dilute phases by Voorn,[16] and theoretical modelling of polyelectrolyte complexation by Kudlay and Olvera de la Cruz.[22] Voorn argued that the ratio K/c, where K is the salt concentration in the coacervate and c the salt concentration in the coexisting dilute phase, is always larger than unity, because salt ions will have a lower electrostatic free energy in a phase with a higher charge concentration, such as a complex coacervate phase (see Equation 3.4).

Both the experiments and theory of Voorn indeed show that K/c is slightly larger than unity. Its value is at most 1.4 for salt concentrations of practically 0, and it decreases quickly to 1.05 at 60 mM salt. This ratio depends on chain length and charge

density of the specific polyelectrolytes. Voorn concluded that the salt concentration in complex coacervate is always higher than in the dilute phase.

This hypothesis was investigated in more detail by Kudlay and Olvera de la Cruz, who showed that K/c is only larger than unity for sufficiently hydrophilic polyelectrolytes. In case of hydrophobic polyelectrolytes, the coacervate is depleted of salt.[22] We assume that the inaccuracy in both the experimental and the theoretical binodal compositions due to unequal salt concentrations is small compared to the experimental error in the measurement of the concentrations.

In our experiments, we also (inevitably) assume that the salt concentrations in both phases are equal. Therefore, we compare our experiments with the simplified Voorn-Overbeek model, where the salt concentrations are assumed equal as well. To verify that this assumption of equal salt concentrations in the simplified model does not change the theoretical phase diagram significantly, we have compared the phase diagram calculated by Voorn for $N = 1000$ polymers with $\alpha = 0.15$ and $A = 3.655$,[16] with the simplified model, which assumes equal salt concentrations, and the full calculation using the simulated annealing procedure. The simulated annealing procedure exactly reproduces Voorn's phase diagram, and the simplified model predicts the same binodal concentrations within a margin of 10% for all salt concentrations. We conclude that the assumption of equal salt concentrations in both phases has a minor effect on the actual appearance of the phase diagrams and we keep the assumption of equal salt concentrations in the remainder of this Chapter.

We have used the mean-field model described above to quantitatively describe our experimental findings on the associative phase separation between PDMAEMA and PAA. For that, we took $A = 0.9$ and used the experimentally known chain lengths and charge densities of both polymers (Table 3.1 and Figure 3.4). This value for parameter A would correspond to a molecular length scale of 0.80 nm at a temperature of 293 K and a dielectric constant $\epsilon_r = 80$. However, the dielectric constant of aqueous solutions at very high ionic strength, such as the concentrated complex coacervate phases of our PDMAEMA/PAA mixtures, is significantly lower than that of pure water. In fact, a KCl solution at an ionic strength of 3 M has a dielectric constant of about 47.[41] Therefore, we use A here only as a general tuning parameter for the effective electrostatic interaction strength between the hydrated ionic groups.

Finally, we converted the calculated volume fractions in the theoretical phase diagrams to molar concentrations, using an effective size of the monomers and salt ions. Voorn originally proposed to use the size of a single water molecule ($l \approx 0.3$ nm).[16] This would, however, underestimate the size of our monomeric units and salt ions and thereby overestimate their concentrations significantly. Instead, we used an average between the Bjerrum length and the size of a water molecule to obtain very similar concentrations as found experimentally. Results of our calculations are shown as solid lines in all remaining Figures in this Chapter.

3.3 Results and discussion

3.3.1 Observations of complex coacervation

Polyelectrolyte complexation between PDMAEMA and PAA manifested itself experimentally as phase separation into two coexisting clear phases: a top phase that is dilute in both polymers and a bottom phase with a high concentration of both polymers. The concentrated phases were transparent and liquid-like for all combinations of chain lengths. This means that all phases flow under the influence of gravity when allowed sufficient time (see Figure 1.3). Figure 3.6a shows an example of one of the phase separated mixtures. These qualifications, liquid-like, highly viscous, transparent and resulting from oppositely charged colloids or polymers, are exactly the qualifications Bungenberg-de Jong and Kruyt originally introduced to describe complex coacervates.[25,42] We therefore conclude that the polyelectrolyte complexes of PDMAEMA and PAA that originate from associative phase separation of a mixture of both polymers can be qualified as complex coacervates in all our experiments. In contrast to what Chollakup et al. found for PAH/PAA complexes, we do not find a region of precipitation preceding the coacervate region.[33] We believe that weaker interactions between PDMAEMA and PAA, as inferred from the lower critical salt concentrations (see Section 3.3.5), prevent irreversible precipitation even at the lowest salt concentrations we used.

Equilibration of the mixtures was verified by measuring local fluorescein concentrations in the coacervate phase. Figure 3.6b shows a confocal microscopy image of a mixture of the coacervate phase and a small amount of dilute phase, both containing fluorescein-labelled PAA. The image shows droplets of dilute phase in a continuous complex coacervate phase. The mixture is made by taking an equilibrated sample, discarding 90% of the dilute phase and gently mixing the remaining of the two phases. We purposefully mixed the two phases to show the contrast in fluorescence intensity between the two phases. The dilute phase contains a much lower concentration of PAA than the complex coacervate phase. Here, the complex coacervate forms the continuous phase because of its relative excess in the mixture. The image shows no inhomogeneities in the coacervate on length scales larger than roughly 1 µm, the optical resolution of this image. This is a strong indication that the mixtures are equilibrated long enough to ensure a homogeneous structure of the coacervate down to 1 µm (see Chapter 7 for more details).

3.3.2 Phase diagrams

The effects of polymer chain length and salt concentration on complex coacervation of PDMAEMA and PAA are summarised in the salt-polymer phase diagram depicted in Figure 3.7.

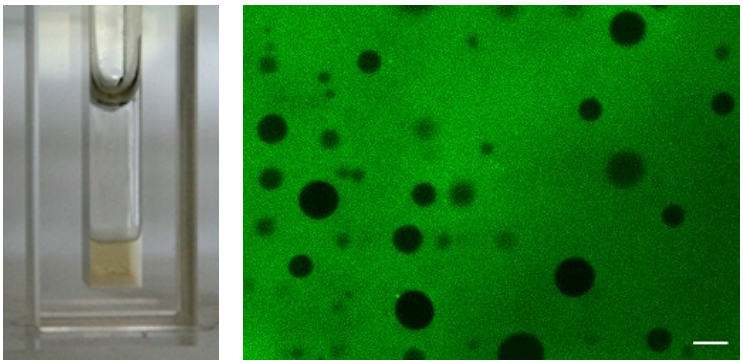

Figure 3.6: (a) Phase separated mixture of $PDMAEMA_{150}$ and PAA_{139} in a 1 mm cuvet at 1.0 M KCl. 20% fluorescein-labelled PAA_{139} was added to enhance the visibility of the comple coacervate phase. (b) Confocal microscopy image of the same complex coacervate phase, with droplets of coexisting dilute phase visible as darker regions. This image is obtained with the FCS setup, using a pinhole of 190 µm. The scale bar represents 10 µm.

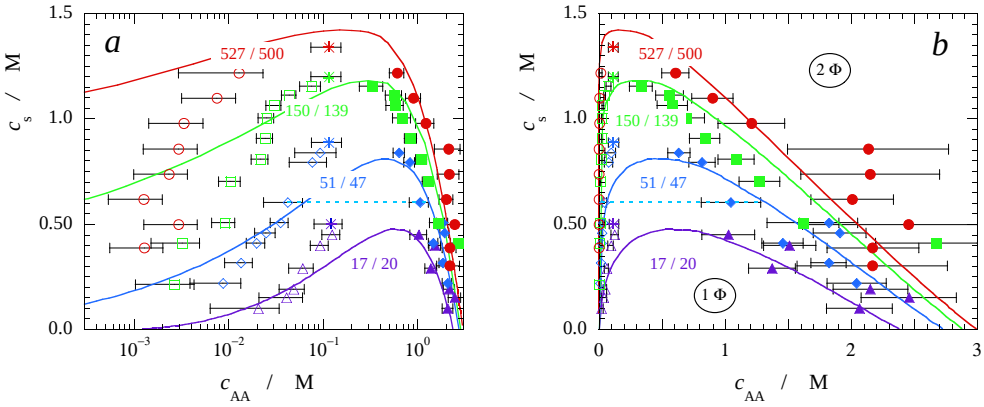

Figure 3.7: Salt-polymer phase diagram for associative phase separation between PDMAEMA and PAA at pH 6.5 on a logarithmic (left) and a linear (right) horizontal scale. Symbols indicate experimentally measured binodal compositions of the coexisting phases, for different combinations of chain lengths, indicated by the labels as N_{cat}/N_{an}. The crossed symbols correspond to the lowest salt concentrations for which phase separation was no longer observed ($c_{s,cr}$). The solid lines are predictions of the phase boundaries based on the mean-field theory of Voorn and Overbeek. The dotted lines are examples of tie lines.

The phase diagram in Figure 3.7 shows concentrations of PAA in the dilute phase (left branch) and complex coacervate phase (right branch), both on a logarithmic and a linear scale. Coexisting phases are connected by tie lines, of which one is drawn as an example. Because we assume equal salt concentrations in both phases, tie lines are horizontal lines in Figure 3.7.

Experimentally, we find that increasing the salt concentration in a complex coacervate phase increases solubility of polymeric components of that complex. The concentration of the polymers in the coexisting dilute phase increases at the expense of the concentration inside the complex coacervate. At sufficiently high salt concentrations, the polymer concentrations in both phases become equal and the mixture no longer phase separates. The experimental critical salt concentrations beyond which no phase separation are observed is indicated by crossed symbols in Figure 3.7. We find that longer polymer chains tend to have higher critical salt concentrations and more extreme coexisting phases: the dilute phase is more dilute and the complex coacervate phase is more concentrated.

Theoretical predictions of binodal compositions are given by solid lines in Figure 3.7. For the complex coacervate phases, the predicted concentrations of polyanion seem to be in good agreement with the experimentally determined values. For dilute phases however, the predicted polyanion concentrations seem to systematically underestimate the actual polyanion concentration for a given salt concentration. The differences become larger for longer chains. The absolute errors here, however, are very small, as the scale is logarithmic. A possible explanation for the underestimation comes from the suggested mechanism of aggregation of oppositely charged polyelectrolytes.

It has been suggested that polyelectrolytes form soluble complexes,[43] or random symmetrical aggregates,[44] as an intermediate state to their macroscopic phase separation. The presence of such soluble complexes in dilute phases of PDMAEMA/PAA mixtures could explain the fact that we experimentally find higher polymer concentrations than predicted by the model. However, we have found no indication at all of the presence of soluble complexes in the 1:1 stoichiometric dilute phase measured with FCS (see Section 3.2.4). Instead, we believe that the differences between our experimental data and the mean-field theory of Voorn and Overbeek are caused by either small amounts of free label that were not detected by FCS, or by the limitations of this mean-field model, as we will discuss at the end of this Chapter, or both.

Qualitatively, our experimentally determined phase diagrams are also similar to the theoretical predictions by Biesheuvel et al. for complexation between oppositely charged biopolymers, in the limit of low χ.[45] For larger values of χ, indicating additional attractive interactions between the biopolymers, these authors predict that the critical point vanishes, which we do not find here.

3.3.3 Compositions of complex coacervate phases

The complex coacervates of PDMAEMA/PAA have a polymer concentration of about 1 – 3 M (typically 140 g/L PAA), expressed as a concentration of monomer units, depending on salt concentration and chain length. However, the limiting concen-

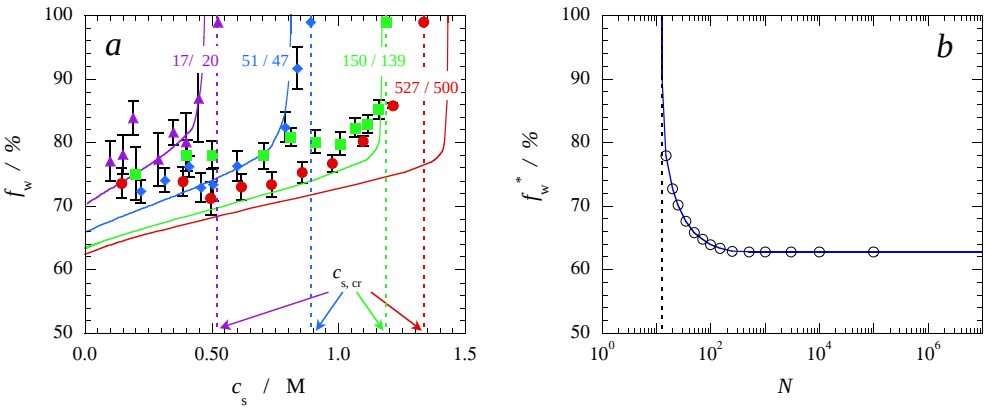

Figure 3.8: (a) Weight fraction of water f_w in complex coacervates of PDMAEMA and PAA at pH 6.5 as a function of salt concentration. Symbols indicate experimentally measured values. Solid lines are theoretical predictions based on the mean-field model of Voorn and Overbeek. (b) Theoretical limiting weight fraction of water $f_w{}^*$ in complex coacervates for $c_s \to 0$ as a function of polymer chain length for polymers of equal length with $\alpha = 0.95$ and $A = 0.9$.

tration of polymer in the complex coacervates, for salt concentrations approaching zero, depends surprisingly weakly on polymer chain length. All limiting polymer concentrations are 2.5 – 3.0 M, corresponding to a volume fraction of approximately 30%. This observation suggests that the water content of the complex coacervates also depends weakly on polymer chain length.

Experimentally, we determined the water content of the complex coacervates by weighing and drying the complex coacervates after separation from their coexisting dilute phases. Figure 3.8a shows the water content inside the complex coacervates as a function of salt concentration for different chain lengths. In general, the water content of the complex coacervates increases with increasing salt concentration. Far from the critical point, at low salt concentrations, the water content of the complex coacervates increases only weakly with increasing salt concentration. Close to the critical point however, the water content increases rapidly to the value of a homogeneously mixed solution, which is close to 99% (w/w). These findings are supported by Figure 3.7, where we see a much stronger salt-dependence of the monomer concentration close to the critical point. Theoretical predictions of the water content are in reasonable agreement with experimentally determined values. For large N, the model seems to underestimate the water content.

The observation that the water content of these complex coacervates depends very weakly on chain length and salt concentration, up to salt concentrations close to the critical point, is in agreement with experimental observations in a number of studies on other types of complex coacervates.[26,28,30,46] In all cases, complex

coacervates are reported to have a water content between 65% and 85%. Bohidar et al. found that BSA-PDADMAC coacervates have a water content of 73%, independent of PDADMAC molecular weight.[28] Since they limited their experiments to very low salt concentrations, it is likely that they never measured close enough to the critical salt concentration to see a similar increase in water content as in Figure 3.8a. Mathieu et al. reported a water content of 70 – 80% for coacervates of gelatin and PAA.[46] Wang et al. reported water contents ranging from 65% to 85% for coacervates of pectin and β-lactoglobulin.[30] They found higher water contents when coacervates were prepared at lower protein to pectin ratios. Finally, Weinbreck et al. reported total solid contents of 25 – 32% (w/w) for coacervates of whey protein and gum arabic, depending on pH.[26] At the pH where they found a maximum degree of coacervation, the total solid content reached 32% (w/w), hence the water content was 68%.

3.3.4 Effect of chain length on complex coacervation

Because we have a theoretical prediction that describes the compositions of the PDMAEMA/PAA complex coacervates quite well, we can calculate the effect of chain length on the coacervate water content in more detail. Figure 3.8b shows the limiting water content, for salt concentrations approaching zero, of a complex coacervate as a function of the chain length of the polyelectrolytes. We find that the limiting water content is truly independent of chain length for chains longer than $N \approx 200$. For shorter polymer chains, the water content of the complex coacervates increases with decreasing chain length. Too short polymers show no phase separation for this choice of A. Below this critical chain length, we therefore find a water content equal to that of a homogeneously mixed solution. The presence of a lower critical chain length in a variety of complex coacervates has been discussed in more detail by Pawar and Bohidar.[47]

The range of chain lengths for which we do find a variation in the water content of complex coacervates is small. However, it is exactly the range that is important for most applications of polyelectrolyte complexes. The assembly of polyelectrolyte complex micelles, vesicles, multilayers or coatings typically occurs with polyelectrolyte block lengths up to $N \approx 200$.[2–6,10,11]

Finally, we emphasise that the predicted water content in Figure 3.8b is valid only for parameters that were found to apply to our pair of strongly charged flexible polyelectrolytes ($\alpha = 0.95$ and $A = 0.9$). However, previous studies have indicated that coacervates with much lower charge densities, consisting for example of proteins and weakly charged polysaccharides, also consist of 80% water.[26,28,30,46] The current mean-field theory predicts a much higher water content for charge densities of 20% for the same value of A. It is therefore not clear yet how such an apparently robust water content can be explained theoretically and we will discuss this further in Chapter 13.

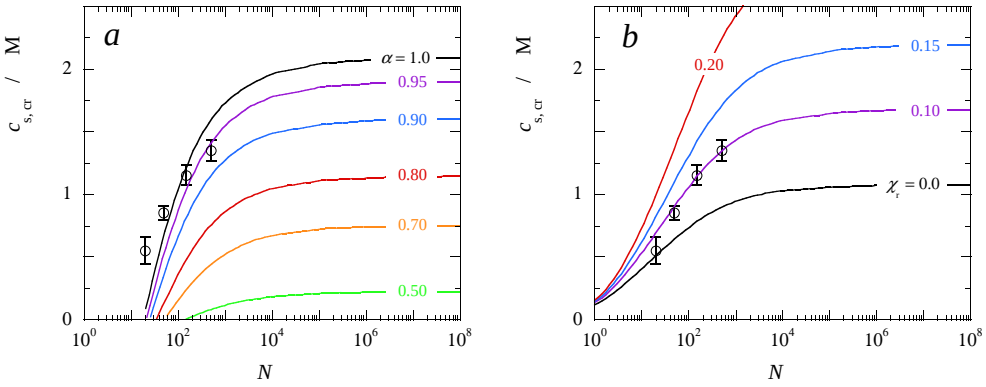

Figure 3.9: (a) Critical salt concentration $c_{s,cr}$ of complex coacervation between PDMAEMA and PAA at pH 6.5 as a function of polymer chain length. Symbols indicate experimentally measured critical salt concentrations. Solid lines are theoretical predictions of the critical salt concentrations for different values of α based on the model. (b) The same critical salt concentrations together with predictions, derived from mapping onto segregative demixing (Equation 3.8).

3.3.5 Critical salt concentration

The critical salt concentration is the salt concentration beyond which phase separation into a dilute phase and a complex coacervate phase is suppressed. Figure 3.9a shows the critical salt concentration for phase separation in PDMAEMA and PAA as a function of polymer chain length. We have determined the critical salt concentration for all four chain length pairs as that salt concentration between the highest salt concentration where phase separation still occurred and the lowest salt concentration where phase separation was suppressed.

The critical salt concentrations we find are rather high, compared to the critical salt concentrations reported by De Ruiter and Bungenberg-de Jong in their original investigation of weakly charged gelatin/gum arabic complex coacervates.[48] The fact that such high salt concentrations are needed to suppress complex coacervation may seem surprising when considering the so-called Debye screening length, which is very small at salt concentrations of 1.0 M and beyond.

For grafted chains of oppositely charged polyelectrolytes, we have argued that such a high critical salt concentration suggests that the weakening of the complexes upon addition of salt is due to a competition effect: monovalent salt ions compete for ion pairing with oppositely charged groups on the polymer chains (see also Chapter 12).[49] The complexes seem to dissociate completely when the bulk salt concentration is comparable to the local charge concentration in the complexes, which can be as high as 1.5 M in case of PDMAEMA and PAA and other combinations of strong

polyelectrolytes (see Figure 3.7 and Chapter 4). Beyond that salt concentration, the complexes are weakened enough by monovalent salt for the translational entropy of the polymer chains to take over.

Theoretical predictions of the critical salt concentration by the mean-field theory of Voorn and Overbeek for various polymer charge densities α are given by solid lines in Figure 3.9a. The predicted critical salt concentration depends strongly on charge density, in agreement with our argument above. We have chosen the molecular length scale l (see Equation 3.4) to match our experimental critical salt concentrations with the theoretical predictions for $\alpha = 0.95$. We find that the effect of chain length on the critical salt concentration is slightly overestimated: for small chains the model underestimates the critical salt concentrations, whereas for long chains it overestimates them. Nevertheless, for all charge densities a levelling off of the critical salt concentrations is predicted for long polymer chains. This is in agreement with Figure 3.8b, which shows that the polymer concentration in complex coacervates becomes constant for long chains, and the notion that translational entropy becomes negligible for infinitely long chains. Again, the experimental range where the critical salt concentration depends on chain length is of great practical importance, since most applications of polyelectrolyte complexation are based on relatively short polyelectrolyte blocks.

A similar dependence of critical salt concentration on polymer chain length was found by Chodanowski and Stoll in Monte Carlo simulations.[50] They measured the critical salt concentration for binding of a strongly charged polyelectrolyte, with a charge density of 1.0, to a strongly charged surface under the Debye-Hückel approximation. They found critical salt concentrations that increase to 0.40 M for chain lengths up to $N = 200$, but seem to level off for longer chains. They also found a lower critical chain length below which no adsorption occurs at all, as Figures 3.8b and 3.9a and the findings of Pawar and Bohidar[47] suggest as well. In the case of Chodanowski and Stoll, this lower critical chain length is $N = 20$. The fact that these authors found lower absolute critical salt concentrations at similar chain lengths can be explained by the fact that they studied single chains adsorbing to a charged surface, which had a lower charge density than the chain itself, whereas our complex coacervates consist of multiple chains with equally high charge densities, aggregating together into a condensed phase.

It is informative to compare the experimental effect of chain length on the critical point in this case of associative phase separation to the expected trends in segregatively phase separating systems. We know that the critical interaction parameter for segregative phase separation depends on the polymer chain length as follows:

$$\chi_{\mathrm{cr}} = \frac{1}{2} + \frac{1}{\sqrt{N}} \,. \tag{3.6}$$

Associative phase separation can be mapped onto the above condition for segregative phase separation, using an effective interaction parameter that depends on salt concentration:[1]

$$\chi_{\mathrm{eff,cr}} = \chi_{\mathrm{r}} + \chi_{\mathrm{ion}} = \chi_{\mathrm{r}} + \frac{2\pi {\ell_{\mathrm{B}}}^2 {\kappa_{\mathrm{cr}}}^{-1} \alpha^2}{3\, l^3} \tag{3.7}$$

where κ^{-1} is the Debye screening length, defined as $\kappa^2 = 8\pi\ell_{\mathrm{B}} N_{\mathrm{Av}} c_{\mathrm{s}}$ (see Chapter 2). χ_{r} is the nonelectrostatic contribution to the effective interaction parameter, which corresponds to χ_{pw} in Equation 3.4. In the mean-field theoretical model of Voorn and Overbeek, which we have used to describe our experimental measurements, we assume that $\chi_{\mathrm{r}} = 0$, in other words, that the polymers are in an athermal solvent. We therefore expect that we can map the obtained chain length dependence for associative phase separation on segregative phase separation using an effective interaction parameter in which the ionic contribution dominates. Substitution of Equation 3.7 in Equation 3.6 and neglecting the contribution of c_{p} to κ^{-1} around the critical point, leads to the following expression for the critical salt concentration as function of polymer chain length:

$$c_{\mathrm{s,cr}} = \frac{A^2\alpha^4}{l^3\left(1 - 2\chi_{\mathrm{r}} + 2/\sqrt{N}\right)^2}\,. \tag{3.8}$$

Figure 3.9b shows that a value of $\chi_{\mathrm{r}} = 0.10$ is in best agreement with our experimentally determined critical salt concentrations. Surprisingly, this prediction, derived from classical segregatively phase separating polymer systems, describes the effect of polymer chain length on the critical point quite accurately. Apparently, the associative phase separation leading to complex coacervates has a strong resemblance to segregative demixing and the translational entropy of the polymer chains, approximated by Flory-Huggins terms, dominates the chain length dependence of the critical point, regardless its origin.

The effect of χ_{r} on the critical salt concentrations shown in Figure 3.9b indicates that polymers that are slightly more hydrophobic, might have a significantly higher critical salt concentration for identical chain lengths. Furthermore, we find that especially for short polymers chains, this approach, derived from segregative demixing, predicts a different behaviour than the mean-field model of Voorn and Overbeek (see Figure 3.9a). The model predicts a lower critical chain length, below which no complexation occurs, whereas Figure 3.9b predicts that complexation occurs even for a chain length of 1 for $\chi_{\mathrm{r}} > 0$. However, in this limit c_{p} can no longer be neglected near the critical point, because $c_{\mathrm{p,cr}}$ increases with decreasing chain length, as shown in Figure 3.7. This means that sufficiently short chains will dissolve even at zero salt concentration, as predicted by Figure 3.9a.

3.3.6 Validity of the mean-field theory

In our attempt to give a theoretical description of the complexation between PDMAEMA and PAA we have used the mean-field theory of Voorn and Overbeek, which uses a Debye-Hückel approximation for the electrostatic interaction. This model has some important limitations. First of all, the approximations within the derivation of the electrostatic free energy of interaction are only valid for low surface potentials, which translates into low charge densities for polymers (see Chapter 2). Secondly, ions are treated as point charges and ion-ion correlations at high salt concentrations and between monomeric units on a polymer chain are neglected. This arguably limits the applicability to low salt concentrations. Finally, ion pairing effects, such as counterion condensation, are not taken into account here. Therefore, this mean-field theory might seem to be inadequate for describing the phase separation in mixtures of the two strongly charged polyelectrolytes, PDMAEMA and PAA, at very high salt concentrations into a highly concentrated complex coacervate phase.

However, Voorn argued that neglecting the correlation effects due to connectivity of the monomer units is justified, especially in the concentrated complex coacervate phase, since the polymers in the complex coacervate phase overlap strongly and hence, the distribution of ions will be determined predominantly by electrostatic effects.[16] Moreover, we believe that applying this model to strongly charged polymers is not necessarily unjustified either. We typically measure and model complexation at high salt concentrations, so that the mean electrostatic potential is small (as for low charge densities at low salt concentrations), high surface potentials are strongly screened and counterion condensation effects are no longer important. Finally, by adapting a lower value of the electrostatic interaction parameter A than proposed by Voorn, we have most likely corrected for several remaining overestimations of interactions and neglect of additional interactions, such as hydration effects.

Summarising, we find that a simple mean-field model based on a Debye-Hückel approximation is able to describe all aspects of the equilibrium complexation of PDMAEMA and PAA surprisingly well. We believe that this successful description is possible for any equilibrium complexation between flexible polyelectrolytes with high charge densities, as long as the salt concentrations are high enough to ensure that the mean electrostatic potential is small and comparable to the thermal energy. Adjusting the electrostatic interaction parameter A, corresponding to different effective sizes of the interacting ions, can help to correct for neglect of, for example, hydration effects. If we compare our results to the work of Chollakup et al., a small adjustment in A, justified by the smaller monomer size of poly(allylamine) compared to PDMAEMA, can predict the correct critical salt concentrations of 2 – 3 M for the chain lengths used in their experiments.[33] Alternatively, a slightly higher χ_r (Figure 3.9b) would have the same effect.

3.4 Concluding remarks

We used fluorescently labelled PAA to directly measure equilibrium compositions of polyelectrolyte complex coacervates of PDMAEMA and PAA and their coexisting dilute phases. We measured binodal compositions of both dilute and complex coacervate phases and the water contents of the complex coacervate phases as a function of polymer chain length and salt concentration. We find that longer polyelectrolytes tend to have more extreme coexisting phases, but that the concentration differences in the complex coacervate phase are small. As a result, the water content of the complex coacervates is only weakly dependent on salt concentration and independent of polymer chain length for sufficiently long polymers. Similarly, the critical salt concentration increases with increasing chain length, but becomes independent of chain length for sufficiently long polymers. However, most practical applications of polyelectrolyte complexation in capsules, coatings and multilayers are in the range where we do find a dependence of chain length.

We describe all our experiments using a mean-field model, with two adjustable parameters for all measurements, to account for the size of the monomers and the strength of the electrostatic interactions. We find that this model can be applied successfully to associative phase separation of strongly charged flexible polyelectrolytes, as long as the salt concentration is high to ensure that the electrostatic interactions are not effectively irreversible.

References

[1] J. Lyklema, *Fundamentals of Interface and Colloid Science V*, Academic Press London, 1991.

[2] M. A. Cohen Stuart, N. A. M. Besseling, and R. G. Fokkink, *Langmuir*, 1998, **14**, 6846–6849.

[3] I. K. Voets, A. de Keizer, and M. A. Cohen Stuart, *Adv. Coll. Int. Sci.*, 2009, **147–148**, 300–318.

[4] B. Hofs, A. de Keizer, S. van der Burgh, F. A. M. Leermakers, M. A. Cohen Stuart, P.-E. Millard, and A. H. E. Müller, *Soft Matter*, 2008, **4**, 1473–1482.

[5] D. Renard, P. Robert, L. Lavenant, D. Melcion, Y. Popineau, J. Guéguen, C. Duclairoir, E. Nakache, C. Sanchez, and C. Schmitt, *Int. J. Pharmaceutics*, 2002, **242**, 163–166.

[6] T. Imura, H. Yanagishita, and D. Kitamoto, *J. Am. Chem. Soc.*, 2004, **126**, 10804–10805.

[7] P. M. Biesheuvel, T. Mauser, G. B. Sukhorukov, and H. Möhwald, *Macromolecules*, 2006, **39**, 8480–8486.

[8] L. A. Luzzi, *J. Pharm. Sci.*, 1970, **59**, 1367–1376.

[9] C. Thomasin, H. Nam-Tran, H. P. Merkle, and B. Gander, *J. Pharmaceut. Sci.*, 1998, **87**, 259–268.

[10] S. Lindhoud, R. de Vries, R. Schweins, M. A. Cohen Stuart, and W. Norde, *Soft Matter*, 2009, **5**, 242–250.

[11] W. M. de Vos, J. M. Kleijn, A. de Keizer, and M. A. Cohen Stuart, *Angew. Chem. Int. Ed.*, 2009, **48**, 5369–5371.

[12] M. Lemmers, J. Sprakel, I. K. Voets, J. van der Gucht, and M. A. Cohen Stuart, *Angew. Chem. Int. Ed.*, 2010, **49**, 708–711.

[13] M. A. E. Bakker, M. M. G. Konig, and J. Visser, *World Patent Application*, 1994, WO94/14334.

[14] S. I. Laneuville and S. L. Paquin, P.and Turgeon, *J. Food Sci.*, 2005, **70**, s513–519.

[15] A. Ohsugi, H. Furukawa, A. Kakugo, Y. Osada, and J. P. Gong, *Macromol. Rapid Commun.*, 2006, **27**, 1242–1246.

[16] M. J. Voorn, *Ph.D. thesis*, University Utrecht, 1956.

[17] J. Th. G. Overbeek and M. J. Voorn, *J. Cell. Comp. Phys.*, 1957, **49**, 7–26.

[18] V. Y. Borue and I. Y. Erukhimovich, *Macromolecules*, 1990, **23**, 3625–3632.

[19] M. Castelnovo and J.-F. Joanny, *Langmuir*, 2000, **16**, 7524–7532.

[20] M. Castelnovo and J.-F. Joanny, *Eur. Phys. J. E*, 2001, **6**, 377–386.

[21] A. V. Ermoshkin and M. Olvera de la Cruz, *J. Pol. Sci. B*, 2004, **42**, 766–776.

[22] A. Kudlay, A. V. Ermoshkin, and M. Olvera de la Cruz, *Macromolecules*, 2004, **37**, 9231–9241.

[23] P. M. Biesheuvel and M. A. Cohen Stuart, *Langmuir*, 2004, **20**, 4764–4770.

[24] P. M. Biesheuvel, S. Lindhoud, M. A. Cohen Stuart, and R. de Vries, *Phys. Rev. E*, 2006, **73**, 014108.

[25] H. G. Bungenberg-de Jong and H. R. Kruyt, *Proc. KNAW*, 1929, **32**, 849–856.

[26] F. Weinbreck, R. H. Tromp, and C. G. de Kruif, *Biomacromolecules*, 2004, **5**, 1437–1445.

[27] C. G. de Kruif, F. Weinbreck, and R. de Vries, *Curr. Opin. Coll. Int. Sci.*, 2004, **9**, 340–349.

[28] H. Bohidar, P. L. Dubin, P. R. Majhi, C. Tribet, and W. Jaeger, *Biomacromolecules*, 2005, **6**, 1573–1585.

[29] A. B. Kayitmazer, S. P. Strand, C. Tribet, W. Jaeger, and P. L. Dubin, *Biomacromolecules*, 2007, **8**, 3568–3577.

[30] X. Wang, J. Lee, Y.-W. Wang, and Q. Huang, *Biomacromolecules*, 2007, **8**, 992–997.

[31] S. L. Turgeon, C. Schmitt, and C. Sanchez, *Curr. Opin. Coll. Int. Sci.*, 2007, **12**, 166–178.

[32] M. Antonov, M. Mazzawi, and P. L. Dubin, *Biomacromolecules*, 2010, **11**, 51–59.

[33] R. Chollakup, W. Smitthipong, C. D. Eisenbach, and M. Tirrell, *Macromolecules*, 2010, **43**, 2518–2528.

[34] P. L. Dubin, *Adv. Coll. Int. Sci.*, 2011, **167**, 1.

[35] E. Kizilay, A. B. Kayitmazer, and P. L. Dubin, *Adv. Coll. Int. Sci.*, 2011, **167**, 24–37.

[36] R. J. Stewart, C. S. Wang, and Hui Shao, *Adv. Coll. Int. Sci.*, 2011, **167**, 85–93.

[37] D. F. Anghel, V. Alderson, F. M. Winnik, M. Mizusaki, and Y. Morishima, *Polymer*, 1998, **39**, 3035–3044.

[38] A. Nakajima and H. Sato, *Biopolymers*, 1972, **11**, 1345–1355.

[39] E. H. L. Aarts and J. H. M. Korst, *Simulated Annealing and Boltzmann Machines*, John Wiley & Sons, 1987.

[40] W. H. Press, S. A. Teukolsky, W. T. Vetterling, and B. P. Flannery, *Numerical recipes in C++*, Cambridge University Press, 2002.

[41] D. V. Loginova, A. S. Lileev, and A. K. Lyashchenko, *Russ. J. Inorg. Chem.*, 2002, **47**, 1426–1433.

[42] P. Koets, *Rep. Prog. Phys.*, 1944, **10**, 129–140.

[43] K.-I. Tainaka, *Biopolymers*, 1980, **19**, 1289–1298.

[44] A. Veis, *Adv. Coll. Int. Sci.*, 2011, **167**, 2–11.

[45] P. M. Biesheuvel, S. Lindhoud, R. de Vries, and M. A. Cohen Stuart, *Langmuir*, 2006, **22**, 1291–1300.

[46] F. Mathieu, S. Ugazio, G. Carnelle, Y. DucinÌ, and J. Legrand, *J. Appl. Pol. Sci.*, 2006, **101**, 708–714.

[47] N. Pawar and H. B. Bohidar, *Adv. Coll. Int. Sci.*, 2011, **167**, 12–23.

[48] L. de Ruiter and H. G. Bungenberg-de Jong, *Proc. KNAW*, 1947, **50**, 836–848.

[49] E. Spruijt, M. A. Cohen Stuart, and J. van der Gucht, *Macromolecules*, 2010, **43**, 1543–1550.

[50] P. Chodanowski and S. Stoll, *Macromolecules*, 2001, **34**, 2320–2328.

Chapter 4

Composition and stability of various polyelectrolyte complex coacervates with high charge densities

In this Chapter we determine the critical salt concentration, the weight fraction of water and the preferred composition of polyelectrolyte complex coacervates of various flexible synthetic polyelectrolytes with high charge densities. In addition, we determine what effect the temperature and the type of salt have on the stability of two of these complex coacervates. We discuss to what extent these properties are generic and to what extent chemical details of the interacting polymers play a role.

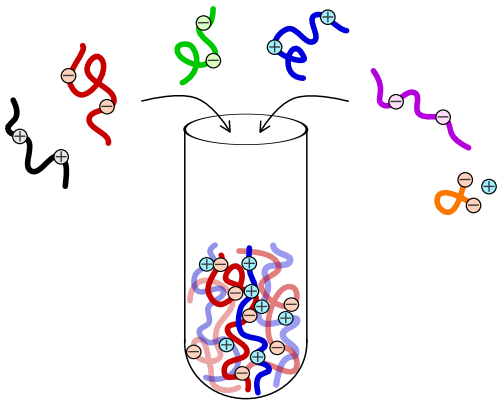

This Chapter is partly based on:
J. van der Gucht, E. Spruijt, M. Lemmers and M. A. Cohen Stuart, *Polyelectrolyte complexes: bulk phases and colloidal systems*, Journal of Colloid and Interface Science **361** (2011), 407–422, doi 10.1016/j.jcis.2011.05.080.

4.1 Introduction

In the previous Chapter, we have studied the associative phase separation of two oppositely charged, flexible polyelectrolytes, poly(N,N-dimethylaminoethyl methacrylate) (PDMAEMA) and poly(acrylic acid) (PAA). We have used these polyelectrolytes as a model system for complex coacervates of flexible polyelectrolytes in general, and we could study the effect of polymer chain length on the phase behaviour for this combination of polyelectrolytes in detail. By using the mean-field theory of Voorn and Overbeek, we implicitly assumed that any pair of oppositely charged polyelectrolytes would show at least qualitatively the same phase behaviour.

In this Chapter, we investigate this hypothesis for various combinations of oppositely charged, flexible polyelectrolytes of approximately the same chain length, and four combinations with a 'living' negatively charged metal-ligand coordination polymer as polyanion.[1] We determined the critical salt concentrations and water content of nineteen different polyelectrolyte combinations in total, at equal overall polymer concentrations. In addition, we determined the preferred compositions of nine of these complex coacervates.

We discuss to what extent these properties are common to all complex coacervates and, hence, to what extent they are intrinsically linked to the underlying associative phase separation by electrostatic attraction. Differences likely originate from other, polymer-specific aspects. These aspects can be related to other kinds of interactions, such as hydrophobic interactions, specific chemical effects, such as hydrogen bonding or charge-transfer interactions,[2] or to the geometrical structure and conformational pairing compatibility. We discuss trends in our measurements to make suggestions which of these factors seems to play a role.

Finally, we take two complex coacervates, PDMAEMA/PAA and PTMAEMA/PSPMA, to investigate the effect of the type of salt and the temperature on the stability of the complex coacervate phases. We determine the critical salt concentrations of different types of salts in a Hofmeister series and find that the hydration of the salt ions plays an important role in the associative phase separation. Nevertheless, this aspect is not taken into account in any of the theoretical models, so far. If we change the temperature of the complex coacervates after they have formed, we find that the optically transparent phase separated mixtures may become turbid again, suggesting that temperature affects the phase diagram shown in Figure 3.5. We explain our observations by discussing the competition between the effect of temperature on the strength of the charge-charge interaction and a classical temperature-dependent interaction between the polymers.

4.2 Experimental details

4.2.1 Materials

We used the polymers depicted in Figure 1.9 to make complex coacervates in aqueous solutions. Some of these polymers were commercially available, others have been synthesised by atom transfer radical polymerisation (ATRP) in solution. The specifications of all the polymers we used are given in Table 4.1.

For ATRP we used ethyl-α-bromo-isobutyrate (EBIB) as initiator and methacryloyloxytrimethylammonium chloride (METAC, 80% w/w solution in water) and potassium 3-sulphopropyl methacrylate (KSPMA, powder) as monomers. In addition, we used 2,2'-bipyridyl (bipy), copper(I) chloride (CuCl), copper(II) chloride ($CuCl_2$), methanol and isopropanol, which were all purchased from Sigma-Aldrich.

For preparation of the complex coacervates we used stock solutions of 3.0 M KCl, 1.0 M HCl and 1.0 M KOH in Milli-Q water (resistance > 18.2 M$\Omega \cdot$cm).

4.2.2 Atom transfer radical polymerisation

Both cationic PTMEAMA and anionic PSPMA were synthesised by ATRP. For cationic PTMAEMA we prepared an ATRP solution of [METAC] : [bipy] : [CuCl] : [$CuCl_2$] : [EBIB] = 100 : 4 : 2 : 0.15 : x in a 4 : 1 (v/v) isopropanol/water mixture, following previously described procedures.[15,16] We added different amounts of EBIB initiator, with $x = 0.64$, 0.38 and 0.19 to obtain $PTMAEMA_{51}$, $PTMAEMA_{96}$ and $PTMAEMA_{162}$. All polymerisation mixtures were left to react for two days.

For anionic PSPMA we prepared an ATRP solution of [KSPMA] : [bipy] : [CuCl] : [$CuCl_2$] : [EBIB] = 75 : 2 : 0.75 : 0.25 : y in a 2 : 1 (v/v) methanol/ water mixture, following a previously described procedure.[17] We added different amounts of EBIB initiator, with $y = 0.70$, 0.35 and 0.26 to obtain $PSPMA_{94}$, $PSPMA_{174}$ and $PSPMA_{365}$. All polymerisation mixtures were left to react for two days.

After polymerisation, all mixtures were opened to air, diluted twice with Milli-Q water and transferred to one or several dialysis tubes with a 3,500 M_w cut-off membrane. We dialysed all polymers at least four times against 1.0 M KCl in Milli-Q water and four times against Milli-Q water. We then concentrated the solution by rotary evaporation of part of the water under reduced pressure, and freeze-dried the solution afterwards. All polymers were finally obtained as a fluffy white powder.

4.2.3 Complex coacervate formation and analysis

We prepared complex coacervates of different combinations of polyelectrolytes in the same way as described in Chapter 3. For all polyelectrolytes, we prepared stock solutions with a concentration of 30 – 100 g/L at pH 6.5. We then mixed polycation,

Table 4.1: Specifications of the polyelectrolytes used in this Chapter.

Polymer	Supplier[a]	M_n (kg/mol)	N	M_w/M_n	b, b_0 [i] (nm)	p$K_{a,eff}$
Polycations						
$PDMAEMA_{150}$	PS	23.5	150	1.04	(b) 2.7–3.7[j] [3]	7.8[p]
$PDMAEMA_{527}$	PS	82.7	527	1.09	(b_0) 1.7–2.7 [3]	
$PTMAEMA_{51}$	H[b]	10.7	51	1.10	(b) 4.1[k] [4]	
$PTMAEMA_{96}$	H[b]	19.8	96	1.26		
$PTMAEMA_{162}$	H[b]	33.7	162	1.09		
$PM2VP_{88}$ (70%)	PS[c]	18.0	88	1.09	(b_0) 1.5–2.0[l] [5]	5.1[q]
$PM2VP_{249}$ (85%)	PS[c]	56.0	249	1.09		
PAH_{68}	SA	6.4	68	2.50	(b_0) 2.0 [6]	8–9 [6]
PAH_{161}	SA	15.0	161	3.60		
PEI	SA	[g]				7–8 [7]
Polyanions						
PAA_{139}	PS	10.0	139	1.15	(b) 3.5[m] [8]	5.0[p]
PAA_{500}	PS	36.0	500	1.10	(b_0) 1.6 [9]–2.9 [8]	
$PSPMA_{94}$	H[d]	23.2	94	1.32	(b) 4.2[n] [10]	
$PSPMA_{174}$	H[d]	42.9	174	1.13		
$PSPMA_{365}$	H[d]	90.2	366	1.34		
PSS_{165} (99%)	PS[e]	34.0	165	1.03	(b) 4.0[o] [11]	
PSS_{294} (99%)	PS[e]	60.6	294	1.04	(b_0) 1.2 [11]–2.4 [12]	
L_2EO_4 / Zn	H[f]	[h]	1	1.00		4.7, 6.8 [13]

Notes

[a] PS = Polymer Source, SA = Sigma-Aldrich, H = in-house synthesis.

[b] Synthesised by ATRP, as described in Section 4.2.2. M_n is calculated from SEC (flow rate 1 mL/min, c_p = 2 g/L, c_s = 0.45 M, pH 7, using PSS for calibration).

[c] Quaternised (%) according to Brzozowska et al. [14]

[d] Synthesised by ATRP, protocol, as described in Section 4.2.2, M_n was determined in the same way as for PTMAEMA[c].

[e] Degree of sulphonation (%).

[f] Synthesised according to Vermonden. [13]

[g] Molecular weight unknown.

[h] These ligands form living polymers: rings and chains of varying lengths. [13]

[i] b denotes the Kuhn length of ionised polymers in low or intermediate salt, b_0 denotes the bare Kuhn length of the polymers in their unionised state.

[j] In water with 0.10 M HCl and 0.10 M KCl.

[k] In water with methyl sulphate as counterion and 1.0 M added $NaNO_3$.

[l] Value for unquaterinised P2VP.

[m] In water at 93% ionisation, with no added salt.

[n] Value for poly(2-sulphoethyl methacrylate) in water with 0.10 M added NaCl.

[o] In water with 0.20 M added NaCl.

[p] See Chapter 3.

[q] Effective pK_a for unquaternised P2VP at 0.10 M NaCl.

salt, water and polyanion together in the same order to obtain an overall monomer concentration of 0.050 M in a total volume of 2 mL. Unless stated otherwise, we prepared all mixtures at an overall 1:1 ratio of chargeable groups.

We left all mixtures to equilibrate for at least five days, shaking the mixtures directly after mixing, and centrifuging them at 1,000 – 3,500×g for five minutes after two days. The occurrence of phase separation was judged by eye (macroscopic phases) and optical microscopy (microcoacervates). We separated the two phases to determine the water content of the complex coacervate phase by drying in an oven at 110 °C to constant weight, and, when necessary, the amount of excess polycation or polyanion in the dilute phase by titration with the oppositely charged species.

The relative errors in critical salt concentrations are based on the difference between the highest salt concentration where phase separation still occurred and the lowest salt concentration where it was suppressed. We note that the value we thus find for the critical salt concentration depends on the polymer concentration (see Figure 3.7). The actual critical point is located at the (critical) polymer concentration where the binodal exhibits a maximum. Nevertheless, in this Chapter we compare the values at a fixed polymer concentration of 0.050 M (monomer units), as this concentration is close to the critical polymer concentration for long polymers of PDMAEMA and PAA (see Figure 3.7). We assume that the uncertainties due to variations in the critical polymer concentrations are small compared to the typical differences in critical salt concentration between two complex coacervates. Finally, the relative errors in the weight fraction of water in the complex coacervates are based on an estimated uncertainty of 10 mg in the mass of the complex coacervates, as a result of small amounts of dilute phase that may not have been separated from the complex coacervates.

4.3 Results and discussion

4.3.1 Appearance of the complex coacervates

For most combinations between the polyelectrolytes in Table 4.1, complexation manifested itself as phase separation into two coexisting clear phases, as shown by the pictures in Figure 4.1, similar to the complex coacervation of PDMAEMA and PAA described in Chapter 3. The concentrated phases were typically transparent and liquid-like, but highly viscous, and can be qualified as complex coacervates.

In two cases, no phase separation occurred, even at very low salt concentrations. Mixtures of PTMAEMA and PSS (Figure 4.1c) and PDMAEMA and PSS (not shown) became turbid at very low salt concentrations, but neither droplets of complex coacervate phase, nor a macroscopically separated phase after centrifugation was observed. At slightly higher salt concentrations, the turbidity even seemed to have

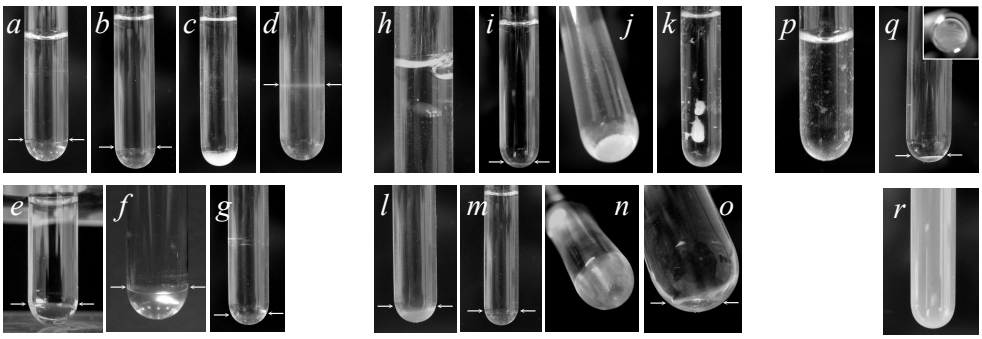

Figure 4.1: Pictures of mixtures of the oppositely charged polyelectrolytes from Table 4.1 in glass tubes of 1 cm in diameter. (a) PTMAEMA/PAA, (b) PTMAEMA/PSPMA, (c) PTMAEMA/PSS, (d) PTMAEMA/L_2EO_4+Zn, (e) PDMAEMA/PAA, (f) PDMAEMA/PSPMA, (g) PDMAEMA/L_2EO_4+Zn, (h) PAH/PAA, (i) PAH/PSPMA, (j) PAH/PSS, (k) PAH/L_2EO_4+Zn, (l) PM2VP/PAA, (m) PM2VP/PSPMA, (n) PM2VP/PSS, (o) PM2VP/L_2EO_4+Zn, (p) PEI/PAA, (q) PEI/PSPMA, (r) PEI/PSS. In the cases where a liquid-liquid phase separation occurred, the interface has been indicated with two arrows.

dissappeared and complexation suppressed. Mixtures of PEI and PSS (Figure 4.1r) showed the same behaviour, but now the turbidity only disappeared at much higher salt concentrations.

In some other cases, the complex coacervates that formed were not really transparent, but rather opaque. PAH/PAA, PEI/PAA and PAH/L_2EO_4+Zn complex coacervates were always opaque, but became more transparent with increasing salt concentration. PAH/PSPMA and PEI/PSPMA seemed to change from opaque complexes to transparent, viscous liquids at 1.0 M salt. We note that this could be the result of incomplete equilibration at low salt concentrations.

Finally, some combinations of polyelectrolytes flocculated into solid-like flocs at low salt concentrations. PAH/PSS (Figure 4.1j) formed such flocs for all salt concentrations up to the critical salt concentration. PM2VP/PSS (Figure 4.1n) formed such flocs at low salt concentrations, but formed an opaque viscoelastic complex phase at higher salt concentrations. Again, we emphasise that the appearance of flocs may be the result of a strong attraction between the polyelectrolytes, leading to a kinetically arrested aggregate that does not represent the thermodynamic equilibrium structure.

4.3.2 Critical salt concentrations

We determined the critical salt concentrations of the complex coacervates and polyelectrolyte complexes shown in Figure 4.1 in the same way as described in Chapter 3. Figure 4.2 shows these critical salt concentrations, grouped by type of polyanion.

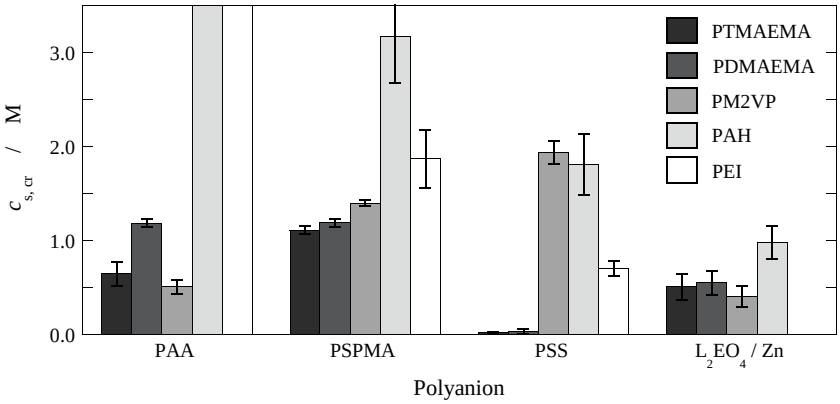

Figure 4.2: Experimentally determined critical salt concentrations for mixtures of oppositely charged polyelectrolytes with an approximate chain length of 100, from Table 4.1: $PTMAEMA_{96}$, $PDMAEMA_{150}$, $PM2VP_{88}$, PAH_{161}, PEI, PAA_{139}, $PSPMA_{94}$, PSS_{165} and L_2EO_4/Zn. The complexes are grouped by polyanion. Different shadings indicate different polycations, as indicated by the labels. In most cases KCl was used as monovalent salt. In the case of PM2VP/PSPMA and PAH/PSPMA we used NaCl and in the case of PAH/PAA and PEI/PAA we used KCl, NaCl and $NaNO_3$, but found no critical point.

In almost all cases, we have used KCl as monovalent salt. PAH/PSPMA complex coacervates did not dissolve even at 3.0 M KCl, which was the highest concentration we could achieve. Therefore, we reported the critical NaCl concentration for this combination of polyelectrolytes in Figure 4.2. PAH/PAA and PEI/PAA did not dissolve at 3.0 M KCl, nor at 5.0 M NaCl, nor at 8.0 M $NaNO_3$.

We find significant differences in the critical salt concentrations of different complex coacervates. Some combinations readily dissolve at 0.50 M KCl (PM2VP/PAA), others form strong complexes that only dissolve above 2 or 3 M KCl (PM2VP/PSS or PAH/PSPMA). Nevertheless, we can identify some trends.

First of all, the complex coacervates with the coordination polymer all have relatively low critical salt concentrations. These coordination polymers form living rings and polymer chains in solution. Their average size is, however, rather small, and they can dissociate into fragments at any point along the chain. The charges on these living polymers are therefore not as closely associated as the charges on conventional polyelectrolytes. Hence, their interactions with oppositely charged polyelectrolytes are weaker than the interactions between other oppositely charged polyelectrolytes, just like the interactions between monovalent salt ions and polyelectrolytes are weaker than between oppositely charged polyelectrolytes.

Secondly, combinations of polyelectrolytes with hydrophobic groups have a higher critical salt concentration. PM2VP/PSS is the most obvious example. This obser-

vation is in agreement with the findings of Kudlay and Olvera de la Cruz (see also Chapter 3) that hydrophobic complex coacervates are depleted of salt, and hence a higher bulk salt concentration is needed to disrupt these complexes.[18]

Thirdly, combinations made with either PAH or PEI all tend to have relatively high critical salt concentrations, except PEI/PSS. One explanation could be that the positive charges on these polymers are present on accessible groups (primary and secondary amines), which means they can form tight ionic bonds. Another possible explanation comes from the chain lengths of these two polycations. Both PAH_{161} and PEI are very polydisperse and contain some very long chains that are likely to have high critical salt concentrations (see Chapter 3). We measured the critical salt concentration beyond which no complexes form at all, which most likely reflects the chain length of the longest polymers in the samples.

Some differences are, however, difficult to explain at this point. For example, PTMAEMA/PAA has a critical salt concentration that is about half the critical salt concentration of PDMAEMA/PAA. Moreover, PTMAEMA/PSS seems to form almost no complexes at all. Flexibility of the chains can hardly play a role here. All polyelectrolytes have Kuhn lengths of the order of a few nm (see Table 4.1) and are considered flexible polymers. The charge density of the polyelectrolytes is also very similar. They all bear one chargeable group for every two carbon atoms along the main chain. At pH 6.5, almost all chargeable groups are charged at salt concentrations above 0.10 M. Could the size or the accessibility of the charged groups play a role? The size of the side groups in PTMAEMA and PDMAEMA is almost the same. The accessibility of the charges is different, however. The charged nitrogen in PTMAEMA is surrounded by more alkyl groups than in PDMAEMA. This could mean that the ionic bonds between the quaternary ammonium groups in PTMAEMA and negatively charged groups are weaker than between the protonated tertiary ammonium groups in PDMAEMA and negatively charged groups. However, this cannot be the only relevant factor, because it would imply that the critical salt concentration of complex coacervates with PTMAEMA always have a lower critical salt concentration than those with PDMAEMA. Yet, the complex coacervates with PSPMA and with L_2EO_4+Zn have almost equal critical salt concentrations, despite the fact that in this case the PTMAEMA chains are shorter than the PDMAEMA chains. Moreover, it cannot explain the large difference in critical salt concentration between PTMAEMA/PSPMA and PTMAEMA/ PSS, where both positively charged groups are quaternary ammonium groups and both negatively charged groups are sulphonates.

In summary, some trends can be identified for complex coacervates of flexible, highly charged polyelectrolytes, but many large differences in critical salt concentrations must be caused by a combination of geometrical, chemical and conformational effects and are difficult to predict in advance.

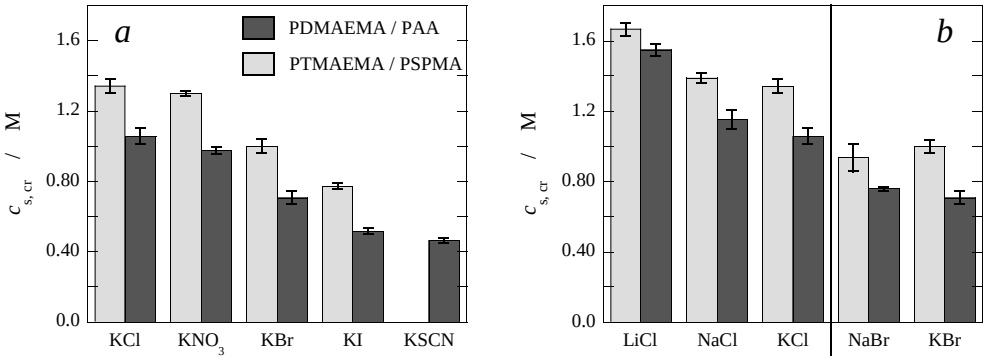

Figure 4.3: Experimentally determined critical salt concentrations for two combinations of polyelectrolytes, using various types of monovalent salts: (a) potassium salts with different anions. (b) chloride and bromide salts with different cations. $PDMAEMA_{527}$ is in itself not soluble in KSCN at the salt concentrations we used for formation of the complex coacervates.

4.3.3 Effect of type of salt on complex coacervate stability

The critical salt concentration is not independent of the type of salt. Figure 4.3 shows critical salt concentrations for two complex coacervates, $PTMAEMA_{96}$/ $PSPMA_{94}$ and $PDMAEMA_{527}/PAA_{500}$, using different monovalent salts.

The specific ion effects exhibited by the salts displayed in Figure 4.3 is commonly known as a Hofmeister series, named after the discovery that the ions of these salts have different abilities to salt out proteins.[19–21] Clearly, larger cations and anions, with smaller hydration shells, tend to give rise to lower critical salt concentrations. This suggests that hydration of the charged groups in the complex coacervates plays an important role, especially for the groups that are involved in ionic bond formation. Probably, strongly hydrated ions, such as Li^+ and Cl^-, partially dehydrate the complex coacervates, thereby strengthening the ionic bonds between oppositely charged polyelectrolytes. Alternatively, the less hydrated and highly polarisable ions, such as K^+ and SCN^-, are more effective in breaking the ionic bonds between oppositely charged polyelectrolytes, because they either lower the energy barrier of the ionic bond rupture process (see Chapter 8) or because the corresponding free energy of the polymer-salt ion pair is lower, or both.

Our findings are in good agreement with the reported specific ion effects in polyelectrolyte multilayers of PDADMAC/PSS.[22,23] In those cases, less hydrated anions were argued to screen polyelectrolyte charges more strongly, leading to a more loosely bound deposition of the layers onto each other, and hence, an increased thickness of the polyelectrolyte multilayers. In fact, following a similar reasoning, the hydration of the ionic groups of the polyelectrolytes most likely also plays a role in explaining

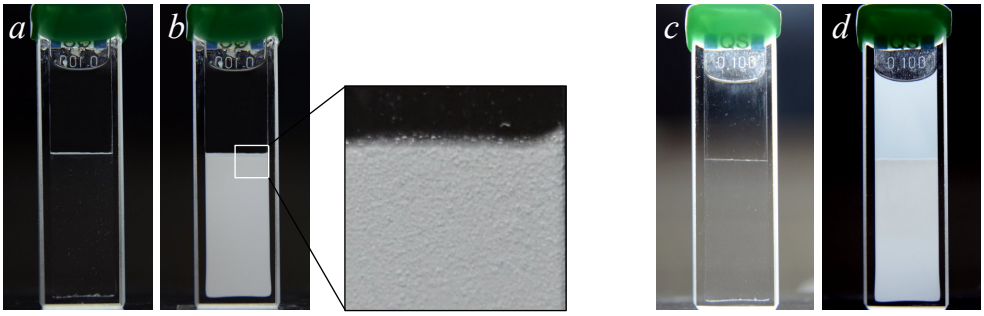

Figure 4.4: Cuvets filled with complex coacervates of $PDMAEMA_{527}/PAA_{500}$ (a and b) and $PTMAEMA_{96}/PSPMA_{94}$ (c and d) and their dilute phases at $T = 20\,°C$ (a and c) and $T = 30\,°C$ (b and d).

the differences in critical salt concentrations between different complex coacervates that are shown in Figure 4.2.

4.3.4 Effect of temperature on phase behaviour

In many classical two-phase polymer systems, temperature has a pronounced effect on the phase behaviour. For the associative phase separated polymer mixtures discussed here, salt appears to partly play the role of an effective temperature (see also Chapter 8). However, temperature affects the phase behaviour as well. For the same two complex coacervates as studied in the previous Section, we investigated what effect increasing or decreasing the temperature would have on the phase behaviour.

Figure 4.4 shows that both complex coacervates, prepared at 20 °C, become turbid when the temperature is increased. The turbidity first appears at the walls of the cuvets and diffuses in, following the gradient of temperature, which reaches a threshold value first at the walls. A close inspection of the turbid complex coacervates under the microscope and complementary scattering experiments reveal that small droplets seem to have formed inside these phases (see also Chapter 7). We tentatively explain these observations by considering the phase diagram of complex coacervation.

We assume that the complex coacervation of both combinations of polyelectrolytes is effectively characterised by the phase diagram we described in Chapter 3 (see Figure 3.7). We argue that the turbidity and appearance of droplets suggests that an increase in temperature is equivalent to shifting the binodal towards a stronger incompatibility between the phases, as shown in Figure 4.5a. Following this argument, increasing the temperature leads to more extreme binodal compositions of the complex coacervates, and hence, an 'undersaturation' of the complex coacervates in their present states, which were defined by a lower temperature. Consequently, the complex coacervates

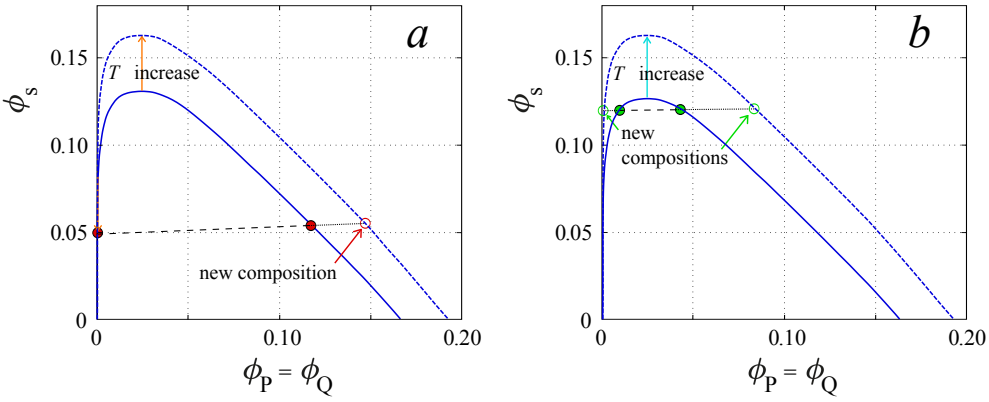

Figure 4.5: Schematic drawing of the salt-polymer phase diagram of complex coacervation, showing the equivalent effect of an increase in temperature for complex coacervates (a) far from and (b) close to the critical point.

expel dilute phase, which grows into droplets, to reach a higher density. Because of the high viscosities of the complex coacervates and relatively low overall density differences, these droplets take a very long time to reach the macroscopic dilute phase. If we use centrifugation again to speed up this separation process, we find that the complex coacervate phase eventually becomes transparent again.

A striking difference between the two combinations shown in Figure 4.4 is the fact that the dilute phase of PTMAEMA/PSPMA became turbid too upon increasing the temperature, whereas the dilute phase of PDMAEMA/PAA remained clear. This difference can be explained by the fact that the PTMAEMA/PSPMA complex coacervate was much closer to its critical point than the PDMAEMA/PAA complex coacervates, and the fact that the polymer chain lengths of PTMAEMA and PSPMA were much shorter than those of PDMAEMA and PAA. Based on our findings in Chapter 3, the polymer concentration in the dilute phase of the PTMAEMA/PSPMA was much higher than in the dilute phase of PDMAEMA/PAA. Upon increasing the temperature, the dilute phase should also get a more extreme, in other words, more dilute, composition. In the case of PTMAEMA/PSPMA, enough polymer was present in the dilute phase to give rise to visible turbidity as a result of complexation taking place, as shown in Figure 4.5b. In the case of PDMAEMA/PAA however, the polymer concentration was too low to give rise to visible droplets of complex coacervate phase. As expected, we found that the turbidity in the dilute phase of the PTMAEMA/PSPMA mixtures disappeared much faster, even without centrifugation, because the viscosity of the dilute phase is much lower than the viscosity of the complex coacervate phase.

If on the other hand, we decreased the temperature of the complex coacervates,

we observed no turbidity. On the contrary, the interface separating the dilute and complex coacervate phase in some mixtures close to the critical salt concentration seemed to become even less sharp, suggesting a smaller difference in composition between both phases. This would indicate that decreasing the temperature does the exact opposite of increasing the temperature: the equivalent of shifting the binodal to that of a mixture with a weaker incompatibility. This highly subjective observation is however very difficult to quantify or demonstrate. In any case, we never observed the actual crossing of the critical point and complete mixing of a phase separated sample by simply decreasing the temperature. The effect of temperature is therefore likely much smaller than the effect of salt.

The tentative explanation we have given above implies that the complexes of these polymers behave similar to classical polymers in a solvent with a lower critical solution temperature (LCST). If the temperature is increased in an already phase separated solution of a polymer with LCST behaviour, the two phases will acquire more extreme compositions. In other words, the entropy change of mixing such a polymer with solvent is negative. Analogously, for the complex coacervates the entropy of mixing complexes of oppositely charged polyelectrolytes and water is negative.

4.3.5 Water content of the complex coacervates

In Chapter 3 we found that the amount of water present in the complex coacervates is practically independent of chain length and hardly dependent on salt concentration far enough from the critical point. Moreover, a comparison with previous reports on other protein complex coacervates revealed that these also seemed to have very similar water contents.

Here, we apply the same procedure as in Chapter 3 to measure the water content of the complex coacervates from Figure 4.2. Figure 4.6 shows that for all complex coacervates we have studied, the water content of the condensed phase falls between roughly 60% and 85%, very similar to the water contents we found in Chapter 3 and the water contents found by others for protein complex coacervates. In contrast to the critical salt concentration, we find, to our surprise, that the water content of these complex coacervates does not depend on the types of polyelectrolytes used for complex coacervation.

We note that not all combinations of polyelectrolytes gave rise to the formation of liquid-like complex coacervates. PTMAEMA/PSS, PDMAEMA/PSS and PEI/PSS contained only small aggregates that could be sedimented by centrifugation, but were difficult to separate completely from the supernatant (see Figure 4.1c and r). PAH/PAA, PAH/PSS, PAH/L_2EO_4+Zn and PEI/PAA all gave opaque viscoelastic macroscopic complex, for which we could determine the water content, but we cannot be sure that they have reached their equilibrium structure and composition.

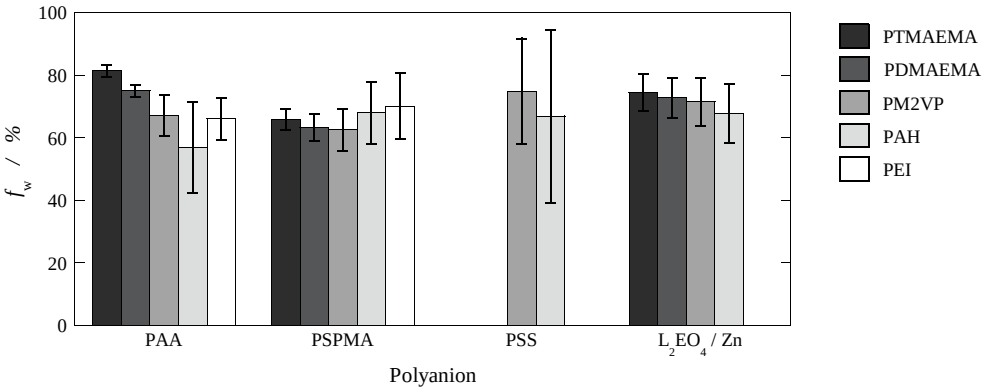

Figure 4.6: Experimentally determined weight fraction of water in the complex coacervates from Figure 4.2, determined at an overall salt concentration at 70 ± 15% of the corresponding critical salt concentration.

The method we have used to determine the water content of the complex coacervates relies on the full evaporation of water from a macroscopic volume of complex coacervate. If the complex coacervate yield is low, the error in the water content is typically large. Moreover, if not all water could be evaporated from the complex coacervates, because strongly hydrated charges retain part of it, we would systematically underestimate the water content. However, we usually dried the complex coacervates at 110 °C. We checked the dry weight regularly and found no changes occurring after a few hours. Finally, we continued the drying process for various complex coacervates in a vacuum oven at 60 °C and 1 mbar and found no further change in dry weight, indicating that effectively all water had evaporated.

At this point we have no satisfactory explanation for this apparently robust water content. We will discuss this observation and possible explanations in more detail in Chapter 13.

4.3.6 Preferred compositions

Finally, we determined the preferred compositions of some of the complex coacervates in Figure 4.2, following the procedure described in Chapter 3. Briefly, we prepared the complex coacervates at a composition of $f^+ = c_+/(c_+ + c_-) = 0.50$, where c_+ is the concentration of chargeable cationic monomeric groups, and c_- is the concentration of chargeable anionic monomeric groups. We then collected the dilute phases and added either polycation or polyanion. If additional complex coacervate was formed, we separated it from the dilute phase again and continued adding polycation or polyanion until no further complexation was observed by eye. From the amount of added

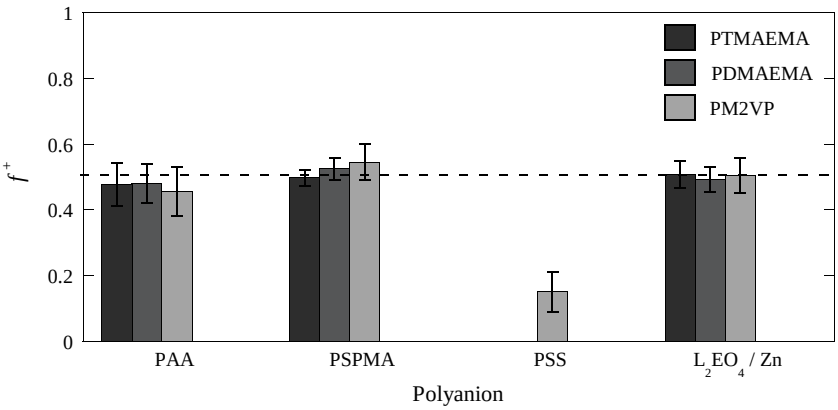

Figure 4.7: Charge fraction of the complex coacervates from Figure 4.2. The error bars calculated from the estimated errors in volumes and concentrations.

polymer we calculated a preferred composition of the complex coacervates, expressed as f^+. In a second titration, we prepared the complex coacervates at the other side of their preferred composition f^+ and determined a second value for the preferred composition by adding the other type of polyelectrolyte. For PDMAEMA/PAA we additionally prepared samples at various overall compositions between $f^+ = 0.2$ and 0.9 (see Chapter 9) and performed similar titrations with the dilute phases.

Figure 4.7 shows these charge compositions for various combinations of polyelectrolytes from Table 4.1. In most cases, we found the same value for f^+ in both titrations, within experimental error. This suggests that the complex coacervates actually have a preferred composition, similar to our findings in Chapter 3 for PDMAEMA/PAA complex coacervates of various chain lengths. If mixtures are prepared at a ratio different from the preferred f^+, excess polycation or excess polyanion will end up in the dilute phase. For PM2VP/PSS and PM2VP/PSPMA we found f^+ values that differed more than the typical experimental error: 0.13 and 0.25 for PM2VP/PSS and 0.47 and 0.62 for PM2VP/PSPMA. These complex coacervates may have slightly more variable compositions, for reasons we do not know at this point.

We find that almost all complex coacervates prefer a composition that is close to $f^+ = 0.50$, that is, a $1:1$ ratio of chargeable groups, suggesting that generic electrostatic interactions dominate the formation of complex coacervates. Only for PM2VP/PSS, we find preferred composition that is very different from the $1:1$ ratio of chargeable groups. The value of f^+ we find is very similar to the compositions of polyelectrolyte multilayers of the same combination of polyelectrolytes reported by Hoogeveen et al.[24] These authors explain their findings from the location of the positively charged group in PM2VP, close to the backbone, which makes it difficult

to access for negative polymeric charges. Nevertheless, for other combinations with PM2VP we do find a preferred composition, corresponding to a 1:1 ratio of charges. This could mean that PM2VP and PSS have such strong attractive interactions that the complexes they form are effectively in a kinetically frozen state during our measurements, and that PSS is taken up more easily into a complex because of its more accessible charged group.

4.4 Concluding remarks

We have made nineteen combinations of different flexible, synthetic polyelectrolytes. We found a typical associative phase separation in most cases, leading to a liquid-like, but highly viscous complex coacervate phase of oppositely charged polyelectrolytes. We measured the critical salt concentrations, water contents and preferred compositions of these complex coacervates. The critical salt concentrations vary widely, probably because of a combination of varying electrostatic interaction strengths, additional hydrophobic, steric and dipole-dipole interactions and geometrical and conformational effects. The water contents of all complex coacervates on the other hand, is remarkably similar, between 60% and 85% and their composition is always close to a 1:1 ratio of chargeable groups.

For two complex coacervates, PDMAEMA/PAA and PTMAEMA/PSPMA, we investigated the effect of the type of salt and temperature on their phase behaviour. We find that specific ion effects, similar to those found in the classical Hofmeister series, affect the stability of the complex coacervates. Less hydrated, highly polarisable cations and anions are more effective in weakening the polyelectrolyte complexes. An increase in temperature has an equivalent effect on complex coacervates as a decrease in salt concentration: the coexisting phases tend to acquire more extreme compositions. Complex coacervates that were prepared at lower temperatures will expell droplets of dilute phase and become turbid.

References

[1] T. Vermonden, J. van der Gucht, P. de Waard, Marcelis A. T. M., N. A. M. Besseling, E. J. R. Sudhölter, G. J. Fleer, and M. A. Cohen Stuart, *Macromolecules*, 2003, **36**, 7035–7044.

[2] C. Wang, Y. Guo, Y. Wang, H. Xu, R. Wang, and X Zhang, *Angew. Chem. Int. Ed.*, 2009, **48**, 8962–8965.

[3] L. N. Andreeva, S. V. Bushin, M. A. Bezrukova, T. N. Nekrasova, R. T. Imanbaev, V. D. Pautov, V. D. Nazarova, Yu. I. Zolotova, and E. F. Panarin, *Russ. J. Appl. Chem.*, 2012, **85**, 417–425.

[4] A. I. Kipper, S. V. Valueva, and N. A. Matveeva, *Russ. J. Appl. Chem.*, 2008, **81**, 2045–2047.

[5] K. Paeng and M. D. Ediger, *Macromolecules*, 2011, **44**, 7034–7042.

[6] R. von Klitzing, *Phys. Chem. Chem. Phys.*, 2006, **8**, 5012–5033.

[7] B. Brissault, A. Kichler, C. Guis, C. Leborgne, O. Danos, and H. Cheradame, *Bioconj. Chem.*, 2003, **14**, 581–587.

[8] W. J. Walczak, D. A. Hoagland, and S. L. Hsu, *Macromolecules*, 1992, **25**, 7317–7323.

[9] G. Miquelard-Garnier, C. Creton, and D. Hourdet, *Soft Matter*, 2008, **4**, 1011–1023.

[10] W. Peiquiang, M. Siddiq, C. Huiying, Q. Di, and C. Wu, *Macromolecules*, 1996, **29**, 277–281.

[11] G. M. Pavlov, G. F. Kolbina, I. I. Gavrilova, and E. F. Panarin, *Pol. Sci. A*, 2010, **52**, 115–118.

[12] G. Weill and G. Maret, *Polymer*, 1982, **23**, 1990–1993.

[13] T. Vermonden, *Ph.D. thesis*, Wageningen University, 2005.

[14] A. M. Brzozowska, A. de Keizer, W. Norde, C. Detrembleur, and M. A. Cohen Stuart, *Coll. Pol. Sci.*, 2010, **288**, 1081–1095.

[15] D. M. Jones, A. A. Brown, and W. T. S. Huck, *Langmuir*, 2002, **18**, 1265–1269.

[16] N. Cheng, O. Azzaroni, S. Moya, and W. T. S. Huck, *Macromol. Rapid Commun.*, 2006, **27**, 1632–1636.

[17] M. Ramstedt, N. Cheng, O. Azzaroni, D. Mossialos, H. J. Mathieu, and W. T. S. Huck, *Langmuir*, 2007, **23**, 3314–3321.

[18] A. Kudlay and M. Olvera de la Cruz, *J. Chem. Phys.*, 2004, **120**, 404–412.

[19] F. Hofmeister, *Arch. Exp. Pathol. Pharmakol.*, 1888, **24**, 247–260.

[20] W. Kunz and J. H. B. W. Ninham, *Curr. Opin. Coll. Int. Sci.*, 2004, **9**, 19–37.

[21] Y. Zhang and P. S. Cremer, *Curr. Opin. Chem. Biol.*, 2006, **10**, 658–663.

[22] M. Salomäki, P. Tervasmäki, S. Areva, and J. Kankare, *Langmuir*, 2004, **20**, 3679–3683.

[23] J. E. Wong, H. Zastrow, W. Jaeger, and R. von Klitzing, *Langmuir*, 2009, **25**, 14061–14070.

[24] N. G. Hoogeveen, M. A. Cohen Stuart, and G. J. Fleer, *Langmuir*, 1996, **12**, 3675–3681.

Chapter 5

Stability and morphology of complex coacervate core micelles

In this Chapter we study the stability and morphology of micelles with complex coacervate cores (C3Ms). We use combinations of poly(acrylic acid) (PAA) and poly(*N*-methyl-2-vinylpyridinium)-*b*-poly(ethylene oxide) (PM2VP-*b*-PEO) of various chain and block lengths to investigate how polymer chain length and salt concentration affect the stability and morphology of complex coacervates in the cores of the micelles. The polymer chain length has a similar effect on the salt stability of both C3Ms and macroscopic complex coacervates. The most surprising difference with macroscopic complex coacervates is that the polymer chain lengths not only affect the salt stability of C3Ms, but also change the morphology of C3Ms from spherical star-like to crew-cut to worm-like micelles. We use a combination of polarised and depolarised static and dynamic light scattering and small angle X-ray scattering to show that worm-like micelles with contour lengths up to 300 nm are formed close to the critical salt concentration when the PAA polymers are short enough. A critical review of existing literature on other C3Ms reveals that this transition is probably a general phenomenon, which can be rationalised in terms of a packing parameter for amphiphiles.

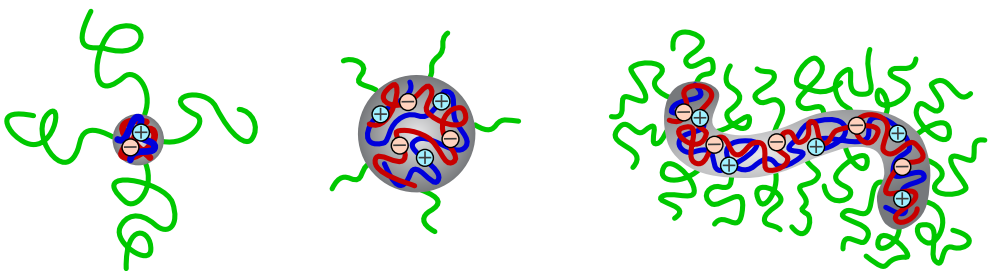

This Chapter is submitted for publication in a slightly modified form as:
H. M. van der Kooij, E. Spruijt, I. K. Voets, R. Fokkink, M. A. Cohen Stuart and J. van der Gucht, *On the stability and morphology of complex coacervate core micelles: from spherical to worm-like micelles*, Langmuir.

5.1 Introduction

Complex coacervate core micelles (C3Ms) are polymeric nanostructures with a complex coacervate core and a neutral hydrophilic corona. They co-assemble spontaneously from ionic-neutral copolymers and oppositely charged macroions below a critical salt concentration in aqueous solution. C3Ms are promising candidates for a variety of applications. In solution, they are potential carriers of charged compounds, such as enzymes,[1,2] DNA,[3] RNA,[4] antibodies,[5] nanoparticles,[6] dendritic photosensitisers[7] and metal ions,[8] and they can be used to purify waste water by flocculation of charged contaminants.[9] At surfaces, C3Ms act as antifouling agents.[10,11] For all these purposes, knowledge of the stability and morphology of these micelles is essential. When the effects of salt concentration, polymer chain length and polymer concentration on the stability and morphology of C3Ms are known in detail, these structures can be optimised to meet the desired conditions.

Despite the considerable interest in C3Ms, systematic studies on their stability and morphology are scarce. The majority of studies on the stability of C3Ms deal with the effect of salt. Kabanov et al. were pioneers in this area: they measured a decrease of light scattering intensity with increasing salt concentration, which they attributed to disintegration of C3Ms.[12] Later, it was found that both the number and mass of C3Ms are reduced upon addition of salt.[13] Beyond a certain critical salt concentration, which varies significantly between different types of C3Ms,[6] all micelles are dissociated. The critical salt concentration also depends on the polymer concentration and chain length. Yan et al.[14] and Wang et al.[13] used the concentration dependence to investigate the effect of salt on the critical micelle concentration (CMC), and found that the CMC increases exponentially with the square root of salt concentration. The influence of polymer chain length on the stability of C3Ms has been studied only qualitatively by Gaucher et al.[15] They concluded that the resistance of C3Ms against salt-induced disintegration ('salt stability') improves with increasing homopolymer chain length. Unfortunately, they limited their research to three homopolymer lengths.

Experimental studies on the size and morphology of C3Ms mainly address the effect of salt on the hydrodynamic radius R_h. Both an increase[2,13,14,16–24] and a decrease[2,25–27] of R_h upon addition of salt have been reported, but the mechanisms underlying these opposite trends are poorly understood. Yan et al. were the first to show that salt sometimes causes a morphological change of C3Ms.[14] Using cryogenic transmission electron microscopy, they revealed that large clusters existed at high salt concentration, of which some seemed to be worm-like micelles. They also observed a peak in light scattering intensity just before the critical salt concentration. This peak appeared to coincide with a maximum in R_h and a local minimum in the polydispersity index, and was only observed for concentrated solutions of C3Ms. A similar scattering

peak has been reported more often, but generally without an explanation.[15,20–22,28] Finally, experiments on the effect of polymer chain length on the morphology of C3Ms are lacking.

In this Chapter we address these two open questions: how does the polymer chain length affect the salt stability of C3Ms, and why do some C3Ms grow whereas others shrink upon addition of salt? We use light scattering salt titrations to answer the first question, and a combination of various light scattering techniques and small-angle X-ray scattering to answer the latter. As a model system, we choose micelles formed from the cationic-neutral diblock copolymer poly(*N*-methyl-2-vinylpyridinium)-*b*--poly(ethylene oxide) (PM2VP-*b*-PEO) and the anionic homopolymer poly(acrylic acid) (PAA), because they are well characterised.[11,29,30] Our measurements indicate that the salt stability of C3Ms increases with chain length for short polymer chains and levels off for longer chains. We support these findings with a model for polyelectrolyte complexation based on the mean-field theory of Voorn and Overbeek.[31] Furthermore, we find that short homopolymers give rise to an increase in the average size of the C3Ms upon addition of salt, whereas long homopolymers give rise to shrinking of C3Ms. The increase in size is accompanied by a peak in scattering intensity. We argue that this peak in intensity is due to a transition from spherical to worm-like micelles, which grow larger with increasing polymer concentration. The insights presented here allow fine-tuning of the stability and morphology of these typical co-assembled nanostructures. We believe that the underlying principles are more general, and also apply to other charge-driven complexes, such as triblock copolymer hydrogels with complex coacervate junction points[32,33] and complex coacervate membranes.[34]

5.2 Experimental details

5.2.1 Materials

We used poly(*N*-methyl-2-vinylpyridinium)-*b*-poly(ethylene oxide) (PM2VP-*b*-PEO), a cationic-neutral diblock copolymer with pH-independent charges and poly(acrylic acid) (PAA), an anionic polyelectrolyte with pH-dependent charges, to form complex coacervate core micelles (C3Ms) in aqueous solutions. We used polymers with various block and chain lengths, as shown in Table 5.1.

The diblock copolymers were quaternised with iodomethane, according to a procedure described elsewhere.[11] The final degree of quaternisation of these block copolymers was 86 – 89% (see Table 5.1).

For preparation of the C3Ms we used stock solutions of 1.0 M NaCl, 0.10 M HCl and 0.10 M NaOH in Milli-Q water (resistance > 18.2 M$\Omega \cdot$cm).

Table 5.1: Specifications of the PM2VP-*b*-PEO and PAA polymers used in this Chapter. N is the number-averaged degree of polymerisation, calculated from M_n.

Polymer	Supplier	M_n (kg/mol)	N	M_w/M_n
PAA_{13}	Polysciences	1.2[a]	13	1.60
PAA_{20}	Sigma-Aldrich	1.5	20	1.32
PAA_{47}	Polymer Source	3.4	47	1.30
PAA_{139}	Polymer Source	10.0	139	1.15
PAA_{162}	Polymer Source	11.7	162	1.07
PAA_{500}	Polymer Source	36.0	500	1.10
PAA_{1630}	Polysciences	153.3[a]	1630	1.60
PAA_{1728}	Polymer Source	124.5	1728	1.25
PAA_{4200}	Sigma-Aldrich	$3.0 \pm 0.8 \times 10^2$	4.2×10^3	?[b]
PAA_{11600}	Sigma-Aldrich	$8.3 \pm 2.1 \times 10^2$	12×10^3	?[b]
PAA_{37000}	Sigma-Aldrich	$2.7 \pm 0.7 \times 10^3$	37×10^3	?[b]
$PM2VP_{41}$-*b*-PEO_{204}	Polymer Source[c]	9.6-*b*-9.0	41-*b*-204	1.05
$PM2VP_{128}$-*b*-PEO_{477}	Polymer Source[c]	29.8-*b*-21.0	128-*b*-477	1.10
$PM2VP_{249}$-*b*-PEO_{134}	Polymer Source[d]	56.5-*b*-5.9	249-*b*-134	1.05

Notes

[a] Sodium salt.

[b] Only the viscosity-averaged molecular weight was specified. M_n was estimated as $M_v/1.5$ ($\pm$ 25%). These polymers are <0.1% cross-linked.

[c] Purchased in unquaternised form as $P2VP_{41}$-*b*-PEO_{204} and $P2VP_{128}$-*b*-PEO_{477}, respectively. DQ $\approx$ 89%.

[d] DQ $\approx$ 86%.

5.2.2 Sample preparation

Stock solutions of PM2VP-*b*-PEO (10 g/L) and PAA (5 g/L) were prepared by dissolving the polymers in water containing 10 mM NaCl. They were filtered through a 0.20 µm polyethersulphone syringe filter, and the first 1 mL of the filtered solution was discarded. Stock solutions were mixed at a 1 : 1 ratio of chargeable polycationic and polyanionic groups and diluted with 10 mM NaCl to the desired concentrations.

The pH was adjusted to 7.1 $\pm$ 0.2, where the PAA is almost fully charged at salt concentrations above 10 mM (see Chapter 3). All experiments were performed at 20.0$\pm$0.3 ℃ at least 18 hours after mixing the polymers. C3Ms formed from $PM2VP_m$-*b*-PEO_x and PAA_n are referred to as C3M-$PM2VP_m/PAA_n$. Polymer concentrations are expressed as the corresponding concentrations of acrylic acid monomers c_{AA} (in mM).

5.2.3 Light scattering salt titrations

Light scattering (LS) salt titrations were performed on an ALV instrument equipped with a 300 mW Cobolt Samba DPSS laser operating at a wavelength of 532 nm, an ALV/SO single photon detector with static and dynamic enhancer fiber-optical technology and an ALV-5000/60X0 external correlator. The detection angle θ was 90°. A Schott-Geräte computer-controlled titration setup was used to regulate the addition of titrant, stirring, and delay time between additions. The titrant was a filtered 1.0 M NaCl solution at pH 7.1 ± 0.2 in all cases. Both the stirring and delay time were typically 60 seconds. After every addition, the light scattering intensity I was recorded in four independent runs of 30 seconds. When a peak in the scattering intensity was observed, the titration was repeated with a delay time of 300 seconds to check that the appearance of the peak was not caused by slow processes taking place during titration. Second-order cumulant analysis[35] (standard ALV software) of the intensity autocorrelation functions $g_2(\tau)$ yielded the characteristic decay rates Γ, from which apparent diffusion coefficients D were calculated. Diffusion coefficients were converted to apparent hydrodynamic radii R_h using the Stokes-Einstein equation.[36] Furthermore, inverse Laplace transformation, carried out using CONTIN software,[37,38] was used to analyse the size distributions of the C3Ms.

The total salt concentration c_s after each addition was calculated as the sum of added NaCl, counterions present in the solid polymer, and counterions from the added acid and base. Scattering intensities were corrected for solvent scattering and variation in solvent refractive index, and normalised by the acrylic acid monomer concentration. From a plot of I/c_AA against c_s, the critical salt concentration $c_\mathrm{s,cr}$ was estimated as follows. First, a 'baseline intensity' I_b was established at high salt concentration as the average I/c_AA over at least 100 mM. Then, we tracked the intensity curve from high to low salt concentration. The critical salt concentration was taken as the first point i (i.e., the highest salt concentration) for which the average intensity of three subsequent points was more than twice the baseline intensity ($\frac{1}{3}\sum_i^{i+2}(I/c_\mathrm{AA})_i > 2I_\mathrm{b}$). This method was verified to yield reasonable estimations of $c_\mathrm{s,cr}$ by visual inspection of curves having a clear breakpoint. Since the errors in the resulting critical salt concentrations arise mainly from the choice of the threshold intensity (here $2I_\mathrm{b}$), these errors were estimated as the difference in $c_\mathrm{s,cr}$ when a threshold of $3I_\mathrm{b}$ was used.

5.2.4 Theoretical calculation of critical salt concentrations

The salt stability of C3Ms is predominantly determined by the strength of the polyelectrolyte complex that composes the core.[13] To calculate theoretical critical salt concentrations, we modelled the C3M core using the mean-field theory of Voorn and Overbeek (see Chapter 3).[31] In this study, we used polyelectrolytes with charge

densities $\alpha_+ = \alpha_- = 1$, instead of 0.95, as used in Chapter 3. The electrostatic interaction parameter A was set to 0.9, as in Chapter 3. Finally, we converted calculated volume fractions into concentrations using an empirical molecular length scale $l = 0.65$ nm to find good agreement with our experimental salt and polymer concentrations. We obtained the critical salt concentration for each combination of $\mathrm{PM2VP}_m$ and PAA_n from the maximum of the corresponding binodal.

5.2.5 Dynamic and static light scattering

Dynamic and static light scattering (DLS and SLS) measurements were performed on an ALV instrument equipped with a 300 mW Cobolt Samba DPSS laser operating at a wavelength of 532 nm, a Thorn-Emi RFIB263KF photomultiplier detector, connected to an external ALV7002 multiple tau digital correlator. Unless stated otherwise, the samples were contained in Hellma cylindrical quartz cells of 25 mm outer diameter. To evaluate the angular dependence of the intensity correlation function and the Rayleigh ratio $R(\theta)$, the scattering intensity was recorded at $15^\circ \leq \theta \leq 145^\circ$ with intervals of 2°, in eight independent runs of 150 seconds (DLS) or 30 seconds (SLS) per angle. The scattering angles θ were converted to scattering wave vectors q, according to

$$q = \frac{4\pi\, n_0}{\lambda} \sin\left(\frac{\theta}{2}\right) \tag{5.1}$$

where $n_0 = 1.3332 + 0.0096 \times c_{\mathrm{NaCl}}$ is the solvent refractive index for c_{NaCl} in M, and λ is the laser wavelength in vacuum. Using toluene as a reference, the Rayleigh ratio $R(\theta)$ was calculated at each scattering angle θ according to

$$R(\theta) = \frac{I_{\mathrm{sample}}(\theta) - I_0(\theta)}{I_{\mathrm{t}}(\theta)} \times R_{\mathrm{t}} \times \left(\frac{n_0}{n_{\mathrm{t}}}\right)^2 \tag{5.2}$$

where $I_{\mathrm{sample}}(\theta)$, $I_0(\theta)$ and $I_{\mathrm{t}}(\theta)$ are the sample, solvent and toluene scattering intensity, respectively. $R_{\mathrm{t}} = 2.10 \times 10^{-5}$ cm^{-1} is the Rayleigh ratio of toluene at $\lambda = 532$ nm [39,40] and $n_{\mathrm{t}} = 1.496$ is the refractive index of toluene. $I_0(\theta)$ was approximated by $I_0(90^\circ)/\sin\theta$, since the scattering volume is proportional to $1/\sin\theta$. The validity of this approximation was confirmed by the fact that the measured values of $I_{\mathrm{t}}(\theta)$ also followed a $1/\sin\theta$ dependence. The detector dark current was at most 1% of the solvent and toluene scattering intensity and was therefore neglected. Rayleigh ratios were normalised by the polymer concentration, expressed as c_{AA}, and the optical constant K,

$$K = \frac{4\pi^2\, {n_0}^2\, (\mathrm{d}n/\mathrm{d}C)^2}{\lambda^4\, N_{\mathrm{Av}}} \tag{5.3}$$

where $\mathrm{d}n/\mathrm{d}C$ is the specific refractive index increment of the C3Ms, which was calculated from a weighted average of the refractive index increments of the components: 0.261 mL/g for PAA,[41] 0.270 mL/g for PM2VP,[41] and 0.138 mL/g for PEO.[42] We assumed that PAA and PM2VP were fully charged, and we have approximated the refractive index increment of PM2VP by that of P2VP. This gives a typical refractive index increment $\mathrm{d}n/\mathrm{d}C$ of 0.197 mL/g for C3M-PM2VP$_{41}$/PAA$_{139}$.

5.2.6 Determination of the rotational diffusion coefficient

To determine the rotational diffusion coefficient D_r of the asymmetric objects present in an 8.8 mM C3M-PM2VP$_{41}$/PAA$_{13}$ solution with $c_\mathrm{s} = 180$ mM, DLS measurements were performed at different detection angles and analysed with CONTIN. All decay rate distributions at $67° \leq \theta \leq 145°$ showed two peaks: a large-amplitude peak at low Γ, corresponding to translational diffusion, and a small-amplitude peak at high Γ, corresponding to a composite of translational and rotational motion, which can be written in first-order approximation as[43]

$$\Gamma_\mathrm{fast} = 6D_\mathrm{r} + q^2 D_\mathrm{t} \,. \tag{5.4}$$

To estimate D_r, Γ_fast was plotted against q^2 and extrapolated to $q = 0$ using the data for $67° \leq \theta \leq 83°$.[43]

For spherocylinders with length L, diameter d, and aspect ratio L/d, D_r can be expressed as[44]

$$D_\mathrm{r} = \frac{3k_\mathrm{B}T}{\pi\eta L^3}\big(\ln(L/d) + X_\mathrm{r}(L/d)\big) \tag{5.5}$$

where η is the solvent viscosity and $X_\mathrm{r}(L/d)$ is an empirical shape function, which takes the form for spherocylinders

$$\begin{aligned} X_\mathrm{r}(L/d) = \; & -0.372093 \\ & - \frac{0.95622}{\sqrt[4]{L/d}} + \frac{1.24792}{\sqrt{L/d}} + \frac{1.23085}{L/d} - \frac{1.99498}{(L/d)^2} + \frac{1.84201}{(L/d)^3} - \frac{0.664147}{(L/d)^4} \,. \end{aligned} \tag{5.6}$$

5.2.7 Depolarised static light scattering

To measure depolarised scattering intensities, a Glan-Laser polarising prism (Melles Griot, 03 PGL 301/A, extinction ratio $< 5\times10^{-5}$) was placed in front of the detector. This polariser could be adjusted to transmit only light with polarisation perpendicular to the laser polarisation (I^vh) or parallel to it (I^vv), allowing determination of the depolarisation ratio

$$\Delta^{\mathrm{vh}} = \frac{I^{\mathrm{vh}} - {I_0}^{\mathrm{vh}}}{I^{\mathrm{vv}} - {I_0}^{\mathrm{vv}}} \tag{5.7}$$

where I_0 denotes the solvent scattering intensity. Since the value of I^{vh} is very low, the scattering intensity in the absence of a polariser $I^{\mathrm{vu}} = I$ is almost equal to I^{vv}. The error introduced by replacing the denominator in Equation 5.7 by $I^{\mathrm{vu}} - {I_0}^{\mathrm{vu}}$ is smaller than the error introduced by changing the orientation of the polariser from 0° to 90° and vice versa, which is needed to measure both I^{vh} and I^{vv}. Therefore, I^{vu} and ${I_0}^{\mathrm{vu}}$ were measured and used instead of I^{vv} and ${I_0}^{\mathrm{vv}}$. For each sample, the intensity was recorded at a scattering angle of 55° in ten independent runs of 30 seconds. We chose $\theta = 55°$, because the amount of depolarised light relative to the polariser leakage increases with decreasing θ. At $\theta < 55°$, the tube walls distort the depolarised scattering intensity too much to yield reliable results.

5.2.8 Critical scattering

To investigate if critical scattering could explain the increase in intensity and hydrodynamic radius close to the critical salt concentration, we carried out angle-dependent SLS measurements on C3M-PM2VP$_{41}$/PAA$_{13}$ solutions with five different salt concentrations (c_{s} = 10, 100, 150, 180 and 200 mM), as obtained from the LS salt titrations. For each salt concentration, the normalised Rayleigh ratio $R(\theta)/Kc_{\mathrm{AA}}$ was plotted as a function of q^2 of the sample. Its value in the limit $q \to 0$ was estimated by linear extrapolation of $R(\theta)/Kc_{\mathrm{AA}}$ in the range $15° \leq \theta \leq 25°$ to $q = 0$. The obtained values of $R(0)/Kc_{\mathrm{AA}}$ were plotted as a function of the separation from the critical point $c_{\mathrm{s,cr}} - c_{\mathrm{s}}$ on a double-logarithmic scale.

5.2.9 Small-angle X-ray scattering

SAXS experiments were performed at the European Synchrotron Radiation Facility (ESRF) in Grenoble, France, at the high brilliance beamline ID02.[45] We used an X-ray energy of 12.46 keV and two detector distances of 1.5 and 3.0 m, to cover a total q-range of $5.5 \times 10^{-3} < q < 3.0 \times 10^{-1}$ Å^{-1}. We used 1.9 mm polycarbonate capillaries (Enki SRL) for all samples and carried out all measurements at a controlled temperature of 20 ± 1 °C. We corrected our data for background scattering, detector response and primary beam intensity fluctuations. The instrument scattering vector was calibrated using a silver behenate standard.

5.3 Results and discussion

5.3.1 Characterisation of C3Ms

We prepared C3Ms from different combinations of PM2VP$_m$-*b*-PEO$_x$ and PAA$_n$. The corresponding hydrodynamic radii R_h in 10 mM NaCl are shown in Figure 5.1a as a function of the PAA chain length N_{PAA} for three different block copolymers. A first observation is that the size of the micelles increases with increasing length of the core-forming block N_{PM2VP}. The overall size of the micelles is determined mainly by aggregation number P, which sets the size of the core R_c and the length of the corona-forming block (PEO), which influences the size of the corona L_{corona}. According to scaling theories, the aggregation number P of C3Ms becomes larger with increasing length of the core-forming block (PM2VP) and decreasing length of the corona-forming block.[46] As a result, the radius of the core increases with increasing N_{PM2VP}. The size of the corona also increases with increasing N_{PEO}, although the aggregation number decreases in that case. This is explained by the fact that the effect of N_{PEO} on the corona size outweighs the effect of N_{PEO} on the aggregation number. The total size of C3Ms with identical core-forming blocks is thus predicted[46,47] and indeed also found[48] to increase with increasing length of the corona-forming block.

The scaling expressions distinguish between two characteristic micelle regimes. Micelles for which the core size R_c is much smaller than the size of the corona L_{corona} are called 'star-like', whereas micelles for which $R_c > L_{corona}$ are called 'crew-cut'.[46,47] For C3Ms with $N_{PM2VP} \ll N_{PEO}$, the size of the micellar core R_c is likely to be smaller than the size of the corona L_{corona} and, hence, the micelles are likely to be star-like.[46] Based on the block lengths of our diblock copolymers, we expect C3Ms formed from PM2VP$_{41}$-*b*-PEO$_{204}$ and PM2VP$_{128}$-*b*-PEO$_{477}$ to be star-like, whereas C3Ms formed from PM2VP$_{249}$-*b*-PEO$_{134}$ are likely to be in or close to the crew-cut regime.

For the micelles depicted in Figure 5.1, the C3Ms formed from PM2VP$_{249}$-*b*-PEO$_{134}$ are expected to be larger than the other two types of C3Ms, because of the combination of a longer core-forming block and a shorter corona-forming block. Both favour a larger aggregation number P, which dominates the decrease of the size of the corona due to a smaller N_{PEO} compared to the other two types of C3Ms. Both star-like C3Ms from PM2VP$_{41}$-*b*-PEO$_{204}$ and PM2VP$_{128}$-*b*-PEO$_{477}$ are nearly identical in overall size. The larger N_{PEO} favours a smaller aggregation number and core size, but a larger corona size. At the same time, a larger N_{PM2VP} favours a larger aggregation number and core size. The latter two effects dominate the overall size in this case, and therefore, C3Ms from PM2VP$_{128}$-*b*-PEO$_{477}$ are slightly larger than C3Ms from PM2VP$_{41}$-*b*-PEO$_{204}$.

A second observation is that a 'critical' PAA length N_{cr} exists for each diblock

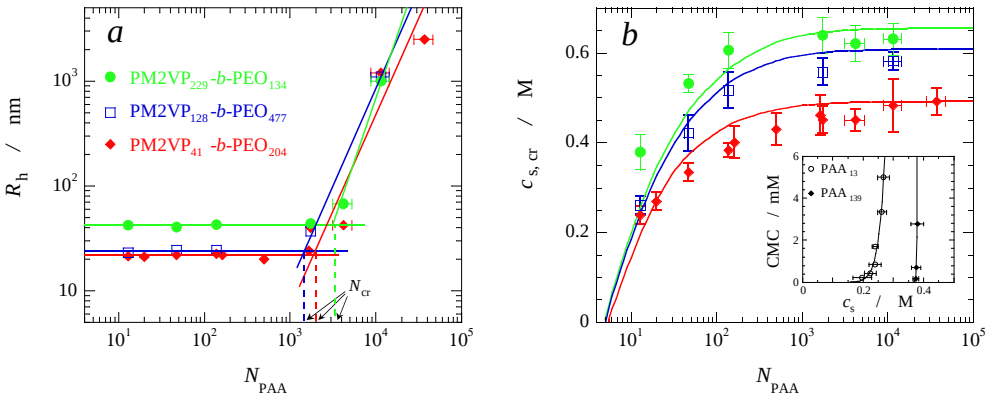

Figure 5.1: (a) Hydrodynamic radii of C3Ms of PM2VP-*b*-PEO and PAA in 10 mM NaCl as a function of PAA chain length, as determined from DLS. Critical PAA lengths N_{cr} are estimated from the intersection between the horizontal line representing a constant radius at small N_{PAA} and a power law fit at large N_{PAA}. (b) Critical salt concentrations of the same C3Ms. The symbols are the experimental values from LS salt titrations. In all titrations, c_{AA} at the critical point was between 0.7 and 2.7 mM. The solid lines are theoretical predictions based on the Voorn-Overbeek theory. The inset shows the exponential dependence of the CMC on the square root of salt concentration for C3Ms of $PM2VP_{41}$-*b*-PEO_{204} and PAA_{13} or PAA_{139}.

copolymer. For $N_{PAA} < N_{cr}$, the hydrodynamic radius is approximately constant, whereas for $N_{PAA} > N_{cr}$, it increases sharply with increasing N_{PAA}. We estimate the critical PAA lengths from the intersection between the horizontal and power-law trendlines in Figure 5.1a. This gives $N_{cr} = 1.4 \times 10^3$, 1.9×10^3 and 3.5×10^3, for $PM2VP_{128}$-*b*-PEO_{477}, $PM2VP_{41}$-*b*-PEO_{204} and $PM2VP_{249}$-*b*-PEO_{134}, respectively. Assuming an error of 0.4×10^3, we conclude that the difference in N_{cr} between the first two diblock copolymers in negligible. $PM2VP_{249}$-*b*-PEO_{134}, however, has a considerably larger N_{cr}. We believe this is due to the higher aggregation number of C3Ms formed from this diblock copolymer, as explained above.

A similar dependence of C3M size on homopolymer length has been reported by Van der Burgh et al.[25] They attributed the increase in hydrodynamic radius above N_{cr} to the limited volume of the micellar core. For $N_{PAA} < N_{cr}$, the total number of monomers in the core is independent of N_{PAA} and equal to $2N_{cr}$, but when the length of a single PAA chain exceeds N_{cr}, the core can no longer accommodate an entire PAA chain without growing in size. The core must expand, causing an increase of both the aggregation number and size of the micelles.

Above N_{cr}, C3Ms are therefore probably co-assemblies of a single PAA chain and N_{PAA}/N_{PM2VP} diblock copolymers. We note that the term C3M may not be appropriate for co-assemblies with $N_{PAA} \gg N_{cr}$, since the PM2VP blocks can

no longer reach the centres of these assemblies, and consequently, the core is not a homogeneous complex coacervate. The hydrodynamic radii of these structures exceed the PM2VP-*b*-PEO contour lengths. We estimate these contour lengths as $L_c \approx 0.26 \times N_{PM2VP} + 0.40 \times N_{PEO}$ nm,[49,50] which amounts to 90 nm for $PM2VP_{41}$-*b*-PEO_{204}, 220 nm for $PM2VP_{128}$-*b*-PEO_{477}, and 110 nm for $PM2VP_{249}$-*b*-PEO_{134}. The radii of some of these structures are even larger than expected for single high M_w PAA chains, suggesting that secondary aggregation has occurred.

The hydrodynamic radii of C3M-$PM2VP_{41}$/PAA_n are in good agreement with literature values. Danial et al. reported that $R_h = 23 \pm 3$ nm for C3M-$PM2VP_{41}$/PAA_{48} in 50 mM $NaNO_3$ at pH 7.7.[29] Both Lindhoud et al. and Brzozowska et al. reported a R_h of 22 nm for C3M-$PM2VP_{41}$/PAA_{139} at pH 7.1.[11,30] Reports on C3M-$PM2VP_{128}$/PAA_n and C3M-$PM2VP_{249}$/PAA_n are lacking.

Finally, we noticed a surprisingly large difference in size between C3M-$PM2VP_{41}$/PAA_{1630} ($R_h = 24$ nm) and C3M-$PM2VP_{41}$/PAA_{1728} ($R_h = 40$ nm) (see Figure 5.1a). We attribute this to the different polydispersity indices of PAA_{1630} and PAA_{1728}, which are 1.60 and 1.25, respectively. Since N_{cr} is around 1.9×10^3, a single PAA_{1630} or PAA_{1728} chain is not sufficient to form a stable micelle. It has to be combined with a very short PAA chain to reach a total number of monomers of 1.9×10^3. Alternatively, two intermediately long chains with N_{PAA} around 1×10^3, or of a single PAA_{1900} chain can be incorporated. The relatively high polydispersity of PAA_{1630} allows all three scenarios. The sample with PAA_{1728}, however, has a narrower distribution of PAA lengths. These C3Ms must probably incorporate two longer PAA chains and are therefore larger.

5.3.2 Stability of C3Ms

When salt is added to a solution of C3Ms, the CMC increases, resulting in disassembly of C3Ms. Here, we define the stability of C3Ms as their ability to resist this salt-induced disintegration. We express stability quantitatively by means of the critical salt concentration $c_{s,cr}$, which is the salt concentration beyond which all C3Ms are disintegrated. A well-established method to study the salt stability of C3Ms is a light scattering salt titration.[21,51] To answer our first question about the effect of polymer chain length on the salt stability of C3Ms, we performed LS salt titrations for the same set of C3Ms as studied in the previous Section. Their critical salt concentrations are shown in Figure 5.1b.

For each diblock copolymer, we find that the critical salt concentration increases with increasing PAA length and levels off for long PAA chains. Increasing the PM2VP block length also leads to an improved salt stability of our C3Ms. We notice a striking similarity between these results and the chain length dependence of $c_{s,cr}$ for macroscopic complex coacervates (see Chapter 3). Apparently, the same forces drive

the formation of the C3M cores. Indeed, the mean-field theory of Voorn and Overbeek predicts the correct trends for the dependence of the critical salt concentrations on both N_{PAA} and N_{PM2VP} using only a single adjustable molecular length scale l. For short PAA chains, the critical salt concentrations of micelles are underestimated slightly by the Voorn-Overbeek theory, similar to our findings for macroscopic complex coacervates. We note that these critical salt concentrations of C3Ms with $\mathrm{PM2VP}_{41}$ and $\mathrm{PM2VP}_{128}$ blocks are in all cases lower than the critical salt concentration of a macroscopic complex coacervate of $\mathrm{PM2VP}_{88}$ and PAA_{139}, which is about 0.55 M (see Chapter 4). For very long PAA chains the critical salt concentration of the C3Ms approaches this value. We conclude from this that the PEO blocks also affect the salt stability of C3Ms, due to steric repulsion between the solvated PEO blocks.

An experimental parameter that we have not taken into account yet is the polymer concentration. In fact, the critical salt concentrations we show in Figure 5.1b are the salt concentrations at which the solubility of the polymeric components equals the CMC. The CMC of C3Ms has been found to increase exponentially with the square root of salt concentration and, hence, at higher polymer concentrations we expect to find higher critical salt concentrations.[13,14] In addition, we expect that the critical salt concentration of C3Ms diverges, as the critical salt concentration of the corresponding macroscopic complex coacervates is approached. To assess the importance of this concentration dependence in our measurements, we performed LS salt titrations for different initial polymer concentrations (see inset Figure 5.1b). We indeed find an exponential dependence of the CMC on salt concentration, but the polymer concentrations in our titrations were sufficiently high to ensure a negligible dependence of $c_{\mathrm{s,cr}}$ on c_{AA}.

5.3.3 Morphology of C3Ms

Now that we know the effect of the polymer chain length on the salt stability of C3Ms and their size at low salt concentration, we will investigate the effect of the chain length on the morphology of C3Ms at higher salt concentrations. The term morphology refers to both the size and the shape of the micelles. We focus here on C3Ms formed from $\mathrm{PM2VP}_{41}$-*b*-PEO_{204}.

Size

The effect of salt on the size of C3Ms is far from trivial. In existing literature, both increasing and decreasing hydrodynamic radii of C3Ms with increasing salt concentration have been found. Salt-induced growth of C3Ms is usually attributed to swelling of the core as a result of solvent uptake.[14,52] An equivalent shrinkage is typically attributed to a decrease of the aggregation number as a result of reduced core-solvent interfacial tension.[27,30] Although both proposed mechanisms have been

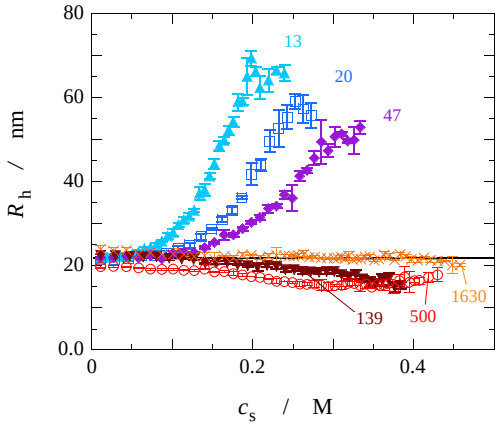

Figure 5.2: Mean hydrodynamic radii of C3Ms of PM2VP$_{41}$-*b*-PEO$_{204}$ and PAA with N_{PAA} = 13, 20, 47, 139, 500 and 1630, as a function of salt concentration. Only data points up to the critical salt concentrations are shown. The symbols are averages of four independent runs, with the error bars representing the standard deviations. The solid horizontal line indicates the average R_h at c_s = 10 mM. The initial polymer concentration c_{AA} was 1.1 mM in all titrations.

experimentally verified for macroscopic coacervates,[53,54] and the decrease of the aggregation number P also for C3Ms,[13,14] it remains unclear what causes the discrete distinction between growing and shrinking C3Ms. From the results of Lindhoud et al., we could infer that the effect of salt depends on the homopolymer chain length: for C3Ms containing the small protein lysozyme, they observed salt-induced growth, whereas they found salt-induced shrinkage when the small lysozyme was partially replaced by the larger homopolymer PDMAEMA$_{150}$ (poly(N,N-dimethylaminoethyl methacrylate)).[2]

To investigate this possible influence of the homopolymer chain length, we have performed LS salt titrations for combinations of PM2VP$_{41}$-*b*-PEO$_{204}$ and various PAA homopolymers. In Figure 5.2 we show the hydrodynamic radii of these C3Ms as a function of salt concentration. We find a systematic effect of the homopolymer length on the size of C3M-PM2VP$_{41}$/PAA$_n$: C3Ms with $N_{PAA} \leq 47$ grow in size upon addition of salt, whereas C3Ms with $N_{PAA} \geq 139$ shrink. Close inspection of the corresponding intensity curves reveals that the increase in size is always accompanied by a peak in scattering intensity. Figure 5.3 shows the normalised light scattering intensity I/c_{AA} of C3M-PM2VP$_{41}$/PAA$_{13}$ and -PAA$_{139}$ as a function of salt concentration. For both PAA lengths, the intensity initially decreases linearly with increasing salt concentration, but for C3M-PM2VP$_{41}$/PAA$_{13}$, a very distinct peak is observed just before the critical salt concentration. This intensity peak is

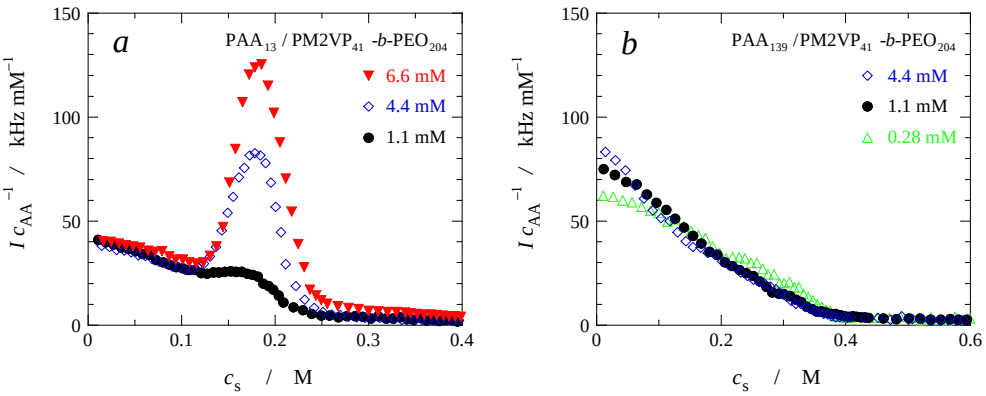

Figure 5.3: Light scattering intensity, normalised by the acrylic acid monomer concentration, as a function of salt concentration for mixtures of $PM2VP_{41}$-*b*-PEO_{204} and (a) PAA_{13} or (b) PAA_{139}. The symbols are averages of four independent runs, for initial polymer concentrations as indicated by the labels.

absent for all concentrations of C3M-$PM2VP_{41}$/PAA_{139}.

A peak in scattering of C3Ms upon addition of salt has been observed by several other authors.[14,15,20–22,28] According to Lindhoud et al., the increase in scattering intensity is caused by structural changes of the corona.[21] Soliman attributes it to fusion of C3Ms into larger structures as a result of partial dehydration of the PEO corona.[22] In the report of Gaucher et al., the presence of an intensity peak seems to depend on homopolymer length, similar to what we find.[15] For C3Ms containing poly(L-lysine) (pLys) as homopolymer, they observed a peak only for $N_{\mathrm{pLys}} = 13$ and not for $N_{\mathrm{pLys}} = 57$ and 207.

In our salt titrations on our C3Ms, the increase in scattering clearly corresponds to the formation of larger objects ($R_{\mathrm{h}} \approx 70$ nm in Figure 5.2). When the polymer concentration is increased from 1.1 to 4.4, 6.6 and 8.8 mM, both the scattering intensity (see Figure 5.3a) and the corresponding hydrodynamic radii increase even further from 69 to 82, 90 and 102 nm. Moreover, analysis of the particle size distributions of these C3Ms by CONTIN (see Figure 5.4a) reveals that a bimodal size distribution underlies the apparent growth of the C3Ms we observe in Figure 5.2. Large objects with hydrodynamic radii close to 100 nm grow at the expense of small micelles of 20 nm. By contrast, the size distribution of C3M-$PM2VP_{41}$/PAA_{139}, which are micelles that shrink upon addition of salt, is always unimodal and no large objects are found (see Figure 5.4b).

These large objects in systems with short PAA chains are not merely 'swollen' C3Ms, since swelling would imply a decrease of the core density and contrast, leaving the scattering intensity virtually unchanged. They must have a higher aggregation

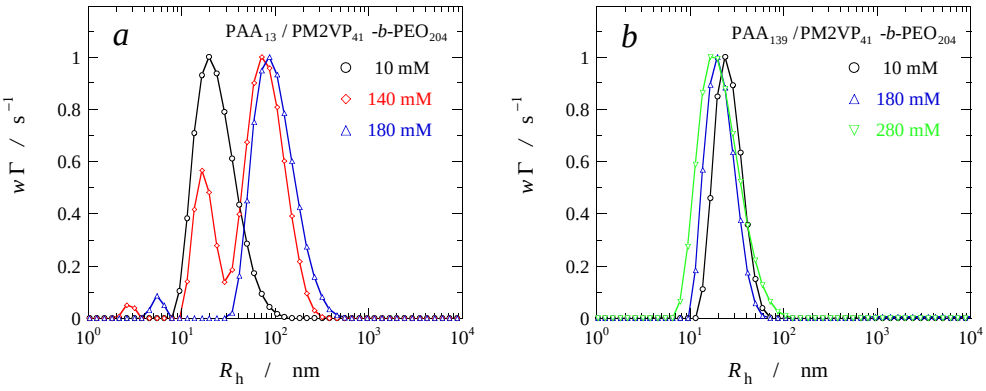

Figure 5.4: CONTIN size distributions from DLS measurements on mixtures of $PM2VP_{41}$-*b*-PEO_{204} and (a) PAA_{13} or (b) PAA_{139}. The distributions for three different salt concentrations are shown, as indicated by the labels. The polymer concentration ranged between $c_{AA} = 4.4$ mM at $c_s = 10$ mM and 3.2 mM at $c_s = 280$ mM. All distributions are normalised to the maximum of the highest mode. The relative heights of the modes are proportional to the product $w \times \Gamma$, with w proportional to R^6 and Γ to $1/R$. The correction factor to arrive at a number average is $1/R^5$.

number. We believe these objects are no longer spherical micelles, since the contour length of the diblock copolymer does not allow for these large sizes, but instead, they are elongated, worm-like micelles. At higher polymer concentrations, these worm-like structures grow and the effective hydrodynamic radius we measure with DLS increases.

Shape

How can we support our hypothesis that worm-like C3Ms are formed close to the critical salt concentration? Unfortunately, we cannot use direct visualisation techniques, such as (cryogenic) transmission electron microscopy (cryo-TEM) and atomic force microscopy (AFM) imaging. C3Ms are known to adsorb on most surfaces, followed by spreading and dissociation,[10,55] making the study of their shape in solution impossible by TEM and AFM. With cryo-TEM, the shape in solution is frozen and then studied, but the small difference in electron density between the core and the surrounding solution, makes observation of the core difficult. In previous cases where cryo-TEM has been used to visualise C3Ms, metal ions in the cores of the C3Ms often provided the necessary contrast.[13,14]

Instead, we use a combination of scattering techniques to support our hypothesis. These techniques allow in situ characterisation of C3Ms without the need of contrast agents. First of all, we measure the rotational diffusion coefficient of the large objects by angle-dependent dynamic light scattering. In the cases where we find

large objects that possibly correspond to worm-like micelles, a small-amplitude mode at very low R_h always accompanies the large amplitude mode at high R_h in our CONTIN analysis (see Figure 5.4a). These fast decay rates (Γ_{fast}) do not correspond to purely translational diffusion of C3Ms. Instead, we argue that they correspond to a combination of rotational and translational motion of the large objects, which depends on q, following the reasoning of Schillén et al.[43] Such modes are only observed for asymmetric structures that have a detectable rotational diffusion coefficient D_r, such as worm-like micelles. We can use the q-dependence of this fast decay rate to estimate D_r. In Figure 5.5a we show a plot of both Γ_{fast} and Γ_{slow} against q^2 for an 8.8 mM C3M-PM2VP$_{41}$/PAA$_{13}$ solution with c_s = 180 mM. Following Schillén et al., we extrapolate Γ_{fast} to $q = 0$ to find $D_r = 1.8 \times 10^3$ s^{-1}. In order to estimate the order of magnitude of the length L and diameter d of these asymmetric objects, we approximate them as rigid cylinders with spherical caps (see Equations 5.5 and 5.6).[44] We set the diameter d to twice the hydrodynamic radius of a spherical C3M ($R_h \approx 20$ nm) and use the length L as the fitting parameter. This procedure gives $L = 130$ nm and $L/d = 3.3$. Clearly, the order of magnitude is in agreement with the hydrodynamic radius obtained from the translational diffusion of these micelles ($2R_h \approx 200$ nm). A possible explanation for the discrepancy between these two values is that, in reality, worm-like micelles exhibit a significant polydispersity and flexibility, so that the approximation of monodisperse, rigid, cylinders does not hold. In addition, the diameter of worm-like C3Ms may be smaller than that of spherical C3Ms, implying a longer contour length than calculated above.

A second confirmation for the presence of non-spherical particles in the C3M-PM2VP$_{41}$/PAA$_{13}$, -PAA$_{20}$ and -PAA$_{47}$ solutions at high salt concentration comes from depolarised light scattering measurements. The intensity associated with light that is polarised perpendicular to the incident light originates from anisotropic objects with different polarisabilities parallel and perpendicular to their major axis ($\alpha_{\parallel} \neq \alpha_{\perp}$).[56] The depolarisation ratio Δ^{vh} reflects the degree of optical anisotropy in solution, which scales with both the number and the length of anisotropic objects. In Figure 5.5b we show depolarisation ratios as a function of salt concentration for mostly the same polymer combinations as in Figure 5.2. For short PAA homopolymers, where we found an increase in size upon addition of salt, we also find a clear increase of Δ^{vh}, indicating that the objects are anisotropic. By contrast, we find no increase of Δ^{vh} for long PAA homopolymers. Interestingly, Δ^{vh} seems to exhibit a maximum at approximately the same salt concentration as the maximum of the corresponding intensity peak (see for example Figure 5.3a). We also notice that the increase of Δ^{vh} is larger for $N_{PAA} = 13$ and 20 than for $N_{PAA} = 47$, which can be explained by the fact that C3M-PM2VP$_{41}$/PAA$_{13}$ and C3M-PM2VP$_{41}$/PAA$_{20}$ grow into longer worm-like micelles than C3M-PM2VP$_{41}$/PAA$_{47}$.

Thirdly, we have carried out a combination of small angle X-ray scattering and

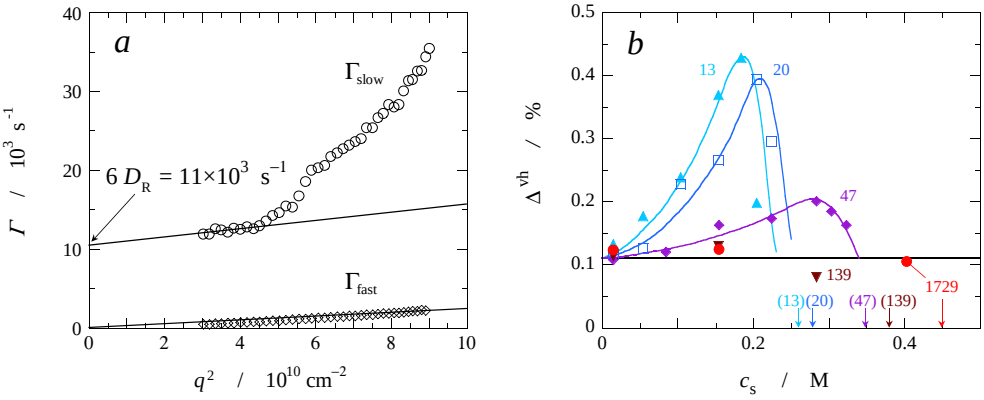

Figure 5.5: (a) Fast and slow mode of the correlation function of the scattering intensity as a function of q^2 for C3Ms of PM2VP$_{41}$-*b*-PEO$_{204}$ and PAA$_{13}$ at c_s = 180 mM and c_{AA} = 8.8 mM. Extrapolation of the fast mode to $q = 0$ yields the apparent rotational diffusion coefficient. (b) Depolarisation ratio Δ^{vh} (in %) from depolarised light scattering measurements as a function of salt concentration for mixtures of PM2VP$_{41}$-*b*-PEO$_{204}$ and PAA with N_{PAA} = 13, 20, 47, 139 and 1728, as indicated by the labels. The symbols are averages over ten independent runs. The solid lines are drawn as guides to the eye. The arrows point at the critical salt concentrations of the C3Ms with N_{PAA} as indicated by the labels in brackets.

light scattering to further confirm the worm-like shape of C3Ms with short PAA chain lengths at high salt concentration. The results of these experiments are given in Figure 5.6. The corona contributes only marginally to the total scattering intensity in these experiments, due to its low polymer volume fraction.[30] For C3M-PM2VP$_{41}$/PAA$_{13}$ (Figure 5.6a), we observe a dramatic change in the shape of the scattering curve with increasing salt concentration. At $c_s = 10$ mM, the scattering intensity exhibits a clear plateau up to $q \approx 0.011$Å^{-1} and then falls off as $I(q) \propto q^{-4}$, indicating that these micelles are spherical objects with a core size of $R_c = 8.7 \pm 2.5$ nm (see Figure 5.6b). The curve appears rather smooth and we find no form factor minima that are typical for monodisperse spherical objects of radius 9 nm. This indicates that the micelles have a significant polydispersity, as has been found before.[51,57]

At c_s = 180 mM, however, the scattering curve has a region with a power-law slope close to −1 in the range $3 \times 10^{-3} < q < 6 \times 10^{-2}$ Å^{-1}. This slope is typical for cylindrical rods and worm-like chains at length scales between the radius of the rods (here R_c) and the persistence length l_p.[58–60] We find a plateau at much lower q than for the spherical micelles, which here corresponds to the typical length L of the worm-like micelles. From the boundaries of these regimes, which can be identified in a bending or Casassa-Holtzer plot of $\log(q\,I)$ versus $\log q$ (Figures 5.6c and d), we derive that $R_c \approx 1.5$ nm, which is significantly smaller than for spherical micelles,

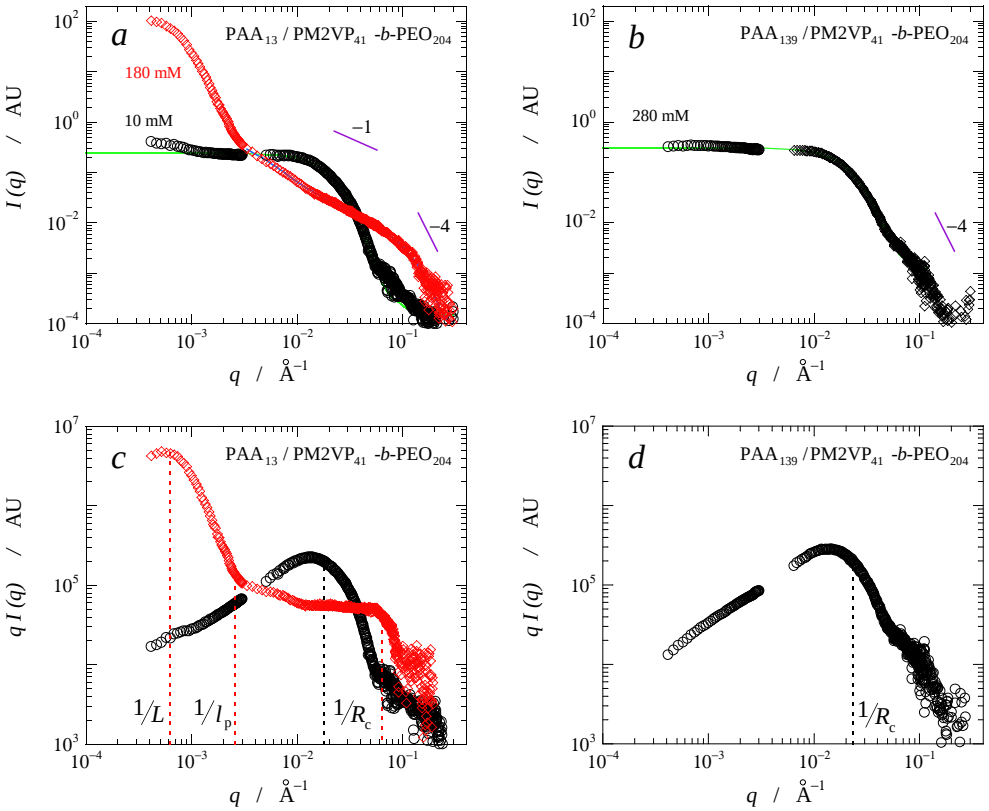

Figure 5.6: A combination of SLS and SAXS measurements for C3Ms of $PM2VP_{41}$-*b*-PEO_{204} and (a) PAA_{13} or (b) PAA_{139}. (c) and (d) are Casassa-Holtzer plots corresponding to the profiles in (a) and (b) respectively. The solid lines in (a) for c_s = 10 mM and in (b) are fits to a form factor for core-shell spherical particles with a monodisperse core with uniform contrast and a polydisperse shell (Gaussian distribution) with a contrast that decreases exponentially between the core radius and the outer shell radius. The solid line in (a) for c_s = 180 mM is a fit to the form factor of a flexible polydisperse cylinder (Gaussian distribution) with a uniform contrast.

$l_p \approx 30$ nm and $L \approx 250$ nm. These values are in good agreement with the values we obtained from a fit of the data in Figure 5.6 to a worm-like chain model. Again, we find no form factor minima at high q, indicating that the cores of these worm-like micelles have a relatively high degree of polydispersity, as the the cores of the spherical micelles.

Figure 5.6b shows that worm-like micelles are not formed for C3Ms of $PM2VP_{41}$-*b*-PEO_{204} and PAA_{139}. At c_s = 280 mM, which is rather close to the critical salt concentration, the scattering curve is very similar to that in Figure 5.6a for c_s = 10

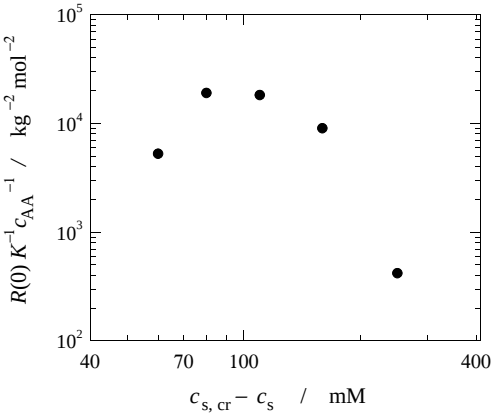

Figure 5.7: Analysis of critical scattering by C3Ms of PM2VP$_{41}$-*b*-PEO$_{204}$ and PAA$_{13}$, showing the normalised Rayleigh ratio, extrapolated to $q = 0$, as a function of the separation from the critical point. The polymer concentration ranges from $c_{AA} = 4.4$ mM for $c_s = 10$ mM to 3.6 mM for $c_s = 200$ mM.

mM. Indeed, we can also fit this curve with the form factor of a polydisperse sphere, yielding $R_c = 5.4 \pm 3.4$ nm.

Finally, we investigate critical scattering as an alternative explanation to worm-like micelles for the observed peak in scattering intensity and swelling of the micelles with increasing salt concentration. Critical scattering has been reported for several micellar systems in the vicinity of a critical point, and gives rise to an increase in scattering intensity and typical size.[61–63] It originates from critical fluctuations in concentration, which are enhanced as the critical point is approached. In the reports mentioned above, the scattering intensity at $q = 0$ follows a critical power-law scaling $R \propto (T_{cr} - T)^{-1}$.[64,65] Here, we approach the critical point by increasing the salt concentration. In Figure 5.7 we show the normalised scattering intensity at five different salt concentrations, which are expressed as separations from the critical point $c_{s,cr} - c_s$. We see no critical scaling and conclude that critical scattering does not underly the increase in scattering intensity and hydrodynamic radii of C3Ms with sufficiently short PAA chains, close to the critical point.

Possible mechanism of worm-like micelle formation

We have found that C3Ms with short PAA chains can undergo a morphological transition from spherical to worm-like micelles at sufficiently high salt concentrations. We rationalise this transition using the concept of the packing parameter p. This parameter is traditionally defined for amphiphilic molecules as $p = v_0/A_h\,l_0$, with v_0 and l_0 the volume and length of the hydrophobic tail, respectively, and A_h the

area of the hydrophilic headgroup.[66] For C3Ms, we assume that the PM2VP block, complexed with an equal number of AA monomers, takes the role of the hydrophobic tail. The area of the PEO block at the interface of the core and the corona is the effective headgroup area A_h. At low salt concentration, our C3Ms are spherical, implying that $p < 1/3$. The effect of salt is twofold. First of all, it screens the electrostatic interactions between PM2VP and PAA, resulting in swelling of the complex and a consequent increase of v_0.[6] Secondly, it decreases the solubility of PEO, causing the PEO blocks to become more compact and thereby decreasing A_h.[67] Both lead to an increase of the packing parameter, which promotes the formation of structures with lower curvature such as worm-like micelles.

The question now arises: why are these worm-like micelles not formed for long PAA homopolymers? We believe this can be explained by the fact that long PAA chains must interact with multiple PM2VP blocks. An increase of the packing parameter requires an increase in separation between the PM2VP blocks that are complexed with PAA segments. Because sufficiently short PAA homopolymers interact with only one PM2VP block, the C3Ms of these short PAA chains can undergo the transition to worm-like micelles. Once the PAA chains become too long, they must form ionic bonds with multiple PM2VP blocks. These PM2VP blocks are bridged by a single PAA chain, and the unfavourable entropy increase of stretching the long PAA chains to bridge the PM2VP blocks may prevent the increase in separation of the PM2VP blocks that is needed for the transition from spherical to worm-like micelles.

5.4 Concluding remarks

We have performed a systematic study on the stability and morphology of complex coacervate core micelles formed from PM2VP-*b*-PEO and PAA. At low salt concentration and charge stoichiometric conditions, these C3Ms are spherical, independent of the chain and block lengths of the polymers. Their hydrodynamic radius is independent of the homopolymer chain length for short PAA lengths and ranges between 20 and 42 nm, depending on the PM2VP/PEO block length ratio. Above a critical PAA length, the hydrodynamic radius increases sharply with increasing PAA length, because the cores of the micelles can no longer accommodate a single PAA chain, without a significant increase in size.

When salt is added, C3Ms start to disintegrate, and at the critical salt concentration all micelles are disassembled. The critical salt concentration increases with increasing PM2VP and PAA length and levels off for long chains, in the same way as for macroscopic complex coacervates. Below the critical salt concentration, we find a nontrivial change in size of the various C3Ms. For long PAA chains, the C3Ms shrink upon addition of salt due to a decrease of the micellar aggregation number, whereas

for short PAA chains they become larger. A surprising change in morphology of the C3Ms from spherical to worm-like micelles underlies this salt-induced size increase.

References

[1] A. Harada and K. Kataoka, *Journal of Controlled Release*, 2001, **72**, 85–91.

[2] S. Lindhoud, R. de Vries, W. Norde, and M. A. Cohen Stuart, *Biomacromolecules*, 2007, **8**, 2219–2227.

[3] Y. Kakizawa and K. Kataoka, *Adv. Drug Deliv. Rev.*, 2002, **54**, 203–222.

[4] M. Oishi, Y. Nagasaki, K. Itaka, N. Nishiyama, and K. Kataoka, *J. Am. Chem. Soc.*, 2005, **127**, 1624–1625.

[5] Y. Lee, T. Ishii, H. J. Kim, N. Nishiyama, Y. Hayakawa, K. Itaka, and K. Kataoka, *Angew. Chem. Int. Ed.*, 2010, **122**, 2606–2609.

[6] I. K. Voets, A. de Keizer, and M. A. Cohen Stuart, *Adv. Coll. Int. Sci.*, 2009, **147–148**, 300–318.

[7] W.-D. Jang, Y. Nakagishi, N. Nishiyama, S. Kawauchi, Y. Morimoto, M. Kikuchi, and K. Kataoka, *J. Controlled Release*, 2006, **113**, 73–79.

[8] Y. Yan, N. A. M. Besseling, A. de Keizer, A. T. M. Marcelis, M. Drechsler, and M.A. Cohen Stuart, *Angew. Chem. Int. Ed.*, 2007, **46**, 1807–1809.

[9] S. Schwarz and S. Dragan, *Macromol. Symp.*, 2004, **210**, 185–192.

[10] S. van der Burgh, R. Fokkink, A. de Keizer, and M. A. Cohen Stuart, *Colloids and Surfaces A*, 2004, **242**, 167–174.

[11] A. M. Brzozowska, P. S. Hofs, A. de Keizer, R. Fokkink, M. A. Cohen Stuart, and W. Norde, *Colloids and Surfaces A*, 2009, **347**, 146–155.

[12] A. V. Kabanov, T. K. Bronich, V. A. Kabanov, K. Yu, and A. Eisenberg, *Macromolecules*, 1996, **29**, 6797–6802.

[13] J. Wang, A. de Keizer, R. Fokkink, Y. Yan, M. A. Cohen Stuart, and J. van der Gucht, *J. Phys. Chem. B*, 2010, **114**, 8313–8319.

[14] Y. Yan, A. de Keizer, M. A. Cohen Stuart, M. Drechsler, and N. A. M. Besseling, *J. Phys. Chem. B*, 2008, **112**, 10908–10914.

[15] G. Gaucher, M.-H. Dufresne, V. P. Sant, N. Kang, D. Maysinger, and J.-C. Leroux, *J. Controlled Release*, 2005, **109**, 169–188.

[16] A. Harada and K. Kataoka, *J. Macromol. Sci. A*, 1997, **34**, 2119–2133.

[17] H. Dautzenberg and G. Rother, *Macromol. Chem. Phys.*, 2004, **205**, 114–121.

[18] A. Matralis, M. Sotiropoulou, G. Bokias, and G. Staikos, *Macromol. Chem. Phys.*, 2006, **207**, 1018–1025.

[19] J.-S. Park, Y. Akiyama, Y. Yamasaki, and K. Kataoka, *Langmuir*, 2007, **23**, 138–146.

[20] S. Pispas, *J. Phys. Chem. B*, 2007, **111**, 8351–8359.

[21] S. Lindhoud, L. Voorhaar, R. de Vries, R. Schweins, M. A. Cohen Stuart, and W. Norde, *Langmuir*, 2009, **25**, 11425–11430.

[22] G. M. Soliman, *Ph.D. thesis*, University of Montreal, 2009.

[23] A. M. Brzozowska, Q. Zhang, A. de Keizer, W. Norde, and M. A. Cohen Stuart, *Colloids and Surfaces A*, 2010, **368**, 96–104.

[24] A. M. Brzozowska, A. de Keizer, W. Norde, C. Detrembleur, and M. A. Cohen Stuart, *Coll. Pol. Sci.*, 2010, **288**, 1081–1095.

[25] S. van den Burgh, A. de Keizer, and M. A. Cohen Stuart, *Langmuir*, 2004, **20**, 1073–1084.

[26] R. Ma, B. Wang, X. Liu, Y. An, Y. Li, Z. He, and L. Shi, *Langmuir*, 2007, **23**, 7498–7504.

[27] M. Lemmers, I. K. Voets, M. A. Cohen Stuart, and J. van der Gucht, *Soft Matter*, 2011, **7**, 1378–1389.

[28] M. A. Cohen Stuart, N. A. M. Besseling, and R. G. Fokkink, *Langmuir*, 1998, **14**, 6846–6849.

[29] M. Danial, H.-A. Klok, W. Norde, and M. A. Cohen Stuart, *Langmuir*, 2007, **23**, 8003–8009.

[30] S. Lindhoud, R. de Vries, R. Schweins, M. A. Cohen Stuart, and W. Norde, *Soft Matter*, 2009, **5**, 242–250.

[31] J. Th. G. Overbeek and M. J. Voorn, *J. Cell. Comp. Phys.*, 1957, **49**, 7–26.

[32] M. Lemmers, J. Sprakel, I. K. Voets, J. van der Gucht, and M. A. Cohen Stuart, *Angew. Chem. Int. Ed.*, 2010, **49**, 708–711.

[33] J. N. Hunt, K. E. Feldman, N. A. Lynd, J. Deek, L. M. Campos, J. M. Spruell, B. M. Hernandez, E. J. Kramer, and C. J. Hawker, *Adv. Mater.*, 2011, **23**, 2327–2331.

[34] R. M. Capito, H. S. Azevedo, Y. S. Velichko, A. Mata, and S. I. Stupp, *Science*, 2008, **319**, 1812–1816.

[35] D. E. Koppel, *J. Chem. Phys.*, 1972, **57**, 4814.

[36] B. J. Berne and R. Pecora, *Dynamic light scattering: with applications to chemistry, biology, and physics*, Dover Publications, 2000.

[37] S. W. Provencher, *Comp. Phys. Commun.*, 1982, **27**, 213–227.

[38] S. W. Provencher, *Comp. Phys. Commun.*, 1982, **27**, 229–242.

[39] E. Moreels, W. De Ceuninck, and R. Finsy, *J. Chem. Phys.*, 1987, **86**, 618–623.

[40] H. Wu, *Chem. Phys.*, 2010, **367**, 44–47.

[41] J. Brandrup and E. H. Immergut, *Polymer Handbook*, John Wiley & Sons, 1966.

[42] A. Harada and K. Kataoka, *Macromolecules*, 2003, **36**, 4995–5001.

[43] K. Schillén, W. Brown, and R. M. Johnsen, *Macromolecules*, 1994, **27**, 4825–4832.

[44] S. R. Aragon and D. Flamik, *Macromolecules*, 2009, **42**, 6290–6299.

[45] T. Narayanan, O. Diat, and P. Bösecke, *Nucl. Instr. Meth. Phys. Res. A*, 2001, **467–468**, 1005–1009.

[46] O. V. Borisov and E. B. Zhulina, *Macromolecules*, 2002, **35**, 4472–4480.

[47] E. B. Zhulina, M. Adam, I. LaRue, S. S. Sheiko, and M. Rubinstein, *Macromolecules*, 2005, **38**, 5330–5351.

[48] I. K. Voets, R. de Vries, R. Fokkink, J. Sprakel, R. P. May, A. de Keizer, and M. A. Cohen Stuart, *Eur.Phys. J. E*, 2009, **30**, 351–359.

[49] J. J. Zhao, S. C. Bae, F. Xie, and S. Granick, *Macromolecules*, 2001, **34**, 3123–3126.

[50] Y.-Y. Won, H. T. Davis, and F. S. Bates, *Macromolecules*, 2003, **36**, 953–955.

[51] I. K. Voets, A. de Keizer, M. A. Cohen Stuart, J. Justynska, and H. Schlaad, *Macromolecules*, 2007, **40**, 2158–2164.

[52] I. K. Voets, R. Fokkink, A. de Keizer, R. P. May, P. de Waard, and M. A. Cohen Stuart, *Langmuir*, 2008, **24**, 12221–12227.

[53] E. Spruijt, J. Sprakel, M. A. Cohen Stuart, and J. van der Gucht, *Soft Matter*, 2010, **6**, 172–178.

[54] E. Spruijt, A. H. Westphal, J. W. Borst, M. A. Cohen Stuart, and J. van der Gucht, *Macromolecules*, 2010, **43**, 6476–6484.

[55] I. K. Voets, W. M. de Vos, B. Hofs, A. de Keizer, M. A. Cohen Stuart, R. Steitz, and D. Lott, *J. Phys. Chem. B*, 2008, **112**, 6937–6945.

[56] R. Pecora, *Nature*, 1971, **231**, 73–75.

[57] I. K. Voets, S. van der Burgh, B. Farago, R. Fokkink, D. Kovacevic, T. Hellweg, A. de Keizer, and M. A. Cohen Stuart, *Macromolecules*, 2007, **40**, 8476–8482.

[58] P. Lindner and Th. Zemb, *Neutrons, X-rays and light: scattering methods applied to soft condensed matter*, Elsevier Science, 2002.

[59] Y.-Y. Won and F. S. Bates, *Giant micelles, properties and applications. Nonionic block copolymer wormlike micelles*, CRC Press, 2007.

[60] R. Borsali and R. Pecora, *Soft-matter characterization*, Springer, 2008.

[61] J. B. Hayter and M. Zulauf, *Coll. Pol. Sci.*, 1982, **260**, 1023–1028.

[62] R. Triolo, L. J. Magid, J. S. Johnson, and H. R. Child, *J. Phys. Chem.*, 1982, **86**, 3689–3695.

[63] C. Liao, S.-M. Choi, F. Mallamace, and S.-H. Chen, *J. Appl. Chrystallography*, 2000, **33**, 677–681.

[64] M. Corti and V. Degiorgio, *J. Phys. Chem.*, 1981, **85**, 1442–1445.

[65] P. Schurtenberger, C. Cavaco, F. Tiberg, and O. Regev, *Langmuir*, 1996, **12**, 2894–2899.

[66] J. N. Israelachvili, D. J. Mitchell, and B. W. Ninham, *J. Chem. Soc. Faraday Trans.*, 1976, **72**, 1525–1568.

[67] L. D. Unsworth, H. Sheardown, and J. L. Brash, *Langmuir*, 2005, **21**, 1036–1041.

Chapter 6

Reversible assembly of oppositely charged hairy colloids in water

In this Chapter we use complex coacervation as driving force for the fully reversible assembly of oppositely charged colloidal particles in aqueous solutions. Our polystyrene colloids are charged by a grafted polyelectrolyte brush on their surface and stabilised at all salt concentrations by an additional neutral adsorbed polymer layer. Below a critical salt concentration oppositely charged colloids form clusters and gels with a fractal nature, whereas the like charged colloids do not cluster. The fractal dimension of the gels increases with increasing salt concentration. Above the critical salt concentration also oppositely charged colloids do not aggregate and already formed aggregates and can be fully redispersed. We confirm that time-dependent interaction forces are at the basis of the formation of clusters in this colloidal system by atomic force microscopy measurements. The force measurements show that the attraction between particles strengthens in time due to interpenetration of the polymer brushes, driven by polyelectrolyte complexation. These particles are a promising step toward a reversible and controlled self-assembling system in water, using colloidal particles as building blocks.

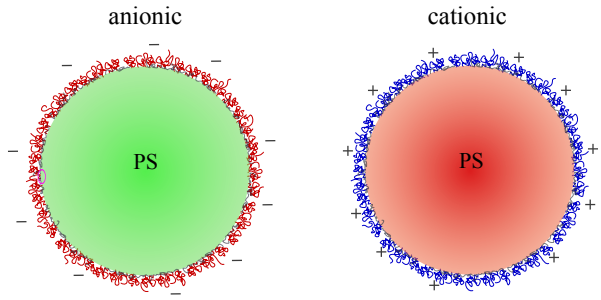

This Chapter is based on:
E. Spruijt, H. E. Bakker, T. E. Kodger, J. Sprakel, M. A. Cohen Stuart and J. van der Gucht, *Reversible assembly of oppositely charged hairy colloids in water*, Soft Matter **7** (2011), 8281–8290, doi 10.1039/c1sm05881a.

6.1 Introduction

The ultimate self-assembling system forms designed structures rapidly, reversibly and controllably.[1] This requires careful selection of the interactions between the assembling building blocks. In aqueous systems, attractive electrostatic interactions have proven to be very promising as driving force for self-assembly.[2] The strength of these interactions can be tuned continuously by screening of the charges and by changing the dielectric properties or the temperature of the medium. Electrostatic interactions can be mediated effectively by charge-carrying polymers. Using polyelectrolytes as building blocks, attractive electrostatic interactions have been used to control the formation of nano- and micrometre-sized structures, ranging from micelles[3,4] and hollow capsules[5] to fibers[6] and semipermeable membranes.[7] Alternatively, the interactions can be used to create responsive functional materials, such as self-healing gels[8] or ultra-dense renewable coatings.[9] In all cases, the assembly is a controlled, rapid and reversible process. Disassembly can be induced easily by increasing the salt concentration.[3–9] This principle has been used to selectively release cargo, such as DNA, from electrostatically assembled materials.[10]

With colloidal particles as building blocks, attractive electrostatic interactions can also be used to control self-assembly. By changing the particle charge and size, oppositely charged colloidal particles in mixtures of cyclohexylbromide and *cis*-decalin can be organised into a variety of ionic crystals,[11] or fractal gels.[12] However, in aqueous media these assemblies are poorly controlled and hardly reversible. Mixtures of large anionic and small cationic polystyrene colloidal particles in water always give rise to formation of fractal aggregates.[13,14] The density of these fractal aggregates and the critical volume fraction of small particles beyond which aggregation takes place can be influenced by changing the salt concentration and temperature. At extreme mixing ratios the small particles can completely cover the surface of the large particles, forming heteroaggregates that are stable against further aggregation.[15] However, once aggregation has taken place, it cannot be reversed.[13] This type of aggregation has much in common with the flocculation of charged colloidal particles by addition of oppositely charged polyelectrolytes, which is a common procedure in soil and waste water treatment.[16] Similar irreversible aggregation in water is found for mixtures of oppositely charged silica particles.[17] Although these mixtures are found to exhibit a surprising stability and spontaneous redispersion of aggregates formed in an early stage when they contain an excess of positive particles, this apparent reversibility originates from recharging of the negative colloids by adsorption of positive aluminate species, such that all colloids effectively bear positive charges.

The poor control and irreversible nature of the assembly of oppositely charged colloidal particles in aqueous media limits their use for controlled self-assembly. Instead, other types of interactions, such as DNA-hybridisation,[18–22] and amphiphilic

colloidal particles with hydrophobic[23] or charged patches,[24] are used to obtain reversible assemblies. Despite their reversibility, these approaches suffer from either slow formation of the assemblies,[19,20,22] poor control over the assembled structures[18,21,22] or the very limited amounts of colloidal particles that can be prepared.[23,24]

In this Chapter we show that attractive electrostatic interactions can be used to drive the reversible assembly of colloidal particles in aqueous solutions. We are able to prepare large quantities of oppositely charged colloidal particles that assemble rapidly into large clusters, and can be disassembled at any moment by increasing the salt concentration. We analyse the structure of the assemblies and the effect of salt on their formation. We find that the interparticle interactions are governed by a time-dependent charge-driven complexation when particles come into contact, which grows stronger in time. We can directly measure this time-dependent attractive force at varying salt concentrations for pairs of our interacting particles using colloidal probe atomic force microscopy. The time-dependence of the attractive force originates from the polymeric nature of the charged groups on the surface. We finally discuss the general nature of such time-dependent attractive interactions and their impact on the self-assembly of colloids.

6.2 Experimental details

To make reversible assemblies of colloids in water based on attractive charge-driven interactions, we used complexation of oppositely charged polyelectrolytes that are covalently attached to the surface of polystyrene colloidal particles. Our charged 'hairy' colloids were synthesised in two steps. First, colloids functionalised with initiator groups for atom transfer radical polymerisation (ATRP) were synthesised via dispersion polymerisation. In this step we used a heterobifunctional monomer that can react both as monomer in the radical polymerisation of styrene and as an initiator in the subsequent ATRP reaction, hence its name 'inimer'. This inimer was synthesised in a separate reaction. In the second colloid synthesis step, polyelectrolyte brushes of either charge are grafted from the surfaces of our colloids using aqueous ATRP. In this section, we briefly describe the synthesis procedures, the fluorescent labelling and the techniques used for characterisation.

6.2.1 Materials

Styrene, 2-hydroxyethyl acrylate (HEA), 2-bromo-isobutyryl bromide, poly(vinyl pyrrolidone) (PVP-40), azo-bisisobutyronitrile (AIBN), methacryloyloxy-trimethyl-ammonium chloride (METAC, 80% solution in water), potassium 3-sulphopropyl methacrylate (KSPMA, powder), 2,2'-bipyridyl (bipy), 1,1,4,7,10,10-hexamethyl-

triethyltetramine (HMTETA), copper(I) chloride (CuCl), copper(II) chloride ($CuCl_2$), ethylenediamine-tetraacetic acid (EDTA), cetyltrimethylammonium bromide (CTAB), sodium dodecylsulphate (SDS) and carbon tetrachloride (CCl_4, tetra) were all purchased from Sigma-Aldrich. Styrene was cleaned by washing with neutral alumina and centrifugation.

For preparation of the particle dispersions we used a stock solution of 3.0 M KCl in Milli-Q water (resistance > 18.2 M$\Omega \cdot$cm).

6.2.2 Synthesis of inimer

The heterobifunctional 2-(2-bromoisobutyryloxy)-ethyl acrylate (BIEA) was used as an acrylic monomer in the radical dispersion polymerisation of polystyrene colloids and as an initiator for atom transfer radical polymerisation. The synthesis of BIEA, or inimer, is described in detail by Matyjaszewski et al.[25] We followed the same procedure and synthesised 30 g of BIEA. ^{1}H NMR ($CDCl_3$) δ (ppm): 6.30 (d, 1H, $\mathbf{H}_2$C=CH), 6.0 (dd, 1H, H_2C=C**H**), 5.80 (d, 1H, $\mathbf{H}_2$C=CH), 4.32 (s, 4H, C$\mathbf{H}_2$C$\mathbf{H}_2$), 1.85 (d, 6H, C(C$\mathbf{H}_3$)$_2$Br).

6.2.3 Synthesis of polystyrene colloidal particles

Monodisperse polystyrene particles were synthesised by dispersion polymerisation, following the method described by Paine.[26,27] For 1.1 µm particles we used the following amounts. We mixed 135 mL methanol, 15 mL inhibitor-free styrene and 7.5 g PVP-40 in a round-bottom flask. After dissolution of the PVP, we added 150 mg of the radical initiator AIBN and closed the flask tightly. We kept the solution at 0 °C and removed all oxygen by four subsequent cycles of evacuating and refilling with argon, ending under a vacuum atmosphere. To start the free radical polymerisation, we quickly heated the mixture to 70 °C causing the AIBN to decompose. The reaction was then left for three hours at 70 °C while continuously rotating under an angle of 30°. During these initial three hours the mixture changed from transparent via blueish transparent to a white opaque dispersion. After three hours the reaction mixture was cooled down to 45 °C. We then injected 2.6 g of a 1 : 1 mixture by weight of inimer and styrene and left the mixture to react for another twelve hours while rotating.

We ended the reaction by cooling down to room temperature. We cleaned the particles by four cycles of centrifugation ($3{,}500\times g$), discarding the supernatant, and redispersing in methanol ($2\times$) and water ($2\times$). By weighing the pellet and assuming a random closed packing conformation of the particles in the pellet ($\phi = 64\%$ (v/v)[28]), we redispersed the particles in the final step to a volume fraction of $\phi = 30\%$.

For 3.5 µm particles, which we used as colloidal probes in force spectroscopy measurements and as core particles in the asymmetric assemblies, we followed a

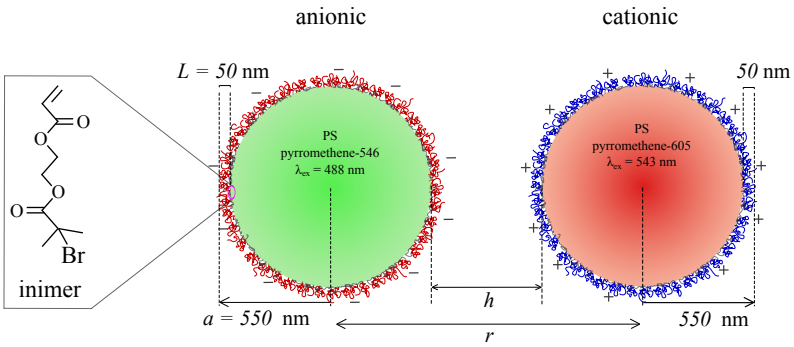

Figure 6.1: Schematic illustration of both anionic and cationic colloidal particles, drawn to scale.

slightly different procedure. We carried out the dispersion polymerisation in ethanol instead of methanol. Furthermore, in order to reach a larger particle size we added an additional 7.5 mL styrene and 7.5 mL ethanol to the reaction mixture after three hours. We then left the reaction mixture for another four hours at 70 °C. After a total of seven hours, we cooled down the reaction mixture to 45 °C and followed the procedure described above from there.

6.2.4 Modification of PS colloids with polyelectrolytes

We modified the polystyrene (PS) particles with either polycationic or polyanionic chains, which were grown from the surfaces of the particles using surface-initiated atom transfer radical polymerisation, SI-ATRP.[29] The BIEA, or inimer, acts as an initiator in this ATRP reaction.

We synthesised positively charged poly(*N*, *N*, *N*-trimethylaminoethyl methacrylate) (PTMAEMA) coated particles as follows. We mixed 1 mL 30% (v/v) polystyrene particle suspension, 2 mL Milli-Q water, 6 mL formamide, 1.5 g METAC (monomer, 80% solution in water) and 90 µL HMTETA together in a 50 mL round-bottom flask. The flask was sealed with a rubber septum. We purged the reaction mixture with argon using a syringe needle for ten minutes. After ten minutes, we added 10 mg Cu(I)Cl and again purged the mixture with argon. The suspension obtained an intense blue color and was stirred gently at 50 °C for two hours.

We synthesised negatively charged poly(3-sulphopropyl methacrylate) (PSPMA) coated particles following a similar procedure. To 1 mL of the 30% (v/v) polystyrene suspension we added 2 mL Milli-Q water, 6 mL methanol, 1.2 g KSPMA (monomer, powder), 20 mg bipy and 4 mg $Cu(II)Cl_2$. After purging with argon for ten minutes, we added 6 mg Cu(I)Cl to start the ATRP reaction. This suspension obtained a typical brown color and we left it to react for 45 minutes at room temperature.

Both ATRP reactions were terminated by purging the reaction mixtures with air. We cleaned the particles again by six cycles of centrifugation (3,500×g), discarding the supernatant every time, and redispersing in methanol (2×), a 20 mM EDTA solution in water (2×) and Milli-Q water (2×).

6.2.5 Fluorescent labelling of PS colloids

We labelled both types of modified particles by adsorbing two different hydrophobic dyes in their cores. In order to get the dyes homogeneously distributed in the cores of the particles, we equilibrated suspensions of the modified particles with a mini-emulsion of the dyes dissolved in CCl_4 (tetra) by gentle tumbling for one to two days in a closed plastic container.

For PTMAEMA-coated particles we used 1 mg pyrromethene-605 (Exciton laser dyes, red emission) in 1.5 mL tetra and mixed this with 10 mg CTAB (cationic surfactant) in 10 mL water using a tip sonicator. For PSPMA-coated particles we used 1 mg pyrromethene-546 (Exciton laser dyes, green emission) in 1.5 mL tetra and mixed this with 72 mg SDS (anionic surfactant) in 10 mL water again using the tip sonicator. After equilibration, we opened the containers and stirred the suspensions gently for six hours to evaporate all tetra. We cleaned the particles again by six to eight cycles of centrifugation (1,000 – 3,500×g), discarding the supernatant, and redispersing them in water (6 – 8×). Finally, the particles were stored in suspension at a concentration of 10% (v/v), which we estimated from a linear plot of the scattered intensity versus ϕ, taking the suspension of unmodified particles ($\phi = 0.10$) as a reference.

6.2.6 Colloidal dispersions and mixing procedures

We prepared one stock solution of positively charged and one of negatively charged particles at 10% (v/v) in water. For all experiments, we first diluted the stock solutions to the desired concentration of particles and salt using Milli-Q water and a solution of 3.0 M KCl. In all cases, we started experiments on the aggregation behaviour from a high salt concentration to avoid aggregation of the particles before they were properly mixed. Then, we gradually added water to the suspension to reach the final concentration of particles and salt.

The density of the aqueous dispersion medium can be matched to that of the colloidal particles by changing the salt concentration or by adding D_2O. Using several centrifugation and redispersion steps, we determined that the density of our particles is matched to that of a 1.35 M KCl solution, indicating that the effective density of the particles is 1.056 g/mL, which is equal to the density of solid polystyrene.[30] All DLS and SLS experiments have been carried out at this salt concentration to

minimise sedimentation or creaming of the particles. In the experiments carried out at different ionic strengths, there is a small density mismatch ($\Delta\rho = \rho_p - \rho_m$) between the particles and the medium, ranging from 0.033 g/mL at 0.35 M KCl to −0.035 g/mL at 1.9 M KCl. We did not add D_2O to counter this effect, as the H_2O/D_2O ratio is known to significantly influence the activity of many strong electrolytes.[31]

The high refractive index of polystyrene ($n = 1.55$[30]) cannot be matched to the refractive index of the dispersion medium in aqueous solutions. As a result, confocal microscopy images can only be recorded up to a few particle sizes, $\mathcal{O}$ (20 µm) away from the cover slip in the densest dispersions.

6.2.7 Light scattering

We used static and dynamic light scattering to determine the size and relative concentration of dispersed particles. Details on the light scattering setup are given in Chapter 5. We have carried out all light scattering measurements at a constant temperature of 20 ± 0.2 °C and at a detector angle of 90°, unless stated otherwise.

6.2.8 Confocal microscopy

We used confocal scanning laser microscopy (CSLM) to visualise the mixtures of oppositely charged particles. CSLM experiments were carried out on a Zeiss Axiovert 200M confocal microscope. The samples were put in glass capillaries of 100 µm thickness and visualised at a focal depth between 2 and 20 µm. For negatively charged particles, labelled with pyrromethene-546, we used an excitation wavelength of 488 nm and a band pass filter for detection of 505 – 530 nm. For positively charged particles, labelled with pyrromethene-605, we used an excitation wavelength of 543 nm and a long pass filter for detection with a lower threshold wavelength of 560 nm. Particle identification in the captured images was done using a Particle Tracker Plugin in Image J.[32] We typically detected >95% of all particles, with less than 1% false positives. 3-D reconstructions from z-stack images were created using Zeiss ZEN software.

6.2.9 Force spectroscopy

We used colloidal probe atomic force microscopy (CP-AFM) to directly measure the interaction forces between pairs of particles and between particles and bare silica surfaces. All force measurements were carried out using a Nanoscope 3A AFM (Digital Instruments), equipped with a PicoForce scanner. We attached both positively and negatively charged particles with a diameter, $2a = 3.5$ µm, as colloidal probes to triangular AFM cantilevers with a spring constant, $k = 0.06 - 0.12$ N/m, using Norland optical adhesive 61. We confirmed that single particles were attached to

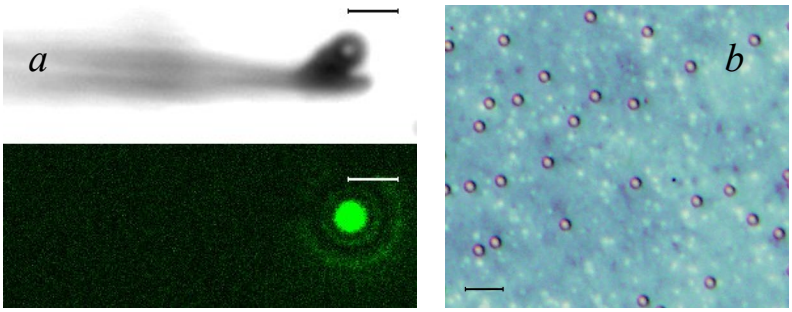

Figure 6.2: (a) PSPMA-coated PS collodal particle as probe on a triangular AFM cantilever, visualised using bright field and fluorescence microscopy. The scale bars represent 5 µm. (b) Microscopy image of PTMAEMA-coated PS colloidal particles on a PSPMA brush on silica. The scale bar represents 10 µm.

the cantilevers in the correct position using the confocal microscope in bright field mode and in fluorescence mode (see Figure 6.2a).

For measurements of the interactions between oppositely charged particles, we immobilised individual cationic particles onto an anionic PSPMA brush with a dry thickness of 200 nm, grafted onto the substrate.[33] The success of this method was verified by optical microscopy (see Figure 6.2b). The interaction forces were measured in a liquid cell, which was filled with a filtered solution of KCl in water, with concentrations varying from 0.15 to 3.0 M. Force distance curves were measured using a scan range of 2.0 µm, scan rates ranging from 10 to 2000 nm/s and a variable contact time between the two particles. We started a series of measurements just below the critical salt concentration (see Section 6.3.2) and scanned the surface until we recorded an attractive interaction. At that location, we recorded force curves at various lower salt concentrations and we finished at the same salt concentration as we started to check that no erosion of the particle surfaces had taken place (see Chapter 12). After measurements, we verified that the colloidal probe was still present.

6.3 Results and discussion

6.3.1 Particle characterisation

Our particles have a diameter $2a$, of 1.1 µm and a polyelectrolyte brush layer on their surface of thickness $L = 50$ nm in water, as determined with various experimental techniques. Figure 6.1 shows a drawing of the particles to scale.

From confocal microscopy we obtain an effective hard particle diameter of 1.1 µm (see Figure 6.3). After drying a suspension of particles we find crystalline domains.

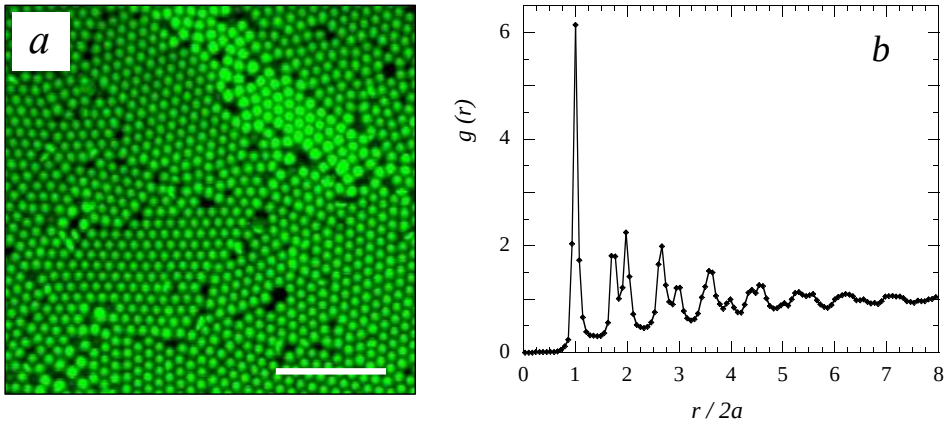

Figure 6.3: (a) PS particles, modified with a PSPMA brush and labelled with pyrromethene-546, after drying in air. The scale bar represents 10 µm. (b) 2-D radial distribution function $g(r)$ for the particles in (a). The x-axis has been rescaled using an effective diameter $2a$ of 1.1 µm.

The corresponding 2-D radial correlation function $g(r)$ was used to obtain the effective particle diameter (see Figure 6.3b). We find clear correlation peaks over distances up to six times this particle diameter, which highlights their monodispersity.

From static light scattering we obtain an effective hard particle diameter of 1.060 µm by fitting the measured form factor $P(q)$ to Mie's scattering theory for polydisperse hard spheres (see Figure 6.4). [34] We find that the particles size is normally distributed with a polydispersity between 3% and 7%. We find no difference in effective hard particle size between the particles before and after modification with a polyelectrolyte brush, which already indicates that the brush is not extremely dense.

Finally, from dynamic light scattering experiments we obtain a hydrodynamic diameter of 1.2 µm for the modified particles. The measured hydrodynamic diameter is larger than the two values for the effective hard particle diameter because of the swollen polyelectrolyte brush layer at the particle surface, which is not visible in static light scattering and collapsed in the dried crystalline domains. A crude approximation of the brush thickness follows from this difference: $L \approx 0.5 \cdot (R_\mathrm{h} - R_\mathrm{hs}) \approx 50$ nm.

We estimate the grafting density of polyelectrolyte chains at the surface of the particles from a combination of electrophoresis and AFM measurements. From measurements of the electrophoretic mobility as a function of salt concentration we find that the molar concentration of polymeric charges surrounding the particles is roughly 0.15 M (see Figure 6.5). From the range of attractive and repulsive forces of the colloidal probe particles against bare silica surfaces in AFM force measurements, we find a more accurate measure for the thickness of the polyelectrolyte layer in water (L

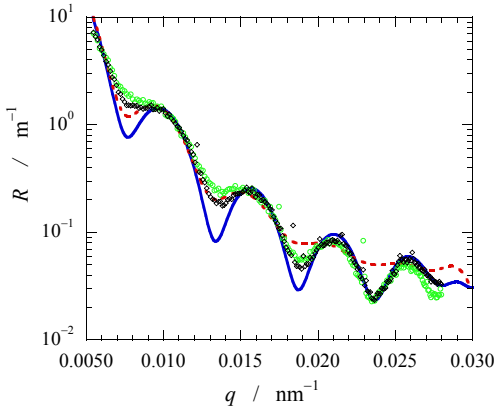

Figure 6.4: Static light scattering of PS particles in 1.35 M KCl, before (◇) and after (○) modification with a polyelectrolyte brush. R is the Rayleigh ratio and q is the wave vector. Lines are calculated using Lorentz-Mie theory for light scattering by objects with a size comparable to the wavelength of light. We have used a wavelength of 532 nm, $m = n_p/n_0 = 1.15$ and a mean diameter of 1.060 µm (Gaussian size distribution). The solid line is calculated for 3% dispersity, the dotted line for 7% dispersity.

= 50 nm, see Figure 6.6). To calculate the grafting density, we assume the simplest model for a flat polyelectrolyte brush (Alexander-de Gennes):

$$\phi \approx b^3 g/\xi^3 \approx \left(\Gamma b^2\right)^{(3\nu-1)/(2\nu)} , \tag{6.1}$$

$$g \approx \left(\frac{\xi}{b}\right)^{1/\nu} \approx \Gamma^{-1/(2\nu)} b^{-1/\nu} , \tag{6.2}$$

$$L \approx N\xi/g \tag{6.3}$$

where b is the Kuhn length of the sulphopropyl methacrylate monomers (≈ 4.0 nm[36]), N is the number of Kuhn monomers, Γ is the grafting density (m^{-2}), ξ is the correlation length in the brush layer (m) and ν is the Flory scaling exponent, expressing the solvent quality. From a combination of Equations 6.1, 6.2 and 6.3, $\Gamma \approx 2.2 \cdot 10^{-4}$ nm^{-2} and the distance between two chains, $1/\sqrt{\Gamma} \approx 68$ nm. From the number of Kuhn monomers, the average degree of polymerisation, measured in chemical monomers (N_m) can be estimated according to

$$Nb \approx N_m {v_m}^{1/3} \tag{6.4}$$

where v_m is the molecular volume of a PSPMA monomer ($2.8 \cdot 10^{-28}$ m^3 [37]). We find an the average degree of polymerisation $N_m \approx 90$.

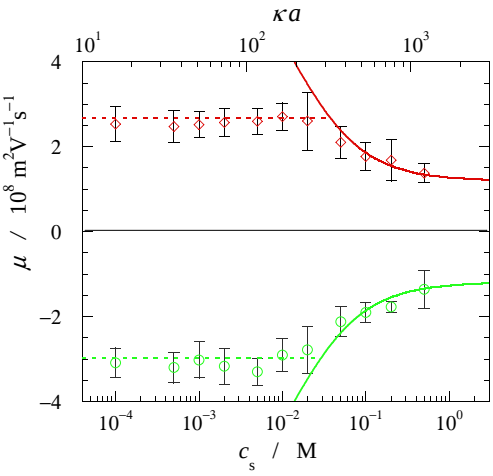

Figure 6.5: Electrophoretic mobility of hairy colloids as a function of salt concentration: (◇) cationic colloids, (○) anionic colloids. Solid lines are a fit of the data points at high salt concentrations to Ohshima's theory.[35] Dashed lines indicate a plateau of the electrophoretic mobility at low salt concentration, probably caused by counterion condensation inside the polyelectrolyte brushes.

Despite being a very crude approximation, this estimate indicates that the polyelectrolyte layer on the surface of the colloidal particles is just on the edge of the brush regime ($L \approx 1/\sqrt{\Gamma}$). We note that this grafting density is much lower than what is typically obtained for surface-initiated ATRP reactions, even for polyelectrolytes.[29,33,37] This is most likely the result of a combination of factors. First of all, we have no control over the location and orientation of inimer molecules on the surface of the polystyrene particles. Jhaveri et al. suggest that the inimer molecules preferentially reside at the interface of PMMA particles,[38] but whether this holds for polystyrene as well, is unknown. Secondly, some inimers might become inactive during the dispersion polymerisation, because they react in the radical polymerisation first. And finally, the adsorbed PVP chains that stabilise the growing particles during dispersion polymerisation might impede the growth of polyelectrolyte chains.

The combination of these factors apparently results in a rather low grafting density for a true polyelectrolyte brush. Nonetheless, the charge-modification of the colloids is still sufficiently efficient to use them as building blocks for reversible self-assembly, as we will demonstrate in the remainder of this Chapter.

It is crucial, for accomplishing a system that can be made to assemble reversibly, that no primary-minimum flocculation occurs between like-charged particles at low or high salt concentration, and between oppositely charged particles at high salt concentration. For this, a minimal grafting density is probably needed. These hairy

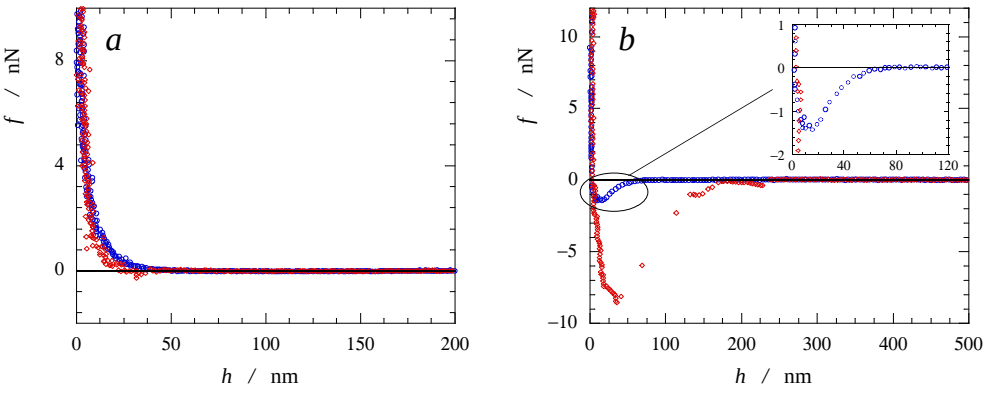

Figure 6.6: AFM force measurements with a 3.5 µm PS particle as colloidal probe, with a surface-grafted (a) anionic PSPMA brush and (b) cationic PTMAEMA brush, against bare silica in Milli-Q water. Both figures show approach (○) and retract (◇) curves.

colloids can in fact be dispersed in water at ionic strengths as high as 8 M (KSCN) without any sign of flocculation, due to their steric stabilisation.

6.3.2 Reversible assembly

Oppositely charged particles aggregate when mixed at sufficiently low ionic strength by charge-driven complexation between the polycationic and polyanionic brushes on the particle surfaces. At high salt concentrations the particles do not aggregate and remain homogeneously dispersed in solution. This indicates the existence of a critical salt concentration, similar to what is observed for common complex coacervation in solutions of oppositely charged polyelectrolytes (see Chapters 3, 4 and 5), and in the case of complexation between oppositely charged grafted polyelectrolyte brushes (see Chapters 11 and 12).

We used light scattering to determine the critical salt concentration for the present system. To do so, we prepared mixtures of oppositely charged particles at various salt concentrations, which we left to equilibrate by tumbling for eight days. After eight days some mixtures had become completely transparent, because all particles had aggregated into large clusters that quickly sedimented (examples shown in Figure 6.7a, d). Some mixtures remained unchanged and homogeneous (Figure 6.7c, e). In a narrow range of salt concentrations the mixtures contained both large aggregates and some free unaggregated particles (Figure 6.7b). For every mixture, we let the aggregates settle and we then take a sample of the remaining suspension. We measure the intensity of scattered light and correct for the refractive index of the solution and the particle concentration (Figure 6.7f).

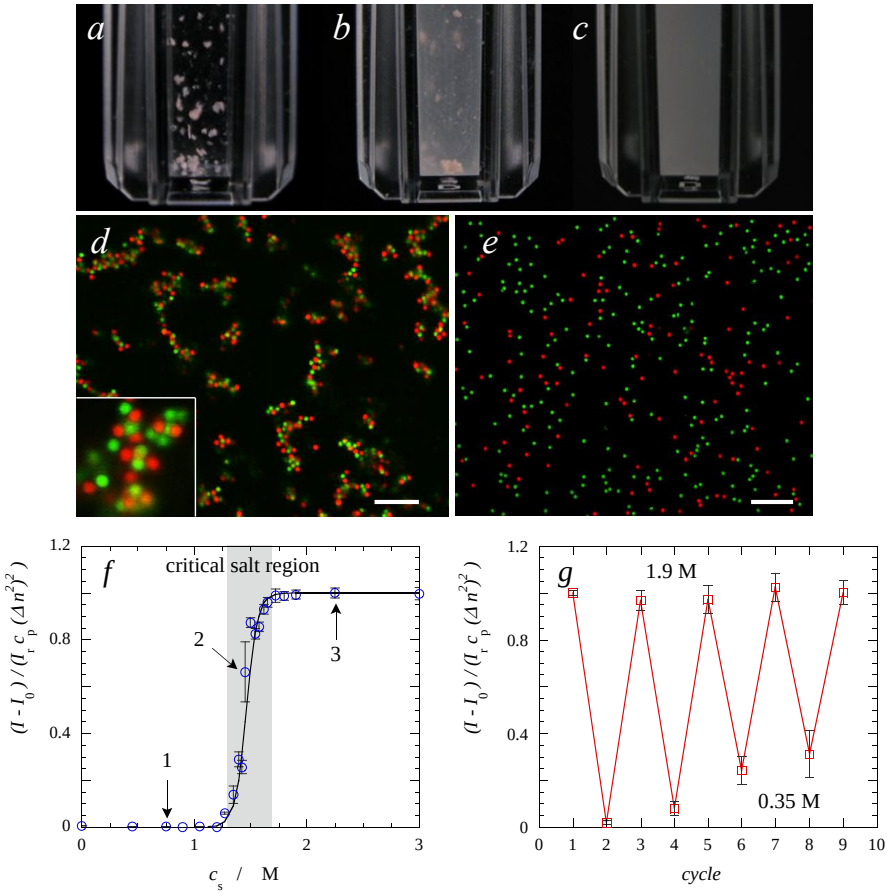

Figure 6.7: Mixtures of oppositely charged PS particles with a diameter of 1.1 µm, modified with either a cationic PTMAEMA (colored red) or an anionic PSPMA brush (colored green), aggregate at an overall volume fraction of 2.5% and at various salt concentrations. (a) Completely aggregated dispersion at low salt concentrations, (b) partly aggregated dispersion at intermediate salt concentration, (c) homogeneous dispersion at high salt concentrations. (d) A confocal microscope image of a fractal gel at $\phi = 3\%$ and 1.5 M salt, ten minutes after mixing. The inset is a zoomed-in part of the sample. (e) A confocal microscope image of the dispersion in (c). The scale bars represent 10 µm, which is also the width and height of the inset. (f) Scattered intensity of the particle suspension after settling, corrected for solvent scattering I_0, the refractive index difference between particles and solvent Δn^2 at various salt concentrations, and overall particle concentration c_p, and normalised by the scattered intensity at 3.0 M KCl, I_r, as a function of salt concentration c_s. The arrows point to the three samples shown in (a – c). The gray area indicates the critical salt region. (g) Scattered intensity of the particle suspension as in (f) when the salt concentration is switched repeatedly from 1.9 M to 0.35 M KCl, that is, between the situations in (c) and (a) respectively. The time difference between cycle 1 and 2 is roughly ten minutes, between cycle 8 and 9 roughly four hours.

The resulting graph indeed shows that above a certain salt concentration no aggregation occurs. A narrow critical salt region forms the transition to a region at low salt concentration where all particles aggregate. Inside the critical salt region a fraction of the particles does not aggregate. This may be explained by the fact that these particles have a slightly lower density of polyelectrolyte chains or slightly shorter chains grafted to their surface. In Chapter 3 we showed that the critical salt concentration depends strongly on chain length and grafting density in the typical experimental regimes ($20 < N_m < 500$). This means that only a small variation in particle charge, which typically occurs during synthesis, will give rise to a broadened critical salt region. For the larger 3.5 µm particles, we find a similar, but slightly broader critical salt region, centered around 1.9 M.

Although all particles aggregate into large clusters at low salt concentrations, this aggregation is completely reversible. When we increase the salt concentration again above the critical salt concentration, all aggregates can be redispersed and we obtained a homogeneous dispersion again (Figure 6.7c, e). In Figure 6.7g we show the results of such a switching experiment, where we switch the salt concentration of a mixture of oppositely charged particles repeatedly from low to high and back. When the salt concentration is increased to 1.9 M KCl, the corrected scattering reaches the same level as before aggregation was induced. By analysing the intensity autocorrelation function (DLS), we confirm that the scattering objects are still of the same size, that is, single particles. The observed reversibility indicates that upon aggregation these oppositely charged hairy particles are not irreversibly trapped in a primary minimum of their pair potential. Such primary-minimum aggregation is thought be common in mixtures of oppositely charged particles in water and to be one of the reasons for the irreversibility of the reported electrostatic particle assembly in literature.[13–15,17] We note that the scattered intensity in Figure 6.7b at low salt concentration slowly increases as we repeat the switching. The reason for this increase is the strong increase in volume during this experiment. While the number of particles stays constant, the volume increases by a factor of 625 between cycle 1 and 9. Since collisions between particles are necessary for the described aggregation, full aggregation will take significantly longer with increasing sample volume. For high cycle numbers we are no longer able to aggregate all particles within experimental timescales, despite extensive mixing for four hours.

6.3.3 Fractal gels

When mixed at an overall volume fraction of 3%, and below the critical salt concentration, the oppositely charged hairy PS particles form weak gels with a fractal appearance. We confirm the formation of weak gels by rheology. The linear storage modulus is typically an order of magnitude larger than the linear loss modulus and is

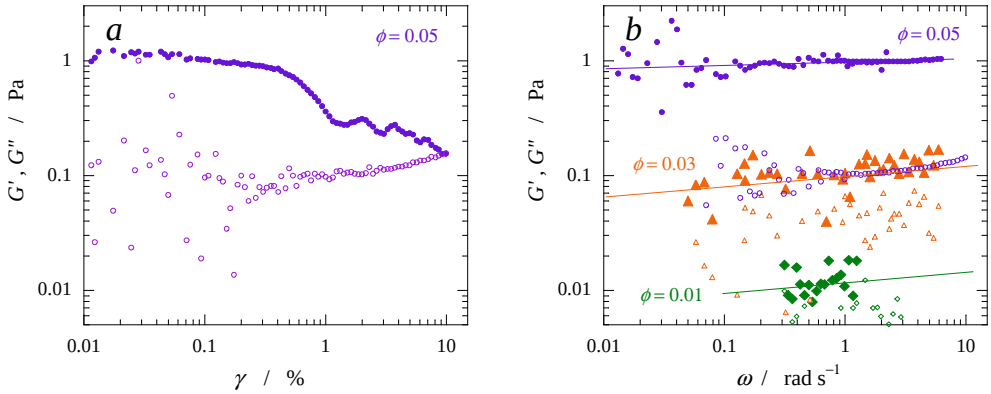

Figure 6.8: (a) Amplitude sweep for a 1 : 1 mixture of cationic and anionic PS particles at $\phi = 0.05$ and $c_s = 0.85$ M, measured at $\omega = 1$ Hz. The regime of linear response is limited to strains of roughly 0.5%. (b) Frequency sweeps for samples similar samples at $\phi = 0.05$, 0.03 and 0.01, measured at $\gamma = 0.2\%$. The filled symbols are storage moduli, the open symbols are loss moduli.

independent of frequency, within a linear viscoelastic regime that only extends up to $\gamma \approx 0.3\%$ (see Figure 6.8).

In Figure 6.7d a typical microscopic cross-sectional image of the gels is shown. By eye, these gels resemble those reported by Sanz et al.[12] They have only short range correlations between oppositely charged particles, as can be shown by calculating the 2-D partial radial distribution functions from microscopy images:

$$g_{\mathrm{cc}}(r) = \frac{1}{2\pi r n^{\mathrm{b}}} \sum_{c_1} \sum_{c_2 \neq c_1} \delta(r - r_{c_1 c_2}) \quad \forall\, c_1, c_2\,, \tag{6.5}$$

$$g_{\mathrm{aa}}(r) = \frac{1}{2\pi r n^{\mathrm{b}}} \sum_{a_1} \sum_{a_2 \neq a_1} \delta(r - r_{a_1 a_2}) \quad \forall\, a_1, a_2\,, \tag{6.6}$$

$$g_{\mathrm{ca+ac}}(r) = \frac{1}{\pi r n^{\mathrm{b}}} \sum_{c} \sum_{a} \delta(r - r_{ca}) \quad \forall\, c, a\,, \tag{6.7}$$

$$g(r) = g_{\mathrm{cc}}(r) + g_{\mathrm{aa}}(r) + g_{\mathrm{ca+ac}}(r) \tag{6.8}$$

where n^{b} is the number density of all particles, $\delta(x)$ is the Dirac delta function, c_i is a counter for all cationic particles and a_i a counter for the anionic particles.

In Figure 6.9a we show these three partial radial distribution functions for the gels shown in Figure 6.7d. We find a large peak for the correlations between unlike particles ($g_{\mathrm{ca+ac}}$) at $r/2a = 1$, whereas the correlations between like-charged particles (g_{cc} and g_{aa}) are still close to zero. This means that positively charged particles are

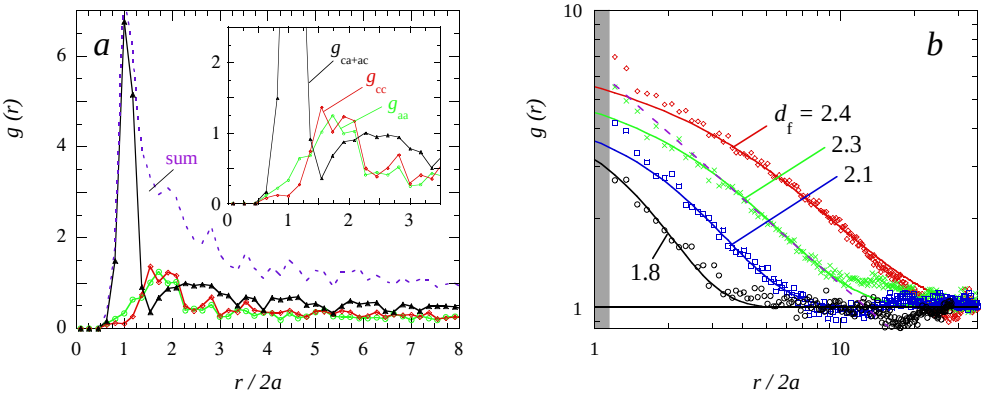

Figure 6.9: (a) 2-D partial radial distribution functions of aggregates of oppositely charged particles at 1.5 M salt, as shown in Figure 6.7d. (b) Radial distribution function of quenched suspensions of oppositely charged PS particles, averaged over 10 – 20 images. The overall particle concentration after the quench is kept constant at $\phi = 3\%$. Different curves correspond to different quench parameters: from 2.0 to 0.70 M salt after 15 minutes (○) and after 60 minutes (□); from 2.0 to 1.0 M after 60 minutes (×) and from 2.0 to 1.3 M after 60 minutes (◇). Solid lines are guides to the eye; the dotted line represents a slope of −0.7 in the fractal region, corresponding to $d_f = 2.3$. Analogously, from the slopes of the other graphs in the fractal region we find values for d_f of 1.8 (○), 2.1 (□), 2.3 (×) and 2.4 (◇). The x-axes have been rescaled using $2a = 1.1$ µm.

always closely connected to negatively charged particles, but rarely to other positively charged particles. Directly after the peak at $r/2a = 1$ for g_{ca+ac}, we find a minimum, followed by a lower, broad second peak between $r/2a = 2$ and 3. This second peak corresponds to two oppositely charged particles, separated by two other particles. Examples of these can be seen in the confocal images (Figure 6.7d). At the minimum in g_{ca+ac}, we find maxima in both g_{cc} and g_{aa}, between $r/2a = 1.6$ and 2. Beyond $r/2a = 3$ the positions of both particle types becomes uncorrelated. From these results we conclude that the gel structure is dominated by the short-range interactions between the oppositely charged particles.

6.3.4 Mechanism of aggregation

The gels we observe have a fractal appearance. In general, gelation can occur via two routes depending on the strength and range of the attractive potential. For high attractive energies, acting over short length scales, aggregation leads to the formation of fractal gels, so-called strong gels, that form via diffusion-limited cluster aggregation (DLCA).[21,39–41] By contrast, gelation in systems with weak and long-ranged interactions, proceeds via kinetically-arrested phase separation leading to

spinodal-like gel structures.[42,43] In our experiments the former mechanism appears to be at play.

Most fractal-like aggregates follow a fractal law over a limited range, bounded by the particle size or resolution of detection as lower limit and the largest cluster size or the density correlation length as upper limit.[44] In this fractal regime, the aggregates are characterised by a fractal dimension, d_f which follows from

$$m \propto R^{d_f} \tag{6.9}$$

where R is the size of a fractal aggregate and m its mass. The fractal dimension depends on the overall dimensionality of the available space d, and on the mechanism of aggregation.

Experimentally, the fractal dimension of gels can be derived from the correlations between particles in a confocal image. The number of particles in an aggregate of size R,

$$n(R) = 4\pi n^b \int_0^R r^2 g(r)\,\mathrm{d}r \tag{6.10}$$

is proportional to the aggregate mass. The fractal dimension follows from[41,44,45]

$$g(r) \propto (r/2a)^{d_f - d} \tag{6.11}$$

where a is the radius of the particles. Based on Equation 6.11 we expect a power law scaling between $g(r)$ and $r/2a$ in the fractal regime. In our experiments we indeed find a fractal regime between about 1.5 µm, slightly larger than the diameter of the particles, and $\mathcal{O}$ (10 µm), hence a truly fractal nature is only found in a relatively small regime.

In Figure 6.9b we show the radial distribution function $g(r)$ (Equation 6.8), for fractal-like gels forming in 'quenched' suspensions, as determined from confocal images. Quenching is achieved by changing the salt concentration of a homogeneous dispersion at 2.0 M salt (see Figure 6.7f) to a value below the critical salt concentration. We tumble all samples continuously until analysis. To obtain the averaged radial distribution functions in Figure 6.9b we analyse several tens of pictures and average the individual radial distribution functions. We find that the fractal dimension increases with time after mixing. For a quench to 0.70 M KCl, the fractal dimension increases from 1.8, 15 minutes after quenching, to 2.1, 60 minutes after mixing, and no further changes could be measured after that time. This increase in fractal dimension occurs due to restructuring of the gel with aging, a feature commonly observed in fractal gels.[46]

Apart from aging, we find that the fractal dimension of the gels depends on salt concentration. Figure 6.9b shows that more shallow quenches lead to higher fractal dimensions after the same aging time. When the salt concentration is lowered to 1.3 M, just below the critical salt concentration, the fractal dimension reaches values as high as 2.4 after 60 minutes. When the quench is made even smaller, no further increase in d_f could be measured. Instead, those gels appear to be similar to the gels quenched to 1.3 M, apart from more single unbound particles, coexisting with the gel (see also Figure 6.7b).

We note that next-nearest neighbour peaks seem to be almost absent in the averaged correlation functions in Figure 6.9b, despite their appearance in some of the individual correlation functions (Figure 6.9a) and in contrast to some other reports on weak fractal gels.[41] Possibly, this is caused by our averaging over many small and large gel strands and clusters, part of which may already contain strongly bound particles.

Since the colloidal particles are not fully density matched to the aqueous medium in Figure 6.9b, it is difficult to exclude the possibility that compression or collapse of the gels under the influence of gravity affects the fractal dimensions, despite the tumbling of the samples. Nevertheless, on a microscopic scale we observe fluctuations of gel strands and occasionally rearrangements of the particles at high enough salt concentrations, that by eye seem to lead to denser gels, consistent with our observations in Figure 6.9b. In Figure 6.10 we show two examples of such restructuring processes observed in the first hour after mixing.

The reported fractal dimensions are calculated from a radial distribution of a 2-D image. However, the actual fractal clusters are 3-D clusters. We have thus taken the 2-D projections of all particle-particle distances in the 2-D images as their actual 3-D distances and assumed that the fractal nature in the third dimension is identical to the other two dimensions. This approach will typically lead to an overestimation of the fractal dimension if the particle size is much smaller than the slice thickness of the confocal microscope, as was shown by Bremer et al.[44,47] However, in our case the opposite is true: confocal slice thicknesses are typically smaller than the particle size, and the analysed confocal images can be assumed true 2-D cross-sections through a 3-D fractal cluster. Unfortunately, the refractive index mismatch between polystyrene and water makes it impossible to accurately capture the three-dimensional structure of these colloidal systems.

The increase in fractal dimension with decreasing quench depth we find here is similar to observations in weak gels of depletion-flocculated particles.[41,43] Both Zhang et al. and Lu et al. found fractal dimensions increasing from 1.7 to about 2.5 with decreasing interaction strength and range, as a result of more reorganisations.[41,43] In our system, we find a similar effect of the interaction strength, which is tuned by salt concentration, although the final structure appears to be that of a strong

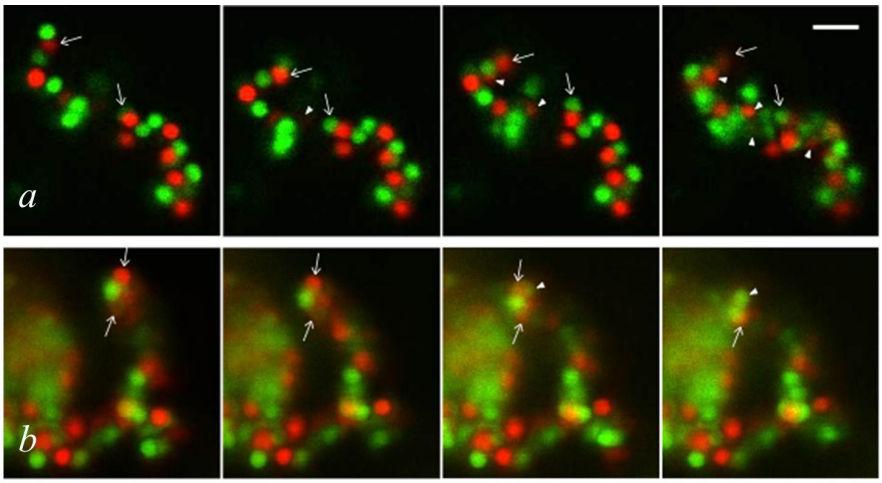

Figure 6.10: Confocal microscopy of a small cluster of 1.1 µm oppositely charged colloidal particles at 1.3 M KCl showing two examples of microscopic processes, (a) and (b), underlying aging of the clusters or gel branches. The full, open arrows point to particles in the focal plane, the truncated, closed arrows to particles that move into focus. The scale bar represents 3 µm. The time difference between the first and last image is in both cases 60 seconds.

gel. We hypothesise here that this is the direct result of the time-dependent nature of the interaction forces between the oppositely charged 'hairy' particles. We can directly measure these particle-particle interaction forces, and as we show in the following section, these may grow in time from weak to very strong, and the extent of strengthening depends again on salt concentration.

6.3.5 Time-dependent particle-particle interactions

When two oppositely charged polyelectrolyte brushes are brought into contact, they form a small polyelectrolyte complex, very similar to a complex coacervate, between them. This process can be followed by AFM (see Chapter 12 for more details). Initially, the complex layer is thin, but the energy of ion pair formation and the entropy of counterion release drive growth of this complex phase (see Chapter 2). Growth involves further interpenetration of the chains, which is slowed down increasingly by friction. As a result, the growth of such complex phases between the two surfaces can easily take minutes.[33] This leads to a transient force between the two surfaces. The salt concentration influences both the driving force for complexation and the friction that slows down the interpenetration, giving rise to a strong salt-dependence of this transient force.

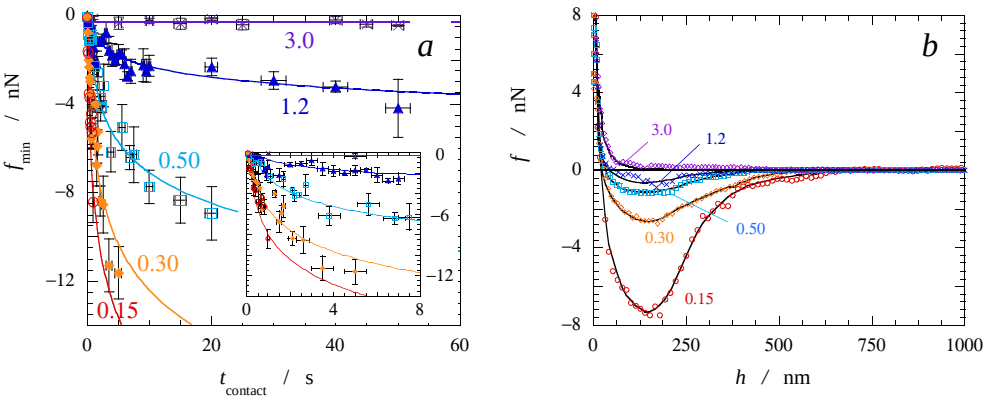

Figure 6.11: (a) Averaged rupture forces of the interaction between cationic and anionic colloidal particles with a diameter of 3.5 µm as a function of time of contact between the colloids. Individual rupture events have been grouped into 100 ms bins between 0 and 10 s and in 1,000 ms bins for longer times. The solid lines are logarithmic fits to the data, according our findings in Chapter 12. The inset shows the first 8 seconds of the rupture force. (b) Averaged retract traces of the same AFM force measurements at different salt concentrations. The numbered labels indicate the concentration of KCl in every set of experiments.

In the present system, this interaction occurs between the oppositely charged particles too. In solution and in gels, interpenetration of the brushes between two unlike particles strengthens their connection and restricts their individual mobility. As a result, the aggregation mechanism may change from weak to strong, eventually leading to kinetically arrested gels.

We can measure the time- and salt-dependence of particle-particle interaction forces using AFM force spectroscopy.[33] Figure 6.11a shows how the attractive force increases with increasing contact time between two oppositely charged particles. As the contact time, we take the total time between the first repulsion as a result of compression of the polyelectrolyte brushes upon approach, and the disruption of the particle-particle connection upon separation, including any waiting time. We find that the adhesive contact becomes stronger in time for all salt concentrations below the critical salt concentration. Moreover, the strengthening occurs faster for lower salt concentrations. For salt concentrations above the critical salt concentration, we find no attractive force between two oppositely charged particles, other than very weak non-electrostatic contact adhesion (see Figure 6.11b). As shown above, this adhesion is weak enough to leave the assembly reversible (see Figure 6.7).

Similar time-dependent effects have been found in assemblies of DNA-coated colloids, and they are inherently linked to the polymeric nature of the interacting groups on the surface of the particles.[48] Bianciello et al. have argued that these

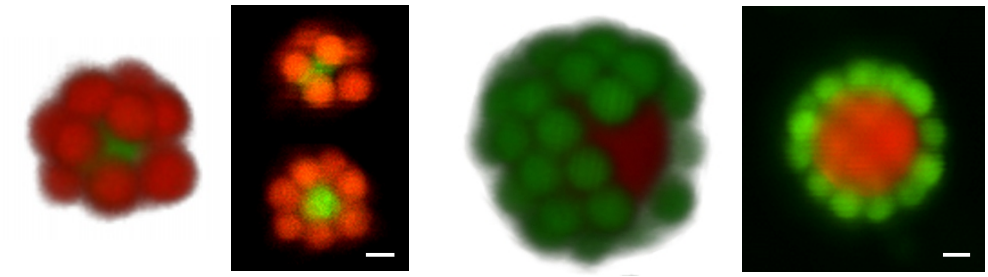

Figure 6.12: Confocal images of two heteroaggregates of cationic and anionic particles below the critical salt concentration with size-symmetric particles on the left and size-asymmetric particles on the right. The overall particle concentration is $\phi = 0.5\%$, the salt concentration is 1.2 M and the mixing ratio is 1 : 20 (v/v). Both 3-D reconstructions of the heteroaggregates and 2-D confocal slices in the xy-plane are shown. The scale bars represent 1 µm.

time-dependent forces have a strong impact on the self-assembly of colloidal particles. Initially, they can be very weak, but in time, they may lead to particles being effectively trapped.

We can construct the initial interaction force between two unlike particles at different salt concentrations by averaging all force curves with $t_{\text{contact}} < 300$ ms, as shown in Figure 6.11b. These force curves are averaged over at least twenty individual force measurements. Clearly, the interaction strength increases with decreasing salt concentration. Moreover, we find no repulsive energy barrier between two oppositely charged particles. The absence of an energy barrier before reaching the potential well and the total interaction strength suggests that the particles aggregate through a DLCA mechanism, which is consistent with the final fractal appearance of the confocal microscopy images.

6.3.6 Controlled assembly in asymmetric mixtures

The colloidal particles we have discussed in this Chapter can be used to further develop rapid, reversible and controllable self-assembling systems in water. We have demonstrated that our particles assemble rapidly and reversibly into fractal-like gels at 1 : 1 mixing ratio. Moreover, we can use this approach to form finite-sized stable colloidal clusters at asymmetric mixing ratios, which can be disassembled again at any time.

When unlike particles are mixed at mixing a ratio of 1 : 20 (v/v) or beyond, they form heteroaggregates on the same timescale as the gels at 1 : 1 mixing ratio. Two examples are shown in Figure 6.12. At a mixing ratio closer to 1 : 1 we usually observe larger clusters with two, three or more particles of the minority species per cluster.

Heteroaggregates can be formed from particles of the same size, but also from asymmetrically sized particles, already at slightly lower mixing ratio's. In part of the heteroaggregates at a ratio of 1 : 20, the surface of the minority species is completely covered with oppositely charged particles, as shown in Figure 6.12a. However, in some cases, we observe patches of uncovered surface, as shown in Figure 6.12b. Nevertheless, these heteroaggregates are stable with respect to further aggregation for at least two days. At any time we can induce disassembly of these heteroaggregates again by increasing the salt concentration to above the critical salt concentration.

6.4 Concluding remarks

Fully reversible assembly of oppositely charged colloidal particles in water can be achieved by grafting polyelectrolyte chains from the surface of the particles. Polyelectrolyte complexation between two brushes is the driving force for assembly of the particles. We have shown that the aggregation is completely reversible by increasing the salt concentration. This indicates that the same polyelectrolyte chains, together with the neutral PVP stabiliser, prevent the particles from aggregating in the primary minimum of their potential energy curve.

Based on our findings, we can draw a schematic pair potential that governs the interactions between our colloidal particles (Figure 6.13).

The bare polystyrene particles have a deep primary minimum, due to the strong Van der Waals attraction at short distances. We synthesised particles with neutral PVP adsorbed onto and polyelectrolyte chains grafted to the surface of these particles. Both layers give rise to a steric repulsion at any salt concentration, preventing the primary-minimum flocculation between unlike and like-charged particles. The polyelectrolyte brush gives an additional electrostatic repulsion between like-charged particles, but a time-dependent attraction between unlike particles. The strength of the attraction may grow in time from very weak to strong, but it never leads to irreversible flocculation. At any time the aggregates can be disassembled by increasing the salt concentration.

At all salt concentrations below the critical salt concentration, a mixture of oppositely charged particles assembles into clusters with a fractal nature. As a result of the time-dependent strengthening of the attractive interaction, the particles cannot rearrange enough to find the state of minimum free energy: a crystalline solid.[12] Paradoxically, the polymeric nature that leads to reversibility of the assembly is also responsible for the kinetic arrest. Initially weak attractions, that should lead to weak gels, quickly grow stronger in time, thereby slowing down the mobility of two connected particles, until they become effectively trapped. A yet unexplored way to improve this would be to graft neutral polymer brushes, with only few charged monomers as a small block at the ends of these chains, on the surfaces of the particles. Oppositely

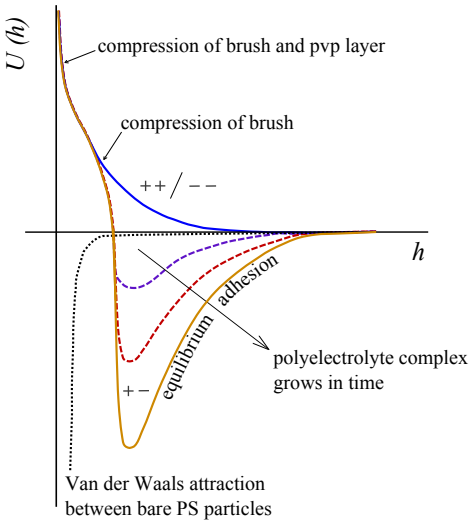

Figure 6.13: Schematic interaction energy between like-charged (++ / −−) and unlike (+−) particles. The adhesive interaction between unlike particles is time-dependent (dashed lines) and eventually grows to the equilibrium adhesive interaction (solid line). Primary-minimum flocculation is prevented by a combination of the neutral PVP layer and the polyelectrolyte brush. The dotted line indicates the primary Van der Waals minimum for bare polystyrene particles.

charged particles could still interact via electrostatic attraction, but growth of the complex between the particles does not occur. Instead, the energy barrier associated with a complex of only few ion pairs between the oppositely charged ends might be low enough for the particles to escape (see also Chapter 11) and reorganisation of clusters into ordered ionic crystals would be possible, even in water.

These particles are a promising step toward a reversible and controlled self-assembling system in water, using colloidal particles as building blocks. The assemblies form reversibly and rapidly, but full control over the final structure is still lacking. We believe that more control over the assembling structures is feasible for these particles, as suggested above. In addition, selective modification of patches on the particles,[24,49,50] and alternative particle shapes[51] are promising approaches to better control these types of assemblies.

References

[1] B. A. Grzybowski, C. E. Wilmer, J. Kim, K. P. Browne, and K. J. M. Bishop, *Soft Matter*, 2009, **5**, 1110–1128.

[2] J. van der Gucht, E. Spruijt, M. Lemmers, and M. A. Cohen Stuart, *J. Coll. Int. Sci.*, 2011, **361**, 407–422.

[3] I. K. Voets, S. van der Burgh, B. Farago, R. Fokkink, D. Kovacevic, T. Hellweg, A. de Keizer, and M. A. Cohen Stuart, *Macromolecules*, 2007, **40**, 8476–8482.

[4] I. K. Voets, A. de Keizer, and M. A. Cohen Stuart, *Adv. Coll. Int. Sci.*, 2009, **147–148**, 300–318.

[5] T. Imura, H. Yanagishita, and D. Kitamoto, *J. Am. Chem. Soc.*, 2004, **126**, 10804–10805.

[6] A. A. Martens, J. van der Gucht, G. Eggink, F. A. de Wolf, and M. A. Cohen Stuart, *Soft Matter*, 2009, **5**, 4191–4197.

[7] R. M. Capito, H. S. Azevedo, Y. S. Velichko, A. Mata, and S. I. Stupp, *Science*, 2008, **319**, 1812–1816.

[8] M. Lemmers, J. Sprakel, I. K. Voets, J. van der Gucht, and M. A. Cohen Stuart, *Angew. Chem. Int. Ed.*, 2010, **49**, 708–711.

[9] W. M. de Vos, J. M. Kleijn, A. de Keizer, and M. A. Cohen Stuart, *Angew. Chem. Int. Ed.*, 2009, **48**, 5369–5371.

[10] A. Ohsugi, H. Furukawa, A. Kakugo, Y. Osada, and J. P. Gong, *Macromol. Rapid Commun.*, 2006, **27**, 1242–1246.

[11] M. E. Leunissen, C. G. Gristova, A.-P. Hynninen, C. P. Royall, A . I. Campbell, A. Imhof, M. Dijkstra, R. van Roij, and A. van Blaaderen, *Nature*, 2005, **437**, 235–240.

[12] E. Sanz, M. E. Leunissen, A. Fortini, A. van Blaaderen, and M. Dijkstra, *J. Phys. Chem. B*, 2008, **112**, 10861–10872.

[13] P. Luckham and B. Vincent, *Colloids and Surfaces*, 1980, **1**, 281–293.

[14] P. Luckham, B. Vincent, J. McMahon, and Th. F. Tadros, *Colloids and Surfaces*, 1983, **6**, 83–95.

[15] A. Y. Kim and J. C. Berg, *J. Coll. Int. Sci.*, 2000, **229**, 607–614.

[16] J. Bratby, *Coagulation and flocculation in water and wastewater treatment*, IWA Publishing, 2nd edn., 2006.

[17] M. Rasa, A. P. Philipse, and J. D. Meeldijk, *J. Coll. Int. Sci.*, 2004, **278**, 115–125.

[18] M.-P. Valignat, O. Theodoly, J. C. Crocker, W. B. Russell, and P. M. Chaikin, *Proc. Nat. Acad. Sci. USA*, 2005, **102**, 4225–4229.

[19] P. L. Biancaniello, A. J. Kim, and J. C. Crocker, *Phys. Rev. Lett.*, 2005, **94**, 058302.

[20] N. Geerts and E. Eiser, *Soft Matter*, 2010, **6**, 664–669.

[21] N. Geerts, T. Schmatko, and E. Eiser, *Langmuir*, 2008, **24**, 5118–5123.

[22] M. E. Leunissen, R. Dreyfus, F. Chiong Cheong, D. G. Grier, R. Sha, N. C. Seeman, and P. M. Chaikin, *Nature Materials*, 2009, **8**, 590–595.

[23] Q. Chen, J. K. Whitmer, S. Jiang, C. B. Sung, E. Luijten, and S. Granick, *Science*, 2011, **331**, 199–202.

[24] L. Hong, A. Cacciuto, E. Luijten, and S. Granick, *Nano Letters*, 2006, **6**, 2510–2514.

[25] K. Matyjaszewski, S. G. Gaynor, A. Kulfan, and M. Podwika, *Macromolecules*, 1997, **30**, 5192–5194.

[26] A. J. Paine, *Macromolecules*, 1990, **23**, 3109–3117.

[27] A. J. Paine, W. Luymes, and J. McNulty, *Macromolecules*, 1990, **23**, 3104–3109.

[28] J. Bernal, *Nature*, 1959, **183**, 141–147.

[29] D. M. Jones, A. A. Brown, and W. T. S. Huck, *Langmuir*, 2002, **18**, 1265–1269.

[30] J. Brandrup and E. H. Immergut, *Polymer Handbook*, John Wiley & Sons, 1966.

[31] V. K. La Mer and E. Noonan, *J. Am. Chem. Soc.*, 1939, **61**, 1487–1491.

[32] I. F. Sbalzarini and P. Koumoutsakos, *J. Struct. Biol.*, 2005, **151**, 182–195.

[33] E. Spruijt, M. A. Cohen Stuart, and J. van der Gucht, *Macromolecules*, 2010, **43**, 1543–1550.

[34] P. Lindner and Th. Zemb, *Neutrons, X-rays and light: scattering methods applied to soft condensed matter*, Elsevier Science, 2002.

[35] H. Ohshima, *Adv. Coll. Int. Sci.*, 1995, **62**, 189–235.

[36] W. Peiquiang, M. Siddiq, C. Huiying, Q. Di, and C. Wu, *Macromolecules*, 1996, **29**, 277–281.

[37] M. Kobayashi, M. Terada, Y. Terayama, M. Kikuchi, and A. Takahara, *Macromolecules*, 2010, **43**, 8409–8415.

[38] S. B. Jhaveri, D. Koylu, D. Maschke, and K. R. Carter, *J. Pol. Sci. A*, 2007, **45**, 1575–1584.

[39] T. A. Witten and L. M. Sander, *Phys. Rev. Lett.*, 1981, **47**, 1400–1403.

[40] T. A. Witten and L. M. Sander, *Phys. Rev. B*, 1983, **27**, 5686–5697.

[41] T. H. Zhang, J. Groenewold, and W. K. Kegel, *Phys. Chem. Chem. Phys.*, 2009, **11**, 10827Ű–10830.

[42] W. Y. Shih, I. A. Aksay, and R. Kikuchi, *Phys. Rev. A*, 1987, **36**, 5015–5019.

[43] P. J. Lu, J. C. Conrad, H. M. Wyss, A. B. Schofield, and D. A. Weitz, *Phys. Rev. Lett.*, 2006, **96**, 028306.

[44] L. G. B. Bremer, B. H. Bijsterbosch, P. Walstra, and T. van Vliet, *Adv. Coll. Int. Sci.*, 1993, **46**, 117–128.

[45] M. Lattuada, H. Wu, A. Hasmy, and M. Morbidelli, *Langmuir*, 2003, **19**, 6312–6316.

[46] L. Cipelletti, S. Manley, R. C. Ball, and D. A. Weitz, *Phys. Rev. Lett.*, 2000, **84**, 2275–2278.

[47] L. G. B. Bremer, B. H. Bijsterbosch, R. Schrijvers, T. van Vliet, and P. Walstra, *Colloids and Surfaces*, 1990, **51**, 159–170.

[48] P. L. Biancaniello, A. J. Kim, and J. C. Crocker, *Biophys. J.*, 2008, **94**, 891–896.

[49] L. Hong, S. Jiang, and S. Granick, *Langmuir*, 2006, **22**, 9495–9499.

[50] T. Tanaka, M. Okayama, Y. Kitayama, Y. Kagawa, and M. Okubo, *Langmuir*, 2010, **26**, 7843–7847.

[51] S. C. Glotzer and M. J. Solomon, *Nature Materials*, 2007, **6**, 557–562.

Part II

Structure

Chapter 7

Structure of complex coacervates studied by scattering of neutrons, X-rays and light

In this Chapter we use scattering of neutrons, X-rays and light to study the microscopic structure of complex coacervates of flexible polyelectrolytes. We use deuterated polymeric tracers in a PDMAEMA/PAA complex coacervate with a neutron scattering length density that is matched to that of the solvent to probe the conformation of a single chain, and complex coacervates in which all polymer chains of one type are deuterated to probe the overall structure. The single chain static structure factors reveal that both polycations and polyanions have an ideal Gaussian chain conformation in the complex coacervates. At the same time, the overall structure is similar to that of a semidilute polymer solution, with polycations and polyanions strongly overlapping to form a network with a mesh size that is much smaller than the radius of gyration of the polymers. The mesh size decreases with decreasing salt concentration, following a scaling with that is in good agreement with predictions from the corresponding salt-polymer phase diagram. In all scattering experiments and for all polymer chain lengths and salt concentrations we find a remarkable low-q excess scattering, following a power law with a slope close to -2. This points to the presence of equilibrium, large-scale density fluctuations in these complex coacervates.

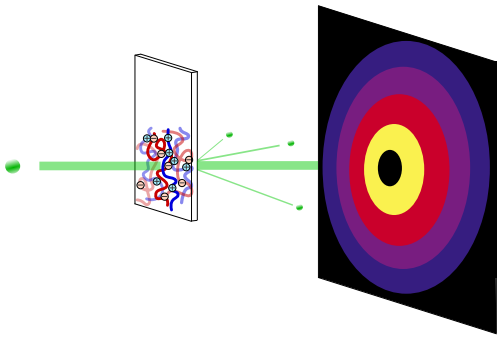

7.1 Introduction

Complex coacervates are dense phases of oppositely charged macroions, which typically contain large amounts of hydration water. The combination of these strong intermolecular associations and strong hydration is expected to give rise to interesting structures. Moreover, many dynamic and mechanical properties of complex coacervates are closely related to their structure. However, little is known about the microscopic structure of complex coacervates, either from proteins, polyelectrolytes or inorganic particles.

Hone et al. were the first to use small-angle neutron scattering (SANS) to study the structure of complexed, but not phase separated polyelectrolytes in solution.[1] They found that the addition of small amounts of poly(styrene sulphonate) or poly(2-acrylamido-2-methylpropanesulphonate) to α-gelatin solutions above the melting temperature gave rise to complexation and a subsequent strong increase in solution viscosity. The structure factors display a peak that is similar in shape and position to the peak of a solution of only PSS or PAMPS polyelectrolytes, but enhanced in intensity by the strongly associated gelatin molecules. Here, the synthetic polyelectrolytes seem to dictate the structure of the complexes, and the gelatin complexation gives rise to the enhanced viscosity. Application of shear flow to these viscous solutions leads to anisotropy in the scattering intensity, due to alignment of the polyelectrolyte chains, but not to changes in the complexation behaviour.[2] Unfortunately, the structural investigation was only carried out at a single mixing ratio of polyelectrolytes and gelatin. Whether the structure would change when a complex coacervate is formed from these macroions, where the polyelectrolytes are, inevitably, also close together in a dense liquid-like phase, remains unclear.

Weinbreck et al. used fluorescence recovery after photobleaching (FRAP), nuclear magnetic resonance (NMR) and diffusive wave spectroscopy (DWS) to obtain information on the structure of whey protein/gum arabic complex coacervates.[3] They found that both components in the complex coacervate had reduced diffusion coefficients compared to dilute solutions, but could not probe length scales smaller than roughly 1 µm. In the case of NMR and DWS, a sample-averaged diffusion coefficient was measured. In agreement with the findings of Hone et al., one of the components had a much lower diffusivity. Here, the gum arabic dictates the complex coacervate structure and is less mobile, whereas the whey protein is associated with this structure, but much more mobile. More importantly, these findings show that both components diffuse independently through the complex coacervate.

Kayitmazer et al. discussed the structure of another protein-containing complex coacervate, PDADMAC/BSA, based on light scattering, cryo-transmission electron microscopy (cryo-TEM), FRAP, SANS and rheology measurements.[4] From rheology and SANS it was found that again the long polyelectrolyte, PDADMAC, dictates

the overall network structure of these complex coacervates, and BSA associates with this structure.[5,6] However, dynamic light scattering (DLS), FRAP, cryo-TEM and NMR all indicated the existence of domains of varying density inside the complex coacervates. Dense domains with high concentrations of BSA, complexed with the PDADMAC network, are thought to coexist with more dilute domains with a lower concentration of BSA, which is also more loosely associated with the PDADMAC. The slow and fast diffusive modes that are measured in DLS, FRAP and NMR thus correspond to BSA diffusion in these respective domains. The low-q scattering intensity in SANS and in static light scattering (SLS) agrees with a range of domain sizes of 300 – 700 nm. Finally, dense domains could be directly observed by cryo-TEM.[4] Similar dense domains have been observed in complex coacervates of lysozyme/PSS, chitosan/BSA and PDADMAC/SDS.[6] Total internal reflection microscopy (TIRF) using fluorescently labelled BSA has revealed the dynamic nature of these domains, showing them disappearing and reappearing on experimental time scales.[7] At this point, it remains unclear how such mesoscale heterogeneity in protein-polyelectrolyte and micelle-polyelectrolyte complex coacervates can be explained.

Singh et al. studied the structure of agar/gelatin complex coacervates by means of SANS and differential scanning calorimetry.[8] Both biopolymers form gels separately and the complex coacervates retain the thermal properties of the constituents to a remarkable extent. The authors argue that the complex coacervates are physically entangled, interpenetrating networks of the two biopolymers, with a mesh size of 1.2 nm. Interestingly, they found excess scattering in the low-q regime of their SANS measurements, similar to Kizilay et al.,[6] which they attribute to large-scale concentration fluctuations, with a typical correlation size of 22 nm, even though no levelling off of the intensity was observed.

Chodankar et al. studied the structure of PSS/BSA complex coacervates at low pH by SANS.[9] They found very similar scattering curves as Singh et al. and Kizilay et al., characterised by a mesh size at high q and large-scale density correlations, following a power law scaling, resembling a fractal aggregate. They also measured the scattering intensity from a sample of the dilute phase and found that aggregates with a typical size of several PSS chains were present there. Unfortunately, no explanation was given for the origin of fractal-like structures and power law scaling of the scattering intensity in complex coacervates.

Summarising the above, the structure of most complex coacervates is far from understood. In protein-polyelectrolyte and micelle-polyelectrolyte complex coacervates, the long polyelectrolyte molecules seem to dictate the overall structure of the complex coacervate networks and proteins are associated with this network. These associations appear to be heterogeneous on mesoscopic length scales between tens of nanometres and a micrometre, giving rise to fluctuations in concentration and excess scattering at low q.

When complex coacervates consist of two flexible polyelectrolytes of almost equal length, the microscopic structure is even less trivial and, so far, not investigated. Several intriguing questions arise. Will one of the components still dictate the overall network structure? Will the strong associations between the flexible polyelectrolytes lead to strong pairing into stiff bundles or will the complex coacervate behave as an ordinary semidilute solution with all overlapping chains? Will the oppositely charged polyelectrolytes diffuse independently and will the concentration fluctuations persist? No experimental or theoretical studies on the structure of these types of complex coacervates have been carried out so far. The questions on the conformation of flexible polyelectrolytes in a complex coacervate, their mutual influence on the network structure and the possibility of concentration fluctuations have therefore not been answered yet.

In this Chapter we use scattering of neutrons, X-rays and light to study the static structure of complex coacervates of flexible polyelectrolytes. We use deuterated polyelectrolytes in complex coacervates with varying neutron scattering length densities to measure the conformation of both flexible polyelectrolytes independently. In addition, we use both polyelectrolytes to determine the structure factor of the complex coacervate networks. We compare our neutron scattering measurements with X-ray scattering and static light scattering measurements, which provide complementary structural information. Finally, from dynamic light scattering we find two modes of relaxation, which we correlate to two types of structural relaxations in the complex coacervates.

7.2 Experimental details

7.2.1 Materials

We used the combination of oppositely charged flexible polyelectrolytes as described in Chapter 3, with PDMAEMA as polycation and PAA as polyanion. We combined fully hydrogenated h-PDMAEMA$_{150}$, h-PDMAEMA$_{527}$, h-PAA$_{139}$ and h-PAA$_{500}$ and fully deuterated d-PDMAEMA$_{148}$, d-PDMAEMA$_{320}$ and d-PAA$_{107}$. The specifications of these polymers are shown in Table 7.1. The pH-dependent charging of PDMAEMA and PAA and the phase behaviour of their complex coacervates is described in Chapter 3.

We prepared stock solutions of all polymers at 50 g/L (PDMAEMA) or 30 g/L (PAA) in Milli-Q water with the pH adjusted to 6.5 $\pm$ 0.2 using 1.0 M HCl and KOH. The meter readings in solutions containing D_2O were corrected for the difference between pH and pD measured by a glass electrode, using pK_w = 14.8 of D_2O.[15] At pH = 6.5 the two oppositely charged polyelectrolytes have equal charge densities for all salt concentrations we used (see Figure 3.3).

Table 7.1: Specifications of the PDMAEMA and PAA used in this study on the structure of polyelectrolyte complex coacervates. N is the number averaged degree of polymerisation, calculated from M_n, ρ is the bulk density of the polymers and ρ_N is the coherent neutron scattering length density. All polymers were purchased from Polymer Source.

Polymer	M_n (kg/mol)	M_w (kg/mol)	M_w/M_n	N	ρ (kg/ m^3)	ρ_N (10^{-6} Å^{-2})
h-PDMAEMA$_{150}$	23.5	24.4	1.04	150	0.934[a]	0.80 [10]
h-PDMAEMA$_{527}$	82.7	90.1	1.09	527		
d-PDMAEMA$_{148}$	25.5	26.5	1.04	148	1.023[b]	5.7 [11]
d-PDMAEMA$_{320}$	55.0	137.5	2.5	320		
h-PAA$_{139}$	10.0	11.5	1.15	139	1.051 [12]	1.46 [13]
h-PAA$_{500}$	36.0	39.6	1.10	500		
d-PAA$_{107}$	8.0	38.4	4.8	107	1.095[b]	5.05 [14]

Notes

[a] Assumed to be equal to the monomer density.

[b] Assuming equal molecular volumes v_m, compared to hydrogenated polymers and correcting for the increase in mass due to deuterium.

For the preparation of the complex coacervates, we used stock solutions of 3.0 M KCl, 1.0 M HCl/DCl and KOH/KOD in Milli-Q water (resistance > 18.2 MΩ · cm) and in D_2O (99.9% D, Sigma-Aldrich), respectively. Before mixing, all stock solutions were filtered using 0.2 µm polyethersulphone membrane syringe filters for H_2O, D_2O and 3.0 M KCl and cellulose filters for the polymer solutions.

The complex coacervate samples were prepared in plastic vials by mixing the PDMAEMA and PAA at the preferred complex coacervate composition, that is, in a 1 : 1 ratio of chargeable groups, according to Chapter 3. After mixing, the samples were left for two days, centrifuged at 3,000×g and then left for another two days for equilibration. The phases were separated and 0.2 or 0.4 mL of the complex coacervate phase was transferred together with 0.1 or 0.2 mL of the dilute phase into 1 mm and 2 mm Hellma quartz cuvets or 2 mm Hilgenberg quartz capillaries. The cuvets were sealed with fitting teflon stoppers and stored at room temperature until we measured them. For light scattering measurements, we transferred 1.5 mL of complex coacervate phase together with 2.0 mL of dilute phase to a Hellma cylindrical quartz cell of 25 mm outer diameter.

7.2.2 Small angle neutron scattering

Small-angle neutron scattering (SANS) experiments were performed at the Institut Laue-Langevin (ILL) in Grenoble, France, at the D11 beam line. We measured at

three detector distances of 1.2, 8.0 and 34.0 m, using collimator distances of 5.5, 8.0 and 34.0 m, respectively. Two incident neutron wavelengths were selected (6 Å and 13 Å, with a resolution $\Delta\lambda/\lambda$ of 9%), to cover a total q-range of $9.8 \times 10^{-4} < q < 5.2 \times 10^{-1}$ Å^{-1}. We used a sample aperture of 7× 10 mm^2 and we corrected our data for background scattering, detector response and the spectral distribution of the incident beam with reference measurements for each detector distance and incident neutron wavelength. We finally radially averaged our data and converted to absolute scattering cross-sections in cm^{-1} using water as a reference, according to standard ILL procedures. The temperature was kept constant at 18 ± 0.5℃, unless stated otherwise, to make the measurement temperature identical to the temperature at which the samples were originally prepared and to avoid changing the binodal compositions by temperature (see Section 4.3.4).

We carried out SANS measurements for two types of samples. First, we prepared complex coacervates from stock solutions of hydrogenated polymers, to which trace amounts (3.3% or 10%) of either of the deuterated polymers were added, at different salt concentrations, to investigate the conformation of individual polymers in the complex coacervates. For these measurements we used a volume fraction of H_2O $\phi_w = 0.73$, and consequently, a volume fraction of D_2O $\phi_d = 0.27$. At this solvent composition the average scattering length density of the complex coacervates is matched to that of the solvent. We verified this match point experimentally by measuring the neutron scattering intensity for five $PDMAEMA_{527}/PAA_{500}$ complex coacervates at $c_s = 1.1$ M at $\phi_w = 0.65$, 0.70, 0.75, 0.80 and 0.85. We found a minimum scattering intensity at an interpolated $\phi_w = 0.73$ for $2\times10^{-2} < q < 5\times10^{-3}$ Å^{-1}. The scattering intensity is not absolutely zero after solvent correction, but a small offset remains at high q, probably because the samples contain two different components and their scattering length densities are different. We subtracted this offset from all our scattering curves, to correct for this effect of scattering length density difference. The second type of samples we prepared were samples in which all polymers of one type were deuterated and the scattering length density of the solvent was matched to that of the other polymer ($\phi_w = 0.81$ for d-PAA/h-PDMAEMA and 0.62 for h-PAA/d-PDMAEMA; the latter value is slightly aberrant because of a miscalculation [13]). All samples were measured in flat Hellma quartz cuvets with a path length of 2 mm for samples with $\phi_w < 0.65$ and a path length of 1 mm for all other samples.

The SANS scattering curves were fitted using Sasfit.

7.2.3 Small angle X-ray scattering

SAXS experiments were performed at the European Synchrotron Radiation Facility (ESRF) in Grenoble, France, at the Dutch-Belgian Beamline (BM26B, DUBBLE). We used an X-ray energy of 10 keV and a single detector distance of 7.0 m, to cover a total

q-range of $6.0 \times 10^{-3} < q < 1.0 \times 10^{-1}$ Å^{-1}. We corrected our data for background scattering, detector response and primary beam intensity fluctuations. We calibrated the instrument scattering vector using a standard specimen of wet rat tail tendon collagen and we converted our data to absolute scattering cross-sections using water and HDPE as secondary standards, according to standard ESRF procedures.[16]

We loaded our samples into 2 mm quartz capillaries (Hilgenberg) using syringes and needles and we placed the capillaries into a home-made multi-capillary holder. All SAXS measurements were carried out at a temperature of 20 ± 1 ℃, the same temperature at which the samples were prepared.

7.2.4 Light scattering

Dynamic and static light scattering measurements were performed on an ALV light scattering instrument, equipped with a 300 mW Cobolt-Samda DPSS laser, operated at a wavelength of 532 nm, an ALV/SO single photon detector with static and dynamic enhancer fiber-optical technology and an ALV-5000/60X0 external correlator. The temperature was kept constant at 20 ± 0.2 ℃ using a Haake F8-C35 thermostat. For static light scattering (SLS) measurements, the detector angle was varied from $\theta = 15°$ to $\theta = 141°$ in steps of 2°, to cover a total q-range of $4.1 \times 10^{-4} < q < 3.0 \times 10^{-3}$ Å^{-1}. We converted our data to absolute scattering cross-sections in cm^{-1} using toluene as a reference ($R_t = 2.10 \times 10^{-5}$ cm^{-1} at $\lambda = 532$ nm, see Equation 5.2).[17,18] At every detector angle we recorded the scattering intensity in ten runs of 30 seconds. We corrected the intensities by subtraction of the solvent scattering, and we report the average corrected values here. For dynamic light scattering (DLS) measurements, we recorded the intensity correlation function $g_2(t)$ and the total scattering intensity I in two subsequent runs of 10^2 seconds at $\theta = 140°$ up to 10^4 seconds at $\theta = 20°$.

7.3 Results and discussion

7.3.1 Small angle neutron scattering

Conformation of single chains in complex coacervates

We carried out small angle neutron scattering (SANS) experiments on complex coacervates with trace amounts of deuterated PDMAEMA or PAA chains, to determine the conformation of individual polymer chains in these complex coacervates. We prepared complex coacervates with trace amounts of d-PDMAEMA$_{148}$ in complex coacervates of h-PDMAEMA$_{150}$/h-PAA$_{139}$ and complex coacervates with trace amounts of either d-PDMAEMA$_{320}$ or d-PAA$_{107}$ in complex coacervates of h-PDMAEMA$_{527}$/h-PAA$_{500}$. The short d-PDMAEMA$_{148}$ and the hydrogenated chains surrounding them in the complex coacervate all have a narrow size distribution and almost equal chain

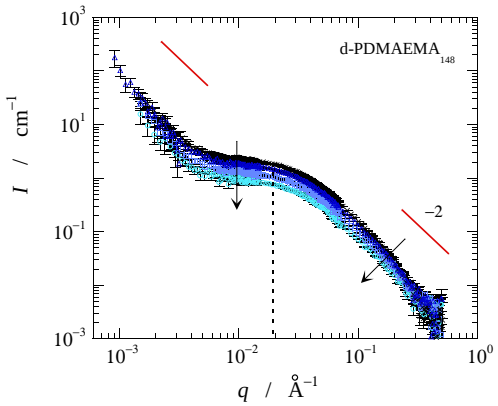

Figure 7.1: Small angle neutron scattering curves of d-PDMAEMA$_{148}$ tracers in complex coacervates at different salt concentrations, increasing in the direction of the arrow: 0.80, 0.90, 1.0, 1.1 M KCl. The solid lines indicate a power law slope of −2.

lengths. The longer d-PDMAEMA$_{320}$ and d-PAA$_{107}$ appear to be shorter than the hydrogenated chains surrounding them in the complex coacervate, but these deuterated chains have a very broad size distribution, and the M_w of these polymers is larger than the M_w of the hydrogenated polymers.

Typical scattering curves for the small d-PDMAEMA$_{148}$ chains with a narrow size distribution are shown in Figure 7.1. We find a Guinier plateau starting at $q = 2{\times}10^{-2}$ Å^{-1}, in agreement with an expected radius of gyration R_g of 5 nm. However, at lower q-values, $q < 5 \times 10^{-3}$ Å^{-1}, the scattered intensity rises sharply again for all salt concentrations. This upturn cannot originate from the tracer molecules, which have a much smaller radius of gyration, but it must originate from the background matrix, which is not perfectly matched to the solvent. We find similar low-q upturns in all scattering curves, with an onset point and a scaling that seems independent of salt concentration, polymer chain length and fraction of deuterated chains. We will discuss the origin of this phenomenon in more detail in the following Sections.

To extract the static structure factor of single polymer chains in complex coacervates, we subtracted two scattering curves with different fractions of deuterated tracers (i.e., 10% and 3.3%). As the low-q upturn does not originate from the tracer molecules, it is the same in both curves and these contributions cancel out. From the resulting scattering profile we obtain the static structure factor of a single polymer chain:[19]

$$S(q) \;=\; \frac{1}{N}\int_0^N\int_0^N \langle \exp\left(iq(\vec{r_n} - \vec{r_m}')\right)\rangle \; \mathrm{d}n\,\mathrm{d}m \tag{7.1}$$

$$= \frac{1}{\nu x^{1/2\nu}} \left[F\left(\frac{1}{2\nu}, x\right) - \frac{1}{x^{1/2\nu}} F\left(\frac{1}{\nu}, x\right) \right] \quad \text{with } x = q^2 b^2 N^{2\nu}/6$$

where N is the chain length and $F(a,b) = \int_b^\infty z^{a-1} \exp(-z)\,\mathrm{d}z$ is the incomplete Gamma function. The shape of the structure factor depends on the solvent quality, expressed by ν, the Flory excluded volume parameter ($\nu = 0.5$ for theta solvents and $\nu = 0.588$ for good solvents). For $1/R_g < q < 1/b$, $S(q) \propto (qb)^{-1/\nu}$ and for $q \ll 1/R_g$, $S(q) \approx N(1 - q^2 {R_g}^2/3)$. For theta solvents, the above equation simplifies to the Debye function for a Gaussian chain: $S(q) = 2N[\exp(-q^2 {R_g}^2) - 1 + q^2 {R_g}^2]/q^4 {R_g}^4$.[19–21]

Figures 7.2 and 7.3a show the single chain static structure factors for all deuterated polymers in their corresponding complex coacervates. The scattering from the same deuterated chains in dilute aqueous solution at high salt concentration (1.0 – 1.2 M) is shown in the same plots for comparison. For dilute solutions, we never find a low-q upturn, as expected. We fitted both curves using the above expression for the static structure factor of a generalised flexible polymer coil.

In all cases, the polyelectrolytes have a conformation very close to the ideal Gaussian conformation. For long enough polyelectrolytes, the scaling exponent ν in the regime $1/R_g < q < 1/b$ is closer to 1/2 for polymers in the complex coacervates than for the same polymers in dilute solution. For d-PDMAEMA$_{320}$, $\nu_{sol} = 0.59$, whereas $\nu_{coac} = 0.52$. For d-PAA$_{107}$, $\nu_{sol} = 0.65$ and $\nu_{coac} = 0.54$. The excluded volume parameter ν for d-PAA in dilute solutions is higher than the expected $\nu \approx 0.588$ for a flexible polyelectrolyte chain at high salt concentrations. We believe this is partly caused by the low average scattering intensity we measured for these d-PAA polymers, both in dilute solutions and in complex coacervates, which makes an accurate fit of the slope troublesome. In samples with d-PAA, the total scattering intensity is roughly an order of magnitude lower than for d-PDMAEMA$_{320}$, despite the fact that the scattering length density of both deuterated polymers is similar (see Table 7.1). Apparently, this d-PAA is only partly deuterated, or the coherent neutron scattering length density is significantly different from the value reported in Table 7.1, which is possibly caused by the close association of sodium or potassium counterions to the charged carboxylic acid groups.[13] Moreover, in dilute solutions the concentration of d-PAA was relatively low and consequently, the error in the detected intensity is large. Finally, for the short d-PDMAEMA$_{148}$, the scattering intensity was similar to that of d-PDMAEMA$_{320}$ samples and we find that the conformation of this short polymer is ideal, both in dilute solution and in complex coacervates ($\nu \approx 0.5$). Most likely, this is caused by the fact that the effect of swelling in solvent is weaker for short chains, and by the fact that the initiator used in the synthesis of this polymer is more hydrophobic than for the other polymers, rendering the final polymer less hydrophilic.

These findings show that flexible polymer chains inside complex coacervates are

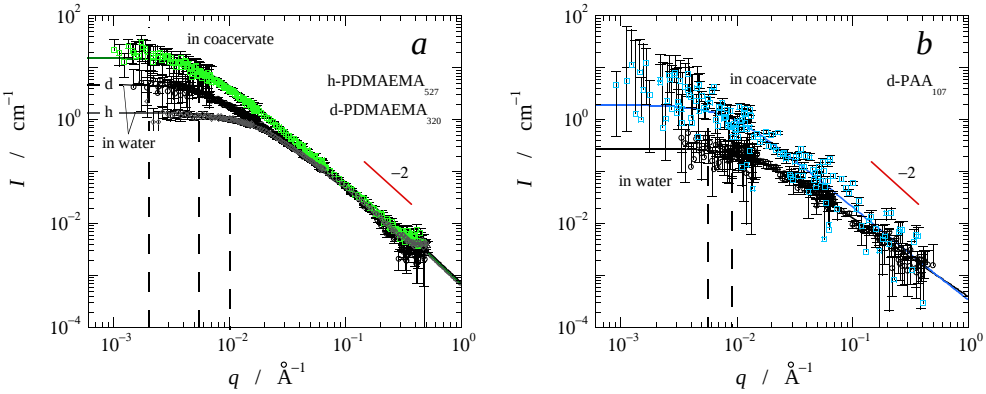

Figure 7.2: SANS curves of (a) d-PDMAEMA$_{320}$ and (b) PAA$_{107}$ tracers in complex coacervates and in dilute solution at 1.2 M KCl. The solid lines are fits to Equation 7.1.

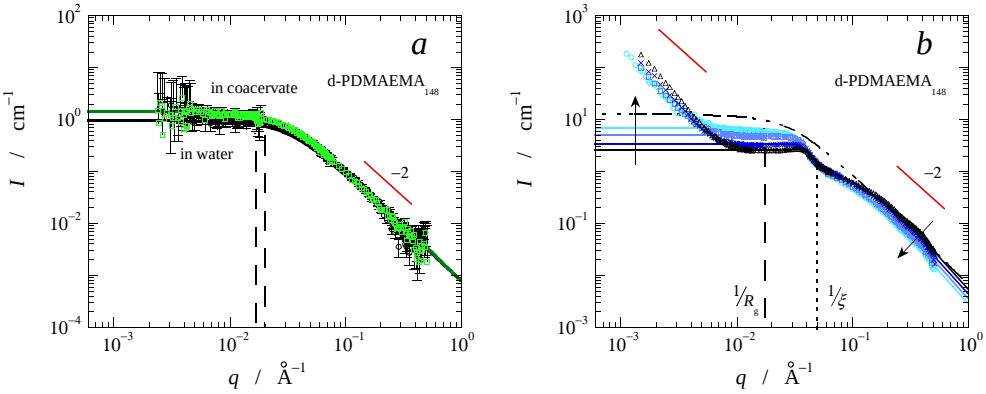

Figure 7.3: (a) SANS curves of d-PDMAEMA$_{148}$ tracers as in Figure 7.2 at 1.0 M salt. (b) SANS curves of the same complex coacervates with all d-PDMAEMA$_{148}$ polymers at 0.80, 0.90, 1.0 and 1.1 M salt, following the direction of the arrows. The solid lines are fits to the data, as explained in the text. The dash-dotted line is the static structure factor of a single polymer chain.

neither much more stiff than in dilute solution, which would be found if oppositely charged chains would form strong parallel chain pairs, corresponding to the 'ladder' model for polyelectrolyte complexation,[22] nor collapsed into globules. Instead, both types of polymers have a similar conformation, close to the ideal chain conformation that is found for polymers in a melt. However, unlike polymer melts, these complex coacervates contain large amounts of water and salt.

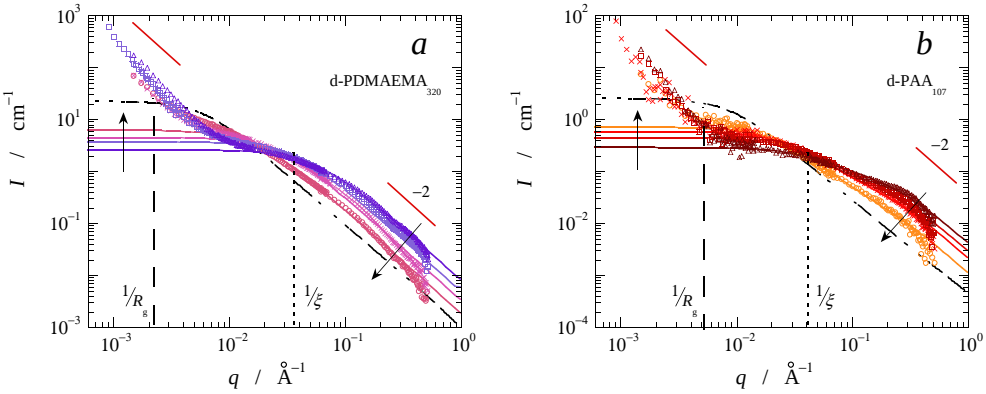

Figure 7.4: SANS curves, presented as in Figure 7.3b, for complex coacervates with (a) d-PDMAEMA$_{320}$/h-PAA$_{500}$ (c_s = 1.0, 1.1, 1.2, 1.3 M, following the direction of the arrows) and (b) d-PAA$_{107}$/h-PDMAEMA$_{527}$ (c_s = 0.90, 1.0, 1.1, 1.2 M, idem).

In contrast to the findings for the swelling parameter ν, the radius of gyration R_g seems to be larger for the polymers in complex coacervates than in dilute solution, although they are less swollen on length scales between the Kuhn length and the radius of gyration. Possibly, the formation of ionic bonds between the oppositely charged polyelectrolytes makes the polymer chains slightly less flexible, which is translated into a larger Kuhn length b. As a result, the chains will be slightly more stiff than when they are uncomplexed in dilute solution, and their radius of gyration is larger.

Alternatively, the larger radius of gyration might originate from a selection mechanism during the formation of the complex coacervates: mixtures of short chains are more soluble at a given salt concentration than mixtures of long chains (see Chapter 3). When two polymer solutions that both contain a range of sizes are mixed together, the longer chains will preferentially end up in the complex coacervate phases, whereas the short chains preferentially end up in the dilute phases. As a result, the complex coacervate contains on average longer polymer chains than the original stock solution. This effect is expected to be more pronounced for polymers with a wider size distribution, such as d-PDMAEMA$_{320}$. Most probably, a combination of both effects, that is, a slight stiffening and a chain length selection mechanism, underlies the observed larger radius of gyration in Figures 7.2 and 7.3a.

Finally, we note that the conformation hardly depends on salt concentration, in the range we examined (0.8 M $< c_s <$ 1.3 M), as can be seen also in Figure 7.1.

Structure of complex coacervate networks

In a second series of measurements, we prepared complex coacervates in which all polymers of one type are deuterated and the neutron scattering length density of the

solvent is matched to the neutron scattering length density of the other polymer type. This approach allows us to investigate the properties of the network of overlapping polymer chains for both types of chains independently.

We first focus on the scattering profile beyond the low-q upturn. We find that the normalised forward scattering of the deuterated networks in the Guinier region is lower than for single polymer chains (see Figure 7.4). Furthermore, the curves start deviating from the $q^{-1/\nu}$ self-avoiding walk scaling already at higher q, that is, at length scales smaller than the radius of gyration. This implies that the polymer chains overlap in the complex coacervate, like ordinary polymers in a semidilute solution. We determine the correlation length ξ experimentally from the static structure factor of a semidilute polymer solution, which is given by

$$S(q) = \frac{S(0)}{1 + q^2\xi^2} \,. \tag{7.2}$$

In other words, the structure factor follows a so-called Ornstein-Zernike law, which arises from the modified monomer correlation function in semidilute polymer solutions.[23] The typical correlation length, or mesh size ξ, of the complex coacervates is a few nanometres, which is indeed smaller than the radius of gyration of the polyelectrolytes, indicating that the polymer chains overlap ($\phi > \phi^*$). We find similar mesh sizes for the polycations and the polyanions. The mesh size decreases with decreasing salt concentration, because the binodal polymer concentration in the complex coacervates is higher at lower salt concentrations, as we discussed in Chapter 3. The mesh sizes we find experimentally agree well with predictions based on the experimental phase diagram in Figure 3.7 and scale as[24]

$$\xi = R_\mathrm{g}\,(\phi^*/\phi)^{m_\xi} \tag{7.3}$$

where $m_\xi = 1$ in theta solvents and 3/4 in good solvents. Figure 7.5 shows the experimental mesh sizes and the prediction based on our phase diagram, using a scaling exponent $m_\xi = 1$, in agreement with the Gaussian conformations we found above.

In the complex coacervates of the small d-PDMAEMA$_{148}$ we observe an additional apparent structure peak around $q = 3 \times 10^{-2}$ Å^{-1}, which the Ornstein-Zernike law cannot capture. We find the same structure peak in these complex coacervates measured with SAXS (see Figure 7.6a and the discussion there). Following a previous suggestion that these PDMAEMA polymers can form micellar structures in water at high salt concentrations, we add a second contribution, due to these micelles, to the total scattering intensity to fit the curves.[25] We model the micelles as hard spheres with radius R_m, which exhibits a Gaussian distribution, in combination with a hard sphere structure factor (Percus-Yevick closure), which is included using a decoupling

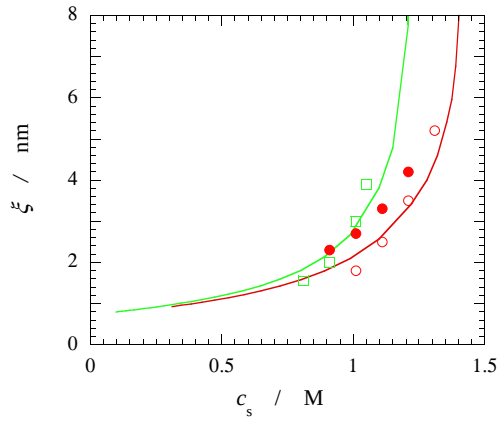

Figure 7.5: Mesh size of complex coacervates as a function of salt concentration, as determined by SANS. Symbols correspond to d-PDMAEMA$_{320}$/h-PAA$_{500}$ (○), d-PAA$_{107}$/h-PDMAEMA$_{527}$ (●) and d-PDMAEMA$_{148}$/h-PAA$_{139}$ (□) complex coacervates. Solid lines are theoretical predictions based on the experimental salt-polymer phase diagrams in Figure 3.7 and Equation 7.3.

approach, for a micellar volume fraction ϕ_m. This model is able to describe the scattering data accurately, as shown in Figure 7.3b. We find that the size and size distribution of the micelles is independent of salt concentration and that the volume fraction increases in the same way as the total polymer concentration with decreasing salt concentration. For the salt concentrations shown in Figure 7.3b, the volume fraction of hard spheres increases from 0.14, close to the critical salt concentration, to 0.29 at 0.8 M.

In the complex coacervates of d-PAA$_{107}$ the total scattering intensity is roughly an order of magnitude lower than for the d-PDMAEMA$_{320}$ samples, similar to our findings for d-PAA$_{107}$ in dilute solutions and as tracers in complex coacervates (see Figure 7.2b). We speculated that these d-PAA are not fully deuterated, or that the neutron scattering length density in aqueous solution with high ionic strength differs significantly from the value in Table 7.1. Nevertheless, we find that these polymers have a typical correlation length in complex coacervates that is similar to the correlation length for the d-PDMAEMA. However, at high q, corresponding to a typical length scale of 0.5 nm, we find a deviation from the expected scaling of the scattering intensity. The length scale associated with this excess scattering is independent of salt concentration, but it becomes more pronounced at low salt concentrations. This length scale is typical for the size of the chemical monomers and arguably for the average distance between oppositely charged monomers in ionic bonds. We note that some of the scattering curves for d-PDMAEMA$_{148}$ and d-PDMAEMA$_{320}$ in Figures

7.3b and 7.4a seem to exhibit a small deviation from the expected scaling at similar length scales, which is most pronounced at low salt concentrations. However, these features are highly obscured for d-PDMAEMA, because of the significantly higher overall scattering intensity.

Although the scattering length density of the solvent was matched to the scattering length density of the oppositely charged hydrogenated polymers in all these complex coacervates, we speculate that the local scattering length density of the charged groups in an ionic bond may be different from the values reported in Table 7.1. Consequently, we expect to find a increased scattering at q-values corresponding to the typical ionic bond distance. Since the polymer volume fraction in the complex coacervates and, hence, also the density of ionic bonds, increases with decreasing salt concentration, this contribution to the scattering profile should become more pronounced at low salt concentrations. If, however, the contrast between the deuterated polymer and the solvent is significantly larger than the contribution from the ionic bonds, as is arguably the case for d-PDMAEMA, we expect the contribution from the ionic bonds to the scattering to be obscured.

Alternatively, the initiator groups of either of the polymers, may cause this excess scattering at $q \approx 3 \times 10^{-1}$ Å^{-1}. This length scale would then correspond to the typical size of the initiator moieties, which have a local neutron scattering length density that is different from the polymer backbone. Since the average polymer volume fraction increases with decreasing salt concentration, the concentration of initiator groups also increases with decreasing salt concentration, and the scattering from these groups should become more pronounced at low salt concentration.

7.3.2 Small angle X-ray and static light scattering

We have complemented our findings on the structure of complex coacervates by SAXS and SLS measurements. In Figure 7.6 we show our SANS results together with results from SAXS and SLS on the same complex coacervate samples. We have shifted the curves along the vertical axis to overlap in the low-q region. We note that the SANS, SAXS and SLS curves show similar characteristics, but they do not overlap completely. In part, this can be explained by the fact that the SANS measurements were carried out for complex coacervates in which all polymer chains of one type were deuterated and the scattering length density of the solvent was matched to that of the oppositely charged polymer, whereas we did not adjust the scattering length densities of the individual components in SAXS and SLS measurements. At the same time, neutrons, X-rays and light interact quite differently with matter: neutrons are scattered by interactions with atomic nuclei, whereas X-rays and light are mainly scattered by interactions with electrons. This leads to a varying relative contrast between the different techniques.[26,27]

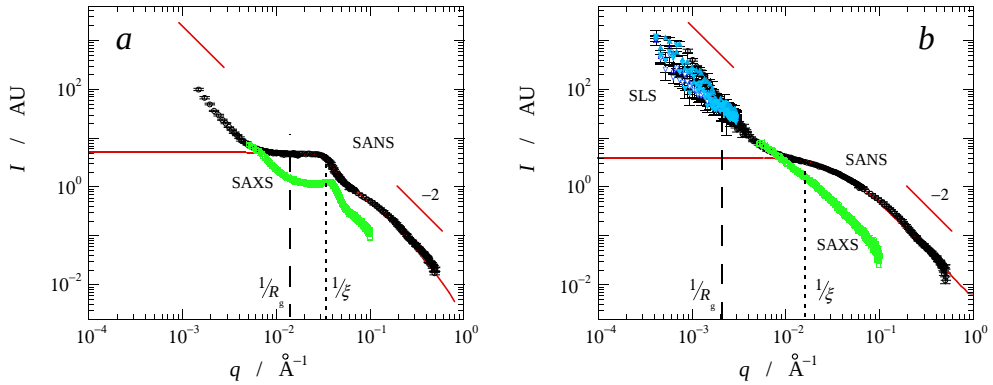

Figure 7.6: Combination of SANS, SAXS and SLS curves for (a) $PDMAEMA_{150}/PAA_{139}$ and (b) $PDMAEMA_{527}/PAA_{500}$ complex coacervates at salt concentrations of 1.0 M and 1.2 M, respectively. The solid line is a fit of the SANS data, as in Figures 7.3b and 7.4a.

Nevertheless, we clearly find that the low-q increase in scattering intensity persists in all three techniques. The scattering at low q seems to follow a power law with a slope close to -2 and extend far beyond the radius of gyration of the polymers, indicating that density fluctuations on large length scales are present in the sample. A similar low-q upturn in scattering intensity has been observed before in polyelectrolyte gels, semidilute polyelectrolyte solutions,[28] neutral hydrogels,[29] reversible transient gels,[30] semidilute polystyrene solutions[31,32] and in various protein-polyelectrolyte complex coacervates.[6,8,9] Although the upturn may have different causes in each case, the phenomenon is sometimes referred to as the Picot-Benoît effect, after its first observation.[33]

In protein-polyelectrolyte complex coacervates, the low-q scattering has been attributed to the presence of domains of increased density in the complex coacervates, in agreement with observations from cryo-TEM and TIRF.[4–6,8,9] To quantitatively describe these scattering curves, an effective power law was added to the structure factor, similar to a fractal packing of scatterers. In our complex coacervates of flexible polyelectrolytes, we find a similar power law scaling of the scattering intensity at low q with an effective fractal dimension of 2, although no collapsed chains are present that might form a fractal aggregate. We therefore attribute this scattering behaviour to the presence of density fluctuations on many length scales, inspired by the observations from cryo-TEM and TIRF.

In our scattering profiles, we find no levelling off of the intensity down to $q = 3 \times 10^{-4}$ Å^{-1}, which would correspond to density fluctuations at length scales up to the micrometre range. Nonetheless, we do not see any inhomogeneities in the complex coacervates with phase contrast microscopy or confocal microscopy on fluorescently

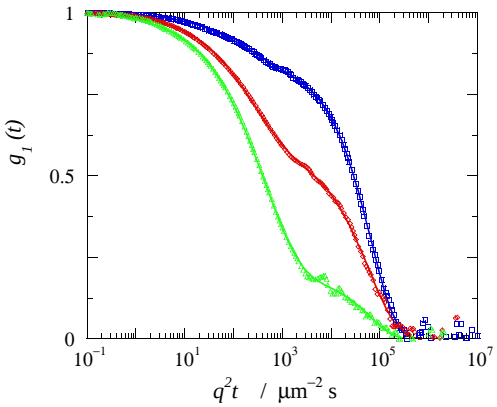

Figure 7.7: Normalised autocorrelation functions from DLS versus q^2t for $PDMAEMA_{527}/PAA_{500}$ complex coacervates at a salt concentration of 1.2 M, measured using a detector angle of 40°, 68° and 110°, from right to left.

labelled polyelectrolytes (see Figure 3.6). We believe that the reason we do not see these density fluctuations with microscopy is fact that the concentration differences and the differences in refractive index are relatively small. Moreover the fluctuations are probably limited to a few µm, based on the observations by TIRF, which is close to the resolution of optical microscopy.

Finally, we note that a structure peak appears in the small angle X-ray scattering of $PDMAEMA_{150}/PAA_{139}$ complex coacervates, similar to what we found with SANS. We have attributed this peak to the presence of micelle-like structures.

7.3.3 Dynamic light scattering

Using dynamic light scattering (DLS), we investigated the dynamics of the structural characteristics we found with SANS, SAXS and SLS. We used the same complex coacervates as for SANS and SAXS ($PDMAEMA_{527}/PAA_{500}$), and in addition, we studied the $PTMAEMA_{96}/PSPMA_{94}$ complex coacervates we also used in Chapters 4 and 8. For both types of complex coacervates, we find two dynamic processes, as can be seen in Figure 7.7. The phase autocorrelation functions can be fitted with the following empirical equation:[34]

$$g_1(t) = A_1 \exp\left(-(t/\tau_1)^{\alpha}\right) + A_2 \exp\left(-(t/\tau_2)^{\beta}\right) \tag{7.4}$$

where t is the correlation time, τ_i represents a relaxation time, α and β are stretch exponents and A_i is the amplitude of mode i, with $\sum_i A_i = 1$.

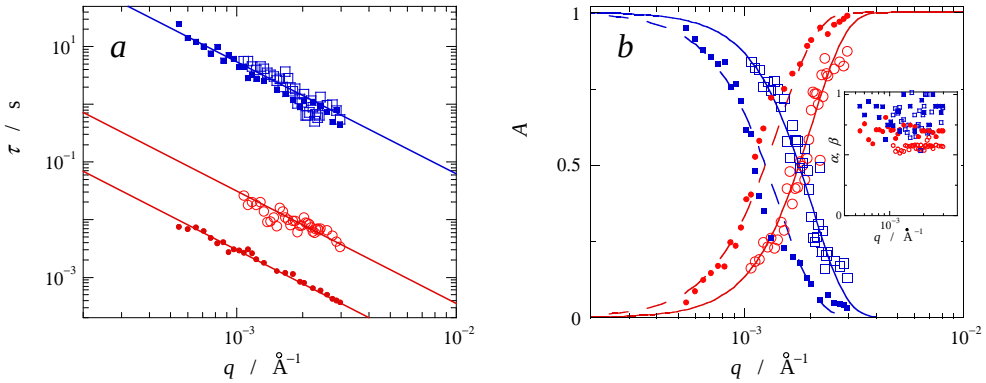

Figure 7.8: (a) Intensity decay times τ, corresponding to the rate of dynamic relaxation in DLS measurements of $PDMAEMA_{527}/PAA_{500}$ (open symbols) and $PTMAEMA_{96}/PSPMA_{94}$ (closed symbols) at 1.2 M and 1.0 M salt respectively, as a function of q. The solid lines all have a slope of -2. (b) Amplitudes corresponding to the decay times in (a) as a function of q. The solid lines are drawn to guide the eye. The inset shows the corresponding stretch factors α and β from Equation 7.4.

Both processes have a diffusive origin, as the corresponding relaxation times scale with q^{-2} (see Figure 7.8a). The stretch exponents vary between 0.6 and 1.0 and are independent of q. For the PDMAEMA/PAA complex coacervate, we estimate the typical size related to the diffusive mode from the Stokes-Einstein equation and the measured viscosity of this particular complex coacervate (η = 400 mPa s). We find that the fast mode corresponds to objects of 1 – 2 nm, that is, comparable to the mesh size of the complex coacervate (see Figure 7.5). This mode probably results from fluctuations of the overlapping chains, which leads to fluctuations of the mesh size. The slow mode corresponds to diffusion of much larger objects (R = 200 – 500 nm). We believe the slow mode is related to the large-scale density fluctuations we find in static scattering experiments. For PTMAEMA/PSPMA complex coacervates the fast mode is roughly ten times faster than in PDMAEMA/PAA. However, the viscosity is almost ten times lower as well, since this complex coacervate was very close to its critical point (η= 45 mPa s) and the corresponding size is identical. The size corresponding to the slow mode is however much larger ($>$ 1 µm), probably reflecting the increased critical fluctuations.

7.3.4 Effect of temperature on scattering profiles

By optical microscopy, we do not see any density fluctuations in the complex coacervates at the temperature where the samples had originally phase separated. However, we clearly see, even by eye, that the complex coacervates become very turbid at higher

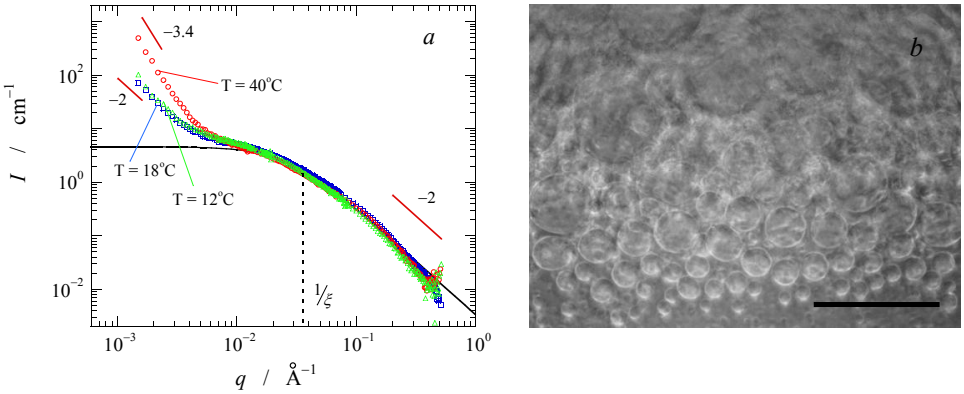

Figure 7.9: (a) SANS curves of d-PDMAEMA$_{320}$/h-PAA$_{500}$ complex coacervates with c_s = 1.2 M at 4, 18 and 40 °C. The solid line is a fit of the SANS data at 18 °C, as shown in Figure 7.4a. (b) Optical microscope image of the interface between the complex coacervate and coexisting dilute phase in (a) at 40 °C. The scale bar represents 100 µm.

temperatures, as we already described in Chapter 4 (see Figure 4.4). The SANS scattering profiles reveal that this turbidity is related to changes in the structure at length scales larger than 200 nm and that no changes occur at smaller length scales. Figure 7.9a shows that the scaling of the scattered intensity changes from q^{-2} to $q^{-3.4}$ as the temperature is raised from 18 °C to 40 °C. The latter scaling is consistent with surface scattering from droplets of varying size with a relatively sharp interface.[28] With optical microscopy, we indeed observe droplets in these heated complex coacervates. Due to the strong light scattering, these droplets are best visible at the interface between the complex coacervate and the dilute phase (see Figure 7.9b). We have rationalised these observations in Chapter 4 by a shifting of the binodal towards more extreme demixing at elevated temperatures (see Figure 4.5).

7.4 Concluding remarks

We have carried out small angle neutron scattering on PDMAEMA/PAA complex coacervates. Using deuterated polymeric tracers in a complex coacervate for which we match the neutron scattering length density to that of the solvent, we measure single chain static structure factors of the polycation and the polyanion. Both have an almost Gaussian conformation, both for short and long polymer chains. Clearly, the charge-driven association of the oppositely charged polyelectrolytes does not lead to collapse into globules, nor to stiffening when they form hypothetical pairs of parallel polymers. Using all deuterated chains of one type in the complex coacervate networks, we find that the complex coacervates are interpenetrated overlapping polymer

solutions, similar to semidilute solutions of neutral polymer chains. Combining our SANS results with small angle X-ray and static light scattering, we find a remarkable excess scattering at low q for all complex coacervates, following a power law scaling with a slope close to -2. We do not find a levelling off down to $q \approx 3 \times 10^{-4}$ Å^{-1}. This scattering is independent of chain length, salt concentration and polymer concentration. We attribute it to equilibrium density fluctuations inside the complex coacervates, similar to the findings for protein-polyelectrolyte complex coacervates. In dynamic light scattering we find two diffusive modes of relaxation, in agreement with the static structure: the fast mode corresponds to fluctuations of the mesh size, the slow mode corresponds to diffusion of the domains of varying density.

References

[1] J. H. E. Hone, A. M. Howe, and T. Cosgrove, *Macromolecules*, 2000, **33**, 1206–1212.

[2] J. H. E. Hone, A. M. Howe, and T. Cosgrove, *Macromolecules*, 2000, **33**, 1199–1205.

[3] F. Weinbreck, H. S. Rollema, R. H. Tromp, and C. G. de Kruif, *Langmuir*, 2004, **20**, 6389–6395.

[4] A. B. Kayitmazer, S. P. Strand, C. Tribet, W. Jaeger, and P. L. Dubin, *Biomacromolecules*, 2007, **8**, 3568–3577.

[5] H. Bohidar, P. L. Dubin, P. R. Majhi, C. Tribet, and W. Jaeger, *Biomacromolecules*, 2005, **6**, 1573–1585.

[6] E. Kizilay, A. B. Kayitmazer, and P. L. Dubin, *Adv. Coll. Int. Sci.*, 2011, **167**, 24–37.

[7] P. L. Dubin, ACS 243rd National Meeting, San Diego, 2012.

[8] S. S. Singh, V. A. Aswal, and H. B. Bohidar, *Int. J. Biol. Macromol.*, 2007, **41**, 301–307.

[9] S. Chodankar, V. A. Aswal, J. Kohlbrecher, R. Vavrin, and A. G. Wagh, *Phys. Rev. E*, 2008, **78**, 031913.

[10] F. Rehfeldt, R. Steitz, S. A. Armes, R. von Klitzing, A. P. Gast, and M. Tanaka, *J. Phys. Chem. B*, 2006, **110**, 9177–9182.

[11] M. Moglianetti, P. Li, F. L. G. Malet, S. A. Armes, R. K. Thomas, and S. Titmuss, *Langmuir*, 2008, **24**, 12892–12898.

[12] J. Brandrup and E. H. Immergut, *Polymer Handbook*, John Wiley & Sons, 1966.

[13] J.-F. Berret, K. Yokota, M. Morvan, and R. Schweins, *J. Phys. Chem. B*, 2006, **110**, 19140–19146. Note: this paper contains a miscalculation, a density of 1.5 leads to a SLD of 2.09.

[14] D. Hourdet, F. L'Alloret, A. Durand, F. Lafuma, R. Audebert, and J.-P. Cotton, *Macromolecules*, 1998, **31**, 5323–5335.

[15] P. K. Glasoe and F. A. Long, *J. Phys. Chem.*, 1960, **64**, 188–189.

[16] M. Lemmers, E. Spruijt, L. Beun, R. Fokkink, F. A. M. Leermakers, G. Portale, M. A. Cohen Stuart, and J. van der Gucht, *Soft Matter*, 2012, **8**, 104–117.

[17] E. Moreels, W. De Ceuninck, and R. Finsy, *J. Chem. Phys.*, 1987, **86**, 618–623.

[18] H. Wu, *Chem. Phys.*, 2010, **367**, 44–47.

[19] B. Hammouda, A. Z. Akcasu, and M. Benmouda, *J. Pol. Sci. B*, 1984, **22**, 853–862.

[20] M. Doi and S. F. Edwards, *The theory of polymer dynamics*, Oxford University Press, 1986.

[21] I. Teraoka, *Polymer solutions: an introduction to physical properties*, John Wiley & Sons, 2002.

[22] A. A. Lazutin, A. N. Semenov, and V. V. Vasilevskaya, *Macromol. Theory Simul.*, 2012, **21**, 328–339.

[23] P. Lindner and Th. Zemb, *Neutrons, X-rays and light: scattering methods applied to soft condensed matter*, Elsevier Science, 2002.

[24] P. G. de Gennes, *Scaling Concepts in Polymer Physics*, Cornell University Press, 1979.

[25] Q. Liu, Z. Yu, and P. Ni, *Coll. Pol. Sci.*, 2004, **282**, 387–393.

[26] J. S. Pedersen, *Adv. Coll. Int. Sci.*, 1997, **70**, 171–210.

[27] C. Sommer, J. S. Pedersen, and V. M. Garamus, *Langmuir*, 2005, **21**, 2137–2149.

[28] F. Horkay, A. Hecht, and E. Geissler, *J. Pol. Sci. B*, 2006, **44**, 3679–3686.

[29] S. Lin-Gibson, R. L. Jones, N. R. Washburn, and F. Horkay, *Macromolecules*, 2005, **38**, 2897–2902.

[30] M. C. Blanco, D. Leisner, C. Vázquez, and M. A. Lopéz-Quintela, *Langmuir*, 2000, **16**, 8585–8594.

[31] H. Dautzenberg, *J. Pol. Sci. C*, 1972, **39**, 123–131.

[32] J. T. Koberstein, C. Picot, and H. Benoit, *Polymer*, 1985, **26**, 673–681.

[33] H. Benoit and C. Picot, *Pure and Applied Chemistry*, 1966, 545–561.

[34] J. Li, T. Ngai, and C. Wu, *Pol. J.*, 2010, **42**, 609–625.

Chapter 8

Relaxation dynamics at different timescales in complex coacervates: time-salt superposition

In this Chapter we show that in the rheology of complex coacervates and other charge-driven soft materials, salt concentration plays a similar role as temperature for polymer melts, and as strain rate for soft solids. We rescale linear and nonlinear rheological data of a set of complex coacervates as model charge-driven soft materials at different salt concentrations to access a range of timescales that is otherwise inaccessible. This provides new insights in the relaxation mechanisms of complex coacervates, which we rationalise in terms of a microscopic mechanism underlying salt-enhanced activated processes.

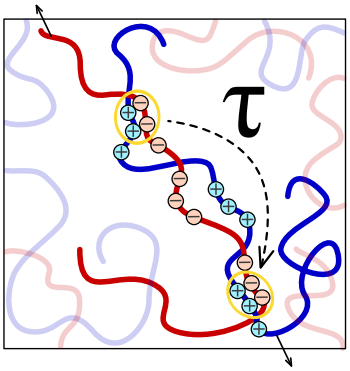

This Chapter is based on:
E. Spruijt, J. Sprakel, M. Lemmers, M. A. Cohen Stuart and J. van der Gucht, *Relaxation dynamics at different timescales in electrostatic complexes: time-salt superposition*, Physical Review Letters **105** (2010), 208301, doi 10.1103/PhysRevLett.105.208301.

8.1 Introduction

Charge-driven assemblies are ubiquitous in natural and man-made soft materials. In nature, attractive electrostatic forces play an important role in the condensation of DNA with histones,[1–3] in the binding of peripheral proteins to membranes[4] and in the exceptional thermal stability of enzymes in thermophilic bacteria.[5] Nature's approaches for electrostatic assembly have been mimicked using synthetic building blocks to create photonic materials,[6] self-healing gels[7] and multilayered capsules of various sizes and cargo.[8] Despite the plethora of phenomena where electrostatic attractions are relevant, it remains poorly understood how environmental factors, such as ionic strength, influence the dynamics of these complexes. Moreover, no clear methods are available to experimentally analyse these effects.

In this Chapter, we propose a new approach to study the dynamics of charge-driven materials. We show that probing the rheological behaviour of a model charge-driven material at different ionic strengths is equivalent to probing the behaviour at different timescales. This equivalence allows superimposing rheological data at different salt concentrations, which together with our model for salt-dependent dynamics of ionic bonds, leads to a new way to systematically investigate the effects of temperature and salt concentration on relaxation behaviour and mechanical properties of complex coacervates and other charge-driven materials.

Superposition is being used as a tool in rheology to probe dynamic processes in a wide variety of soft materials. For example, time-temperature superposition (TTS) relies on the acceleration of all activated processes at high temperatures, enabling probing of longer effective timescales at high temperatures.[9] Analogously, strain-rate-frequency superposition (SFRS) allows probing the low-frequency structural relaxation of soft solids, such as concentrated suspensions and foams, by enhancement of activated processes by external force.[10] We apply a similar approach to study the dynamics of a yet underrepresented class of soft materials: complex coacervates. In addition to the model materials we study in this Chapter, our approach could easily be extended to other charge-driven materials, both natural and man-made, to help elucidate their unresolved dynamics.

8.2 Experimental details

8.2.1 Materials

We used a combination of oppositely charged polyelectrolytes, with PDMAEMA (N_{cat} = 17, 51, 150 and 527) and PTMAEMA ($N_{\mathrm{cat}} = 96$) as polycations and PAA (N_{an} = 20, 47, 139 and 500) and PSPMA ($N_{\mathrm{an}} = 94$) as polyanions. The specifications of these polymers are given in Tables 3.1 and 4.1. The pH-dependent charging of PDMAEMA

and PAA and the phase behaviour of their complex coacervates is described in Figures 3.3 and 3.4. In addition, we used a PSPMA-PEO-PSPMA triblock copolymer (N = 28–230–28) and a poly(allylamine), PAH (N_{cat} = 68, see Table 4.1), to prepare transient physical gels with complex coacervate junction points. The synthesis and rheological properties of these gels are described elsewhere in detail.[7,11]

8.2.2 Complex coacervate formation

We made complex coacervates of PDMAEMA and PAA and of PTMAEMA and PSPMA from 50 g/L, 30 g/L, 100 g/L and 100 g/L stock solutions, respectively. We prepared the complex coacervates at a 1:1 ratio of monomeric groups in aqueous solutions with varying salt concentrations (KCl), as described in Chapters 3 and 4. In all cases we prepared a total volume of 4.0 mL with an overall polymer concentration of 0.20 M, measured in monomer units. The complex coacervate phase had a volume of approximately 0.8 mL. For rheological measurements, we separated the dilute phase from the complex coacervate and load the complex coacervate phase onto the rheometer.

8.2.3 Rheological measurements

All rheological measurements were carried out on Anton Paar MCR301 and MCR-501 stress-controlled rheometers using a cone-plate geometry with a cone radius of 25 mm and a cone angle of 1°. We kept the temperature controlled at 20 °C with Peltier elements and we used an evaporation blocker to minimise water evaporation.

With every sample, we performed a series of measurements, all separated by a waiting step that is at least five times longer than the apparent longest relaxation time we found in step-strain or step-stress experiments. We made sure that the total duration of a measurement series never exceeded five hours to ensure that the slow solvent evaporation that occurs despite our use of an evaporation blocker, had a negligible effect on the rheological measurements, which we verified by repeating frequency sweep measurements at the beginning and end of the measurement series.

8.3 Results and discussion

8.3.1 Frequency sweeps of complex coacervates

We recorded amplitude sweeps (see Figure 8.1) to determine the regime of linear response for our model complex coacervates. We find that the linear viscoelastic regime extends to deformations of approximately 100%, typical for polymeric materials, and is only weakly dependent on salt concentration.

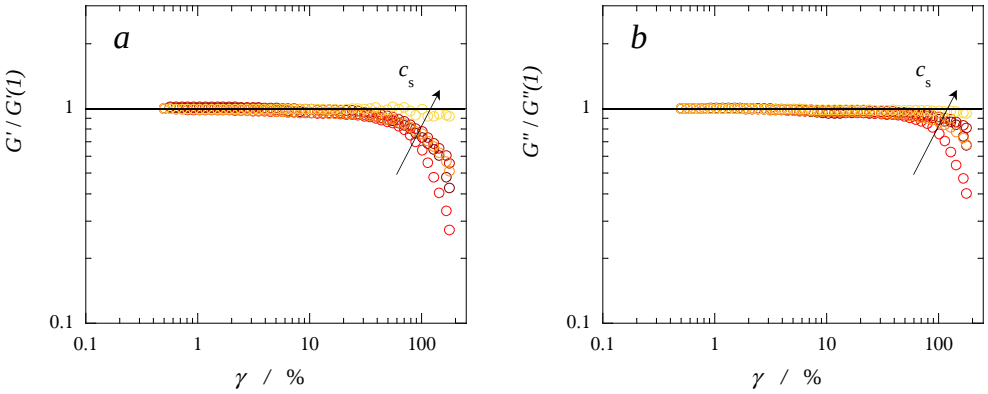

Figure 8.1: Amplitude sweeps of $PDMAEMA_{527}/PAA_{500}$ complex coacervates at $\omega = 1$ rad/s at different salt concentrations (in direction of the arrows: 0.50, 0.60, 0.75, 0.85 and 1.1 M). (a) Storage modulus versus strain amplitude, normalised by the storage modulus at $\gamma = 1\%$. (b) Loss modulus versus strain amplitude, normalised by the loss modulus at $\gamma = 1\%$.

The frequency sweeps shown in Figure 8.2 are typical for these complex coacervates deformed in the linear viscoelastic regime. Here, the rheological response of the complex coacervates to an oscillatory strain depends strongly on salt concentration. At low salt concentration the response is similar to that of soft solids,[10] whereas the response is liquid-like at high salt concentration. These observations are in line with results on other biological complex coacervates.[12]

8.3.2 Superposition of linear and nonlinear rheology

Salt is known to accelerate dynamic processes in polyelectrolyte complexes and complex coacervates (see Chapters 9 and 11). This leads to faster equilibration and eventually to hysteresis-free cycles of compression and disruption of polyelectrolyte complexes (see Chapter 12). In well-known superposition methods in rheology, such as time-temperature superposition (TTS) and strain rate-frequency superposition (SFRS), such acceleration of dynamic processes provides the basis for a way to probe dynamic processes on a range of timescales that is otherwise experimentally inaccessible.

Could we use analogous rescaling of measurements shown in Figure 8.2 in order to get more insight in the dynamics of these complex coacervates as well? Figure 8.3 shows that the frequency sweeps measured at different salt concentrations can indeed be rescaled onto a single mastercurve for all combinations of chain lengths, and for both types of complex coacervates. We use salt concentration-dependent shift factors for the frequency (τ_c) and for the moluli (G_c). The reference condition for all chain

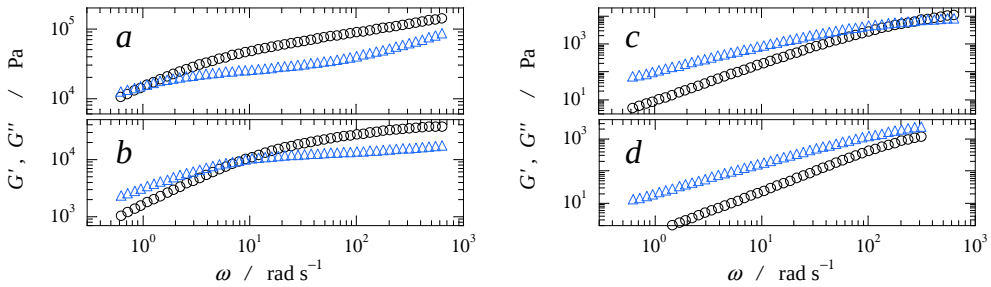

Figure 8.2: Frequency sweeps of a $PDMAEMA_{527}/PAA_{500}$ complex coacervates at $\gamma = 2\%$ and different salt concentrations: (a) 0.50 M, (b) 0.85 M, (c) 1.05 M, (d) 1.2 M. Both storage (○) and loss (△) moduli are shown.

lengths is chosen such that the cross-over between G' and G'', as extrapolated from the low-frequency viscous limit in the frequency sweeps, occurs at a rescaled frequency $\omega\,\tau_c = 1$ and a rescaled modulus $G'/G_c = G''/G_c = 1$. The superposition in Figure 8.3 implies that all relevant dynamic processes in these complex coacervates respond similarly to a change in salt concentration. This important implication enables us to probe the dynamics of these complex coacervates over more than seven decades in frequency.

The limits of the accessible dynamic range are dictated by a combination of instrumental and thermodynamic factors. The upper limit is given by the maximum accessible frequency of the rheometer and a theoretical minimum salt concentration close to zero. In practice, the minimum salt concentration is higher and the upper frequency limit is lower, because both polyelectrolytes carry their own counterions, which are released on complexation, and because the dynamics of formation and equilibration becomes so slow at very low salt concentration that the complex coacervates may not reach their equilibrium structure and composition within experimental timescales. The lower frequency limit is given by the critical salt concentration, beyond which complex coacervates no longer form (see Chapter 3). In this case, we further extend the dynamic range to lower frequencies using a step-stress (creep) experiment. Data of creep compliance versus time can be converted into frequency-dependent storage and loss moduli using a direct relation.[13]

If all dynamic processes in these complex coacervates respond similarly to a change in salt concentration, we expect that they can be used to rescale nonlinear flow measurements as well. Indeed, Figure 8.4a shows that both linear and nonlinear regimes of strain rate sweeps (flow curves) at various salt concentrations can be rescaled using the same shift factors as in Figure 8.3 for all chain lengths. The flow curves all start with a Newtonian regime, followed by a nonlinear regime of strong shear thinning, which becomes more pronounced at low salt concentrations.

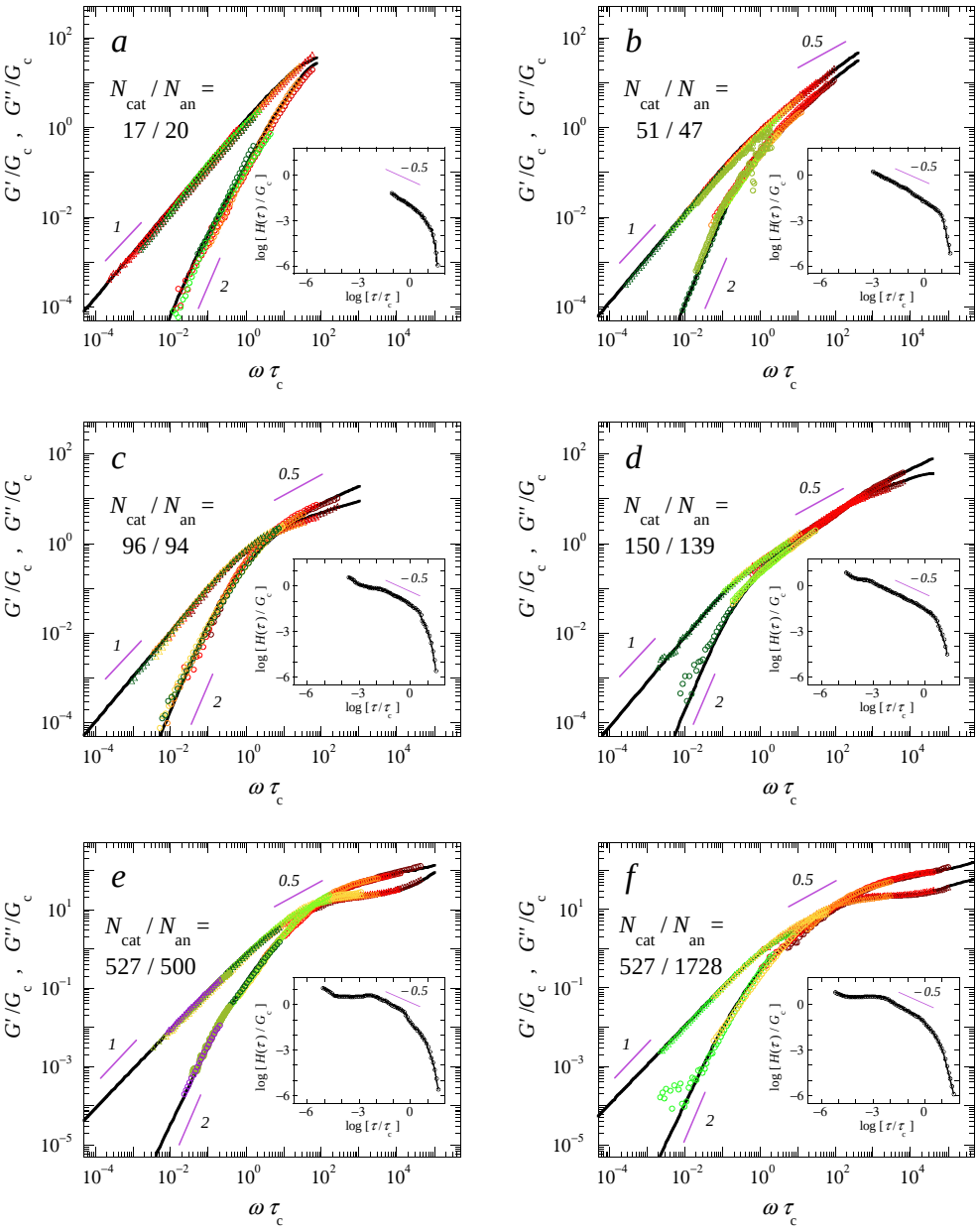
a
N cat / N an =
17 / 20
b
N cat / N an =
51 / 47
c
N cat / N an =
96 / 94
d
N cat / N an =
150 / 139
e
N cat / N an =
527 / 500
f
N cat / N an =
527 / 1728
G' /G c , G'' /G c
ω τ c
log [H(τ) / G c]
log [τ / τ c]
0.5
1
2
−0.5

Figure 8.3: (previous page) Rescaled frequency sweeps of complex coacervates of different polymer chain lengths: N_{cat}/N_{an} = (a) 17/20, (b) 51/47, (c) 96/94, (d) 150/139, (e) 527/500, (f) 527/1728. The axes have been rescaled using salt-dependent shift factors for the frequency τ_c, and for the moduli G_c. The $N_{cat}/N_{an} = 96/94$ complex coacervates consist of PTMAEMA and PSPMA, respectively. All other complex coacervates consist of PDMAEMA and PAA, at pH 6.5. For all frequency sweeps a strain amplitude of 5% or less was applied. Storage moduli are indicated by circles (○), loss moduli by triangles (△). The solid lines are fits of the frequency sweeps to a sum of Maxwell elements, with relaxation spectra displayed in the insets, and will be discussed in detail in Chapter 9.

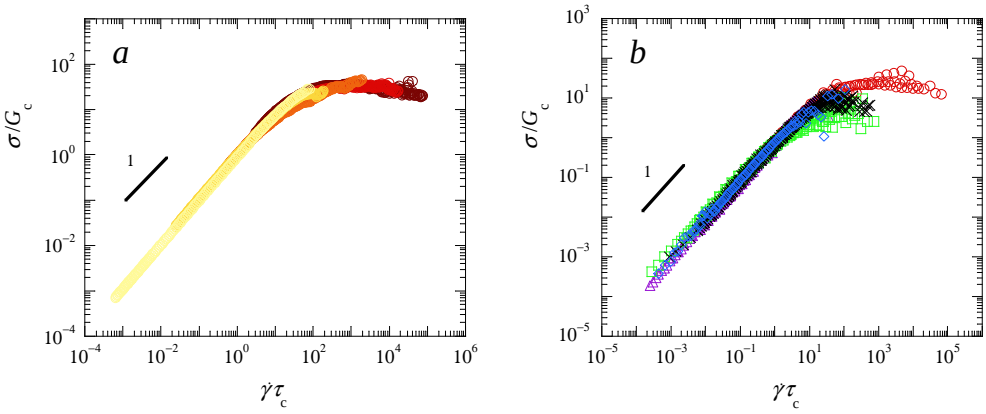

Figure 8.4: (a) Rescaled flow curves for $PDMAEMA_{527}/PAA_{500}$ complex coacervates, using the same shift factors as in Figure 8.3. (b) Rescaled flow curves complex coacervates of other chain lengths: N_{cat}/N_{an} = 17/20 (△), 51/47 (◇), 96/94 (×), 150/139 (□) and 527/500 (○, same as in (a)). The $N_{cat}/N_{an} = 96/94$ complex coacervates consist of PTMAEMA and PSPMA, respectively. All other complex coacervates consist of PDMAEMA and PAA, at pH 6.5. For reasons of clarity, one per five data points is shown.

The shear thinning regime is characterised by large intermittent stress fluctuations (see Figure 8.5), reminiscent of classical hydrophobically associating networks,[14] followed by shear fracture at some unpredictable shear rate that varies between measurements. On shear fracture, the shear stress typically drops by orders of magnitude and part of the sample is expelled from the gap between cone and plate. We discarded all measured points after shear fracture had taken place. In regimes with fluctuating stresses before shear fracture, we verified that the sometimes periodic fluctuations do not originate from the frequency of rotation. We then took the long-time average stress as the steady state stress for Figure 8.4. Interestingly, similar strong shear thinning, and possibly also stress fluctuations and eventual shear fracture, have been observed in other complex coacervates too.[12,15,16]

As shown in Figure 8.4b, the same rescaling can be applied to polyelectrolytes of different chain lengths, and even to a different set of polyelectrolytes ($PTMAEMA_{96}$/

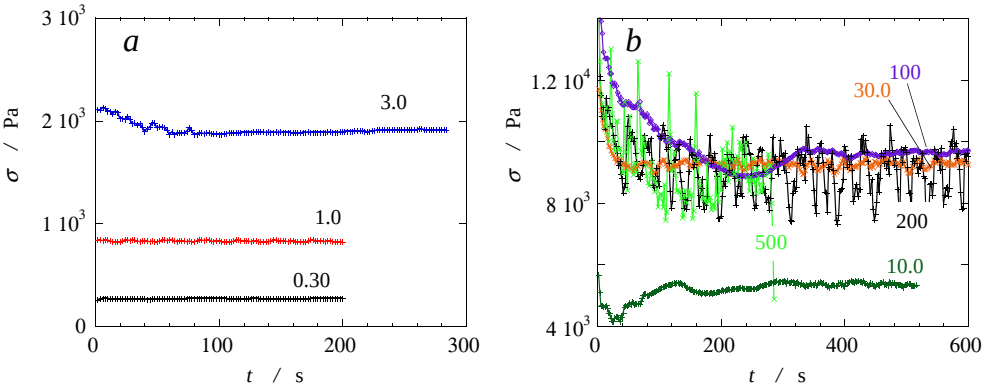

Figure 8.5: Stress fluctuations during steady shear flow measurements of $PDMAEMA_{527}/PAA_{500}$ complex coacervates at $c_s = 0.85$ M, measured in a cone-plate geometry. The labels indicate shear rates in s^{-1}.

$PSPMA_{94}$). A close inspection of the curves reveals that the onset of the nonlinear regime is not exactly the same for all chain lengths. This can be explained by the fact that polymer concentrations in these complexes are not completely independent of chain length (see Chapter 3), and higher order Rouse modes (see Chapter 9) and entanglements become more important for longer polymers.

8.3.3 Molecular mechanism underlying salt-dependent dynamics

Our observation that both linear and nonlinear rheological data can be superimposed using two salt-dependent shift factors, τ_c and G_c, suggests that a simple mechanism underlies the dynamics of these charge-driven complexes. Figure 8.6 shows that there is a strong dependence of the apparent relaxation time, τ_c and a much weaker dependence of the modulus, G_c, on salt concentration for all chain lengths.

The depicted dependence of τ_c and G_c is closely related to the stress relaxation mechanism inside the complex coacervates. These complex coacervates can be seen as concentrated two-component polymer solutions. Stress relaxation occurs by movement of chains, which is hindered by associations in the form of ion-ion pairs (ionic bonds) between two oppositely charged polyelectrolytes. These bonds act as 'sticky' points that enhance the effective friction of polymer chains and slow down their mobility.[17] This suggests that the dynamics of chains with sticky points should apply, for which[17]

$$\tau_c \approx N^{\alpha}\, {\phi_p}^{\beta}\, \zeta_0(c_s) \tag{8.1}$$

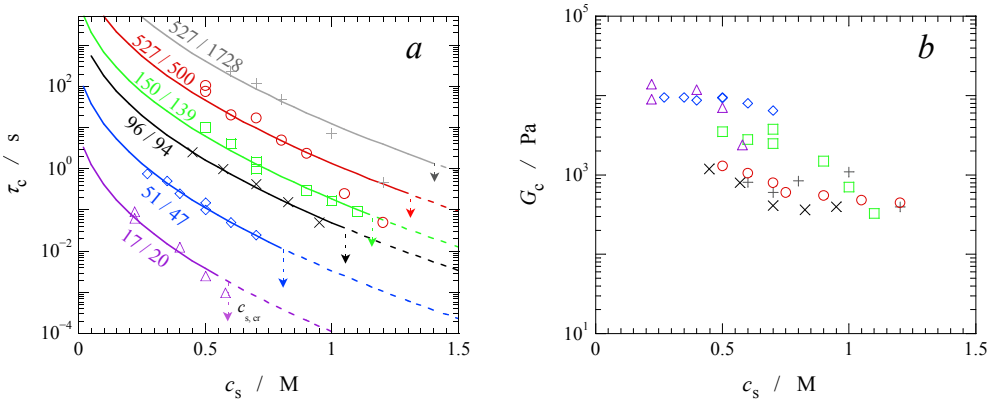

Figure 8.6: (a) Relaxation times τ_c as shift factors for frequency and shear rate and (b) moduli G_c as shift factors for storage moduli, loss moduli and shear stresses. Symbols represent different combinations of polymer chain lengths and polymer types: N_{cat}/N_{an} = 17/20 (△), 51/47 (◇), 96/94 (×), 150/139 (□), 527/500 (○) and 527/1728 (+). The N_{cat}/N_{an} = 96/94 complex coacervates consist of PTMAEMA and PSPMA, respectively. All other complex coacervates consist of PDMAEMA and PAA, at pH 6.5. Solid lines in (a) are fits to equation 8.4. The boundary between the dashed and solid parts of the fits and the arrows indicate the critical salt concentrations for each polymer combination.

where N is the polymer chain length, ϕ_p is the polymer volume fraction and ζ_0 is an effective friction coefficient, which depends on salt concentration. The magnitude of α depends on the regime of relaxation: for Rouse-like relaxation $\alpha = 2$, for reptation $\alpha = 3.4$. The magnitude of β depends somewhat on solvent quality, but is typically close to unity.[17] Breaking of association points in these complex coacervates is related to the dissociation of ion-ion pairs. We assume this is an activated process, governed by an energy barrier E_a,

$$\zeta_0(c_s) = \frac{1}{\omega_0} \exp\left(\frac{E_a(c_s)}{k_B T}\right) . \tag{8.2}$$

Reorganisation of associations encompasses breaking of polymeric ion-ion pairs, separating each two ionic groups, thereby surrounding them with monovalent counterions, and reforming polymeric ion-ion pairs at different positions (see Figure 8.7). This route contains an energy barrier that can be estimated as the difference between the Coulombic energy of two ion-ion pairs in contact (E_{Coul}) and the electrical free energy of four separated ionic groups of charge $\pm e$ in an electrolyte solution (E_{corr}): $E_a \approx E_{corr} - E_{Coul}$.

We write the electrical energy of the four separated ionic groups in an electrolyte solution using the Debye-Hückel approximation: $E_{corr}/k_B T \approx -4{z_i}^2 e^2/8\pi\epsilon_r\epsilon_0 k_B T = -2\kappa\ell_B \propto \sqrt{c_s}$,[18] where κ^{-1} is the Debye length, defined for the monovalent KCl

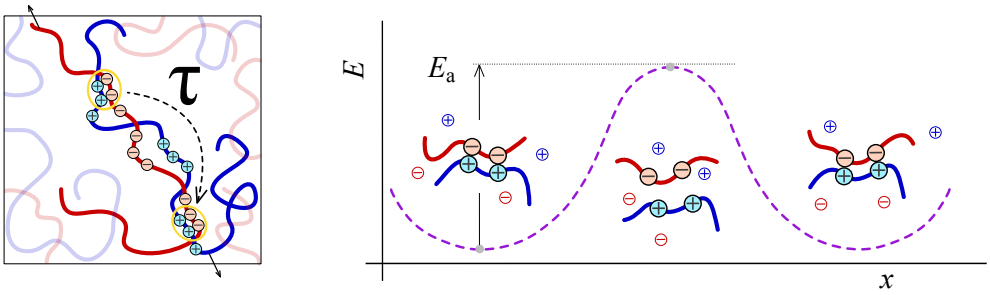

Figure 8.7: Schematic illustration of the suggested microscopic mechanism and corresponding energy diagram underlying stress relaxation in complex coacervates.

salt as $\kappa^2 = 8\pi\ell_B N_{Av} c_s$, with c_s the salt concentration in mM and $\ell_B = e^2/4\pi\epsilon_r\epsilon_0 k_B T$ the Bjerrum length, which is 0.71 nm in pure water.

The effective Coulombic energy for two ion-ion pairs can be written as: $E_{Coul}/k_BT = -2e^2/4\pi\epsilon_r\epsilon_0 k_B T d = -2\ell_B/d$, where d is the effective contact distance of the charged groups. Our final expression for the energy barrier, corresponding to the process depicted in Figure 8.7, can be written as

$$\begin{aligned} \frac{E_a}{k_BT} &= -2\kappa\ell_B + \frac{2\ell_B}{d} \\ &= -\frac{\sqrt{2\times10^3 N_{Av}}\, e^3}{2\pi(\epsilon_r\epsilon_0 k_B T)^{3/2}}\sqrt{c_s} + \frac{e^2}{2\pi\epsilon_r\epsilon_0 k_B T d} = -2a_s\sqrt{c_s} + 2b_s\,. \end{aligned} \tag{8.3}$$

Combining with Equation 8.1, we find

$$\tau_c \propto {\omega_0}^{-1} {N^\alpha}{\phi_p}^\beta \exp\left(-2a_s(T)\sqrt{c_s} + 2b_s(T)\right) \tag{8.4}$$

where $a_s(T) = \sqrt{8\times10^3\pi N_{Av}{\ell_B}^3}$, c_s is the ionic strength in mol/L for a 1 : 1 electrolyte, $b_s(T) = \ell_B/d$, and the factor 2 accounts for the fact that rearrangements involve two ion-ion pairs that exchange their partners.

Equation 8.4 predicts that the energy barrier for ion-ion pair rearrangements in complex coacervates depends on the square root of salt concentration, leading to a stretched exponential dependence of τ_c on c_s. We have previously found that also ϕ_p depends weakly on c_s (see Chapter 3). This dependence is however significantly weaker than the variations in τ_c shown in Figure 8.6. The relaxation times presented in Figure 8.6a have therefore been fitted to Equation 8.4, using only an adjustable prefactor ($B = {\omega_0}^{-1} {N^\alpha}{\phi_p}^\beta e^{b_s(T)}$), and a fixed value of 6 for $a_s(T)$. We find good agreement between our data and the presented model for all chain lengths. Moreover, the value of $a_s(T)$ we have used is quantitatively in agreement with the theoretical value of

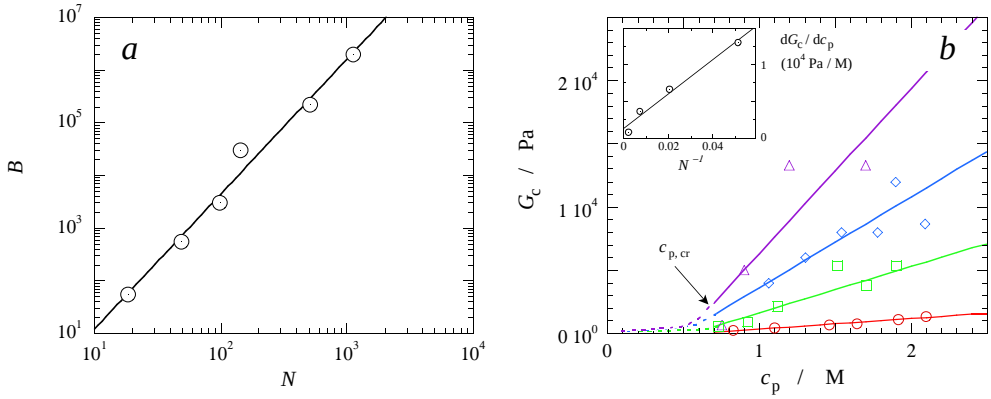

Figure 8.8: (a) Prefactors B versus average polymer chain length $N = (N_{\mathrm{cat}} + N_{\mathrm{an}})/2$. (b) Modulus shift factors versus c_{p} in M monomer units, estimated from Figure 3.7, suggesting a linear relation between G and ϕ_{p}. High c_{p} correspond to low salt concentrations and vice versa. At the critical point, the polymer concentration goes to zero. The inset shows the approximate linear dependence between the slopes of the linear fits $\mathrm{d}G_{\mathrm{c}}/\mathrm{d}c_{\mathrm{p}}$ on N^{-1}.

5.9 for $\epsilon_{\mathrm{r}} = 43$ and $T = 293$ K, which is a reasonable assumption for concentrated complex coacervates at high salt concentrations (see also Chapter 3).[19]

Finally, we find that the prefactors B scale according to N^{α}, with $\alpha \approx 2.5$ (see Figure 8.8a).

In contrast to the relaxation times, we find that the typical complex coacervate moduli G_{c} depend only weakly on c_{s} (see Figure 8.6b). This weak dependence is due to the coupling between salt concentration and overall polymer density, as was shown in Chapter 3.

We can calculate polymer concentrations that correspond to the salt concentrations in Figure 8.6 using the experimentally determined phase diagram for these complex coacervates (see Chapter 3). We find that the moduli G_{c} increase linearly with polymer concentration for all chain lengths, as illustrated in Figure 8.8b. The slopes in this figure are inversely proportional to N, as is indicated in the inset. This scaling $G_{\mathrm{c}} \propto \phi_{\mathrm{p}}/N$ is expected for semidilute solutions of unentangled polymers, as we believe is the case here. In simple models, such as the Rouse model we have applied in Equation 8.1, every polymer chain contributes $k_{\mathrm{B}}T$ to the modulus at the terminal relaxation time, implying $G \propto \phi_{\mathrm{p}}$. Both the dependence on polymer concentration and the dependence on chain length will be discussed in more detail in Chapter 9, where we analyse the complete relaxation spectrum of these polyelectrolyte complex coacervates.

A key assumption in our conceptual mechanism is that an activated dissociation of ion-ion pairs governs the relaxation dynamics of charge-driven materials. Con-

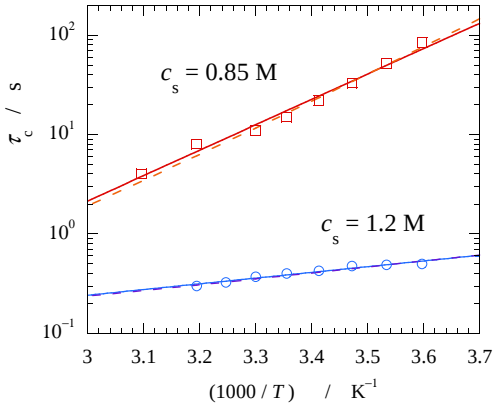

Figure 8.9: Relaxation times τ_c at different temperatures, plotted as $1000/T$, for $PDMAEMA_{527}/PAA_{500}$ complex coacervates at two different salt concentrations c_s. The solid lines are linear fits of $\log \tau_c$ to $\exp(T^{-1})$, dashed lines are linear fits of $\log \tau_c$ to $\exp(T^{-1.5})$.

sequently, τ_c should be a function of temperature as well. We verify this in a classical time-temperature superposition experiment, where we determine relaxation times as a function of temperature (see Figure 8.9).[(i)] Assuming that $\epsilon_r\epsilon_0$ is independent of T at the high salt concentrations we use,[19] we expect τ_c to be proportional to $\exp(T^{-1})$ or $\exp(T^{-1.5})$ as the two limiting cases (Equation 8.4). The fits in Figure 8.9 for $\exp(T^{-1})$ (solid lines) and $\exp(T^{-1.5})$ (dashed lines), show that it is experimentally not possible to distinguish between these limiting cases for aqueous systems. In any case, τ_c is a clear function of temperature and the relaxation mechanism is indeed governed by an activated process.

8.3.4 Time-salt superposition in charge-driven gels

The presented analysis of the dynamics in complex coacervates provides a general tool to study dynamics in other soft materials that are assembled by charge-driven complexation. To support this generality, we follow the same approach for a transient network formed by telechelic polymers.[7,11] This network is made from $A_xB_yA_x$ triblock copolymers with charged end-blocks that are complexed with oppositely charged homopolymers (C_z). Small complex coacervate domains of A-blocks and C-homopolymers form the nodes of this network, while the neutral and soluble B-blocks

[(i)] We note that these complex coacervates become turbid upon heating (see Chapter 4), due to excretion of small droplets of dilute phase. We did not account for that in these TTS measurements.

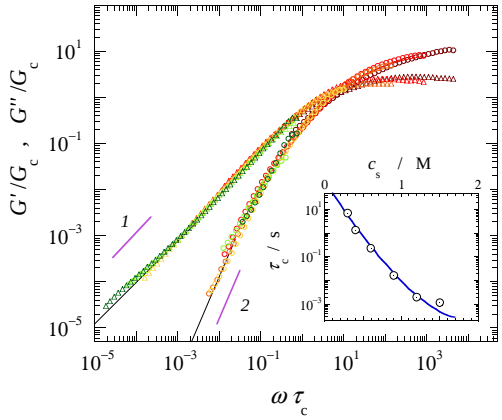

Figure 8.10: Rescaled frequency sweeps of a telechelic network of $PSPMA_{28}$–PEO_{230}–$PSPMA_{28}$ and PAH_{68} at $\gamma = 5\%$. Storage moduli are shown using circles, loss moduli using diamonds. The inset shows τ_c as a function of c_s.

form the links between the nodes. We find that frequency sweeps of these networks at different salt concentrations can be rescaled onto a single mastercurve as well, as shown in Figure 8.10. Using superposition we can now access over eight decades in frequency and study the typical relaxation behaviour at different salt concentrations (see Lemmers et al.[11] for more details).

8.4 Concluding remarks

The dynamics of charge-driven materials, such as complex coacervates, depends strongly on salt concentration. A detailed understanding of these effects requires an effective method to probe the widely varying dynamic behaviour of charge-driven materials at different salt concentrations. By rescaling rheological data with salt-dependent shift factors one can probe linear and nonlinear mechanical properties of these materials over a wide range of, otherwise inaccessible, timescales and hence study the salt dependence of their relaxation mechanisms. We call this type of rescaling 'time-salt superposition' (TSS).

References

[1] J. Widom, *Ann. Rev. Biophys. Biomol. Struct.*, 1998, **27**, 285–327.
[2] A. Perico, G. La Penna, and L. Arcesi, *Biopolymers*, 2006, **81**, 20–28.
[3] C. Herold, P. Schwille, and E. P. Petrov, *Phys. Rev. Lett.*, 2010, **104**, 148102.

[4] M. B. Sankaram and D. Marsh, in *Protein-Lipid Interactions*, ed. A. Watts, Elsevier, 1993, ch. Protein-lipid interactions with peripheral membrane proteins, pp. 127–167.

[5] M. F. Perutz, *Science*, 1978, **201**, 1187–1191.

[6] M. E. Leunissen, C. G. Gristova, A.-P. Hynninen, C. P. Royall, A . I. Campbell, A. Imhof, M. Dijkstra, R. van Roij, and A. van Blaaderen, *Nature*, 2005, **437**, 235–240.

[7] M. Lemmers, J. Sprakel, I. K. Voets, J. van der Gucht, and M. A. Cohen Stuart, *Angew. Chem. Int. Ed.*, 2010, **49**, 708–711.

[8] M. A. Cohen Stuart, B. Hofs, I. K. Voets, and A. de Keizer, *Curr. Opin. Coll. Int. Sci.*, 2005, **10**, 30–36.

[9] J. D. Ferry, *Viscoelastic properties of polymers*, John Wiley & Sons Inc., 3rd edn., 1980.

[10] H. M. Wyss, K. Miyazaki, J. Mattsson, Z. Hu, D. R. Reichman, and D. A. Weitz, *Phys. Rev. Lett.*, 2007, **98**, 238303.

[11] M. Lemmers, E. Spruijt, L. Beun, R. Fokkink, F. A. M. Leermakers, G. Portale, M. A. Cohen Stuart, and J. van der Gucht, *Soft Matter*, 2012, **8**, 104–117.

[12] R. C. W. Liu, Y. Morishima, and F. M. Winnik, *Pol. J.*, 2002, **34**, 340–346.

[13] R. M. L. Evans, M. Tassieri, D. Auhl, and T. A. Waigh, *Phys. Rev. E*, 2009, **80**, 012501.

[14] J. Sprakel, E. Spruijt, M. A. Cohen Stuart, N. A. M. Besseling, M. P. Lettinga, and J. van der Gucht, *Soft Matter*, 2008, **4**, 1696–1705.

[15] J. H. E. Hone, A. M. Howe, and T. Cosgrove, *Macromolecules*, 2000, **33**, 1199–1205.

[16] V. E. Dreval, G. B. Vasil'ev, E. A. Litmanovich, and V. G. Kulichikhin, *Pol. Sci. A*, 2008, **50**, 751–756.

[17] M. Rubinstein and A. N. Semenov, *Macromolecules*, 2001, **34**, 1058–1068.

[18] T. L. Hill, *An introduction to statistical thermodynamics*, Dover Publications Inc., 1986.

[19] D. V. Loginova, A. S. Lileev, and A. K. Lyashchenko, *Russ. J. Inorg. Chem.*, 2002, **47**, 1426–1433.

Chapter 9

Linear viscoelasticity of polyelectrolyte complex coacervates

In this Chapter we study the linear viscoelastic properties of a model system of polyelectrolyte complex coacervates. We investigate the effects of salt concentration, chain length, chain length matching and mixing stoichiometry on the structure, relaxation behaviour, viscosity and mechanical properties of the complex coacervate networks. In our analysis, we treat clusters of ionic bonds as sticky points. Salt is a plasticiser for these cross-links and affects all relaxation processes in the same way. We can use time-salt superposition (Chapter 8) to rescale all dynamic viscoelastic measurements and we find that there is a remarkable resemblance between the relaxation time spectra of these complex coacervates and the sticky Rouse model for single-component polymer systems.

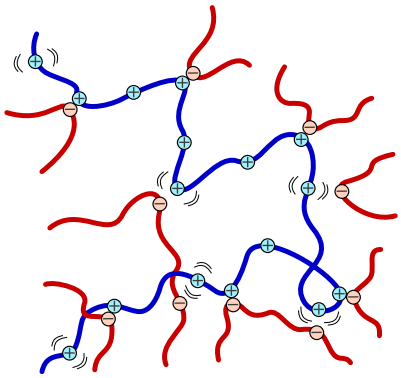

This Chapter is submitted for publication in a slightly modified form as:
E. Spruijt, M. A. Cohen Stuart and J. van der Gucht, *Linear viscoelasticity of polyelectrolyte complex coacervates*, Macromolecules.

9.1 Introduction

Complex coacervates are dense, liquid-like phases of oppositely charged hydrophilic colloids. They have rich but poorly understood viscoelastic properties. Most complex coacervates are highly viscous, but salt can change the viscosity significantly. The origin of this strong salt dependence of viscosity and other mechanical properties lies in the strong attractive interactions between oppositely charged groups. Salt is a plasticiser for these cross-links and affects all relaxation processes in the same way (Chapter 8) In this Chapter, we further explore time-salt superposition to elucidate the full stress relaxation spectrum and get insight into the dynamic structural properties of PDMAEMA/PAA complex coacervates as a model system for many charge-driven soft materials.

Previous reports on the rheology of complex coacervates mostly focus on soluble complexes in aqueous solution, because of their potential application as vehicles for drug delivery.[1,2] These complexes are typically formed at very low salt concentrations and a mixing ratio far outside the region where associative phase separation takes place (see Chapter 3). Dilute solutions of soluble complexes have a slightly increased zero shear viscosity compared to solutions with only one type of polymer and show moderate shear thinning behaviour at very high shear rates.[1,2] In concentrated polyelectrolyte solutions, well above the entanglement concentration, addition of small amounts of an oppositely charged polyelectrolyte leads to a more pronounced increase in viscosity and in both shear moduli, but the underlying relaxation mechanisms remain unclear.[3] On the other hand, in three studies on phase separated complex coacervates of proteins and flexible polymers molecular models for the complexes have been proposed based on the rheological measurements. In all models, the proteins form junction points in a network of flexible polyelectrolytes.[4–6] The strength of the junction points varies from weak and reversible[4,5] to nearly permanent,[6] depending on the type and charge density of the protein and the salt concentration in solution. A similar structural model was proposed based on rheological measurements of complex coacervates of laponite and flexible polyelectrolytes, with laponite disks acting as junction points.[7]

When complexes are formed between two flexible polyelectrolytes, the structure of the complex might be significantly different from the structure of a protein-polyelectrolyte complex.[4–6] Junction points between two flexible polyelectrolytes can span a much wider range of sizes, and they may become much tighter, due to the high charge density of some polyelectrolytes. In order to obtain insight in the dynamic properties of these flexible complex networks, we investigate the linear rheology of a model polyelectrolyte complex coacervate of two flexible polyelectrolytes. We focus on the effect of salt, polymer chain length, chain length matching and mixing stoichiometry. Finally, we discuss to what extent our understanding of the

rheological behaviour can be used to elucidate the microscopic structure of these flexible polyelectrolyte complexes.

9.2 Experimental details

9.2.1 Materials

We used a combination of oppositely charged polyelectrolytes with pH-dependent charges, with PDMAEMA (N_{cat} = 17, 51, 150 and 527) as polycation, and PAA (N_{an} = 20, 47, 139, 500 and 1728) as polyanion. The specifications of these polymers, the details of their pH-dependent charging and the phase behaviour of their complex coacervates are described in Chapter 3.

9.2.2 Complex coacervate formation

We made complex coacervates of PDMAEMA and PAA from 50 g/L and 30 g/L stock solutions, respectively. We prepared the complex coacervates at a 1 : 1 ratio of monomeric groups in aqueous solutions, unless stated otherwise, with varying salt concentrations (KCl), as described in Chapters 3 and 4. In all cases, we prepared a total volume of 4.0 mL with an overall polymer concentration of 0.20 M, measured in monomer units. The complex coacervate phase had a volume of approximately 0.8 mL. For rheological measurements, we separated the dilute phase from the complex coacervate and loaded the complex coacervate phase onto the rheometer.

9.2.3 Rheological measurements

All rheological measurements were carried out on Anton Paar MCR301 and MCR501 stress-controlled rheometers using a cone-plate geometry with a cone radius of 25 mm and a cone angle of 1°. We kept the temperature controlled at 20 °C with Peltier elements and we used an evaporation blocker to minimise water evaporation. With every sample, we performed a series of measurements, all separated by a waiting step that is at least five times longer than the apparent longest relaxation time we found in a step-strain experiment. We made sure that the total duration of a measurement series never exceeded five hours to ensure that the slow solvent evaporation that occurs despite our use of an evaporation blocker, had a negligible effect on the rheological measurements, as verified by repeating frequency sweep measurements at the beginning and end of the measurement series.

We studied the relaxation behaviour of these complex coacervates by both step-strain, creep (step-stress) and frequency sweep experiments, to cover a range of timescales from milliseconds (frequency sweep) to hours (step-strain). In all measurements

we applied a maximum deformation γ that is in the linear viscoelastic regime, which extends to deformations of approximately 100% (see Figure 8.1).

9.2.4 Interconversion between linear viscoelastic functions

We calculated relaxation spectra $H(\tau)$ from step-strain and frequency sweep experiments by approximating the relaxing complex coacervates as a sum of Maxwell elements:

$$G(t) = \sum_{i=0}^{M} G_i \, e^{-t/\tau_i} \,, \tag{9.1}$$

$$G'(\omega) = \sum_{i=0}^{M} \frac{G_i \, \omega^2 \tau_i^2}{1 + \omega^2 \tau_i^2} \,, \tag{9.2}$$

$$G''(\omega) = \sum_{i=0}^{M} \frac{G_i \, \omega \tau_i}{1 + \omega^2 \tau_i^2} \tag{9.3}$$

where the M relaxation modes, defined by their relaxation strength G_i and their relaxation time τ_i, were taken equally spaced on a logarithmic scale.[8] The corresponding relaxation spectra $H(\tau)$ of the complex coacervates were obtained by iterative fitting of both the relaxation modulus $\log G(t)$, and the storage $\log G'(\omega)$ and loss modulus $\log G''(\omega)$, using a least squares approximation, and are defined by[9,10]

$$H(\tau) = \sum_{i=0}^{M} G_i \, \delta \left(1 - \frac{t}{\tau_i} \right) \tag{9.4}$$

where $\delta(x)$ denotes the Dirac delta function. We confirmed that our fitting yields typical relaxation spectra, characteristic for the complex coacervates we studied, in two ways. First of all, we checked that the feedback loop in the stress-controlled rheometer allows carrying out the step-strain measurements with sufficient accuracy, by converting our step-strain measurements $G(t)$ into creep functions $J(t)$ using the numerical Hopkins-Hamming method for the convolution integral of the relaxation modulus and creep compliance:[11]

$$\int_0^t \phi(\tau)\psi(t-\tau) \, \mathrm{d}t = 1 \tag{9.5}$$

where $\psi(t)$ is the normalised relaxation modulus $G(t)/G(0)$ and $\phi(t)$ is the normalised creep compliance $J(t)/J(0)$. We compared the converted creep functions to experi-

mentally measured creep curves and found they agree well, predicting equal terminal relaxation times and viscosities.

Secondly, we converted storage moduli $G'(\omega)$ and loss moduli $G''(\omega)$ directly into relaxation spectra $H(\tau)$ using approximate relations between these functions, according to Williams and Ferry.[12] The relation between the relaxation spectrum and the local derivative $\mathrm{d}\log G'(\omega)/\mathrm{d}\log\omega$ of the storage modulus depends on the slope of the relaxation spectrum $m = -\mathrm{d}\log H(\tau)/\mathrm{d}\log\tau$. For regions with a (negative) slope $m < 1$

$$H(\tau) = A_1(m)\, G'(\omega) \left.\frac{\mathrm{d}\log G'(\omega)}{\mathrm{d}\log\omega}\right|_{\frac{1}{\omega}=\tau} \tag{9.6}$$

where the correction factors $A_1(m)$ are defined by

$$A_1(m) = \frac{2-m}{2\,\Gamma(2-m/2)\,\Gamma(1+m/2)} = \frac{\sin(m\pi/2)}{m\pi/2} \tag{9.7}$$

where $\Gamma(x)$ is the Gamma function. For the regions with a slope $1 < m < 2$:

$$H(\tau) = A_2(m)\, G'(\omega) \left(2 - \left.\frac{\mathrm{d}\log G'(\omega)}{\mathrm{d}\log\omega}\right)\right|_{\frac{1}{\omega}=\tau} \tag{9.8}$$

where the correction factors $A_2(m)$ are defined by

$$A_2(m) = \frac{m}{2\,\Gamma(2-m/2)\,\Gamma(1+m/2)} = \frac{\sin(m\pi/2)}{\pi(1-m/2)} \tag{9.9}$$

Similarly, the relaxation spectrum is related to the local slope of the loss modulus $\mathrm{d}\log G''(\omega)/\mathrm{d}\log\omega$ by

$$H(\tau) = B(m)\, G''(\omega) \left(1 - \left.\left|\frac{\mathrm{d}\log G''(\omega)}{\mathrm{d}\log\omega}\right|\right)\right|_{\frac{1}{\omega}=\tau} \tag{9.10}$$

where the correction factors $B(m)$ are defined by

$$B(m) = \frac{1+|m|}{2\,\Gamma(3/2-|m|/2)\,\Gamma(3/2+|m|/2)} = \frac{\sin(\pi(1+|m|)/2)}{\pi(1-|m|)/2} \tag{9.11}$$

Calculation of the relaxation spectra according to Equations 9.6 to 9.11 is an iterative procedure as well. First, all correction factors $A(m)$ and $B(m)$ were set to unity and $H(\tau)$ was calculated to first approximation from the frequency sweeps. We then calculated the first order corrections from the local derivative of $\log H(\tau)$ versus $\log\tau$. We repeated this step until we found a self-consistent solution for $H(\tau)$.

9.3 Results and discussion

9.3.1 Relaxation dynamics in matched complexes

The phase behaviour of complex coacervates of PDMAEMA and PAA depends both on salt concentration and on chain length. The polymer volume fraction inside the complexes varies between 0.05 and 0.3 (effective concentration of monomeric units c_p = 0.5 – 3 M),[13] whereas the overlap concentration varies between c_p^* = 0.01 and 0.1 M, depending on the chain length (N = 1728 – 20, assuming random walk statistics in the complex coacervates). By analogy with ordinary polymer solutions, these complex coacervates are typically in a concentration range between semidilute and concentrated. However, because of the sometimes strong interactions between the two polymeric components, their rheological behaviour is very different from solutions of the individual polymers at the same concentration.

Figure 9.1a shows the relaxation moduli $G(t)$ of polyelectrolyte complex coacervates in which the polycation length is matched closely to the polyanion length (0.85 < N_{cat}/N_{an} < 1.1), and one for which the polyanion is significantly longer than the polycation (N_{cat}/N_{an} = 527/1728). The salt concentration was varied from a lower limit of 0.40 M to the critical salt concentration as an upper limit. Curves corresponding to the same combination of chain lengths are shifted vertically using the same prefactor for clarity.

At all timescales up to the terminal relaxation time, we clearly find a continuous decrease of the relaxation modulus $G(t)$ in all curves, indicating that relaxation processes occur on all timescales between tens of milliseconds and the terminal relaxation time. The terminal relaxation time in itself increases with increasing chain length and decreasing salt concentration. Neither chain length nor salt concentration has a strong effect on the shape of the relaxation curve in between the terminal relaxation time and the inertial lower limit. In fact, all curves seem to exhibit a regime with a constant slope, close to −0.5, in which the modulus scales as $G(t) \sim (t/\tau)^{-0.5}$. At short times, this regime is bound by a levelling off to a presumed plateau, for the lowest salt concentrations and longest chain lengths.

The relaxation time spectra that correspond to these step-strain experiments show the same characteristics (see Figure 9.1b). Such relaxation behaviour is characteristic for Rouse dynamics of polymer chains.[12,14] For ideal chains, the predicted slope of both $\log G(t)$ versus $\log t$ and $\log H(\tau)$ versus $\log \tau$ is $-1/2$.[14] From the neutron scattering experiments described in Chapter 7, we know that the polyelectrolytes in PDMAEMA/PAA complex coacervates have a conformation close to that of an ideal chain. Indeed, the relaxation moduli and relaxation spectra in Figure 9.1 all exhibit a regime with a slope close to −0.5.

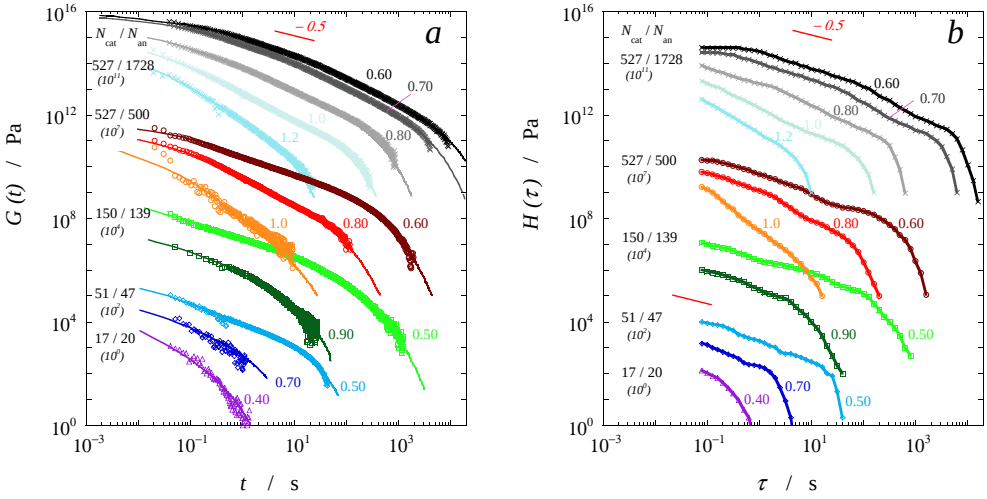

Figure 9.1: (a) Stress relaxation modulus of PDMAEMA/PAA complex coacervates at different salt concentrations and for different polymer chain lengths. In all cases a step strain of 10 – 20% is applied. (b) Logarithmic relaxation time spectra of the same samples. The labels to the left of the curves (N_{cat}/N_{an}) indicate the chain length of the polycation and the polyanion respectively. All curves are shifted vertically for clarity using the shift factor that is shown in brackets to the left of the curves. The numbers at the right indicate overall salt concentrations (KCl, in M).

We note that our approach to calculate the relaxation spectra can also be applied to the frequency sweeps that were rescaled based on a time-salt superposition principle, depicted in Figure 8.3. The relaxation spectra shown in the insets of Figure 8.3 are very similar to the relaxation spectra shown in Figure 9.1b, which confirms their value in describing the relaxation behaviour of complex coacervates.

The relaxation spectra that were calculated from fits to a sum of Maxwell elements are in good agreement with the approximate relaxation spectra that were calculated from the corresponding storage and loss moduli directly. Figure 9.2a shows that all three approaches yield relaxation spectra that are identical to within experimental error. The advantage of using the fitting procedure to a sum of Maxwell elements is the fact that information from both frequency sweeps and relaxation moduli can be combined into the relaxation spectrum. The frequency sweeps generally provide more accurate measurements of short-time relaxation behaviour, whereas the relaxation moduli can probe long relaxation processes more accurately. As a result, the relaxation spectra calculated using Equations 9.1 to 9.3 (see Figure 9.2b) are limited as short times to several milliseconds by the highest measured frequency where inertia is still negligible in a frequency sweep experiment, and at long times by the terminal relaxation time measured in a step-strain experiment.

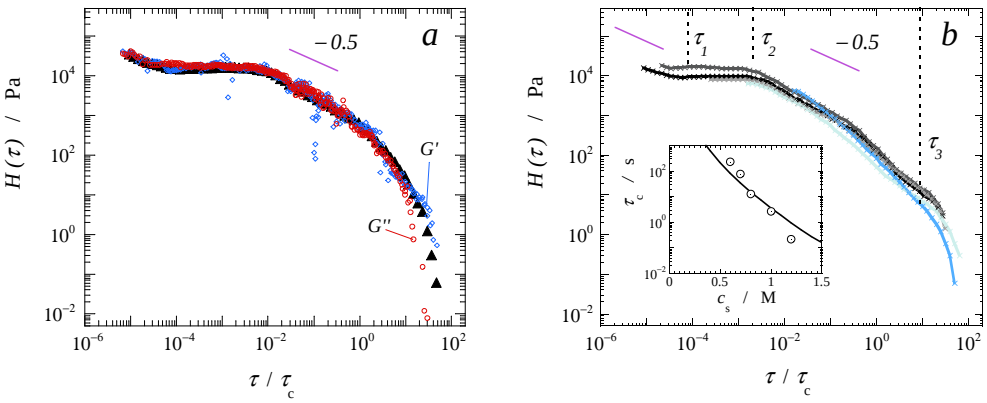

Figure 9.2: (a) Relaxation time spectrum, corresponding to the frequency sweep master curve, displayed in Fig. 4e in the main text, calculated by fitting both storage and loss modulus to a sum of Maxwell elements (), from the storage modulus data (Equations 9.6 and 9.7, ◇) and from the loss modulus data (Equations 9.10 and 9.11, ○). (b) Rescaled logarithmic relaxation time spectra of the $N_{cat}/N_{an} = 527/1728$ complex coacervates at different salt concentrations. The inset shows the time scaling factors τ_c as a function of salt concentration, with a fit to Equations 9.12 and 9.13.

9.3.2 Molecular relaxation model for matched complexes

Our observation of Rouse-like relaxation at timescales up to 1000 seconds is, at first sight, rather surprising. The typical timescales where Rouse dynamics are observed for ordinary polymer chains of similar length is orders of magnitude lower than the timescales where we observe Rouse-like dynamics.[12,15] We have shown in Chapter 8 that the short range attractive interactions between two oppositely charged polyelectrolytes give rise to the formation of ionic bonds. These bonds act as 'sticky' points that enhance the effective friction of polymer chains and slow down their mobility.[16] Since stress relaxation in these polymeric systems occurs by movement of chains, we expect ionic bonds to slow down the stress relaxation. We have approximated the average time these ionic bonds keep two oppositely charged segments in contact by an activated process:[16,17]

$$\tau_0 \approx \frac{1}{\omega_0} \exp\left(\frac{E_a(c_s)}{k_B T}\right) \tag{9.12}$$

where ω_0 is the relaxation rate in the absence of ionic bonds and where E_a represents the energy difference between the bound and unbound oppositely charged segments.[17] Following Chapter 8, we estimate the energy barrier from the process of rearrangement of two ion pairs (Figure 8.7):

$$\frac{E_a}{k_B T} = -2\kappa\ell_B + \frac{2\ell_B}{d} = -2a_s\sqrt{c_s} + 2b_s \tag{9.13}$$

where $\ell_B = e^2/4\pi\epsilon_r\epsilon_0 k_B T$ is the Bjerrum length, and d is the effective contact distance of an ionic bond. The constant $a_s = \sqrt{8\times10^3\pi N_{Av}\ell_B{}^3}$ and $b_s = \ell_B/d$. The factor 2 accounts for the fact that rearrangements in our model involve two ion pairs that exchange their partners.

In the complexes studied here the sticky points are present along the entire polymer chain. Consequently, broken bonds may easily reform with new partners and renormalisation of bond lifetimes may be neglected.[16] Moreover, when geometric positioning of the groups allows, several subsequent segments of a polymer chain may bind to another polymer chain to form sticky clusters with multiple ionic bonds. These cooperative clusters of bonds should have a proportionally higher bond energy, when no external force is applied to the bonds (see Chapter 11). However, we will see hereafter that these higher energy barriers seem not to play a role in the rheological behaviour of complex coacervates.

According to the sticky Rouse model, the stress relaxation modulus decays as a power-law at timescales that are much larger than for non-sticky polymers. The Rouse modes are given by

$$\tau_p \approx \tau_0 \left(\frac{f}{p}\right)^2 \quad 1 < p < f, \qquad \tau_R = \tau_0 f^2 \tag{9.14}$$

where f is the number of ionic bonds per chain. At short times ($p \approx f$), only small parts of the polymer chain are mobile and part of the stress can relax. As time progresses, more and more ionic bonds break and reform in different places and larger parts of the polymer chain become mobile. Finally, after some terminal Rouse time τ_R ($p = 1$), determined by the chain length and salt concentration, the whole polymer chain can move and all stress is relaxed. After the terminal relaxation time, we therefore expect an exponentially decreasing stress, as is observed in the relaxation curves in Figure 9.1a.

The modulus level at the Rouse time is roughly $k_B T$ per chain: $G(\tau_R) \approx k_B T\phi/Nb^3$. The modulus at the elementary lifetime of a single sticky point τ_0 is approximately $k_B T$ per sticky point. The full stress relaxation modulus can be approximated as

$$G(t) \approx \frac{k_B T}{b^3}\phi_p \left(\frac{t}{\tau_0}\right)^{-1/2} e^{-t/\tau_R} \tag{9.15}$$

where b is the Kuhn length and $\phi_p/b^3 N$ is the number density of chains. For all salt concentrations and chain lengths we find a regime in the stress relaxation modulus and in the relaxation spectrum that is in agreement with the mechanism we describe,

where the stress relaxation modulus and the relaxation spectrum have a constant slope, close to −0.5. In addition, we find similar signatures of the sticky Rouse mechanism underlying Rouse-like stress relaxation in frequency sweeps where $G'(\omega) \propto \omega^{0.5}$ and $G''(\omega) \propto \omega^{0.5}$ (see Figure 8.3).

An important consequence of Equations 9.12 and 9.13 is that salt affects all sticky Rouse modes in the same way. In other words, salt can be used as a plasticiser for the ionic bonds to access a different part of the relaxation spectrum of polyelectrolyte complexes, as we described in Chapter 8. Indeed, the relaxation spectra at different salt concentrations in Figure 9.1b can be rescaled by shifting along the τ-axis to obtain a relaxation spectrum mastercurve (see Figure 9.2b).

In the relaxation spectra in Figure 9.2b three regimes can be distinguished. At intermediate timescales ($\tau_2 < t < \tau_3$), we find a regime of Rouse-like stress relaxation, as described above. Just before the terminal relaxation time τ_3 the relaxation spectra fall off more rapidly than in the Rouse regime, most likely because all single ionic bonds have relaxed and only clusters of ionic bonds still contribute to the modulus.

At short timescales we observe a plateau ($\tau_1 < t < \tau_2$) and subsequent upturn ($t < \tau_1$) in the relaxation spectra of the longest polymer chains. Intuitively, we would attribute the onset of this plateau (τ_2) to the elementary lifetime of a single sticky point τ_0. Based on the relaxation spectrum in Figure 9.2b and the corresponding shift factors τ_c, the lifetime of a single ionic bond would be 200 ms at 0.6 M, which is of the same order of magnitude as the unperturbed ionic bond lifetimes we found in single molecule force spectroscopy measurements (see Chapter 11). From the modulus level at this single ionic bond lifetime $G(\tau_0) \approx k_B T\phi/b^3$ and the modulus level at the apparent Rouse time $G(\tau_R) \approx k_B T\phi f/Nb^3$, we estimate the number of ionic bonds per chain to be $10^2 - 10^3$ for $PDMAEMA_{527}/PAA_{500}$ complex coacervates, which is quite reasonable for these chain lengths.

The presence of a plateau ($\tau_1 < t < \tau_2$) suggests that relaxation processes still take place at timescales shorter than the lifetime of a single ionic bond, which can also be seen from the fact that the relaxation modulus at the lowest salt concentrations in Figure 9.1a is decreasing with increasing time. At timescales $t < \tau_1$, we even observe an increased relaxation in the high frequency region of some of the frequency sweeps at these low salt concentrations (see Figure 8.3). Possibly, this relaxation at timescales shorter than the elementary lifetime of an ionic bond originates from Rouse modes of not fully complexed chains in regions within the sample where the density of polymer chains is slightly lower (see for example Figure 13.1). Alternatively, these modes might originate from ionic bonds that are less tightly bound due to local steric or conformational hindrance. Based on the timescales where we find the increased relaxation, $\mathcal{O}$ (10 ms), and the estimated number of ionic bonds per chain, we believe these relaxation processes are unlikely to originate from 'normal' Rouse modes of the chains segments between associations.

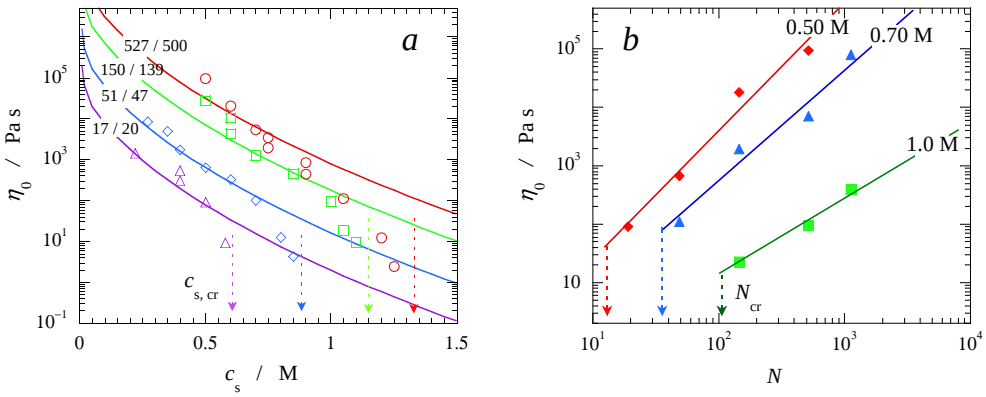

Figure 9.3: (a) Zero shear viscosity as a function of overall salt concentration for PDMAEMA / PAA complex coacervates of different polymer chain length. Solid lines are fits to Equation 9.16. The dashed arrows indicate the experimentally determined critical salt concentrations $c_{s,cr}$ (see Chapter 3). (b) Zero shear viscosity as a function of average polymer chain length in the complex coacervate for different salt concentrations. Solid lines are power law fits to the data. Vertical dashed arrows indicate (a) critical salt concentration above which or (b) critical chain lengths below which we no longer find complexation.

9.3.3 Viscosity of complex coacervates

The sticky Rouse model for polyelectrolyte complexes as presented above not only provides an accurate description of the relaxation mechanisms occurring in the complexes, but also gives a prediction for the zero-shear viscosity as a function of salt concentration, chain length and polymer concentration. The zero shear viscosity is proportional to the sticky Rouse time, τ_R and modulus at this Rouse time, which is k_BT per chain:[16]

$$\eta_0 \approx \tau_R G_R \approx \frac{k_B T \phi_p \tau_R}{b^3 N} \propto N^{\alpha'} \phi_p(N, c_s)^{\beta'} \exp\left(-2a_s\sqrt{c_s} + 2b_s\right) . \qquad (9.16)$$

In the sticky Rouse model, the Rouse time scales with $\tau_0 f^2 \propto \tau_0 N^2$ (Equation 9.14) and α' is unity.[16] In Chapter 8, we verified that the typical modulus of complex coacervates is proportional to ϕ_p/N (see Figure 8.8), in other words, that every polymer chain contributes to the modulus. We therefore expect that Equation 9.16 gives an accurate prediction of the salt concentration and chain length dependence of the viscosity.

Figure 9.3 shows the zero-shear viscosity of the complex coacervates as a function of salt concentration and chain length. Equation 9.16 predicts a stretched exponential dependence of the viscosity on the salt concentration, as ϕ_p depends only weakly

on salt concentration.[13,17] We find good agreement of our data with a stretched exponential fit for all chain lengths, using the same parameters a_s and b_s as in Figure 8.6. Close to the critical salt concentration (indicated by arrows) the model breaks down and the viscosity decreases more rapidly than predicted.

The parameter a_s takes the value of 6, which is in close agreement with the expected energy barrier corresponding to the rearrangement of single ionic bonds (as depicted in Figure 8.7) in a solution at $T = 293$ with an effective dielectric constant of $\epsilon_r = 43$, that is, the dielectric constant for a 2 – 3 M total ionic strength solution.[18] Interestingly, the presence of clusters of ionic bonds, for which the energy barrier for dissociation should be significantly higher, does not affect the value of a_s, which represents the relevant energy barrier for stress relaxation. Apparently, stress relaxation of clusters of ionic bonds proceeds via small steps of single rearrangements with an energy barrier equal to Equation 9.13, similar to trains of multiple polymer segments that are adsorbed to a surface, where the relevant energy barrier governing the lateral mobility of chains on the surface is also the adsorption energy of a single segment.[19–21]

The predicted dependence of the viscosity on the polymer chain length (Equation 9.16) is not trivial. The modulus is approximately proportional to ϕ_p/N (see Figure 8.8b). We also found that $\tau_c \propto N^{2.5}$ (Figure 8.8a), a slightly stronger dependence than expected for the classical Rouse model. However, this scaling was based on an average over all salt concentrations. In fact, ϕ_p in itself depends on salt concentration and chain length. From Chapter 3, we know that the complex coacervate binodal concentrations ϕ_p increase moderately with increasing chain length. Moreover, ϕ_p increases with decreasing salt concentration. This leads to a slightly weaker than linear dependence of the modulus G_c on N^{-1}, as shown in Figure 8.8b. The viscosity dependence on the polymer chain length will be different for different salt concentrations. Based on the arguments above, we expect the viscosity to depend stronger on chain length than predicted for the classical Rouse model, where $\eta_0 \propto N^1$. Experimentally, we find a power law dependence, with slopes decreasing with salt concentration from 2.3 at 0.50 M salt to 1.2 at 1.0 M salt. The much stronger dependence of the viscosity on polymer chain length for low salt concentrations might be explained by the fact that the complex coacervate binodal concentrations become high enough for entanglements to occur between the longest polymer chains, which further increases the viscosity.

In analogy with Figure 9.3a, there is a critical chain length, below which no complexation occurs at a given salt concentration. The existence of a critical chain length in complex coacervates at a fixed salt concentration has been observed before and is predicted to be more general.[7]

Finally, we can estimate the terminal relaxation time τ_R from Figure 9.1b. We find that these terminal relaxation times show a similar power law dependence on chain

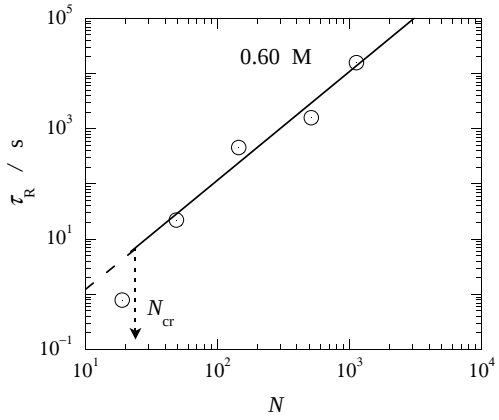

Figure 9.4: Terminal relaxation time (τ_R) from Figure 9.1a as a function of the average polymer chain length (N_{cat} and N_{an}) in the complex coacervate for a salt concentration of 0.6 M. The terminal relaxation time for N_{cat}/N_{an} = 51/47 and 150/139 are estimated by interpolation between the salt concentrations depicted in Figure 9.1a using Equations 9.12 and 9.13. For N_{cat}/N_{an} = 17/20 the terminal relaxation time for 0.40 M salt is shown, as 0.60 M is above the critical salt concentration for this chain length. The solid line is a power law fit to all chain lengths above 40, and has a slope of 2.0 ± 0.3.

length (see Figure 9.4). Here, the dependence is affected less by the N-dependence of ϕ_p, and we find a power law slope of 2 ± 0.3.

9.3.4 Non-stoichiometric complex coacervates

When polycations and polyanions are mixed in a non-stoichiometric ratio, complex coacervates may still form.[5,6,22] In some cases, the rheological properties of the complex coacervates depend strongly on the mixing ratio.[6] In other cases, no dependence or a much weaker dependence is found.[2,5] The degree of charging of the polyelectrolytes may play an important role in explaining this difference.[22] In addition, if the complex coacervates have a preferred composition, excess polycations or polyanions mainly end up in the dilute phase, thereby leaving the rheological properties of the complex almost unchanged. By contrast, if the composition of the complex coacervates changes notably with a changing mixing ratio of polycation and polyanion, then its rheological properties may also change significantly.

In order to investigate the effect of mixing stoichiometry on the relaxation behaviour of PDMAEMA/PAA complex coacervates, we have prepared complex coacervates of two flexible polyelectrolytes (N_{cat} = 527 and N_{an} = 500) at different overall mixing ratios. For each sample we perform a frequency sweep, creep test and flow curve. We use the dilute phase of each sample to establish whether excess of one of

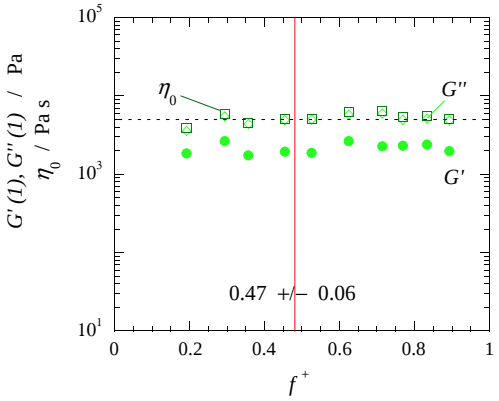

Figure 9.5: Linear viscoelastic properties of $PDMAEMA_{527}/PAA_{500}$ complex coacervates as a function of the overall stoichiometry f^+, defined as the molar ratio of positive chargeable monomeric units to total chargeable monomeric units. The horizontal line indicates the average zero shear viscosity for all compositions. The vertical line indicates the average stoichiometry of the complex coacervate phase that was formed. Storage and loss moduli are determined at an angular frequency of 1 rad/s.

the polymers is present in the dilute phase by adding a solution of either polycation or polyanion and checking for complexation by eye. For these polyelectrolytes we find that, irrespective of the initial mixing stoichiometry, the complex coacervates acquire a fixed composition of $f^+ = 0.47 \pm 0.06$ (based on monomer units), as described in Chapter 4. This composition is close to the 1 : 1 charge ratio ($f^+ = 0.5$) that is typically found for polyelectrolyte complexes in micelles,[23] in soft gels[24] and in bulk.[25]

Figure 9.5 shows the storage and loss moduli of the complexes at $\omega = 1.0$ rad/s and the zero-shear viscosity η_0 as a function of the fraction of positively charged monomers in the overall mixture. As expected, we find no significant difference between the samples. Excess polycations or polyanions end up in the dilute phase and the complex coacervate phase maintains a more or less constant, 'preferred' composition.[22]

9.3.5 Complex coacervates with unmatched chain lengths

Polycations and polyanions of unequal length can form complexes as well. The length asymmetry of the polymers may have a pronounced effect on the rheological behaviour.[2,4] In Figure 9.6 we show the effect of chain length mismatch on the rheological behaviour of complex coacervates of flexible polyelectrolytes. We find that there is an asymmetry between changing the length of the polycation and changing the length of the polyanion.

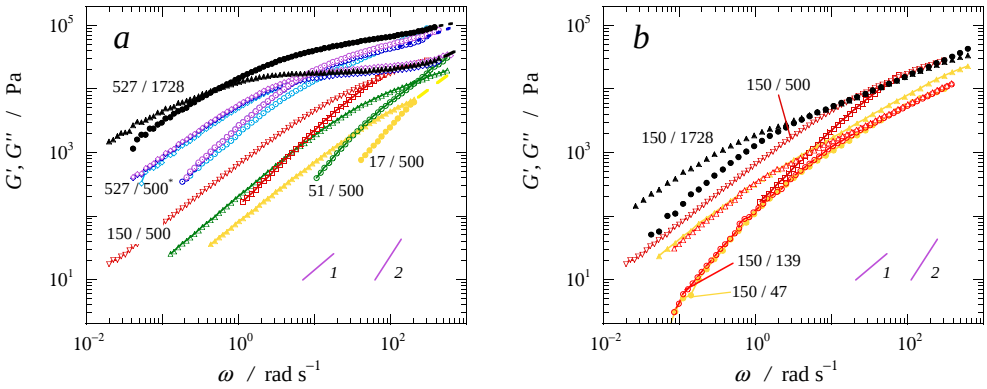

Figure 9.6: Frequency sweeps of PDMAEMA/PAA complex coacervates with unmatched chain lengths, as indicated by the labels (N_{cat}/N_{an}), at 0.70 M salt and $f^+ = 0.5$. In all cases a strain amplitude of 5% was applied. The frequency sweeps of complex coacervates with chain lengths 527/500, 527/139, 527/47 and 527/20 overlap to a large extent. For reasons of clarity, we show only the 527/500 label, marked with $*$.

When we decrease the length of PDMAEMA and leave the length of PAA unchanged at $N_{an} = 500$, the viscoelastic response changes significantly. Both storage and loss moduli are slightly lowered, as a result of the slightly lower polymer volume fraction in the complex coacervates with shorter chains.[13] More importantly, the crossover point shifts to much higher frequencies when the PDMAEMA length is decreased, indicating that the long-time sticky Rouse modes, corresponding to long parts of a polymer chains, vanish, and only the short-time modes, corresponding to small segments or small chains, remain.

By contrast, when we decrease the length of the PAA, while leaving PDMAEMA unchanged, we find that the linear viscoelastic response of the complex remains almost unchanged for $N_{cat} = 527$ ($N_{an} = 500, 139, 47$) and $N_{cat} = 150$ ($N_{an} = 139, 47$). When the PAA becomes too short ($N_{an} = 20$), the viscoelastic response seems to change slightly and the crossover shifts to higher frequencies.

However, when we increase the length of the PAA, we do find significant change in the viscoelastic response and the apparent crossover point, extrapolated from the viscous regime, shifts to lower frequencies for $N_{cat} = 527$ ($N_{an} = 1728$) and $N_{cat} = 150$ ($N_{an} = 500, 1728$). Instead of PDMAEMA, PAA now seems to dictate the rheological behaviour.

These results indicate that, although the polymers are present in a 1 : 1 ratio of chargeable groups, they do not have the same effect on the sticky network of overlapping polymer chains. It seems that mainly PDMAEMA governs the relaxation behaviour, as decreasing the PAA length does not affect the linear viscoelastic

response of the complex coacervates. Possibly, the PAA chains play a similar role as the negatively charged BSA in PDADMAC/BSA complex coacervates,[4] acting only as sticky temporary cross-links in a PDMAEMA-dominated network. Only when the PAA becomes much longer, it starts affecting the linear viscoelastic response, because PAA chains start overlapping. However, additional structural information on these complex coacervates to support this hypothesis is still lacking.

9.4 Concluding remarks

We find that the rheological behaviour of polyelectrolyte complexes composed of flexible polyelectrolytes is dominated by the dynamics of the single ionic bonds between the polyelectrolyte chains. This mechanism is in line with the suggested network structure of PDADMAC/BSA complex coacervates.[4] The ionic bonds act as temporary cross-links and their dynamic formation and rupture can be influenced by adding salt. Relaxation of stress occurs via sticky Rouse dynamics of the chains, hindered by the ionic bonds of a chain with oppositely charged neighbouring chains. Because salt affects the bond energy of all ionic bonds to the same extent, all relaxation modes are shifted equally by adding salt. This gives rise to a generic relaxation time spectrum for complex coacervates.

References

[1] J. H. E. Hone, A. M. Howe, and T. Cosgrove, *Macromolecules*, 2000, **33**, 1199–1205.

[2] O. Nikolaeva, T. Budtova, Yu. Brestkin, Z. Zoolshoev, and S. Frenkel, *J. Appl. Pol. Sci.*, 1999, **72**, 1523–1528.

[3] V. E. Dreval', G. B. Vasil'ev, E. A. Litmanovich, and V. G. Kulichikhin, *Pol. Sci. A*, 2008, **50**, 751–756.

[4] H. Bohidar, P. L. Dubin, P. R. Majhi, C. Tribet, and W. Jaeger, *Biomacromolecules*, 2005, **6**, 1573–1585.

[5] F. Weinbreck, R. H. W. Wientjes, H. Nieuwenhuijse, G. W. Robijn, and C. G. de Kruif, *J. Rheol.*, 2004, **48**, 1215–1228.

[6] X. Wang, J. Lee, Y.-W. Wang, and Q. Huang, *Biomacromolecules*, 2007, **8**, 992–997.

[7] N. Pawar and H. B. Bohidar, *Adv. Coll. Int. Sci.*, 2011, **167**, 12–23.

[8] M. Baumgaertel and H. H. Winter, *J. Non-Newt. Fluid Mech.*, 1992, **44**, 15–36.

[9] M. Baumgaertel and H. H. Winter, *Rheologica Acta*, 1989, **28**, 511–519.

[10] R. Mao, J. Tang, and B. G. Swanson, *Journal of Food Science*, 2000, **65**, 374–381.

[11] I. L. Hopkins and R. W. Hamming, *J. Appl. Phys.*, 1957, **28**, 906–909.

[12] J. D. Ferry, *Viscoelastic properties of polymers*, John Wiley & Sons Inc., 3rd edn., 1980.

[13] E. Spruijt, A. H. Westphal, J. W. Borst, M. A. Cohen Stuart, and J. van der Gucht, *Macromolecules*, 2010, **43**, 6476–6484.

[14] M. Rubinstein and R. H. Colby, *Polymer Physics*, Oxford University Press, 2003.

[15] L. A. Archer, *J. Rheol.*, 1999, **43**, 1555–1571.

[16] M. Rubinstein and A. N. Semenov, *Macromolecules*, 2001, **34**, 1058–1068.

[17] E. Spruijt, J. Sprakel, M. Lemmers, M. A. Cohen Stuart, and J. van der Gucht, *Phys. Rev. Lett.*, 2010, **105**, 208301.

[18] D. V. Loginova, A. S. Lileev, and A. K. Lyashchenko, *Russ. J. Inorg. Chem.*, 2002, **47**, 1426–1433.

[19] A. Milchev and K. Binder, *Macromolecules*, 1996, **29**, 343–354.

[20] J. Klein Wolterink, G. T. Barkema, and M. A. Cohen Stuart, *Macromolecules*, 2005, **38**, 2009–2014.

[21] J. S. S. Wong, L. Hong, S. C. Bae, and S. Granick, *Macromolecules*, 2011, **44**, 3073–3076.

[22] P. M. Biesheuvel and M. A. Cohen Stuart, *Langmuir*, 2004, **20**, 2785–2791.

[23] S. van den Burgh, A. de Keizer, and M. A. Cohen Stuart, *Langmuir*, 2004, **20**, 1073–1084.

[24] M. Lemmers, E. Spruijt, L. Beun, R. Fokkink, F. A. M. Leermakers, G. Portale, M. A. Cohen Stuart, and J. van der Gucht, *Soft Matter*, 2012, **8**, 104–117.

[25] R. Chollakup, W. Smitthipong, C. D. Eisenbach, and M. Tirrell, *Macromolecules*, 2010, **43**, 2518–2528.

Part III

Strength

Chapter 10

Interfacial tension of complex coacervates

In this Chapter we use colloidal probe atomic force microscopy to measure the interfacial tension between a complex coacervate phase and its coexisting dilute aqueous phase as a function of salt concentration. Complex coacervate capillary bridges can nucleate in the confined space between a colloidal probe and flat surface in close proximity. We extract the interfacial tension from the capillary adhesion force where the surfaces are in contact. The interfacial tensions are low, $\mathcal{O}$ (100 µN/m), and follow a critical scaling, similar to the scaling found for classical segregative demixing. We rationalise our findings using a mean-field model for complex coacervation, mapped onto a classical polymer-solvent mixture.

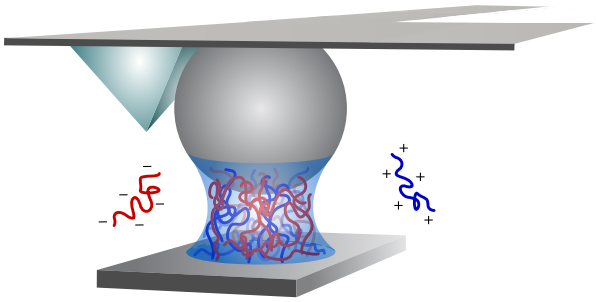

This Chapter is based on:
E. Spruijt, J. Sprakel, M. A. Cohen Stuart and J. van der Gucht: *Interfacial tension between a complex coacervate phase and its coexisting aqueous phase*, Soft Matter **6** (2010), 172–178, doi 10.1039/b911541b.

10.1 Introduction

The interfacial tension between a complex coacervate phase and its coexisting dilute aqueous phase is an important thermodynamic parameter that is related to the interaction between the macroions. In many potential applications of complex coacervate phases, knowledge of the interfacial tension is essential for predictions about the stability and practical applicability of such systems. In complex coacervate core micelles (see Chapter 5), the interfacial tension is related to the driving force of micelle formation,[1,2] and it can thus be used to predict the critical aggregation concentration.[3] In complex coacervate microdroplets, the interfacial tension dictates the relative importance of interfacial forces over viscous forces and it can thus be used to predict flow properties and interface deformations.[4,5] Finally, the interfacial tension plays an important role in wetting of surfaces by complex coacervates, which could be used to prevent fouling.[6]

Despite the crucial role of the interfacial tension in the balance of complex coacervate formation, interface stability and flow properties, there is no experimentally verified theory, nor a systematic study on the interfacial tension between a complex coacervate phase and its equilibrium aqueous phase. Kramarenko et al. present an indirect expression for the interfacial tension of a polyelectrolyte complex that is difficult to compare to experimental data.[7] Their calculations reveal that the aggregation number of a polyelectrolyte complex decreases with increasing salt concentration, as a result of a decreasing interfacial tension.

Experimentally, many qualitative studies on complex coacervation indicate that complex coacervation and the interfacial tension are highly sensitive to added salt.[8,9] Most of these studies concern complex coacervates of arabic gum and gelatin or whey protein, which all have a very low charge density. The only quantitative report of an interfacial tension between a complex coacervate and its equilibrium aqueous phase was made by De Ruiter and Bungenberg-de Jong.[10] They used the method of capillary rise to measure the interfacial tension at varying compositions and at three salt concentrations. They reported very low values for the interfacial tension at three different salt concentrations: $\mathcal{O}$ (1 µN/m), with a maximum at equimolar composition and the lowest salt concentration. However, they also indicated that the results they obtained were inaccurate and unsatisfactory, for several reasons: (i) the method relies on optical contrast between the phases, while the interface is usually wide and visible only as a diffuse band; (ii) the system is very sensitive to pH, because of ionisable groups on both polymers and the silanol groups of the capillary wall, which can cause significant changes in local pH values; (iii) for measurement of ultralow interfacial tensions the capillaries need to be very narrow, leading to frequent obstruction by small particles or aggregates.

In this Chapter we present accurate measurements of the interfacial tension between

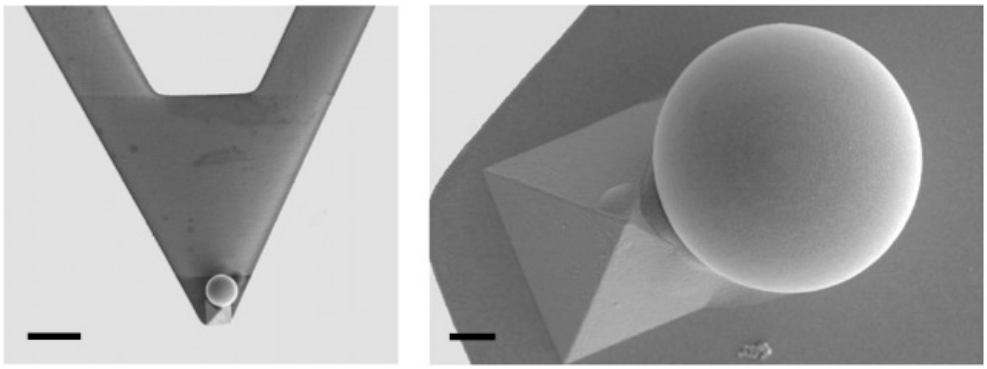

Figure 10.1: Scanning electron microscopy image of a triangular AFM silicon nitride cantilever with a $R = 3$ µm silica colloidal probe glued to its tip. The scale bar represents 10 µm in the left image and 1 µm in the right image.

a complex coacervate and its coexisting aqueous phase for the general case of two flexible polyelectrolytes with high charge densities. Our data indicate that the interfacial tension is significantly higher than for the biopolymers with very low charge densities.[10] Furthermore, we show that salt has a strong effect on the interfacial tension and the kinetics of complex coacervate formation and disruption. On the one hand, we find a critical point at high salt concentration, near which the interfacial tension approaches zero. On the other hand, we find slow kinetics of the phase separation and strong hysteresis in our measurements at low salt concentrations, which we ascribe to a highly asymmetric composition of the coexisting phases. In our analysis of the influence of salt on the interfacial tension we find a critical scaling of the interfacial tension with the salt concentration that is similar to the scaling found for classical segregative demixing. We rationalise this using a mean-field theory of complex coacervation. Finally, we compare our results with recent additional experiments and field theoretical calculations of the interfacial tension of other complex coacervates.

In our measurements of the interfacial tension, we make use of colloidal probe atomic force microscopy (CP-AFM) to measure the forces associated with a capillary bridge between a flat surface and a spherical colloidal probe (see Figure 10.1). CP-AFM was introduced independently by Ducker et al.[11] and Butt[12] and it was first used to measure ultra-low, equilibrium interfacial tensions by Sprakel et al.[13] In contrast to other techniques for measuring low interfacial tensions, such as the spinning drop method, this method does not use strong external fields. Moreover, this method can be applied without problems in any liquid-liquid two-phase system, because it does not require an optical contrast or a density difference between the two phases. Because of the vanishing optical contrast between a complex coacervate phase

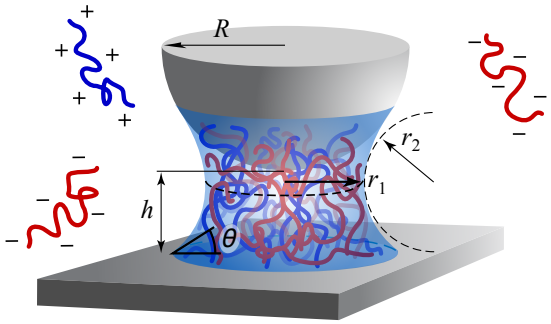

Figure 10.2: Schematic illustration of a capillary bridge that is formed by a complex coacervate, between a sphere and a flat surface in close proximity.

and its coexisting aqueous phase near the critical point, we expect that the spinning drop method is not suitable to measure the interfacial tension of complex coacervate systems close to their critical point. For another liquid-liquid two-phase system, gelatin-dextran, Sprakel et al. have shown that both methods give identical results for the interfacial tension.[14] The CP-AFM method does not require optical contrasts or density differences, because it is based on the principle of capillary condensation. In a system that is almost saturated with a component, a capillary bridge consisting of a condensed phase of this component can form spontaneously between two surfaces if the condensed phase naturally spreads on the surfaces ($\theta < 90°$), as is shown schematically in Figure 10.2. In everyday life this phenomenon causes, for example, the adhesion between sand grains in humid air, which makes the sand suitable for shaping into sandcastles. If, on the other hand, the liquid between the two surfaces does not spread on the surface ($\theta > 90°$), the analogous capillary evaporation, also known as cavitation, may occur. In both cases an attractive force arises between the surfaces, which can be measured in an AFM setup, where one of the surfaces is connected to a cantilever.[13]

10.2 Experimental details

10.2.1 Materials

We used a combination of oppositely charged polyelectrolytes, with PTMAEMA (M_n = 11 kg/mol, M_w/M_n = 1.1) as polycation and PSPMA (M_n = 90 kg/mol, M_w/M_n = 1.3) as polyanion, as described in Chapter 4.

Triangular AFM contact-mode cantilevers with a spring constant k of 0.06 – 0.12 N/m were purchased from Veeco. Silica colloidal probes (R = 3.0 µm) were a gift from Philips Laboratories. We glued them to the tip of a cantilever using a single-

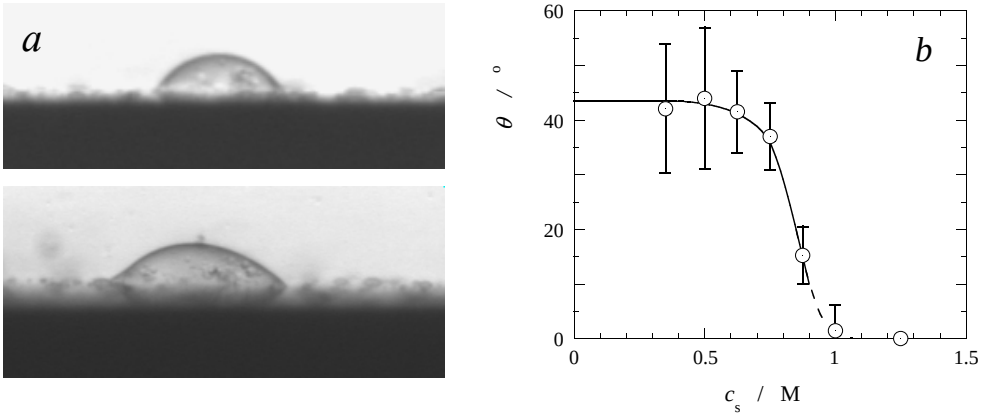

Figure 10.3: (a) Examples of droplets of complex coacervate on silica, in their coexisting aqueous phase, used to measure advancing contact angles. (b) Average advancing contact angle of complex coacervate droplets as in (a) as a function of salt concentration. The solid line is drawn to guide the eye.

component epoxy glue that melts above 90 °C (see Figure 10.1). Flat silicon wafers were purchased from WaferNet. All silicon surfaces and colloidal probe cantilevers were cleaned by rinsing with water and ethanol, drying under a stream of N_2 and plasma treatment for two minutes. The probes and wafers were then left in water until use. After plasma treatment the flat silicon wafers had a 3 nm thick oxidised layer of silica on the surface, as determined by ellipsometry.

10.2.2 Complex coacervate formation

We prepared complex coacervates of PTMAEMA and PSPMA at a 1 : 1 ratio of monomeric groups in aqueous solutions with varying salt concentrations (KCl), as described in Chapters 3 and 4.

10.2.3 Contact angle measurements

Advancing contact angles of the complex coacervates on plasma-treated flat silicon wafers were measured as follows. We mixed the phase separated complex coacervates, until the complex coacervate phase was dispersed as small droplets in the dilute aqueous phase. We then injected this emulsion in a glass cuvet with the cleaned silicon wafer at the bottom. The cuvet was placed on the stage of a Krüss G10 goniometer and contact angles of sedimented complex coacervate droplets, advancing on the silica surface, were measured over a period of three hours. Droplet pictures were then analysed using a drop analysis plugin based on active contours in ImageJ (Figure

10.3a).[15] The resulting average advancing contact angles of a PTMAEMA/PSPMA complex coacervate on silica in equilibrium with the dilute aqueous phase are shown in Figure 10.3b. At salt concentrations beyond 1.0 M we observe a transition from partial to complete wetting and the contact angle decreases to 0°. The optical contrast between the complex coacervate and its dilute phase also vanishes near the critical point (see Chapter 3) and droplets become increasingly difficult to distinguish. However, we believe the contrast between the two phases is still large enough at 1.0 M to distinguish them, because the macroscopically separated phases can still be distinguished as well.

10.2.4 Colloidal probe AFM

Force measurements were carried out on a Nanoscope 3A AFM (Digital Instruments), equipped with a PicoForce scanner. We mounted a cleaned silicon wafer and a cantilevers with a silica colloidal probe in a liquid cell with a volume of approximately 250 µL that was sealed with a rubber ring. The liquid cell was then filled with the dilute phase of the phase separated complex coacervate samples.

We measured force distance curves with a typical scan range of 1.0 µm, a scan rate ranging from 20 to 1000 nm/s and a relative force trigger upon approach of 5 nN. We recorded at least twenty separate force curves for every sample and every scan rate. The position where the two surfaces are in direct contact ($h = 0$) was taken in the region of constant compliance. Absolute separations between the surfaces were derived from this reference position. The cantilever deflection data were converted to interaction forces using Hooke's law, $f = k\Delta z$, where k is the cantilever spring constant. We determined the spring constant for every cantilever separately using the thermal tuning method,[16] and correcting for nonideality and cantilever support.[17]

10.3 Results and discussion

10.3.1 Force-distance curves

Typical force distance curves of two silica surfaces, immersed in the dilute aqueous phase of a phase separated complex coacervate, are shown in Figure 10.4. We emphasise that the immersing liquid is at or near its binodal concentration (see Chapter 3), in other words, saturation conditions apply. We find hysteresis between the approach and retract parts of these force curves. The approach curves display no attractive interaction for any scanning velocity, but the retract curves show a long-range attractive force for sufficiently low salt concentrations, which we attribute to capillary condensation, following a similar reasoning as Sprakel et al.[13] First of all, the attractive force can not be attributed to bridging by one of the polymers,

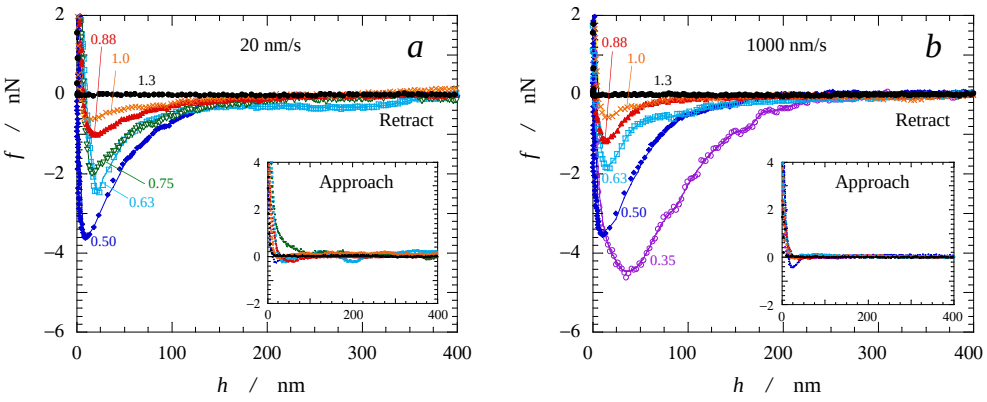

Figure 10.4: Typical retraction force-distance curves between silica surfaces immersed in saturated solutions of oppositely charged strong polyelectrolytes, using a scan rate of (a) 20 nm/s and (b) 1000 nm/s. Different symbols corresponds to different salt concentrations, as indicated by the labels (in M KCl). The insets show the corresponding approach force curves.

since we find no similar attraction in solutions of either polymer. Secondly, the range of attraction $\mathcal{O}$ (200 nm), is much larger than can be expected for depletion interactions, which have a range comparable to the radius of gyration of the polymers (here approximately 5 and 20 nm). Thirdly, we may exclude an attractive Van der Waals interaction between the two silica surfaces as the origin of the attraction in Figure 10.4, because we do not measure any attraction between the same surfaces in solutions of only salt. Therefore, we conclude that capillary condensation must cause the attractive forces. A dense complex coacervate phase condenses as a capillary bridge in the confined space between the two silica surfaces at close separation (see Figure 10.2), like water condenses in hydrophilic pores in humid air. The possibility of the capillary condensation of a complex coacervate between silica surfaces is confirmed by the contact angle measurements in Figure 10.3, which show that this complex coacervate spreads spontaneously on silica surfaces.

The hysteresis between approach and retract parts of the force curves in Figure 10.4 can be explained by the nucleation barrier for capillary condensation. The formation of a capillary bridge of the complex coacervate requires the nucleation of the condensate phase between the two surfaces. This nucleation is accompanied by an energy barrier that is proportional to γA^*, with γ the interfacial tension between the complex coacervate and the dilute aqueous phase and A^* the area of the critical nucleus, which at least needs to bridge the two surfaces. As a result, nucleation will only take place at considerable rate ($k \propto \exp(-\gamma A^*)$) when the surfaces are close together, so that A^* is small, or when the interfacial tension between the two phases

is extremely small.[13]

Our second observation in Figure 10.4 is that the attractive force upon retraction vanishes at salt concentrations beyond 1.25 M. This is in agreement with our observation that macroscopic phase separation is absent in solutions with salt concentrations beyond 1.25 M. This means we have crossed the critical point in the corresponding salt-polymer phase diagram for complex coacervates (see Chapter 3) and the mixed polyelectrolytes remain dissolved. Moreover, below this critical salt concentration the attractive force increases with decreasing salt concentration. Clearly, salt has a strong effect on the interfacial properties of these complex coacervates, which we will discuss in more detail below.

We can determine the interfacial tension of the complex coacervates that forms the capillary bridge following the method of Sprakel et al.[14] Briefly, there are two contributions to the attractive force originating from capillary condensation in general: the Laplace pressure difference across the interface ($\Delta P = \gamma J$) and the interfacial tension acting along the interface ($f = -\gamma L_c \cos\theta$):[14,18]

$$f = \pi {r_1}^2 \gamma \left(\frac{1}{r_1} + \frac{1}{r_2} \right) - 2\pi r_1 \gamma \cos\theta \tag{10.1}$$

where γ is the interfacial tension, θ is the contact angle at the three-phase contact line and r_1 and r_2 are the principal radii of curvature of the condensed phase as shown in Figure 10.2. In this case, we have a system where the phase surrounding the capillary bridge is at or near its binodal concentration, hence, saturation conditions apply. Under these conditions, the Laplace pressure term in Equation 10.1 vanishes ($r_1 = -r_2$), as dictated by Kelvin's law. For the sphere-plate geometry of the colloidal probe AFM set-up, this leads to a simple expression for the attractive force, extrapolated to zero separation ($\lim_{h\to 0} r_1 = R$):

$$\lim_{\mu \to \mu^*} f_{h\to 0} = -2\pi R \gamma \cos\theta \tag{10.2}$$

where R is the radius of the spherical probe (see Figure 10.2). We carried out the above extrapolation by plotting at least twenty force curves simultaneously and using the last 30 nm of the region of attraction to extrapolate linearly to zero separation, as is shown in Figure 10.5. We can estimate the accuracy of our extrapolation based on Figure 10.5 as follows. The noise associated with Brownian motion of the cantilever in a single force-distance curve is $\mathcal{O}$ (10 pN). The difference between subsequent force-distance curves is somewhat larger: $\mathcal{O}$ (100 pN), leading to an estimated error for the interfacial tension after extrapolation of roughly 10%. In addition to this extrapolation method, we have fitted our force-distance curves to the constant volume model for capillary bridge forces of Willett et al.[19] This model describes the complete curve, but assumes that the volume of the capillary bridge remains constant at all

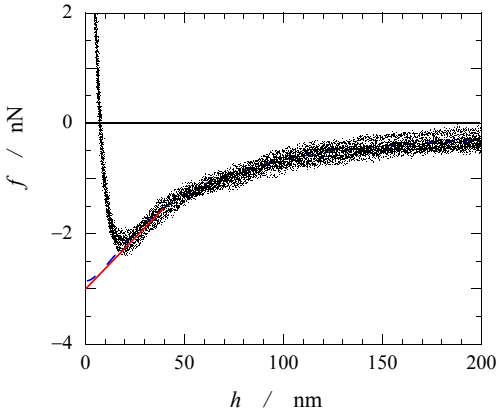

Figure 10.5: Extrapolation of the attractive capillary force to zero separation for a scan rate $v = 20$ nm/s and a salt concentration $c_s = 0.75$ M KCl. Twenty independent force curves are shown. The solid line is an linear extrapolation of the last 30 nm of the region of attraction to zero separation, the dashed line is a fit of the data to the constant volume capillary bridge model of Willett et al. [19]

separations. We find that the resulting interfacial tensions are equal to the values obtained by extrapolation within 10% at all salt concentrations (see also Figure 10.5).

The interfacial tensions of these complex coacervates are rather low, taking into account the strength of the individual ionic bonds between the oppositely charged polymers: $\mathcal{O}$ (100 µN/m). However, classical examples of segregatively demixed polymer solutions and demixed solutions of hydrophobically associating polymers display similar or even lower interfacial tensions. [4,13] We will discuss the magnitude of these interfacial tensions in more detail, in comparison with those recently reported by others for different complex coacervates at the end of this Chapter.

We note here that the low interfacial tensions, combined with the finite contact angles (see Figure 10.3), imply that the difference between the silica-dilute phase interfacial tension (γ_{SG}) and the silica-complex coacervate interfacial tension (γ_{SL}) is small as well ($\gamma \cos\theta = \gamma_{SG} - \gamma_{SL}$). This is indeed reasonable for nonadsorbing polymers and sufficiently high and equal salt concentrations in both the dilute and the complex coacervate phase.

10.3.2 Kinetics of capillary bridge formation

The capillary forces we measured do not depend on the scan rate. Figure 10.6a shows the extrapolated force at zero separation, which is directly proportional to the apparent interfacial tension (Equation 10.2), as a function of the scan rate. For salt concentrations above 0.50 M the capillary force is independent of scan rate over

the complete range of scan rates that we use. In addition, the measured force does not depend on the time that the two surfaces are kept in contact before retraction, as indicated in Figure 10.6b. This suggests that the capillary bridge grows very fast, once nucleated, at these salt concentrations. At a salt concentration of 0.35 M however, we do find an increase in the attractive force with increasing contact time (Figure 10.6b). We can explain this by considering the kinetics of capillary bridge formation in more detail.

The growth rate of the capillary bridge is determined by the diffusion of polymers from the dilute phase toward the capillary bridge. If we take the experimentally determined binodal concentrations of PDMAEMA/PAA complex coacervates (see Chapter 3) to be representative for these complex coacervates as well, we can calculate the typical time needed to form a capillary bridge by diffusion. The typical volume of the capillary bridge is 10 fL,[13,19] the concentration difference between the dilute phase and the complex coacervate phase forming the capillary bridge is roughly a factor 10^2 at high salt concentrations (see Figure 3.7). Hence, the typical diffusion length for polymer chains is 2 µm. Taking the diffusion coefficient of the largest of the two polymers to be 2×10^{-11} m^2s^{-1}, we find a typical diffusion time of 100 ms, which is well within the timescale of most AFM measurements. However, at low salt concentrations the ratio of polymer concentration in the dilute phase and the complex coacervate phase can easily reach 10^5, hence the diffusion time becomes $\mathcal{O}$ (10 s), which is longer than the duration of most AFM measurements.

Experimentally, we find that the capillary force increases to what seems to be a plateau value in roughly 100 seconds for a salt concentration of 0.35 M. Moreover, at the shortest contact time (100 ms), we do already measure a weak attractive force in all force curves. This is another indication that nucleation is not the rate-limiting step in the formation of the capillary bridges here.

In an attempt to further quantify our kinetic data, we numerically fit the data in Figure 10.6b to a model for the diffusion-limited growth of a capillary bridge between a sphere and a plate introduced by Kohonen et al.[20] They use Langmuir's treatment of the diffusion-limited growth of atmospheric water droplets to arrive at the following differential equation for the change of the radius of curvature with time:

$$\frac{\mathrm{d}r_1}{\mathrm{d}t} = \frac{Dc^*}{\rho}\left(\frac{c}{c^*} - \exp\left(-\frac{\gamma v_\mathrm{m}}{k_\mathrm{B}Tr_1}\right)\right) \tag{10.3}$$

where D is the diffusion coefficient of the polyelectrolytes, c^* is the concentration at saturation, ρ is the density of the condensate and v_m is the molecular volume of the polyelectrolytes. We assume there is a concentration gradient near the capillary bridge and that the dilute aqueous solution will remain close enough to its saturation point to apply Equation 10.2. This leads to the following relation for the change of the capillary force with time:

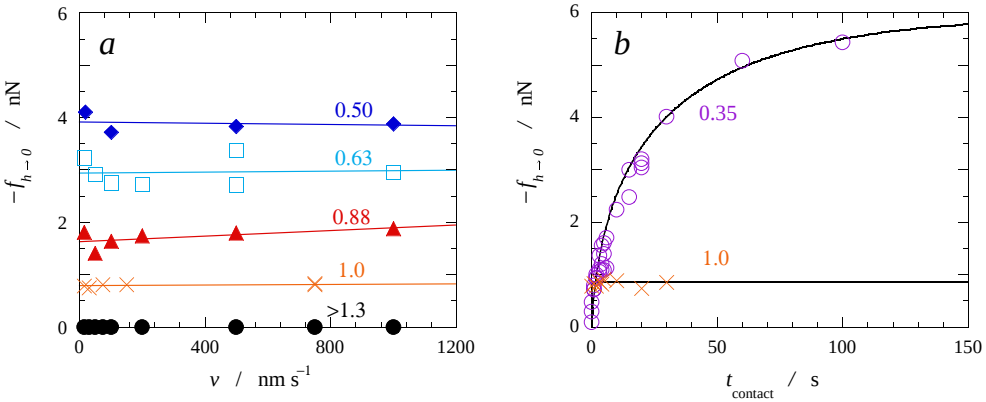

Figure 10.6: (a) Extrapolated capillary adhesion force between two silica surfaces, connected by a capillary bridge of a complex coacervate phase, as a function of scan rate for different salt concentrations, as indicated by the labels (in M KCl). (b) Change of the extrapolated capillary adhesion force with contact time between the two surfaces for two salt concentrations. For a salt concentration of 0.35 M the kinetics of capillary bridge formation could be measured almost until completion by CP-AFM, during 100 seconds. For a higher salt concentration no change in the extrapolated force was detected. Data for a salt concentration of 1.0 M are shown as example. The solid lines are fits of the experimental data to Equation 10.4.

$$\frac{\mathrm{d}f_{h\to 0}(r_1)}{\mathrm{d}t} = -\frac{2\pi\gamma D c^*}{\rho}\left(\frac{c}{c^*} - \exp\left(-\frac{\gamma v_\mathrm{m}}{k_\mathrm{B}T r_1}\right)\right) . \tag{10.4}$$

The solid lines in Figure 10.6b are numerical fits of the data to the above equation, using $r_1 = R$ and three fit parameters: $A = 2\pi\gamma Dc/\rho$, $B = 2\pi\gamma\, Dc^*/\rho$ and the Kelvin length $\lambda_\mathrm{K} = \gamma v_\mathrm{m}/k_\mathrm{B}T$, which characterises the length scale of capillary forces. The ratio $A/B = c/c^*$ is a measure for the saturation of the surrounding solution. We find that $A/B \approx 1$ for both salt concentrations in Figure 10.6b, which is an indication that our assumption that saturation conditions applied is reasonable. Furthermore, we find that the Kelvin length λ_K is approximately 500 nm. The Kelvin length is determined by the interfacial tension and the molecular volume v_m. From the plateau value of the capillary force in Figure 10.6b, we find that the interfacial tension for this salt concentration is about 400 µN/m. Using this value for the interfacial tension, we can estimate the molecular volume v_m in Equation 10.4, leading to a molecular volume v_m of $\mathcal{O}$ (10^{-23} m^3). This molecular volume corresponds to the total volume occupied by a polyelectrolyte chain, including solvent within the coil. The effective radius of the polyelectrolytes is therefore $\mathcal{O}$ (10 nm), which is a realistic value for the polyelectrolytes we use.

Finally, we note that the diffusion-limited growth of the capillary bridge at low

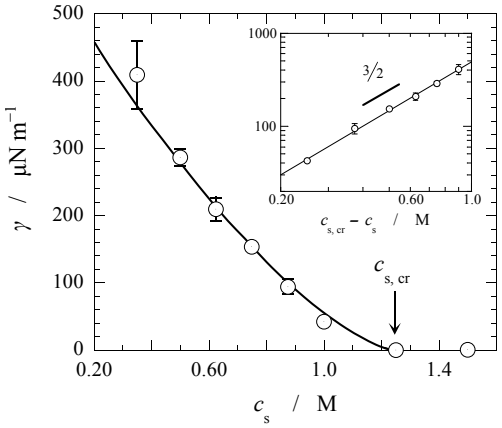

Figure 10.7: Interfacial tension of complex coacervates, measured by CP-AFM, as a function of salt concentration. The error bars represent the standard deviation of the interfacial tension around their average value at different scan rates, except for 0.35 M. For this lowest salt concentration, the standard deviation between ten independent measurements was taken. The critical salt concentration $c_{\mathrm{s,cr}}$, beyond which no capillary force could be measured is indicated by the arrow. The inset shows the same data plotted against the separation from the critical point on a double logarithmic scale. The solid line is a power law fit to the experimental data, with an exponent 1.5.

salt concentrations imposes a lower boundary for the salt concentrations that can be used with this method. At even lower salt concentrations, growth of the capillary bridge becomes even slower. However, at longer timescales than roughly 100 seconds drift problems in the AFM setup make it impossible to measure reliable retract force curves. Therefore, we can only make an estimate of the interfacial tension between a complex coacervate and its equilibrium aqueous phase at low salt concentrations by extrapolation.

10.3.3 Effect of salt on interfacial tension

Figure 10.7 shows the interfacial tension between the coacervate phase and its coexisting dilute phase as a function of salt concentration in the solution. The interfacial tension decreases with increasing salt concentration and vanishes at the critical salt concentration $c_{\mathrm{s,cr}}$ of 1.25 M.

In the inset of Figure 10.7 we plot the interfacial tension γ as a function of the separation from the critical salt concentration, $c_{\mathrm{s,cr}} - c_{\mathrm{s}}$. We find a power law scaling with an exponent of approximately 1.5. To explain this scaling, we use the mean-field model of Voorn and Overbeek, which estimates the total free energy of a polyelectrolyte mixture as a sum of Flory-Huggins mixing entropy terms, and

electrostatic interaction terms, based on a Debye-Hückel approximation, for every component (see Chapter 3).[21]

Our system can be expressed as a three-component system in the model of Voorn and Overbeek with a stoichiometric polyelectrolyte salt (PQ), a microsalt (KCl) and a solvent (water). At this stoichiometric charge ratio, the phase diagram of the complex coacervate and salt mixture can be mapped onto a classical polymer-solvent mixture that can undergo segregative demixing, using χ_{eff} as effective interaction parameter:[22]

$$\chi_{\text{eff}} = \chi_{\text{r}} + \frac{2\pi {\ell_{\text{B}}}^2 \kappa^{-1} \alpha^2}{3\, l^3} \tag{10.5}$$

where $\ell_{\text{B}} = e^2/4\pi\epsilon_{\text{r}}\epsilon_0 k_{\text{B}}T$ is the Bjerrum length, α is the fraction of charged groups on the polymer, l is the typical monomer size, κ^{-1} is the Debye screening length, defined for the monovalent KCl salt as $\kappa^2 = 8\pi\ell_{\text{B}} N_{\text{Av}} c_{\text{s}}$ and c_{s} the salt concentration in mM. For a three-component system, the above equation only applies if $\alpha \approx 1$, that is, for strong polyelectrolytes, which is indeed the case for our complex coacervates.

In general, in a mean-field approximation, the interfacial tension in a segregatively separated mixture vanishes at the critical point as[23]

$$\gamma \propto (\chi - \chi_{\text{cr}})^{3/2}\,. \tag{10.6}$$

Using the effective interaction parameter, $\chi_{\text{eff}} \propto \kappa^{-1} \propto {c_{\text{s}}}^{-1/2}$, we find that for associative demixing, the interfacial tension vanishes close to the critical salt concentration according to

$$\gamma \propto \left(\frac{1}{\sqrt{c_{\text{s}}}} - \frac{1}{\sqrt{c_{\text{s,cr}}}}\right)^{3/2} \propto \left(\frac{1}{\sqrt{c_{\text{s,cr}} - \Delta c_{\text{s}}}} - \frac{1}{\sqrt{c_{\text{s,cr}}}}\right)^{3/2} \propto (\Delta c_{\text{s}})^{3/2} \tag{10.7}$$

where we expand the first term with $\Delta c_{\text{s}} = c_{\text{s,cr}} - c_{\text{s}}$ in a Taylor series. This is in agreement with our results in the inset in Figure 10.7. We find that our experimental data are in agreement with this mean-field critical scaling over a remarkably long range of salt concentrations. A similarly extensive mean-field scaling has been observed before in case of segregative polymer-polymer demixing.[24] Based on Figure 10.7 we also estimate, by extrapolation, that the interfacial tension of a complex coacervate phase of strong polyelectrolytes at zero salt concentration is $\mathcal{O}$ (1 mN/m).

Finally, we can make a comparison between our interfacial tension values and the values reported by De Ruiter and Bungenberg-de Jong for a complex coacervate of gelatin and arabic gum.[10] Our interfacial tensions are one to two orders of magnitude larger than the values for gelatin and gum arabic, which were 1 – 2 µN/m. This difference can be explained by considering the nature of the different

complex coacervates. In our case the complex coacervate is formed by two strong polyelectrolytes with very high charge densities ($\alpha \approx 1$). Gelatin and gum arabic are both weak polyelectrolytes with an estimated 1% of the groups bearing a charge. A higher charge density most likely results in a stronger cohesive force within the complex coacervate phase and therefore a higher value of the interfacial tension. This is also expressed by Equation 10.5.

10.3.4 Recent developments

Riggleman et al. have recently used field-theoretic simulations to calculate the interfacial tension of complex coacervates of Gaussian polycations and polyanions of equal length and homogeneous charge density.[25] Mechanically, the interfacial tension in their simulations follows from the difference between the components of the pressure tensor normal and tangential to the interface. They compare these mechanical interfacial tensions to the thermodynamic estimates obtained from Bennett's method, for which two calculations at different interfacial areas were carried out. They find good agreement between both estimates of the interfacial tension, and values that are quantitatively comparable to the values we reported in this Chapter: $\mathcal{O}$ (100 µN/m). Moreover, the interfacial tension decreases with increasing salt concentration, following an apparent critical scaling $\gamma \propto (c_{s,cr} - c_s)^{3/2}$, and vanishes at the critical point. These field-theoretic calculations are the first simulations in which thermodynamic properties of complex coacervates, such as the interfacial tension, could be calculated accurately. They are of great value for the understanding of the effects of chain length and charge density on various thermodynamic properties of complex coacervates, since those parameters can be adjusted more easily and with much greater precision in simulations than in experiments.

Antonov et al. have recently used a rheo-optical technique, based on small angle light scattering and light transmission, to measure the interfacial tension of the classical complex coacervates of gelatin and gum arabic.[5] The technique they used relies on the breakup of fluid filaments of complex coacervates in shear flow. The interfacial tension they find is roughly an order of magnitude higher than the interfacial tension found by De Ruiter and Bungenberg-de Jong, highlighting the possible uncertainty in the original measurements by De Ruiter and Bungenberg-de Jong. Interestingly, this technique can also be used to study the effect of shear on the complex coacervate phase diagram. For the complex coacervates of gelatin and gum arabic the two phase region becomes smaller under shear.

Finally, Priftis et al. have used the same approach we describe in this Chapter to measure the interfacial tension of complex coacervates of two oppositely charged polypeptides, poly(L-glutamic acid) and poly(L-lysine), of equal length using the surface force apparatus (SFA).[26] Like Riggleman et al. and our results presented in

this Chapter, they find an interfacial tension that is $\mathcal{O}$ (100 µN/m), which decreases with increasing salt concentration and vanishes at the critical point. Moreover, they find a strong dependence of the interfacial tension on the polymer chain length, with γ reaching 4.5 mN/m for $N = 400$ at 0.10 M salt.

10.4 Concluding remarks

We have measured the interfacial tension of complex coacervate phases of two highly charged polyelectrolytes with CP-AFM. The force curves show no attraction upon approach, but upon retraction a capillary bridging force is measured. From these forces we could obtain the interfacial tension between the complex coacervate and the coexisting aqueous phase, which is $\mathcal{O}$ (100 µN/m). The interfacial tension decreases with increasing salt concentration and vanishes at the critical point. We were able to measure the interfacial tensions in a range of salt concentrations from the critical salt concentration, where no phase separation occurs, to a lower experimental limit. Below this lower limit, diffusion-limited growth of the capillary bridge is too slow for AFM to yield accurate measurements. The dependence of the interfacial tension on the salt concentration is in agreement with a mean-field model for complex coacervation. These results will be valuable in predicting the proper conditions for applications of these complex coacervates. In the case of supramolecular assemblies based on oppositely charged polymers (C3Ms), combination of our results for interfacial tension as a function of salt with a nucleation theory for such assemblies in which the interfacial tension is used,[3] gives a prediction for the critical aggregation concentration as a function of salt concentration.[27]

References

[1] M. A. Cohen Stuart, N. A. M. Besseling, and R. G. Fokkink, *Langmuir*, 1998, **14**, 6846–6849.

[2] I. K. Voets, A. de Keizer, and M. A. Cohen Stuart, *Adv. Coll. Int. Sci.*, 2009, **147–148**, 300–318.

[3] J. Sprakel, F. A. M. Leermakers, M. A. Cohen Stuart, and N. A. M. Besseling, *Phys. Chem. Chem. Phys.*, 2008, **10**, 5308–5316.

[4] P. Van Puyvelde, Y. A. Antonov, and P. Moldenaers, *Food Hydrocolloids*, 2002, **16**, 395–402.

[5] Y. A. Antonov, P. Van Puyvelde, and P. Moldenaers, *Food Hydrocolloids*, 2012, **27**, 264–268.

[6] A. M. Brzozowska, E. Spruijt, A. de Keizer, M. A. Cohen Stuart, and W. Norde, *J. Coll. Int. Sci.*, 2011, **353**, 380–391.

[7] E. Y. Kramarenko, A. R. Khokhlov, and P. Reineker, *J. Chem. Phys.*, 2006, **125**, 194902 1–8.

[8] H. Sato and A. Nakajima, *Coll. Pol. Sci.*, 1974, **252**, 944–948.

[9] F. Weinbreck, R. H. Tromp, and C. G. de Kruif, *Biomacromolecules*, 2004, **5**, 1437–1445.

[10] L. de Ruiter and H. G. Bungenberg-de Jong, *Proc. KNAW*, 1947, **50**, 836–848.

[11] W. A. Ducker, T. J. Senden, and R. M. Pashley, *Nature*, 1991, **353**, 239–241.

[12] H.-J. Butt, *Biophys. J.*, 1991, **60**, 1438–1444.

[13] J. Sprakel, N. A. M. Besseling, F. A. M. Leermakers, and M. A. Cohen Stuart, *Phys. Rev. Lett.*, 2007, **99**, 104504.

[14] J. Sprakel, N.A.M. Besseling, M.A. Cohen Stuart, and F.A.M. Leermakers, *Langmuir*, 2008, **24**, 1308–1317.

[15] A. F. Stalder, G. Kulik, D. Sage, L. Barbieri, and P. Hoffmann, *Colloids and Surfaces A*, 2006, **286**, 92–103.

[16] J. L. Hutter and J. Bechhoefer, *Rev. Sci. Instrum.*, 1993, **64**, 1868–1873.

[17] R. W. Stark, T. Drobek, and W. M. Heckel, *Ultramicroscopy*, 2001, **86**, 207–215.

[18] H.-J. Butt and M. Kappl, *Adv. Coll. Int. Sci.*, 2009, **146**, 48–60.

[19] C. D. Willett, M. J. Adams, S. A. Johnson, and J. P. K. Seville, *Langmuir*, 2000, **16**, 9396–9405.

[20] M. M. Kohonen, N. Maeda, and H. K. Christenson, *Phys. Rev. Lett.*, 1999, **82**, 4667–4670.

[21] J. Th. G. Overbeek and M. J. Voorn, *J. Cell. Comp. Phys.*, 1957, **49**, 7–26.

[22] J. Lyklema, *Fundamentals of Interface and Colloid Science V*, Academic Press London, 1991.

[23] J. Charvolin, J.-F. Joanny, and J. Zinn-Justin, *Liquids at Interfaces, Les Houches 1988*, Elsevier Science Publishers, 1988.

[24] E. Scholten, R. Tuinier, R. H. Tromp, and H. N. W. Lekkerkerker, *Langmuir*, 2002, **18**, 2234–2238.

[25] R. A. Riggleman, R. Kumar, and G. H. Fredrickson, *J. Chem. Phys.*, 2012, **136**, 024903.

[26] D. Priftis, R. Farina, and M. Tirrell, *submitted to Langmuir*, 2012.

[27] J. Wang, A. de Keizer, R. Fokkink, Y. Yan, M. A. Cohen Stuart, and J. van der Gucht, *J. Phys. Chem. B*, 2010, **114**, 8313–8319.

Chapter 11

Direct measurement of the strength of single ionic bonds between hydrated charges

In this Chapter we use single molecule force spectroscopy to measure the strength of single and multiple ionic bonds between hydrated charges. We disrupt a complex between two oppositely charged polyelectrolyte chains and measure the required force as a function of loading rate and salt concentration. We always find two modes of rupture: one ionic bond at a time, or the cooperative rupture of many bonds at once. For both modes, disruption of the ionic bonds can be described quantitatively as a salt-enhanced activated process. The height of the energy barrier is not only lowered by added salt, but also by the applied force. We extract unperturbed ionic bond lifetimes that range from milliseconds for single ionic bonds at high salt concentration to tens of years for small complexes of five ionic bonds at low salt concentration.

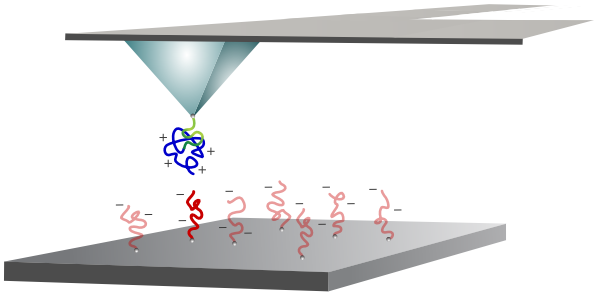

This Chapter is based on:
E. Spruijt, S. A. van den Berg, M. A. Cohen Stuart and J. van der Gucht: *Direct measurement of the strength of single ionic bonds between hydrated charges*, ACS Nano **6** (2012), 5297–5303, doi 10.1021/nn301097y.

11.1 Introduction

Ionic bonds are the main determining factor in the strength and stability of complex coacervates. Moreover, they play a key role in many natural macromolecular assemblies that are formed by a similar charge-driven assembly process (see Chapter 1). Because of their strength and tunability, ionic bonds see a growing interest for use in man-made responsive materials, nanostructures and photovoltaic devices.

For ions in a vacuum, Coulomb's law gives a precise value of the force, but the presence of a medium such as water containing salt ions leads to hydration, dielectric effects and screening of the charges. How the combination of these effects modifies the short-range attractive force – commonly called 'ionic bond' – is still poorly understood. As a result, the strength of ionic bonds between opposite hydrated charges is essentially unknown, making predictions of their stabilising effect in charge-driven materials impossible.

In this Chapter, we use atomic force microscopy (AFM) to directly measure the strength of single ionic bonds. AFM has proved to be a successful method for measuring the strength and rupture dynamics of single covalent,[1] hydrogen,[2] metal-ligand coordination[3] and antibody-antigen[4] bonds. In all single molecule force measurements, the sample molecules are covalently bound to AFM cantilevers via a polymeric linker molecule.[1–5] The polymeric linker not only separates the rupture of the investigated complex from contact adhesion of the tip to the substrate, it also exhibits a well-defined relation between extension and the applied force prior to the eventual complex rupture, from which the single molecule origin of the measured force can be established.[5]

11.2 Experimental details

11.2.1 Materials

We used triangular DNP silicon nitride cantilevers (Bruker), with a spring constant $k = 0.06 \pm 0.01$ N/m and a tip radius $R_{\text{tip}} = 20$ nm. Flat silicon wafers with a 3 nm layer of native oxide were purchased from WaferNet. Before surface modification all cantilevers and substrates were cleaned by immersion in piranha solution (70/30 96% H_2SO_4/35% H_2O_2) for 30 minutes, rinsing thoroughly with Milli-Q water and ethanol and drying under nitrogen.

11.2.2 Tip modification

We have covalently attached poly(*N*-methyl-2-vinylpyridinium)-*b*-poly(ethylene oxide) ($PM2VP_{249}$-*b*-PEO_{134}), a cationic diblock copolymer (see Figure 1.9), to a sil-

icon nitride AFM cantilever, following an adapted method of Hinterdorfer et al.[5] Briefly, the dried cantilevers were modified by reacting them in a solution of 2.8 g 2-aminoethanol hydrochloride in 5 mL dry dimethylsulfoxide (DMSO) with 4 Å molecular sieves for 16 hours. After 16 hours, the cantilevers were rinsed with dry DMSO, transferred into a 40 mM *p*-phenylene-diisocyanate solution in dry DMSO and left to react for no longer than 30 minutes, to avoid precipitation of solution-polymerised isocyanates onto the cantilever surface. The cantilevers were rinsed once again and transferred to the final solution of 10 g/L hydroxy-EO-terminated $PM2VP_{249}$-*b*-PEO_{134}-OH (Polymer Source, degree of quaternisation: 86%) in dry DMSO and left for one hour. After one hour the cantilevers were rinsed thoroughly with Milli-Q water and ethanol, dried under nitrogen and stored in a gel pack until use.

11.2.3 Substrate modification

Polyanionic brushes of PSPMA were synthesised by surface-initiated atom transfer radical polymerisation (SI-ATRP), as described in Chapter 12. For single molecule force spectroscopy measurements we used substrates with a dry brush thickness of 13 ± 2 nm (Sentech SE-400 ellipsometer), obtained after a polymerisation time of twenty minutes. We estimate the number average degree of polymerisation to be $N_{\mathrm{neg}} = 40$ and the grafting density $\Gamma = 0.8 \pm 0.3\ \mathrm{nm}^{-2}$, based on our findings in Chapter 12.[6,7]

11.2.4 Force spectroscopy experiments

All force curves were recorded with the ForceRobot 300 (JPK), using a small volume liquid cell (70 µL), sealed with a rubber ring at a temperature of $T = 293 \pm 2$°C. In all experiments the liquid cell was filled with an aqueous solution of NaCl (various concentrations) in Milli-Q water at pH 7 ± 0.5. The cantilevers were calibrated at 3.0 M NaCl, where the brushes are collapsed and no attraction is recorded. We obtained the deflection sensitivity s from the slope at $f > 1$ nN and the spring constant k using the thermal tune method[8] with corrections for nonideality and cantilever support.[9] We verified that this procedure yields correct calibration values (difference < 2%) from a reference calibration against silica with and without brush modification.

Typical force-distance cycles (approach and retract) were recorded for an approach range of 500 nm, a tip velocity v of 500 nm/s, no surface delay and a sampling rate of 4 kHz. In every force-distance cycle the tip was lowered to a constant load of 1 – 2 nN. The actual loading rates at rupture were calculated from extensible freely jointed chain (EFJC) fits of the stretching events. Every 100 force curves, the substrate was moved by 1.2 µm and the photodiode was realigned. In total 1,000 – 10,000 force-distance cycles were recorded for every tip-substrate-solvent combination. For every salt concentration, we measured at least two independent tip-substrate combinations.

In our analysis we combined the results for different tip-substrate combinations. Because inevitably some physically adsorbed polymers are present on the AFM tips after modification and thorough rinsing, we discarded the first 100 force curves from our analysis and started collecting the data after moving to a second location on the substrate. We then made a raw selection of all force curves using a custom-made Matlab routine, selecting only those curves that exhibit (1) a jump in the force averaged over three subsequent points that is larger than 3× the typical variations in averaged force in the baseline, with (2) a location of the jump that is further than 50 nm from the 'wall' (where the force turns repulsive). We then discarded the force curves that show interactions originating from two tip-bound polymers.

We sorted the remaining force curves in two types, as discussed hereafter: curves with a plateau of constant force and curves with a stretching event. All curves with a region of constant force (standard deviation $\leq$ 1.1× the standard deviation in the baseline) over more than 10 nm from the previously established jump in force were automatically classified as exhibiting a plateau. We manually checked the classifications to rule out obvious errors. Finally, the selected force curves were further analysed using the JPK data processing software.

11.3 Results and discussion

11.3.1 Single molecule ionic interactions

To assess the strength of ionic bonds between single molecules by AFM, we have covalently attached the cationic diblock copolymer, poly(*N*-methyl-2-vinylpyridinium)-*b*-poly(ethylene oxide) ($PM2VP_{249}$-*b*-PEO_{134}), to a silicon nitride AFM cantilever. The polymer is covalently bound to the AFM tip with its PEO-end, which acts as a neutral, flexible linker, while the PM2VP block is positively charged. We bring this cantilever in contact with a substrate on which an anionic poly(3-sulphopropyl methacrylate) brush ($PSPMA_{40}$) is grown. In contact, the oppositely charged polyelectrolytes form complexes consisting of one or multiple ionic bonds. We measured the strength of these bonds in aqueous solutions at various salt concentrations. The overall fraction of force curves in which we find an attractive interaction outside the region of contact adhesion (closer than 50 nm) is $> 20\%$ for salt concentrations below the critical salt concentration (see hereafter), of which typically $16 \pm 5\%$ are used in our analysis. When we repeated experiments with tips without any modification or with only physically adsorbed polymers, we find such interactions in $< 0.2\%$ of all force curves (see Figure 11.1).

Figure 11.2 shows some examples of force curves for a salt concentration of 1.0 M. The interactions due to polyelectrolytes come in two characteristic types.

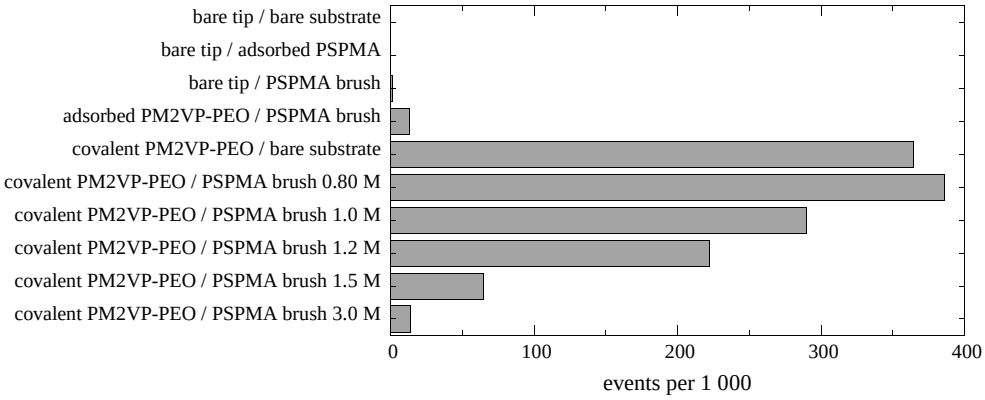

Figure 11.1: Reference measurements showing the number of events per 1,000 force curves, after automatic selection using $\langle|\Delta f|\rangle_{3\text{pts}} > 100$ pN and $h > 50$ nm, for bare tips and substrates and tips and substrates with physically adsorbed polymers.

In 8.5 ± 2% of all force curves we find a constant force plateau (type I). Neither the frequency of these events, nor the plateau height changes significantly in the first 1,000 force curves, indicating that no brush or tip erosion takes place. Similar plateau regions in other polymeric systems have been observed for the detachment of polymers adsorbed to a solid surface[11–13] and for the unzipping of complementary DNA strands.[14] They were attributed to the continuous disruption of successive bonds, one by one, in a zipper-like fashion. In our case, we expect to find a zipper-like disruption of single bonds when the polymer on the AFM tip binds to an oppositely charged polymer in the brush in a parallel fashion as depicted in Figure 11.4-I. Alternatively, the polymer on the tip may form single ionic bonds with several brush polymer chains, as if it were adsorbed on top of the brush. When the tip is retracted, the linker is stretched and a force is exerted on the first ionic bond. Upon failure, partial relaxation of the stretched polymer occurs and only part of the built-up load is transferred to the next ionic bond.[15] This bond in turn breaks at a similar load, resulting in a plateau of constant force during separation.

Another 8 ± 3% of all force curves display a characteristic polymer stretching before a rupture event (type II). These rupture forces are typically much larger than the rupture forces of type I events at the same salt concentration. This must mean that rupture involves multiple ionic bonds between the same two polymers, in such a way that the applied force is shared between the bonds: a shear alignment of antiparallel polymer chains (see Figures 11.4-II and 11.7). This clear distinction between parallel and antiparallel orientations is well known for DNA and β-sheets in proteins; the significant difference in rupture force can in fact be used to selectively deposit DNA onto a surface.[16] In our experiments, combinations of modes I and II

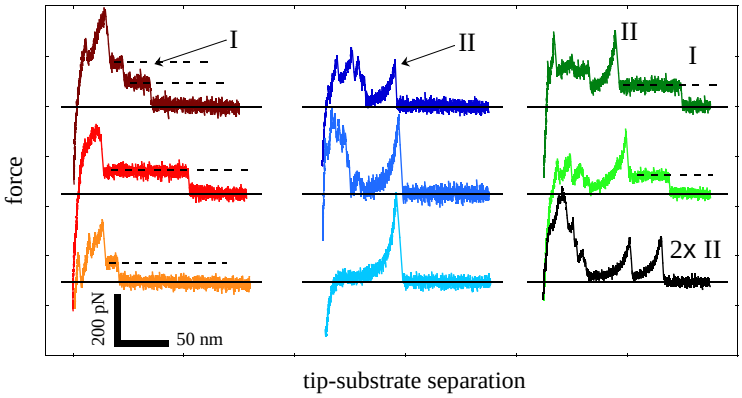

Figure 11.2: Typical force curves for the disruption of ionic bonds between a single polycation and a polyanionic brush at a salt concentration of 1.0 M (NaCl). The retract curves show the disruption of a zipper of ionic bonds, one at a time (I), and simultaneous disruption of cooperative complexes with multiple bonds (II), and both. Occasionally two polymers interact with the brush (bottom right curve).

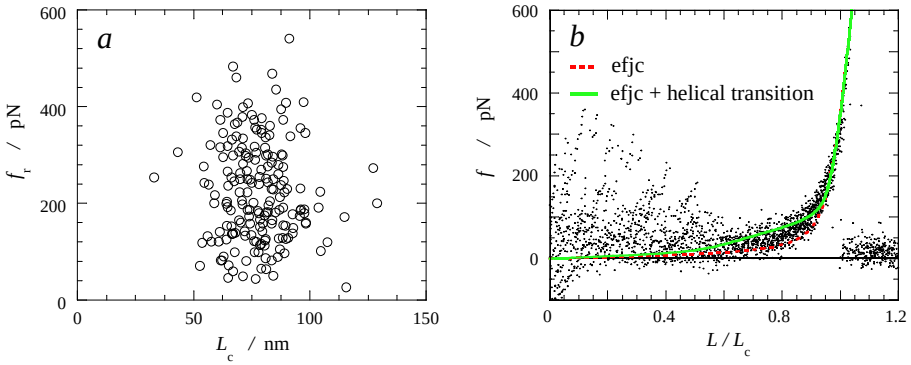

Figure 11.3: (a) Distribution of rupture forces and contour lengths of 200 type II events from Figure 11.2. (b) Rescaled overlay of 30 of these force curves, fitted to the model for an extensible freely jointed chain (EFJC) (dotted line) and the EFJC model with a helical to planar transition for the PEO block (solid line, Equation 11.1). [10] For reasons of clarity, one in every five data points is shown.

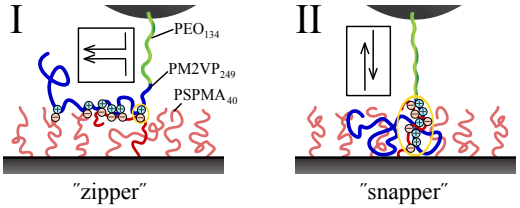

Figure 11.4: Schematic drawing of the ionic bonds in type I and type II events.

are possible, since part of the long polymer on the AFM tip can bind antiparallel to a brush polymer chain (II), while another part can bind a second brush polymer in a parallel fashion (I). Indeed, we find both modes combined in about 1% of all curves (see Figure 11.2a).

We have attributed both rupture modes to interactions of single polymers with the brush on the substrate. Indeed, the sharpness of the tip ($R_{\mathrm{tip}} = 20$ nm) and the low surface coverage expected for our modification method[5] make it very unlikely that two polymers have exactly the same pull-off distance. Occasionally we find a force curve with two separated rupture events or a desorption in multiple steps (0.5 – 0.7% of all curves, see Figure 11.2), but these are not used in our analysis. Further evidence for the single molecule origin of the rupture comes from analysing the polymer stretching curves that precede type II rupture. These curves could be fitted to the extensible freely jointed chain (EFJC) model:[10]

$$L(f) = N\left(\frac{L_{\mathrm{planar}}}{e^{\beta}+1}+\frac{L_{\mathrm{helical}}}{e^{-\beta}+1}\right)\left(\coth\left(\frac{fb}{k_{\mathrm{B}}T}\right)-\frac{k_{\mathrm{B}}T}{fb}\right)+\frac{Nf}{k_{\mathrm{seg}}}, \tag{11.1}$$

$$\beta = \frac{\Delta G - f\Delta L}{k_{\mathrm{B}}T}. \tag{11.2}$$

This model includes the force-induced helical-to-planar transition characteristic for PEO, with ΔG the energy difference between these states, and L_{planar} and L_{helical} the EO segment lengths in the planar and helical conformation respectively. For $\Delta G \to \infty$ and $L_{\mathrm{planar}} = L_{\mathrm{helical}} = b$, this model reduces to the classical freely jointed chain (FJC) model. For our fits we have used the following fit parameters: the Kuhn length $b = 0.7 \pm 0.1$ nm, the contour length $L_{\mathrm{c}} = Nb = 78 \pm 15$ nm, the segment elasticity $k_{\mathrm{seg}} = 10 \pm 2.9$ nN/nm and fixed values for the planar-helical energy difference, $\Delta G/k_{\mathrm{B}}T = 2.9$, the planar segment length, $L_{\mathrm{planar}} = b$ and the helical segment length, $L_{\mathrm{helical}} = 0.78\,b$. All parameters are consistent with single PEO chains in water.[10,17] Moreover, the distribution of the contour lengths and rupture forces shows no sign of interactions of multiple polymers (see Figure 11.3a).

11.3.2 Effect of salt on the interaction forces

If the rupture events shown in Figure 11.2 indeed correspond to the breaking of ionic bonds between the oppositely charged polyelectrolytes, then their magnitude should be highly sensitive to the salt concentration. In experiments on complex formation of the same polyelectrolytes ($PM2VP_{88}$ and $PSPMA_{94}$) in bulk solutions, we found that the driving force for complexation decreases with increasing salt concentration and vanishes completely above a critical salt concentration of 1.4 ± 0.10 M (NaCl) (see Chapter 4). Indeed, the rupture forces of both type I and II events decrease with

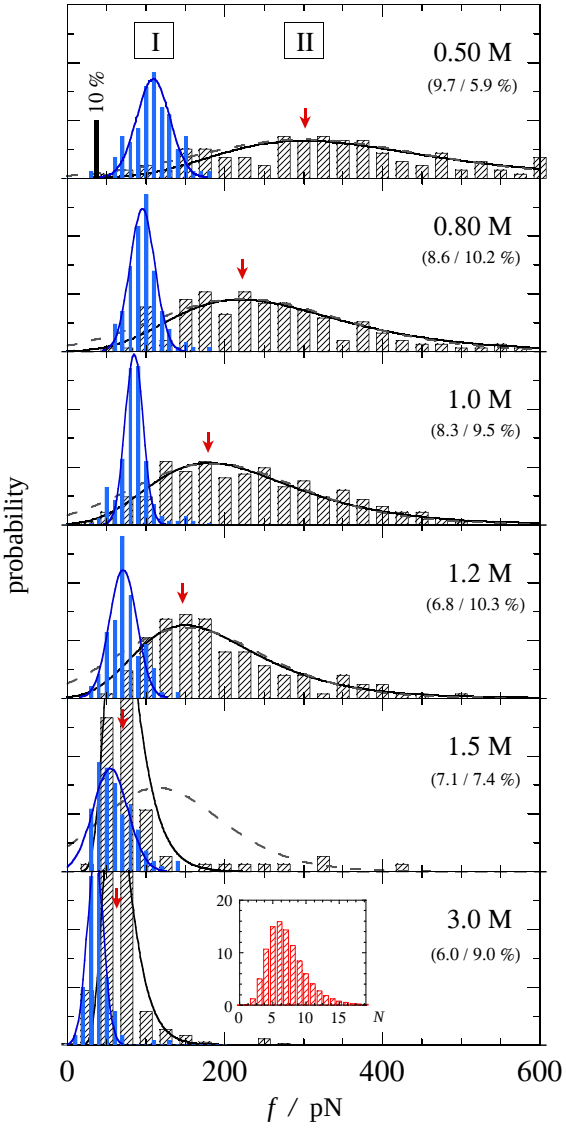

Figure 11.5: Histograms of type I and II ionic bond rupture forces at various salt concentrations. For each histogram at least 1,200 force curves are analysed. The percentages indicate the fraction of rupture events (I/II). Solid lines are Gaussian (type I) and Gumbel (type II) fits of the data. Dashed lines are model predictions of the distribution of type II rupture forces (Equation 11.8). Above the critical salt concentration the model and Gumbel fits mostly overlap. The arrows indicate the most probable rupture force for type II rupture events. The inset shows the Gumbel probability distribution of the number of ionic bonds in a type II complex we used in our model for the force distribution data of type II rupture events.

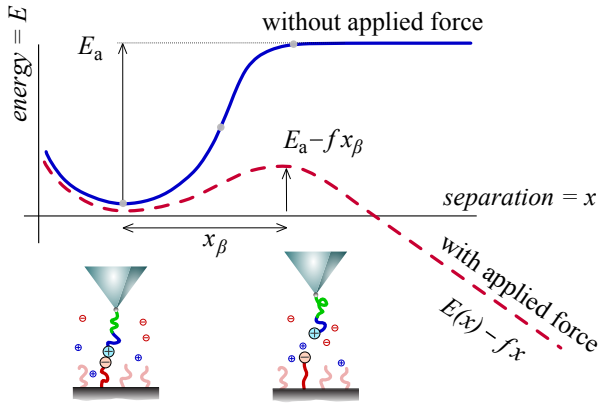

Figure 11.6: Schematic energy landscape of the disruption of an ionic bond.

increasing salt concentration, as shown in Figure 11.5. The critical point is reflected by a sudden jump to a lower mean rupture force between 1.2 and 1.5 M for both types of events, after which the mean rupture force remains approximately constant up to 3.0 M. The nonzero residual rupture force above 1.5 M salt is attributed to nonelectrostatic interactions between the two types of polymers that do not depend on salt concentration. Finally, the reference measurements with either bare tips or bare substrates (see Figure 11.1) further support our conclusion that the rupture events shown in Figure 11.2a correspond to the breaking of ionic bonds between the two polyelectrolytes.

11.3.3 Molecular rupture model for ionic bonds

For a quantitative understanding of the ionic bond rupture processes in Figure 11.2, we consider the energy landscape of the disruption of an ionic bond (see Figure 11.6). When no external force is applied, the energy barrier can be estimated, following Chapter 8, as the difference between the effective electrostatic energy of an ion pair in contact (E_{Coul}) and the energy of the separated polymeric chains, where both ionic groups are surrounded by salt (E_{corr}). For the latter we use a Debye-Hückel approximation.[18] In contrast to Chapter 8, no rearrangement of pairs of ionic bonds is required, but the ion pairs in a single ionic bonds are simply separated (see Figure 11.6) . Therefore, the relevant energy barrier is that of a single ionic bond,

$$\frac{E_{\mathrm{a}}}{k_{\mathrm{B}}T} = -\kappa\ell_{\mathrm{B}} + \frac{\ell_{\mathrm{B}}}{d} = -a_{\mathrm{s}}\sqrt{c_{\mathrm{s}}} + b_{\mathrm{s}} \tag{11.3}$$

where d is the contact distance of the charged groups in an ion pair, which is of the order of a few Å,[19] $\ell_{\mathrm{B}} = e^2/4\pi\epsilon_{\mathrm{r}}\epsilon_0 k_{\mathrm{B}}T$ is the Bjerrum length, which is 0.71 nm in

pure water, and κ^{-1} is the Debye length, which depends on the salt concentration and is defined as $\kappa^2 = 8\pi\ell_B N_{Av} c_s$ for a 1:1 electrolyte, with concentration c_s in mM. The parameters a_s and b_s follow from rearrangement and are temperature-dependent constants: $a_s = \sqrt{8\times10^3\pi N_{Av}{\ell_B}^3}$, for c_s in M, and $b_s = \ell_B/d$ (see also Chapter 8).

When an external force is applied to an ionic bond on a timescale that is much shorter than its natural life time ($t_{exp} \ll \tau_0$, with $\tau_0 = {\omega_0}^{-1}\exp(E_a/k_BT)$), the energy landscape is distorted (Figure 11.6a). This leads to a lowering of the energy barrier and an enhancement of the dissociation rate.[20] If the natural dissociation occurs much faster than the loading of the bonds in the AFM setup ($t_{exp} \gg \tau_0$), rebinding may occur during the separation of the surfaces and near-equilibrium conditions apply.[17,21] Under those conditions the rupture force is independent of the loading rate.[22] In general soft linkers between the bond and the AFM cantilever and high loading rates favour far-from-equilibrium conditions. Under those conditions the rupture force depends in a characteristic way on the loading rate. For a single rupture process the lowering of the energy barrier is written as

$$k_{off}(f) = \omega_0\, g(f) \exp\left(-\frac{E_a - f x_\beta}{k_B T}\right) = k_0\, g(f)\, e^{f/f_\beta} \tag{11.4}$$

where k_{off} is the dissociation rate, k_0 is the dissociation rate in the absence of force ($k_0 = 1/\tau_0 = \omega_0 \exp(-E_a/k_BT)$), x_β is the distance from the energy minimum to the transition state (see Figure 11.6) and $f_\beta = k_BT/x_\beta$. If the energy barrier is sharp, an applied force mainly alters the barrier height and $g(f) \approx 1$.[23] In an AFM experiment with a constant loading rate ($f = r_f t$), the probability of bond rupture at a given force can be found from the product of the rupture probability at that force and the survival probability up to that force:[20]

$$\begin{aligned} p(f) &= \frac{1}{r_f} k_{off}(f) \exp\left[-\int_0^f \frac{1}{r_f} k_{off}(f')\, \mathrm{d}f'\right] \\ &\approx \frac{k_0}{r_f}\, e^{f/f_\beta} \exp\left[\frac{k_0 f_\beta}{r_f}\left(1 - e^{f/f_\beta}\right)\right] . \end{aligned} \tag{11.5}$$

For the rupture process described by Equation 11.4, this leads to a characteristic probability distribution with a maximum at $f^* = f_\beta \ln(r_f/f_\beta k_0)$, assuming a constant loading rate.[24] A combination of Equation 11.3 and 11.4 provides a prediction for the effect of salt on the mean rupture force of a single ionic bond:

$$f^* = f_\beta \ln\left(\frac{r_f}{\omega_0 f_\beta}\right) - f_\beta a_s \sqrt{c_s} + f_\beta b_s\, . \tag{11.6}$$

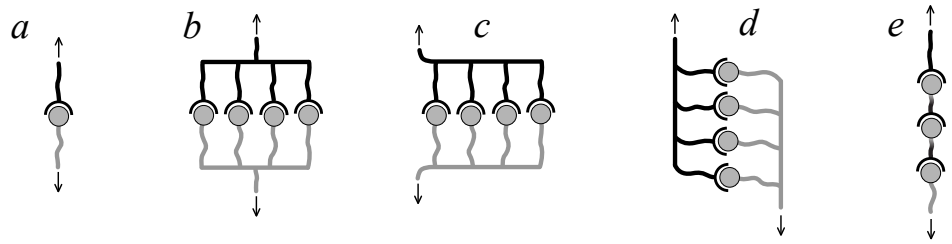

Figure 11.7: Different ways of arranging multiple bonds. (a) Single bond, (b) multiple bonds in parallel, (c) zipper of bonds, (d) shear arrangement of bonds ('snapper') and (e) bonds in series.[23]

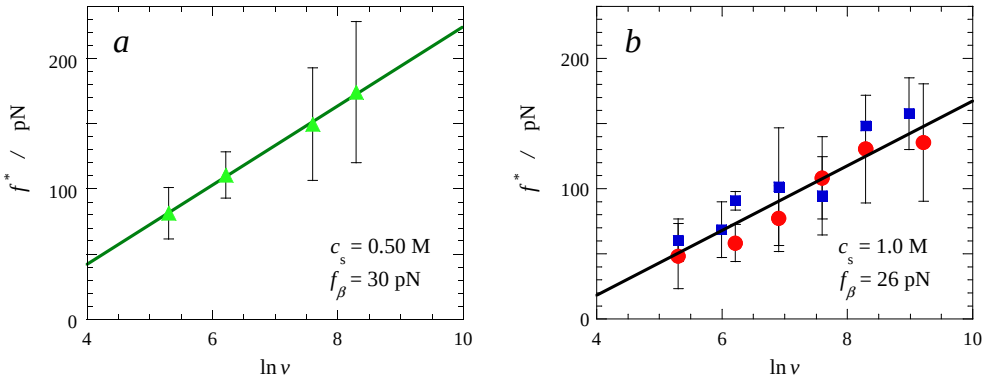

Figure 11.8: Plateau force versus the logarithm of the scan rate in nm/s for type I events. (a) Results for two independent tips at 1.0 M salt. (b) Results for a single tip at 0.50 M salt. The slopes of the linear fits are indicated in the Figures.

In a complex with multiple ionic bonds (Figure 11.4-I and II), the relevant energy barrier and the effect of loading depend on the way one applies the force to the complex (see Figure 11.7). As argued above, in the case of polyelectrolyte chains, the bonding groups are located along a polymer backbone, and we have two ways of loading the ionic bonds: as a zipper (parallel strands, Figures 11.4-I and 11.7c) and in shear (antiparallel strands, 11.4-II and Figures 11.7d).[15]

In the case of zipper-like disruption, the relevant energy barrier is still that of a single ionic bond. The plateau we measure is the average force of many stochastic single bond rupture events, each following Equation 11.5. A distribution of the plateau force is therefore expected to be Gaussian, as shown in Figure 11.5. The width of the corresponding energy barrier can be obtained from a plot of the most probable force versus $\ln v$, where $v = r_f/k_{seg}$ is the average tip velocity (see Figure 11.8). We find that f_β does not depend strongly on salt concentration, varying from 26 pN at

1.0 M salt to 30 pN at 0.5 M salt. Consequently, $x_\beta = 0.144$ nm, which is similar to the barrier width of hydrogen bond rupture[2] and is in good agreement with the dimensions of the ionic groups on the polymer chains.

Taking this value for x_β, we can use Equation 11.6 to describe the effect of salt on the strength of single ionic bonds, as shown in Figure 11.9. We find that $a_s = 4.5 \pm 0.5$ M$^{-0.5}$ and $B = f_\beta \ln(r_f/\omega_0 f_\beta) + f_\beta b_s = 170 \pm 10$ pN, corresponding to an effective dielectric constant of $\epsilon_r = 53$ at $T = 293$ K. This value is slightly different from the dielectric constant we found in Chapters 8 and 9. Most likely, this is caused by the fact that the ionic strength in the PSPMA brush (see Chapter 12) is lower than the typical ionic strength in a complex coacervate (see Chapter 3), and hence, the dielectric constant is higher.[25] The complex formed between the tip-bound cationic polymeric block and several chains in the PSPMA brush is also not as dense as the complex coacervates we used in Chapters 8 and 9, which leads to a higher dielectric constant. Furthermore, the combination of polyelectrolytes we used in this Chapter is different from the combination we used in Chapters 8 and 9 and the complex coacervates they form may have a lower equilibrium density as well.

If we take these fitted parameters, a_s and B, and assume the ionic bond distance, d, to be 0.2 ± 0.03 nm, which is slightly larger than typical covalent N-O bond lengths,[26] and independent of salt concentration, we find that the energy barrier varies from 6 k_BT in salt-free aqueous solutions to 1 k_BT around the critical salt concentration (see inset in Figure 11.9). These values are in good agreement with the computed energies for salt bridges occurring in proteins.[19]

Disruption of multiple (N) ionic bonds in a shear arrangement (Figure 11.2a-II) requires much larger forces than disruption of a zipper of ionic bonds, because the force is shared between all N bonds. The complex is expected to fail at a force ${f_{sh}}^*$, where $\partial \ln p(f)/\partial f = 0$, which leads to an implicit relation for ${f_{sh}}^*$,[15]

$$k_{sh}^{N\to 0}(f) = \left[\sum_{n=1}^{N} \frac{1}{nk_0} \exp\left(-\frac{f}{nf_\beta}\right)\right]^{-1}, \tag{11.7}$$

$$\begin{aligned} {f_{sh}}^* &= N f_\beta \ln\left(\frac{r_f}{k_0 {f_{sh}}^*}\right) \\ &= N f_\beta \ln\left(\frac{r_f}{\omega_0 {f_{sh}}^*}\right) - N f_\beta a_s \sqrt{c_s} + N f_\beta b_s \,. \end{aligned} \tag{11.8}$$

Further evidence for the proposed shear arrangement in type II events comes from the nonlinear relation between f^* and $\ln r_f$ (see Figure 11.10). In fact, the most probable rupture force seems to depend almost linearly on the loading rate, suggesting that the disruption of type II complexes can be described by an effective friction force.

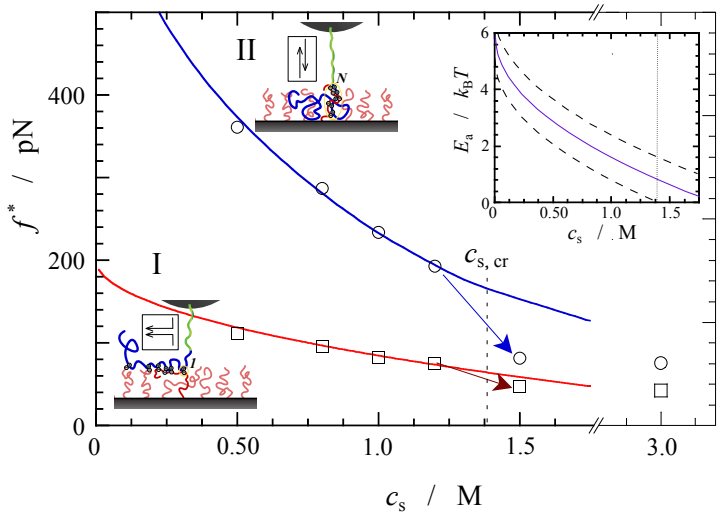

Figure 11.9: Experimental (symbols) and theoretical (lines) mean rupture forces for single ionic bonds (type I) and complexes of multiple ionic bonds (type II) as a function of salt concentration, measured at a tip velocity of 500 nm/s (approximate loading rate at rupture 3×10^3 pN/s). Close to the critical salt concentration ($c_{s,cr}$) we experimentally find a jump to lower forces and the model breaks down. The inset shows the predicted energy barrier for single ionic bond rupture. The dashed lines correspond to the upper and lower margins of error, based on $d = 0.20 \pm 0.03$ nm.

Before analysing the data, we note that an additional complication in the disruption of polyelectrolyte complexes is that the number of ionic bonds (N) formed when the tip-bound polymer penetrates into the brush is not constant, but can vary. Sequences of ion pairs alternate with more loosely arranged parts of the chain (see Figure 11.11).

We presume that the maximum rupture force measured in experiments is determined by the longest sequence of consecutive ion pairs. For a given probability of ion pair formation, the probability distribution of this longest sequence converges to the same distribution as the longest run of heads in a series of coin flips: a Gumbel extreme value distribution, with a tail at large N:[27]

$$p_G(N) = \frac{1}{\sigma_N} \exp\left[-\frac{N-\mu_N}{\sigma_N} - \exp\left(-\frac{N-\mu_N}{\sigma_N}\right)\right] \tag{11.9}$$

where μ_N is the mean and σ_N is the width of the distribution of N. The rupture force distribution of all type II stretching events is a weighted sum of all possible complex sizes N,

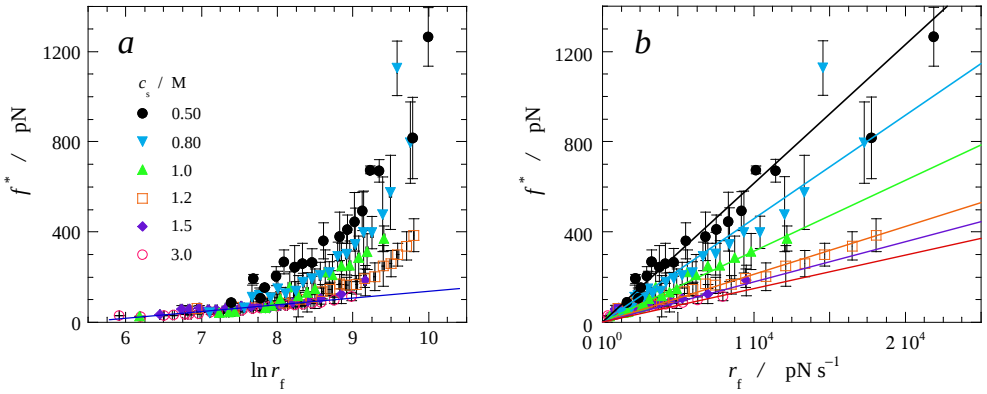

Figure 11.10: (a) Rupture force versus the logarithm of the loading rate in pN/s for type II events. (b) Same data on plotted against the loading rate. The loading rates are determined from the slope of the force curve at the point of rupture (EFJC fit). Different symbols correspond to different salt concentrations, as indicated by the labels in (a).

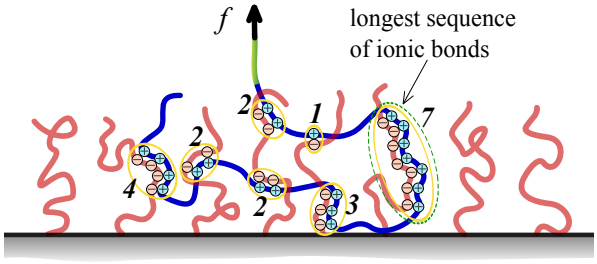

Figure 11.11: Schematic drawing of the multiple bonds formed in type II events. The longest sequence of ionic bonds determines the maximum rupture force.

$$p_{\mathrm{shear}}(f) = \sum_{N=1}^{N_{\max}} p_G(N) \frac{1}{r_f} k_{\mathrm{sh}}^{N\to 0}(f) \exp\left[-\int_0^f \frac{1}{r_f} k_{\mathrm{sh}}^{N\to 0}(f')\, \mathrm{d}f' \right] . \qquad (11.10)$$

We can now verify our ionic bond rupture model in Equations 11.3, 11.5 and 11.8 for the disruption of cooperative complexes of ionic bonds. Since type II events are measured in the same series as type I events, the values of x_β, a_s and b_s should not change. Indeed, we find excellent agreement between our experimentally measured rupture force distributions of type II events and the theoretical predictions, as shown in Figure 11.5. The longest sequence of ionic bonds is given by the Gumbel distribution shown in the inset of Figure 11.5, with $\mu_N = 6$ and $\sigma_N = 2.3$. For this

distribution of ionic bond sequences, the rupture force distributions themselves can be approximated by a Gumbel distribution. The mean rupture forces of the type II events decrease more strongly with increasing salt concentration than in the case of single ionic bonds, as predicted by our model (see Figure 11.9). Just like for single ionic bonds, our model breaks down close to the critical salt concentration, where the energy barrier per ionic bond becomes of order $k_{\mathrm{B}}T$.

11.3.4 Single molecule interactions with multilayers

Ionic bonds have a strongly salt-dependent strength and collectively they can become as strong as covalent bonds, even in water. These interactions and rupture mechanisms can play an important role in protein-protein and protein-ligand interactions.[28] However, in nature and in man-made applications using electrostatic complexes, the relevant interactions often occur between charged macromolecules and existing complexes of oppositely charged macromolecules.[29–34] Our experimental setup can easily be adjusted to measure these interactions as well. Without changing the tips, we simply increase the number of polyelectrolyte layers on our substrates by subsequently dipping the substrate with PSPMA brushes in 1 g/L solutions of $\mathrm{PM2VP}_{88}$ and PSPMA_{94} in 1.0 M NaCl. In this way we create substrates with one (only PSPMA brush), two (PSPMA + PM2VP), three (PSPMA + PM2VP + PSPMA) or more "layers", although complete mixing between the nongrafted polyelectrolytes on the surface is expected at the applied salt concentration.[33] We indeed measure an increase in dry layer thickness from 13 to 16 to 19 nm using ellipsometry. For more than three layers, we find a constant layer thickness of 20 ± 2 nm, consistent with complete mixing of the layers.

Figure 11.12 shows the force histograms for type II rupture events at 1.0 M NaCl for one, two and three layers on the substrate. With two or more layers covering the underlying silica, we no longer find type I events, probably because a different rupture process from the one depicted in Figure 11.6 takes place. Interestingly, the rupture force of the type II rupture events decreases significantly with the number of layers. Moreover, the force distributions become narrower and closer to a Gaussian distribution. For more than three layers, we find no further change in the rupture force distributions.

Both effects can be explained by considering the rupture mechanism between a single polyelectrolyte and the substrate. In the case of one layer, separation of the tip and the substrate involves rupture of ionic bonds, as discussed above. However, when the substrate is already covered with a stoichiometric polyelectrolyte complex (two layers: PSPMA + PM2VP), there is no longer a strong electrostatic driving force for formation of ionic bonds and either fewer or weaker ionic bonds will be formed between the cationic block copolymer and complex. Moreover, the presence

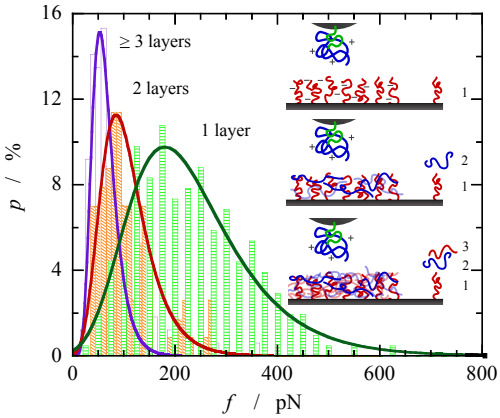

Figure 11.12: Histograms of rupture forces of a PM2VP$_{249}$ cationic block from a substrate with a varying number of polyelectrolyte "layers" at 1.0 M salt. One layer corresponds to a PSPMA brush only, two layers indicate that free PM2VP is adsorbed into the PSPMA brush and three layers indicate a second adsorption step with free PSPMA. Solid lines are Gumbel fits to the data.

of a complex on the substrate increases the local charge density and thus decreases the activation energy for separation of the ion pairs (see Equation 11.3). Indeed, we find that the distribution resembles that of a higher salt concentration than 1.0 M (see Figure 11.5). Finally, when the substrate contains three or more layers, also free PSPMA polymers are present that can (partly) neutralise the cationic block copolymer when tip and substrate are separated. Separation now occurs between two neutral complexes, and the energy barrier involved in this process is determined by the interfacial energy of the polyelectrolyte complex. Even for strongly charged polyelectrolytes, these interfacial energies are relatively low (see Chapter 10). As a result, the rupture forces measured for a substrate with three layers are lower than those for one or two layers; they are even lower than the expected rupture forces for single ionic bonds at the same salt concentration (see Figure 11.5).

11.4 Concluding remarks

Ionic bonds are reversible and highly tunable connections. For the *N*-methyl-2-vinyl pyridinium/sulphopropyl methacrylate bonds considered here, the strength ranges from roughly 1 k_BT close to the critical salt concentration to over 6 k_BT at low salt concentration. Cooperativity of the ionic bonds further amplifies this difference. As a result, the lifetime of ionic bonds in natural aqueous systems can range from milliseconds for single ionic bonds at high salt concentration to tens of years for small

complexes of five ionic bonds at low salt concentration. This versatility offers many opportunities for use of ionic bonds in new man-made materials. Under the right conditions a small complex of ionic bonds may be stronger than a covalent bond,[1] yet remain completely reversible: it can be 'unlocked' at any time by addition of salt.[35] In practical applications, the way charged groups are grafted to scaffolds or surfaces will play an important role in the stability of the complexes they form. When disassembly involves separation of the charges, much higher forces are required than for multilayer assemblies.

References

[1] M. Grandbois, M. Beyer, M. Rief, H. Clausen-Schaumann, and H. E. Gaub, *Science*, 1999, **283**, 1727–1730.

[2] A. Embrechts, H. Schönherr, and G. J. Vancso, *J. Phys. Chem. B*, 2008, **112**, 7359–7362.

[3] M. Kudera, C. Eschbaumer, H. E. Gaub, and U. S. Schubert, *Adv. Funct. Mater.*, 2003, **13**, 615–620.

[4] P. Hinterdorfer, W. Baumgartner, H. J. Gruber, K. Schilcher, and H. Schindler, *Proc. Nat. Acad. Sci. USA*, 1996, **93**, 3477–3481.

[5] C. K. Riener, C. M. Stroh, A. Ebner, C. Klampfl, A. A. Gall, C. Romanin, Y. L. Lyubchenko, P. Hinterdorfer, and H. J. Gruber, *Anal. Chim. Acta*, 2003, **479**, 59–75.

[6] M. Ramstedt, N. Cheng, O. Azzaroni, D. Mossialos, H. J. Mathieu, and W. T. S. Huck, *Langmuir*, 2007, **23**, 3314–3321.

[7] E. Spruijt, M. A. Cohen Stuart, and J. van der Gucht, *Macromolecules*, 2010, **43**, 1543–1550.

[8] J. L. Hutter and J. Bechhoefer, *Rev. Sci. Instrum.*, 1993, **64**, 1868–1873.

[9] R. W. Stark, T. Drobek, and W. M. Heckel, *Ultramicroscopy*, 2001, **86**, 207–215.

[10] F. Oesterhelt, M. Rief, and H. E. Gaub, *New J. Phys.*, 1999, **1**, 6.1–6.11.

[11] T. Hugel, M. Grosholz, H. Clausen-Schaumann, A. Pfau, H. E. Gaub, and M. Seitz, *Macromolecules*, 2001, **34**, 1039–1047.

[12] A. Scherer, C. Zhou, J. Michaelis, C. Brauchle, and A. Zumbusch, *Macromolecules*, 2005, **38**, 9821–9825.

[13] L. Sonnenberg, J. Parvole, O. Borisov, L. Billon, H. E. Gaub, and M. Seitz, *Macromolecules*, 2006, **39**, 281–288.

[14] B. Essevaz-Roulet, U. Bockelmann, and F. Heslot, *Proc. Nat. Acad. Sci. USA*, 1997, **94**, 11935–11940.

[15] P. M. Williams, *Anal. Chim. Acta*, 2003, **479**, 107–115.

[16] S. K. Kufer, E. M. Puchner, H. Gumpp, T. Liedl, and H. E. Gaub, *Science*, 2008, **319**, 594–596.

[17] S. Zou, H. Schönherr, and G. J. Vancso, *Angew. Chem. Int. Ed.*, 2005, **44**, 956–959.

[18] T. L. Hill, *An introduction to statistical thermodynamics*, Dover Publications Inc., 1986.

[19] S. Kumar and R. Nussinov, *Biophys. J.*, 2002, **83**, 1595–1612.

[20] E. Evans and K. Ritchie, *Biophys. J.*, 1997, **72**, 1541–1555.

[21] H. Schönherr, M. W. J. Beulen, J. Bügler, J. Huskens, F. C. J. M. van Veggel, D. N. Reinhoudt, and G. J. Vancso, *J. Am. Chem. Soc.*, 2000, **122**, 4963–4967.

[22] S. Cui, C. Liu, Z. Wang, X. Zhang, S. Strandman, and H. Tenhu, *Macromolecules*, 2004, **37**, 946–953.

[23] E. Evans and P. M. Williams, *Physics of bio-molecules and cells, Écoles des Houches d'Été LXXV: Dynamic force spectroscopy*, Springer Verlag, 2002.

[24] C. Ray, J. R. Brown, and B. B. Akhremitchev, *J. Phys. Chem. B*, 2007, **111**, 1963–1974.

[25] D. V. Loginova, A. S. Lileev, and A. K. Lyashchenko, *Russ. J. Inorg. Chem.*, 2002, **47**, 1426–1433.

[26] J. Israelachvili, *Intermolecular and surface forces*, Academic Press London, 1992.

[27] L. Gordon, M. F. Schilling, and M. S. Waterman, *Probability Theory and Related Fields*, 1986, **72**, 279–287.

[28] P. J. Kundrotas and E. Alexov, *Biophys. J.*, 2006, **91**, 1724–1736.

[29] G. Decher, *Science*, 1997, **277**, 1232–1237.

[30] M. Lemmers, J. Sprakel, I. K. Voets, J. van der Gucht, and M. A. Cohen Stuart, *Angew. Chem. Int. Ed.*, 2010, **49**, 708–711.

[31] M. A. Cohen Stuart, B. Hofs, I. K. Voets, and A. de Keizer, *Curr. Opin. Coll. Int. Sci.*, 2005, **10**, 30–36.

[32] P. M. Biesheuvel, T. Mauser, G. B. Sukhorukov, and H. Möhwald, *Macromolecules*, 2006, **39**, 8480–8486.

[33] J. L. Lutkenhaus and P. T. Hammond, *Soft Matter*, 2007, **3**, 804–806.

[34] R. de Vries, *Biochimie*, 2010, **92**, 1715–1721.

[35] E. Spruijt, H. E. Bakker, T. E. Kodger, J. Sprakel, M. A. Cohen Stuart, and J. van der Gucht, *Soft Matter*, 2011, **7**, 8281–8290.

Chapter 12

Direct measurement of the interaction forces between oppositely charged polyelectrolyte brushes

In this Chapter we use colloidal probe atomic force microscopy to measure the interactions between oppositely charged polyelectrolyte brushes. The complexes they form consist of many ionic bonds and require much larger forces for disruption than complex coacervate capillary bridges of nongrafted polymers (Chapter 10). We study the effect of salt and scan rate on the interaction strength and hysteresis. We find that near-equilibrium force distance measurements are only possible close to the critical salt concentration at low scan rates. Furthermore, we can directly measure the kinetics of complex formation, by changing the compression time of the brushes and the scan rate. Surprisingly, the complexes form as zipper-like arrangements of ionic bonds and grow linearly, but slowly in time.

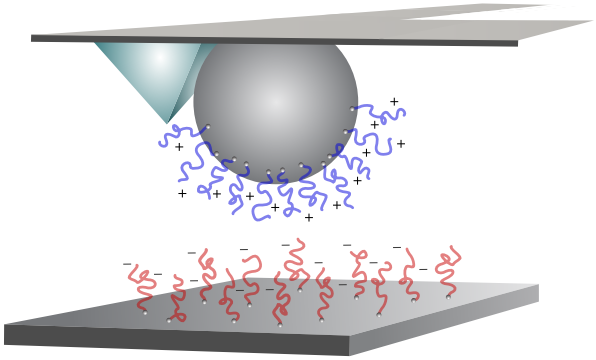

This Chapter is based on:
E. Spruijt, M. A. Cohen Stuart and J. van der Gucht: *Dynamic force spectroscopy of oppositely charged polyelectrolyte brushes*, Macromolecules **43** (2010), 1543–1550, doi 10.1021/ma902403a.

12.1 Introduction

The attractive interaction between two oppositely charged grafted polymers is directly related to the strength of ionic bonds, as we discussed in the previous Chapter. However, in many applications of charge-driven complexes the interactions are not limited to single polymers, but instead many chains or particles interact with each other, strengthening the resulting complexes of oppositely charged species. In Chapter 6 we have shown how oppositely charged polyelectrolyte brushes can drive the assembly of colloidal particles into fractal gels. In the composite shelters constructed by marine organisms (see Chapter 1), mineral particles and are held together by many interacting polypeptides that are mostly anchored to the particle surfaces by adhesive pads.[1,2] Finally, complexation between oppositely charged polyelectrolytes can be used to coat surfaces with polymer brushes at grafting densities well above 1 nm^{-2}.[3] Removing these coatings by shear or by pulling requires the disruption of a many-chain complexes as well. Instead, these coatings can be renewed by washing off an old, worn-down coating at high salt concentration and reapplying the block copolymer solution to the underlying surface.

In this Chapter we use colloidal probe atomic force microscopy (CP-AFM) to directly measure the forces between oppositely charged polyelectrolyte brushes. CP-AFM provides a geometrically well-defined setup in which two surfaces can be brought into contact, as schematically shown in Figure 12.1. We have used this method in Chapter 10 to study the cohesive energy in a complex coacervate phase of two oppositely charged polyelectrolytes by measuring capillary bridging forces. Here, we use the same pair of polyelectrolytes, but now each polyelectrolyte is covalently attached to its own surface, thus forming two oppositely charged brushes. We find that the critical salt concentration beyond which no interaction is measured is comparable to that of the situation where the polyelectrolytes are not covalently attached, but the attractive forces below the critical point are significantly larger in the grafted case. We attribute these large forces to the formation and rupture of ionic bonds between the oppositely charged polyelectrolyte chains, analogous to our results in Chapter 11, as opposed to the interfacial energies associated with bringing neutral complexes together, which we described in Chapter 10. To describe growth of the polyelectrolyte complexes in time we carry out dynamic force spectroscopy measurements. Unlike in the previous Chapter, we find that the complexes between oppositely charged dense brushes have a predominant zipper arrangement of the oppositely charged chains.

Both AFM and the surface force apparatus (SFA)[6] have been used before to study forces induced by polyelectrolytes. Most studies focused on interactions between like-charged polyelectrolytes, or interactions between polyelectrolytes and surfaces. Chen et al. recently studied the lubricating properties of covalently attached polyzwitterionic brushes, which resemble complex coacervates at low enough salt concen-

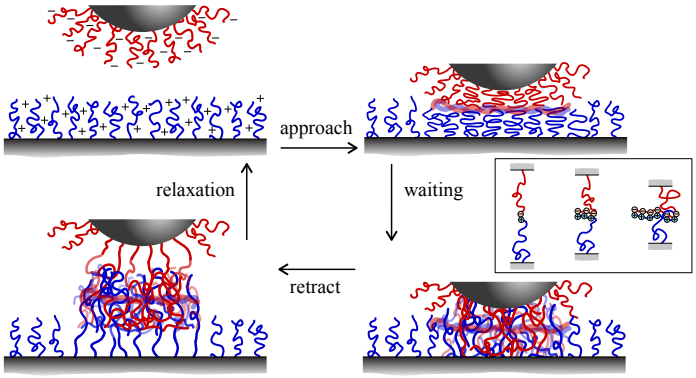

Figure 12.1: Schematic illustration of the processes involved in dynamic force spectroscopy of oppositely charged polyelectrolyte brushes, showing approach of the surfaces, immediate complex formation upon first contact, interpenetration of chains and complex growth during a waiting step, stretching of the chains upon separation and finally rupture of the complex before returning to the initial state.

trations, using SFA.[7,8] They found that the strong hydration of these brushes leads to extreme lubrication, mimicking the low friction at natural synovial joints. Estel et al.[9] and Salmi et al.[10] measured the adhesion of bare silica and cellulose layers to microscopic polyelectrolyte complex particles (microcoacervates) by AFM. They found no consistent effect of salt concentration, but the adhesion could be modified by changing the pH. Johansson et al. measured interaction normal forces between polyelectrolyte multilayers in a CP-AFM setup and found that the adhesive forces increase with increasing contact time between the surfaces, even for multilayers with an identical top layer.[11] This suggests diffusion of the chains across the interface, but the actual chain mobility could not be quantified. We will use a similar experimental setup as Johansson et al., but use grafted, oppositely charged polyelectrolyte brushes instead, to study the formation of complexes at the point where they come in contact (see Figure 12.1). In our case, the brushes may interpenetrate because of chain mobility, but we return to the same initial state after each cycle, allowing a systematic study of the various parameters that affect polyelectrolyte complexation.

Following our study presented in this Chapter, the lap shear strength of a complex between the same polyelectrolyte brushes we use here has been measured in a tensile tester by Kobayashi et al.[12] They found that these oppositely charged polyelectrolyte brushes can be used to adhere various heterogeneous surfaces, ranging from silicon wafers to stainless steel, with high shear adhesion strengths. Moreover, this charge-driven 'glue' was found to be completely reversible, and the surfaces can be unbound at high enough salt concentration, analogous to our findings here and in Chapter 6.

12.2 Experimental details

12.2.1 Materials

We used the same two polyelectrolytes as were used in Chapter 10 for measurements of the attractive interactions between oppositely charged polyelectrolyte brushes: PTMAEMA and PSPMA (see Figure 1.9). We grew these polyelectrolyte brushes on silica surfaces from the corresponding methacrylate monomers by of atom transfer radical polymerisation (ATRP). As initiator for this living polymerisation we used 3-trimethoxysilylpropyl-2-bromo-2-methylpropionate (silane initiator), which was purchased from Gelest Inc. (UK).[13] Before polymerisation, we removed the inhibitor from the METAC solution by running it through a neutral alumina column, similar to the procedure for bulk ATRP polymerisation we described in Chapter 4.

For AFM measurements, we used triangular AFM contact-mode cantilevers with spring constants k of 0.06 – 0.50 N/m, which were purchased from Veeco and modified by a glued silica colloidal probes ($R = 3.0$ µm), as described in Chapter 10. We glued the colloidal probes after modification with a polyelectrolyte brush (see below). As facing surface, we used flat silicon wafers with a 3 nm thick layer of native oxide, or brush-coated silica wafers (see Figure 12.1).

12.2.2 Polyelectrolyte brush growth

We prepared cationic PTMAEMA and anionic PSPMA brushes on flat and spherical (colloidal probe) silica surfaces by surface-initiated aqueous ATRP. First, all surfaces were cleaned by rinsing with water and ethanol and subsequent plasma treatment for two minutes. We centrifuged the colloidal silica particles at $1{,}000\times g$ for two minutes between every rinsing step and redispersed them by sonication in the next rinsing or modification step. After cleaning, we modified both flat wafers and colloidal particles with the silane initiator by placing them in a 5% (v/v) solution of the silane initiator in n-hexane for two hours, rinsing twice with n-hexane, twice with ethanol and drying under a stream of N_2.

The preparation of the polymerisation solutions is described elsewhere in detail.[14–16] Briefly, for cationic PTMAEMA brushes we prepared an ATRP solution of [METAC] : [BiPy] : [CuCl] : [$CuCl_2$] = 100 : 4 : 2 : 0.1 in a 4 : 1 (v/v) isopropanol/water mixture. We carried out the polymerisation at room temperature for two hours, leading to brushes that were approximately 50 nm thick when dried. For anionic PSPMA brushes we prepared a solution of [KSPMA] : [BiPy] : [CuCl] : [$CuCl_2$] = 75 : 1 : 0.2 : 0.1 in a 2 : 1 (v/v) methanol/water mixture and we used a polymerisation time of two hours, leading to approximately 50 nm thick dried brushes as well. After the polymerisation all flat surfaces were rinsed twice with water, twice with methanol and twice with ethanol. The colloidal silica particles were washed five

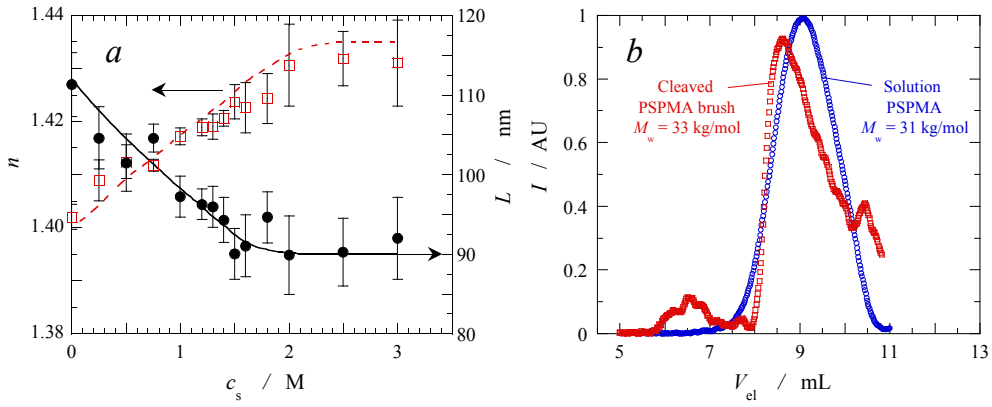

Figure 12.2: (a) Ellipsometric thickness and refractive index of PTMAEMA brush in aqueous solution as a function of salt concentration. Solid lines are drawn to guide the eye. (b) Size-exclusion chromatograms of a cleaved PSPMA brush and a solution-grown PSPMA polymer, under same conditions. This SEC was measured on a Biosilect 500 column, using 2 g/L solutions at pH 7 and a salt concentration of 0.15 M KCl, operated at 1.0 mL/min and detected by Uv/Vis absorption at 212 nm and refractive index. For calibration, we used PSS of various sizes.

times with water and five times with methanol and redispersed after centrifugation by sonication, in order to remove all copper crystals. Thorough cleaning of the colloidal particles is necessary but difficult, because the particles tend to stick together. After washing, both flat surfaces and colloidal particles were dried under a stream of N_2.

We measured the thicknesses of dried and swollen brushes by ellipsometry (Multiskop, Optel GBR), using an angle of incidence of 70°, a laser wavelength of 632.8 nm and a two-layer model (substrate and brush layer) for fitting. We measured the thickness L and refractive index n of the brush layer for at least five independent locations on each sample. We found that the average dry brush thicknesses L_{dry} was approximately 50 nm for the protocol described above, leading to 100 – 120 nm thick swollen brushes in pure water (see Figure 12.2a). The grafting density Γ of these brushes is measured by cleaving the polymer chains from a flat gold wafer (4×4 cm^2), for which we used a different thiol initiator, according to a procedure described by Jones et al.,[17] and found to be 0.8 ± 0.3 nm^{-2}. We assume that brush thickness and grafting density on spherical surfaces are the same as on flat surfaces, because the size of the spherical particles is large compared to the thickness of the brushes ($R \gg L$).

We note that this grafting density is significantly higher than the grafting density for SI-ATRP of PTMAEMA brushes on silicon wafers reported by Kobayashi et al.[18] The initiator they used is different from our ATRP initiator (on gold, but also on

silica), the type of polymer they grow is not the same and their polymerisation and cleavage procedures are different. Nevertheless, we treat our results for the grafting density with caution, since the uncertainty is expected to be large for SEC on such small sample volumes and the grafting density of our brushes is likely to be different for brushes grown on gold using a thiol initiator and brushes grown on silicon wafers using a silane initiator.

12.2.3 Force spectroscopy

Force measurements were carried out on a Nanoscope 3A AFM (Digital Instruments), equipped with a PicoForce scanner (see also Chapter 10). We used a liquid cell with a volume of approximately 250 µL, sealed with a rubber ring. The flat surface, modified with a PTMAEMA brush, was facing up, and the colloidal silica particle, modified with a PSPMA brush, was glued to the AFM tip using an epoxy glue and facing down. The liquid cell was filled with a filtered solution of KCl in water, with concentrations varying from 0 to 3.0 M.

We measured force distance curves with a typical scan range of 500 nm to 2.0 µm and scan rates ranging from 4.0 to 2000 nm/s. We recorded at least twenty separate force curves for every sample and every scan rate, except for the lowest scan rate, for which ten force curves were recorded. The distance of closest approach was taken in the constant compliance region. At this separation distance, the two silica surfaces are not in direct contact, because of the polyelectrolyte brushes that are sandwiched between the surfaces. The reference $h = 0$ will therefore refer to the separation distance at which the two polyelectrolyte brushes are compressed strongly, without relating this to an absolute separation distance between the silica surfaces. All other distances are derived from this reference position. We converted the cantilever deflection data to interaction forces using Hooke's law, $f = k\Delta z$, where k is the cantilever spring constant. In this study we have used different cantilevers with spring constants in the range of 0.06 – 0.50 N/m to cover the range of attractive forces from very weak at high salt concentrations to very strong at low salt concentrations. We determined the actual spring constants for every cantilever separately using the thermal tuning method,[19] and correcting for nonideality and cantilever support.[20]

We studied the dynamics of polyelectrolyte complexation using AFM by applying a waiting step between the approach and retract parts of the force distance cycles. During the waiting step the piezo attached to the cantilever is kept at a fixed force, which keeps the two surfaces in contact. A typical force trigger of 30 nN was used to define the start of the waiting step, making sure that the brushes were compressed strongly before the waiting step. We checked that no significant drift of either position or force occurred during this waiting step.

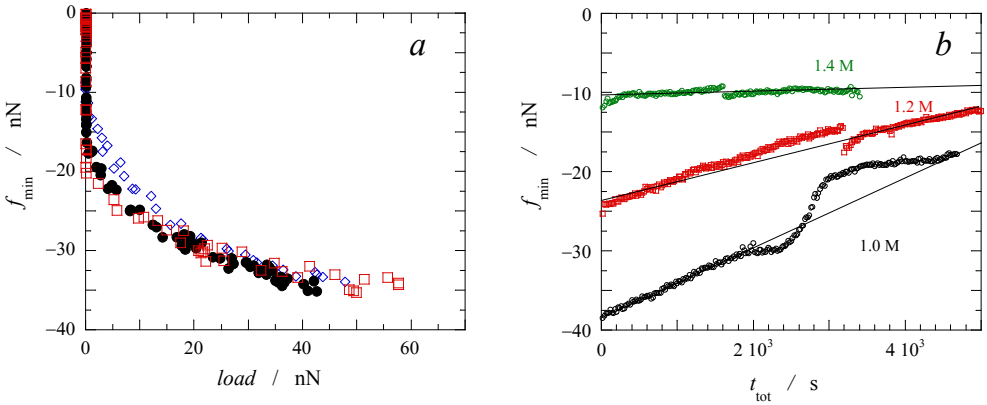

Figure 12.3: (a) Load experiment in which the attractive force between two oppositely charged polyelectrolyte brushes in a 1.4 M salt solution is plotted as a function of the applied load, using a scan rate of 2000 nm/s. Every data points correspond to a separate force curve. Different symbols correspond to different colloidal probes and flat substrates. (b) Erosion of the same polyelectrolyte brushes during force measurements. For this experiment force curves are recorded continuously, with a 20 s delay between two curves.

12.2.4 Reproducibility

We checked the reproducibility of our data on two levels: reproducibility between different probes and surfaces at the same salt concentration and reproducibility of the attractive force of a single probe in time. To achieve good reproducibility of force measurements for different samples, all colloidal silica particles we used were modified in a single synthesis batch and checked by optical microscopy to be spherical and free from solid precipitates. Freshly prepared polyelectrolyte brushes on flat surfaces were always evaluated by ellipsometry, to measure thickness ($L_{\mathrm{dry}} = 50 \pm 5$ nm, $n_{\mathrm{dry}} = 1.47 \pm 0.01$), and by optical microscopy to make sure no solid residues were present on the flat surfaces either. This resulted in an estimated error in the measured attractive forces between different samples of less than 20%, based on a separate loading experiment with different surfaces (see Figure 12.3a).

Secondly, we found that force curves that were measured continuously with a single combination of modified surfaces, show a gradual decrease of the attractive force (see Figure 12.3b). We attribute this decrease to erosion of the brushes, in other words, covalent bonds are broken and grafted chains are pulled out of the brushes. The speed of erosion depends strongly on the salt concentration. Based on Figure 12.3b, we use every combination of modified surfaces at most one hour, and always start a series of measurements at high salt concentration.

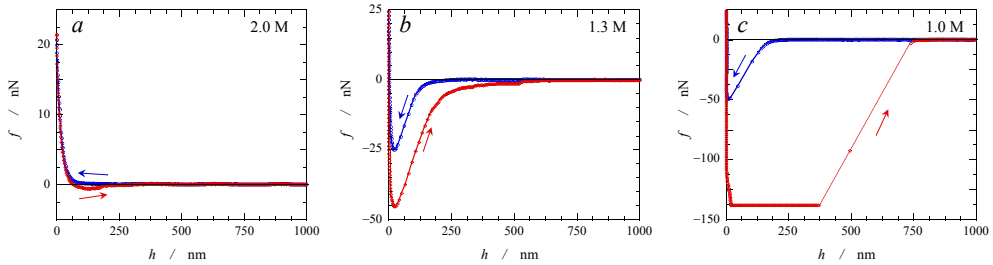

Figure 12.4: Typical force-distance curves between a negatively charged PSPMA and a positively charged PTMAEMA brush at three different salt concentrations (KCl) as indicated by the labels. Both approach and retract curves are shown, as indicated by the arrows. All force curves were recorded at a scan rate of 2000 nm/s, a scan range of 2.0 µm and a relative force trigger of +25 nN to start the retract curve after approaching.

12.3 Results and discussion

12.3.1 Force-distance curves

Surfaces covered with oppositely charged polyelectrolyte brushes give rise to very large attractive forces in AFM, much larger than recently reported for surfaces covered with adsorbed polyelectrolyte multilayers,[11] or surfaces bridged by a complex coacervate capillary bridge (see Chapter 10), even though the colloidal probe dimensions are comparable. For the 50 nm thick PTMAEMA/PSPMA brushes we used in our experiments the attractive force becomes so large in aqueous solutions with no added salt that on separation of the two surfaces the glue connection between the colloidal probe and the AFM tip breaks first as the weakest link, instead of the noncovalent ionic interactions between the oppositely charged brushes. Therefore, we always have to start our force measurements in an aqueous solution with a high salt concentration: 2 – 3 M, and then gradually proceed to lower concentrations.

A typical series of force curves, starting at a high salt concentration and changing to lower salt concentrations, is shown in Figure 12.4. In solutions with a salt concentration of 2.0 M, no attractive force is measured upon approach, and only a very small contact adhesion is measured when the surfaces are separated again. This small adhesion force of 0.1 – 1 nN is measured for all brushes in solutions with a salt concentration in the range 2 – 3 M. In addition to the small contact adhesion force, we find a repulsive force between the two brushes in both the approach and retract part of the force curve for distances smaller than 50 nm. This repulsion results from mutual compression of the brushes.

In solutions with a lower salt concentration (1.3 M), we find an attractive force in both the approach and retract curve. The hysteresis in both the strength of the

attractive force and range of attraction between approach and retract suggests that a dynamic process is taking place in the time between first contact of the brushes upon approach and final release of the brushes upon retract. This process will be discussed in detail in the following sections. We note that the range of the attractive force is in agreement with the thickness of the swollen polyelectrolyte brushes that we used in these experiments ($\approx 2\times$ 100 nm). We do not find a repulsive force here until the constant compliance region is reached, because the attraction dominates until the brushes are strongly compressed, swamping the tail of the repulsive interaction.

In solutions with a salt concentration below 1.0 M, the attractive force in the retract part of the force curve has become too large to be measured with our AFM. This is reflected in Figure 12.4c by a horizontal plateau at an attractive force that represents the detection limit of our AFM for this specific cantilever. Upon retract, the colloidal probe sticks to the facing flat surface and the cantilever bends as the piezo element moves the two surfaces apart. At a certain point, enough energy has been stored in the cantilever to disrupt the contact between the two brushes and the cantilever jumps back over a distance of 400 nm to an undeflected position.

12.3.2 Dynamics of complexation

Hysteresis in the force curves (see Figure 12.4b-c) originates from slow processes that occur once the brushes are brought into contact. Figure 12.1 gives a schematic overview of the different steps that we believe take place during the measurement of one force distance curve. When the brushes approach, a complex is formed at the point where the brushes come in contact. This complex is a skin-like layer between the two brushes, similar to the complex formed between hyaluronic acid and cationic peptide amphiphiles.[21] As the brushes are compressed, the complex grows either by bending of the chains and additional complexation between more distant parts of the chains, or by partial rupture of the complex and rebinding further along the chains. During an optional waiting step the brushes stay compressed and complex growth continues. Then, the surfaces are separated again and the polyelectrolyte chains are stretched until enough energy is stored to disrupt the complex. The detachment is of a catastrophic nature: once a few ion pairs within the polyelectrolyte are disrupted, the force is transferred to the remaining ion pairs which will be disrupted as well until the whole complex has disappeared. Now the brushes are completely separated again and relaxation of the polyelectrolyte chains takes place.

Based on the picture sketched above, we expect that hysteresis in the force-distance curves can be minimised by reducing the scan rate of the piezo element while also reducing the time the brushes are compressed, that is, beyond the point where the interaction turns repulsive, as much as possible. Using this approach, the waiting time in Figure 12.1 is minimised and only a skin layer of complex is formed. In the

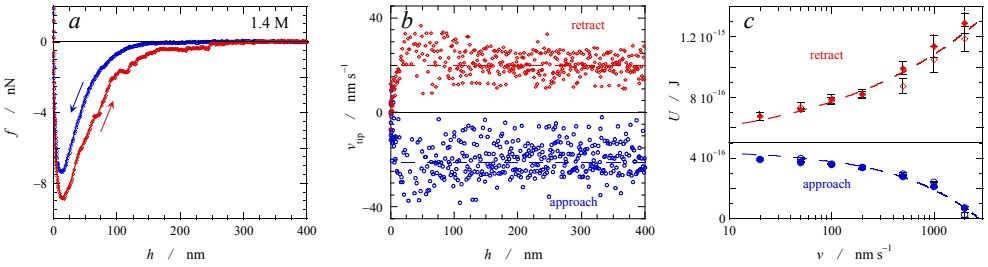

Figure 12.5: (a) Approaching a hysteresis-free force-distance curve between PTMAEMA and PSPMA polyelectrolyte brushes in solution with a salt concentration of 1.4 M, using a low scan rate of 20 nm/s and a total time of compression of less than 50 ms. (b) Actual tip velocity as a function of separation for the measurement shown in (a). The dotted line is the input value for the scan rate. (c) Energy of interaction between a PTMAEMA and PSPMA polyelectrolyte brush surface, approximated as the area under the force-distance curve, as a function of scan rate. The dotted lines are a power law fits of the data according to $U = U_{\mathrm{eq}} + Av^B$, with identical U_{eq} of 5×10^{-16} J.

limit of very low scan rates we should then approach a reversible, in other words, equilibrium force curve.

Figure 12.5a shows a force curve using the lowest scan rate accessible with our setup where interference from drift is not significant yet: 20 nm/s over a total scan range of 1.0 µm. We reduce the compression time of the brushes to less than 50 ms. Upon approach of the two surfaces an attractive force is measured with a range of 200 nm. The attraction increases with decreasing distance between the surfaces because an increasing area of the two brushes comes into contact. At the point of contact between the brushes a complex is formed instantaneously. As we separate the brushes again after minor compression we measure an almost identical attraction between the brushes with a range of attraction that is only slightly larger than in the approach curve. No sudden jumps of the tip occur, as shown in Figure 12.5b, where the actual tip velocity, derived as $v_{\mathrm{tip}} = \mathrm{d}h/\mathrm{d}t$ from Figure 12.5a, is plotted as a function of its position, h.

The fact that approach and retract forces are almost identical suggests that we are indeed measuring a near-equilibrium process. For such processes the area under the curve in Figure 12.5a is a measure for the free energy of interaction of the skin layer of complex. Figure 12.5c shows how the energy of interaction, taken as the integral of the force-distance curve, changes as a function of the scan rate. The interaction energy of both the approach and the separation curve seem to level off to an equilibrium value for the free energy of interaction, which is estimated to be 5×10^{-16} J, based on extrapolation of the data. An important reason why the interaction energy of the approach and retract parts of the force curve will never be identical

in this experiment, is the fact that the complex between the polyelectrolyte brushes starts to grow from the moment their outermost parts come in contact, which occurs already at a separation distance of 200 nm in the approach curve.

An estimate of the number of contacts is more difficult to make. The contact area can be approximated by $2\pi R\Delta h$,with Δh the range of interaction (approximately 200 nm). If we assume that every polymer chain in the contact area makes a single contact in the skin-like layer with an oppositely charged polymer, we find a total number of contacts, $n_0 = 2\pi R\Gamma\Delta h = 3 \times 10^6$. The average free energy of interaction per ion pair at this particular salt concentration (1.4 M), close to the critical point, is then 0.04 k_BT. However, single molecule force spectroscopy measurements (see Chapter 11) indicate that the energy of single ionic bonds must be larger (about 1 k_BT near the critical point). Probably, the effective contact area is smaller, the grafting density is lower and only a fraction of the polymer chains in this area will actually form an ionic bond with an oppositely charged chain from the facing surface. Especially if the polymers in the brushes are a little polydisperse, long chains are known to stretch at the expense of shorter chains,[22] and the shorter chains will never reach the top of the brush, where the ionic bonds are formed upon first contact.

12.3.3 Effect of salt on polyelectrolyte complex strength

Qualitatively we have shown above that salt has a strong effect on the interaction between oppositely charged polyelectrolyte brushes. Salt can be used to change the interaction from repulsive in solutions with a high salt concentration (Figure 12.4a) via reversibly attractive in solutions with an intermediate salt concentration (Figure 12.5) to nearly irreversible sticking in solutions with no or a low salt concentration (Figure 12.4c). Here, we determine the value of the interaction force, the range of attraction and the position of the attractive force minimum as a function of salt concentration.

Figure 12.6a shows the attractive force minimum for both approach and retract parts of the force distance curve as a function of salt concentration for a fixed scan rate. We note that attraction between the surfaces is observed only below a critical salt concentration. In our experiments we find a critical salt concentration of 1.5 M, independent of scan rate. This critical salt concentration is comparable to the critical salt concentration of complex coacervates formed from these polyelectrolytes (see Chapter 4 and 10).

Below the critical salt concentration we measure an attractive force that rapidly becomes larger with decreasing salt concentration. The hysteresis between approach and retract grows bigger with decreasing salt concentration as well. This indicates that the stronger contacts between the brushes slow down the dynamics of ion pair disruption (see Figure 12.1). For even lower salt concentrations the attractive forces

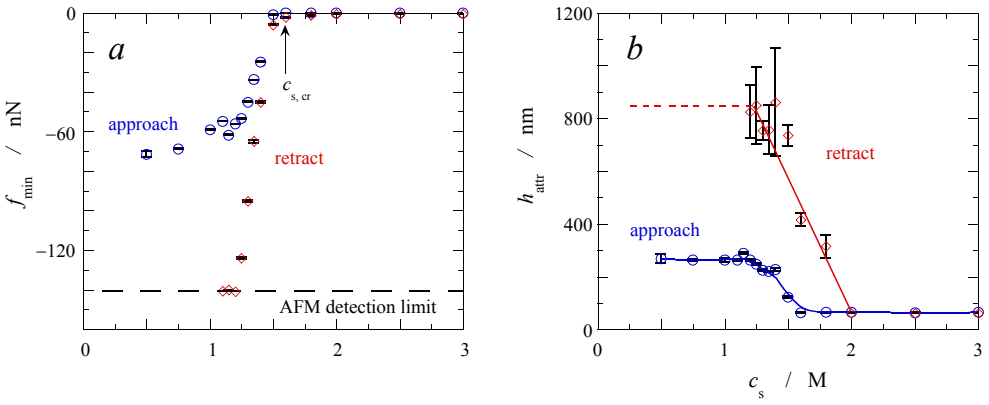

Figure 12.6: Effect of salt concentration on (a) the attractive force and (b) the range of attraction in force curves of the interaction between PTMAEMA and PSPMA polyelectrolyte brushes. All corresponding force curves were recorded with a scan rate of 2000 nm/s, a scan range of 2.0 µm and a relative force trigger of +25 nN.

upon separation of the brushes become larger than the detection limit of our AFM (depending on the cantilever and setpoint).

Figure 12.6b shows the range of attraction, defined as the distance over which the attractive force is larger than 1 nN, as a function of salt concentration. Below the critical salt concentration the range of attraction increases with decreasing salt concentration. It reaches a plateau of approximately 250 nm, which is about 2× the swollen brush thickness, for the approach. For the retract curves where a jump occurs (e.g., Figure 12.4c), we could not determine the range of attraction. Therefore, we only show the data for force curves lacking a jump out of contact in Figure 12.6b.

Finally, we measured the position of the attractive force minimum as a function of salt concentration. We find that the position is not dependent on salt concentration and always occurs at distances smaller than 40 nm, where most chains on the curved surface can make contact.

12.3.4 Kinetics of complex formation and disruption

The slow dynamics of the polyelectrolyte chains precludes the measurement of a hysteresis-free force curve and, hence, the determination of a true free energy of ion pairing without extrapolation. An alternative approach to determine the relevant interaction forces between the two oppositely charged polyelectrolyte brushes is therefore to take the dynamics explicitly into account. In dynamic force spectroscopy, kinetic processes are studied by changing the loading rate of the disruption process. We have carried out the dynamic force spectroscopy for different compression times

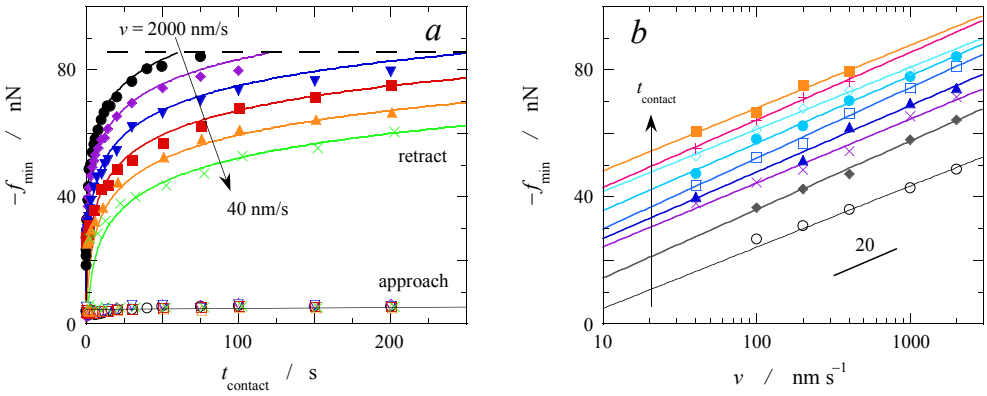

Figure 12.7: (a) Attractive force between a PTMAEMA and PSPMA polyelectrolyte brush as a function of compression time in solution with a salt concentration of 1.3 M for different scan rates. Different symbols correspond to a different scan rates (in direction of the arrow): 2000, 1000, 400, 200, 100 and 40 nm/s. Forces from the approach curve are displayed using open symbols, forces from retract curves using closed symbols. The solid lines are drawn to guide the eye. (b) Attractive force as a function of scan rate for the same brushes. Different symbols correspond to different compression times (in direction of the arrow): 2, 10, 20, 30, 50, 75, 100, 150 and 200 seconds. Solid lines are fits to Equation 12.4. All data points were recorded with a scan range of 2.0 µm and a constant compression force in contact of +30 nN.

of the brushes in order to quantify the process of polyelectrolyte complex growth as schematically shown in Figure 12.1.

Figure 12.7a shows the dependence of the attractive force during approach and retract as a function of compression time for various scan rates. As expected, we find no dependence of the attractive force in the approach part of the force curve on the compression time of the brushes, since it follows the approach chronologically. The measured rupture force in the retract part of the force curve however, shows a clear increase with both increasing compression time and increasing scan rate.

For a quantitative understanding of the rupture process of the ionic bonds between the polymer brushes, we consider the bond rupture model derived in Chapter 11. If the natural life time of these bonds would be fast and bond reformation could take place during the separation, we would expect near-equilibrium conditions to apply and to find no dependence of the rupture force on the loading rate.[23–25] If on the other hand, rebinding may be neglected, because of the soft linkers between the ionic bond and the AFM cantilever and the high loading rates, the rupture force will depend on the loading rate. For single bonds and sharp energy barriers, the rupture force is proportional to the logarithm of the loading rate (Equation 11.6). For multiple bonds, the exact relation between rupture force and loading rate depends on the arrangement

of the subsequent bonds. In case of a zipper-like arrangement (see Figure 11.7c), again a logarithmic dependence is found.[26] In case of a shear or parallel arrangement (see Figures 11.7b, d), the dependence is much stronger than logarithmic (see Chapter 11). In the limit where the interactions can be described by an effective friction force between the chains instead of discrete bonds, the rupture force is proportional to the loading rate.[27]

Based on Chapter 11 and the results discussed in the previous section, we expect far-from-equilibrium conditions to apply to the rupture of the ionic bonds between two oppositely charged brushes. Moreover, the attractive force clearly grows with increasing compression time, indicating that more ionic bonds are formed for every polymer chain with increasing compression time. To determine what model for multiple bond rupture applies to the ionic bonds between two brushes, we plot the rupture force as a function of the logarithm of the loading rate (Figure 12.7b).

Figure 12.7b shows a clear logarithmic dependence of the rupture force on loading rate for all compression times we apply. This suggests that a zipper model should apply to the disruption of the complexes of ionic bonds between two oppositely charged brushes we study here. Apparently, sideways bending of the chains and an increasing complexation of more distant parts of the chains without partial dissociation is favoured over bond dissociation and rebinding further along the chain when we compress the brushes (see Figure 12.1). In fact, natural dissociation of a complex becomes less and less likely as a zipper of ionic bonds is growing ($\tau_N \propto \exp(NE_a/k_BT)$), which supports this hypothesis.

In the zipper model for bond rupture, an applied force is focused on the first connecting bond. After failure of the first bond, the force is transferred to the next bond and the force scale (f_β, Equation 11.4) remains unchanged. The failure of all N connections takes place at a rate of

$$k_{\mathrm{zip}}^{N\to 0}(f) = \frac{1}{\tau_{\mathrm{zip}}} = \left[\sum_{n=1}^{N} \frac{1}{k_0} \exp\left(-\frac{f}{f_\beta}\right)\right]^{-1} = \frac{1}{N}\, k_0 \exp\left(\frac{f}{f_\beta}\right) \tag{12.1}$$

where all parameters are identical to those in Equations 11.5 and 11.7. The second equality applies if the N bonds are uncooperative.[26] The survival probability of the whole zipper follows from

$$p(t) = \frac{1}{r_f} k_{\mathrm{zip}}(f(t)) \exp\left[-\int_0^t \frac{1}{r_f} k_{\mathrm{zip}}(f(t'))\, \mathrm{d}t'\right] \tag{12.2}$$

and the average zipper lifetime follows from integration over the survival probability.

$$t^* = \int_0^\infty p(t)\,\mathrm{d}t = \frac{f_\beta}{r_\mathrm{f}} \ln\left(\frac{r_\mathrm{f} N}{k_0 f_\beta}\right) \tag{12.3}$$

where the second equality follows from substitution of $f = r_\mathrm{f} t$, that is, a constant loading rate. The total rupture force is

$$f^* = n_0 r_\mathrm{f} t^* = n_0 f_\beta \ln\left(\frac{k}{k_0 f_\beta}\right) + n_0 f_\beta \ln N + n_0 f_\beta \ln v \tag{12.4}$$

where $r_\mathrm{f} = kv$, k is the effective spring constant,[28] v is the scan rate, and n_0 is the total number of chains in contact. We multiply by n_0, because we assume that the different polyelectrolyte chains in the brush act as independent springs and are not linked as in the case of a parallel arrangement of bonds connected by a single spring, as shown in Figure 11.7b.

Figure 12.7b shows the predicted logarithmic dependence of the mean rupture force f^* on the scan rate v. The slope of the fits is equal to $n_0 f_\beta \ln(10)$. Again, estimating the number of contacts is difficult. However, we found that $f_\beta \approx 26$ pN for single ionic bonds, independent of salt concentration (Figure 11.8). Using this value as an estimate for the force scale in this experiment as well, we find that the number of contacting chains is approximately 10^3, which is more than three orders of magnitude lower than we predicted, based on geometric arguments (Figure 12.5). Apparently, only a fraction of the chains on the surface is involved in complex formation at the brush interface,[22] and more than one ionic bond is formed in the experiment shown in Figure 12.5, because of the low scan rate.

With the zipper model for complex disruption between two brushes, we can find additional information on the dynamics of complex growth from analysis of the intercept of the fits in Figure 12.7b. According to Equation 12.4 the intercept should increase as $\ln N$. By plotting $f^* - n_0 f_\beta \ln v$ as a function of time, we should obtain a mastercurve that is independent of scan rate and only reflects the effect of complex growth in terms of N. This plot is shown in Figure 12.8a. Figure 12.8b shows a plot of $\exp(f^*/n_0 f_\beta - \ln v)$, which is directly proportional to the size of the complex N, according to Equation 12.4. We find that the size of the complex grows linearly in time, indicating that the chains bend or move with a constant, but low velocity. In other words, the forces acting on every segment of the chain, including the electrostatic interaction forces driving complex growth and the friction forces slowing down growth of the complex, balance each other. We note that eventually the complex growth should slow down, when almost all charges along the polyelectrolyte chains have formed an ionic bond with an oppositely charged chain inside the complex, but this regime was not experimentally accessible.

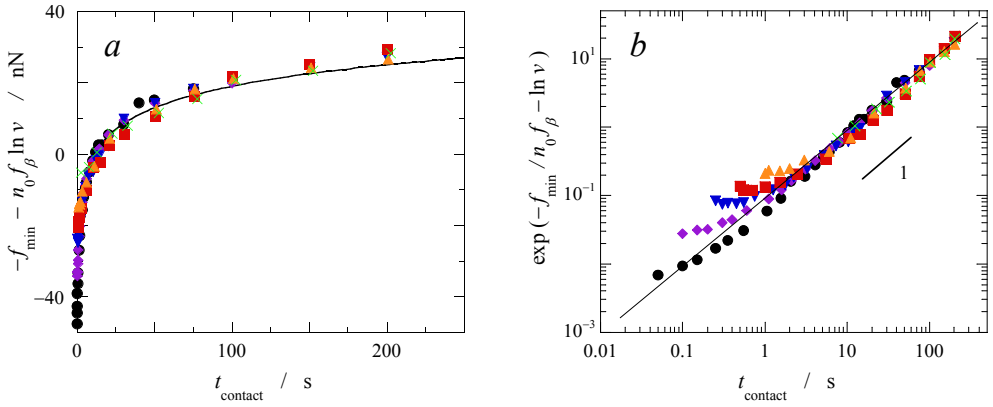

Figure 12.8: a) Rescaled attractive forces f_{min} from Figure 12.7aa as a function of compression time. The solid line is a logarithmic fit to the combined data. (b) Same measurements, rescaled by plotting $\exp(f_{min}/n_0 f_\beta - \ln v)$, which is directly proportional to the size of the complex N, assuming a zipper arrangement, as a function of compression time on a double logarithmic scale. The solid line is a power law fit to the combined data.

At very short times we find that N deviates from linearity and seems to be slightly larger than predicted based on linear growth. We attribute this deviation to a systematic underestimation of the total compression time of the brushes. The compression time is estimated as the sum of the set delay time between approach and retract and the time during which we measure a repulsive force between the brushes in the constant compliance region. However, upon approach the contact between the outer parts of the brushes is already established before a repulsive force is measured. Growth of the complex between the brushes will already start there, thus leading to longer actual contact times. The relative magnitude of this systematic error is larger for small set delays, that is, at short total compression times, in Figure 12.8b.

Finally, we have carried out similar dynamic force spectroscopy measurements at different salt concentrations to demonstrate the effect of salt on the growth rate of the polyelectrolyte complexes. Figure 12.9 shows the growth of a complex phase at different salt concentrations, together with a logarithmic fit of the data, according to Equation 12.4 and the assumption that $N \propto t_{contact}$. We find significantly larger forces at lower salt concentrations, originating from the strong decrease in k_0 (Equation 12.4) with increasing salt concentration (see also Figure 11.9). In addition, the logarithmic dependence seems to describe all curves below the critical salt concentration quite well, suggesting that N indeed increases linearly with t for all salt concentrations. The apparent increase in slope with decreasing salt concentration could have two causes. First of all, f_β increases slightly with decreasing salt concentration, as found in Chapter 11. Secondly, the number of contacts n_0 may increase with decreasing

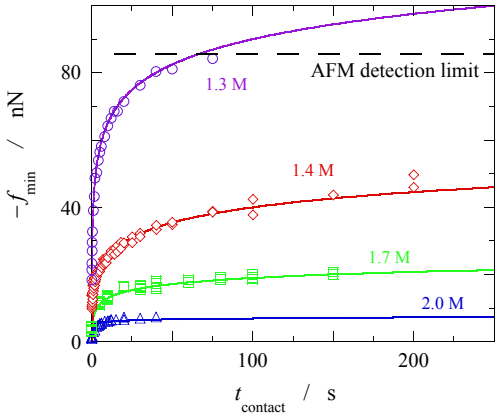

Figure 12.9: Attractive force between PTMAEMA and PSPMA brushes as a function of compression time at different salt concentrations, as indicated by the labels. All data points were recorded using a scan rate of 2000 nm/s, a scan range of 2.0 µm and a constant compression force in contact of +30 nN. Solid lines are logarithmic fits to the data.

salt concentration, because the chains in the brushes are more strongly stretched at lower salt concentrations and because the effective critical salt concentration may be different for chains of different length, as we discussed already in Chapter 6. At lower salt concentration, also shorter chains participate in complex formation.

12.4 Concluding remarks

We have described a direct way to measure the interaction forces between oppositely charged polyelectrolyte brushes. The rupture forces are directly related to the strengths of single ionic bonds (Chapter 11), but much larger because many bonds are formed between the brushes. We showed that the colloidal probe AFM setup allows direct measurement of these forces and that equilibrium complexation and disruption is accessible at very low scan rates. By varying the scan rate and compression time, we found that multiple ionic bonds along one polymer chain are formed in a zipper-like arrangement. The growth of these complexes in time occurs at a constant speed, indicating that no net force is acting on the chain segments during complexation. Our approach to directly measure these interactions in dense complex coacervates is a unique way to quantitatively study the formation and strength of polyelectrolyte complexes of grafted polyelectrolytes.

References

[1] H. Lee, N. F. Scherer, and P. B. Messersmith, *Proc. Nat. Acad. Sci. USA*, 2006, **103**, 12999–13003.

[2] R. J. Stewart, C. S. Wang, and Hui Shao, *Adv. Coll. Int. Sci.*, 2011, **167**, 85–93.

[3] W. M. de Vos, J. M. Kleijn, A. de Keizer, and M. A. Cohen Stuart, *Angew. Chem. Int. Ed.*, 2009, **48**, 5369–5371.

[4] W. A. Ducker, T. J. Senden, and R. M. Pashley, *Nature*, 1991, **353**, 239–241.

[5] H.-J. Butt, *Biophys. J.*, 1991, **60**, 1438–1444.

[6] M. Tirrell, *Curr. Opin. Coll. Int. Sci.*, 1997, **2**, 70–75.

[7] M. Chen, W. H. Briscoe, S. A. Armes, H. Cohen, and J. Klein, *ChemPhysChem*, 2007, **8**, 1303–1306.

[8] M. Chen, W. H. Briscoe, S. A. Armes, and J. Klein, *Science*, 2009, **323**, 1698–1701.

[9] K. Estel, G. Kramer, and F.-J. Schmitt, *Colloids and Surfaces A*, 2000, **161**, 193–202.

[10] J. Salmi, M. Österberg, and J. Laine, *Colloids and Surfaces A*, 2007, **297**, 122–130.

[11] E. Johansson, E. Blomberg, R. Lingström, and L. Wå gberg, *Langmuir*, 2009, **25**, 2887–2894.

[12] M. Kobayashi, M. Terada, and A. Takahara, *Soft Matter*, 2011, **7**, 5717–5722.

[13] I. E. Dunlop, W. H. Briscoe, S. Titmuss, R. M. Jacobs, V. M. Osborne, S. Edmondson, W. T. S. Huck, and J. Klein, *J. Phys. Chem. B*, 2009, **113**, 3947–3956.

[14] N. Cheng, O. Azzaroni, S. Moya, and W. T. S. Huck, *Macromol. Rapid Commun.*, 2006, **27**, 1632–1636.

[15] M. Ramstedt, N. Cheng, O. Azzaroni, D. Mossialos, H. J. Mathieu, and W. T. S. Huck, *Langmuir*, 2007, **23**, 3314–3321.

[16] E. Spruijt, E.-Y. Choi, and W. T. S. Huck, *Langmuir*, 2008, **24**, 11253–11260.

[17] D. M. Jones, A. A. Brown, and W. T. S. Huck, *Langmuir*, 2002, **18**, 1265–1269.

[18] M. Kobayashi, M. Terada, Y. Terayama, M. Kikuchi, and A. Takahara, *Macromolecules*, 2010, **43**, 8409–8415.

[19] J. L. Hutter and J. Bechhoefer, *Rev. Sci. Instrum.*, 1993, **64**, 1868–1873.

[20] R. W. Stark, T. Drobek, and W. M. Heckel, *Ultramicroscopy*, 2001, **86**, 207–215.

[21] R. M. Capito, H. S. Azevedo, Y. S. Velichko, A. Mata, and S. I. Stupp, *Science*, 2008, **319**, 1812–1816.

[22] W. M. de Vos and F. A. M. Leermakers, *Polymer*, 2009, **50**, 305–316.

[23] H. Schönherr, M. W. J. Beulen, J. Bügler, J. Huskens, F. C. J. M. van Veggel, D. N. Reinhoudt, and G. J. Vancso, *J. Am. Chem. Soc.*, 2000, **122**, 4963–4967.

[24] S. Cui, C. Liu, Z. Wang, X. Zhang, S. Strandman, and H. Tenhu, *Macromolecules*, 2004, **37**, 946–953.

[25] S. Zou, H. Schönherr, and G. J. Vancso, *Angew. Chem. Int. Ed.*, 2005, **44**, 956–959.

[26] P. M. Williams, *Anal. Chim. Acta*, 2003, **479**, 107–115.

[27] V. N. Koinkar and B. Bhushan, *J. Appl. Phys.*, 1997, **81**, 2472–2479.

[28] C. Ray, J. R. Brown, and B. B. Akhremitchev, *J. Phys. Chem. B*, 2007, **111**, 1963–1974.

Part IV

General discussion and summary

Chapter 13

General discussion: from ionic bonds to liquid phases

In this final Chapter we broaden our scope again and try to look beyond the current complex coacervate horizon. This thesis was divided into three main parts, going from the macroscopic stability of complex coacervates to microscopic structures, down to the strength of the individual ionic bonds between oppositely charged macromolecules. In each Chapter, we have discussed our results and summarised our findings on a specific topic related to one of these parts. Here, we highlight some important connections between various parts and Chapters and between our findings and other areas of research. While making such connections, we find that the research questions we addressed at the beginning of this thesis can be answered in more or less detail. Inevitably, and perhaps more importantly as well, we also find new questions and challenges related to complex coacervates and their applications. We discuss those open questions here and speculate on possible approaches to answer them.

13.1 Introduction

In the introduction to this thesis we have indicated that complex coacervates are dense phases of oppositely charged hydrophilic colloids that contain a significant amount of 'hydration' water or another solvent. They form by associative phase separation of a mixture of the oppositely charged colloids and are essentially liquids ("tropfbare Flüssigkeiten"). Complex coacervates and the underlying aggregation by association of opposite charges are present in many natural and man-made systems, most likely because, on the one hand, charges are ubiquitous in the world of molecules and particles in water, and on the other hand, complex coacervation seems not to discriminate against different charged polymers, colloids or micelles. [1]

This short introduction not only summarises many important aspects of complex coacervates, but also includes several assumptions and uncertainties about complex coacervates, which are worthwhile to discuss in more detail here.

1. The *associative phase separation* that leads to the formation of complex coacervates with a binodal composition implies that a thermodynamic equilibrium state is reached upon phase separation. However, in many applications and in most naturally occurring complex-coacervate-like aggregates, where the same ionic bonds are formed, a similar equilibrium state and corresponding structure is arguably never reached. We discuss this discrepancy and the equilibrium state of the complex coacervates we have studied in Section 13.2.

2. Complex coacervates are dense phases containing significant amounts of hydration water, but their actual structure, from the size of individual monomers up to several micrometres, remains largely unknown. Scattering techniques reveal that large-scale density fluctuations must be present, but they do not resolve them into structural arrangements, nor do they give an explanation for the presence of hydration water. Assuming that the complex coacervates have reached an equilibrium state, simulations may offer a tool to study the structure in more detail. We discuss the challenges in such simulations and show some preliminary results of a new approach in Section 13.3.

3. The apparent non-discriminatory nature of complex coacervates suggests that generic electrostatic interactions prevail over specific interactions. In fact, we have frequently used arguments based on generic electrostatic interactions to explain effects we observed. We discuss the validity of this assumption of generality, its limitations and its connection with the preferred compositions of complex coacervates in Section 13.4.

4. The process of formation of complex coacervates, going from separate polyelectrolyte solutions to a semidilute, randomly mixed polymeric liquid contains

many steps that are essentially unknown. Nevertheless, these steps are highly relevant for many naturally occurring complex-coacervate-like assemblies, as they almost never reach the final stage of random mixing. In Section 13.5 we discuss an approach to study this formation process in detail.

5. The ultimate goal of some of the measurements presented at the end of this thesis would be to predict the stability of various complex-coacervate-like structures *a priori* from the strength of individual ionic bonds. In Section 13.6 we discuss the fiction and feasibility of this goal. How close is the relation between individual bond strengths and stability of complex coacervates?

13.2 The question of equilibrium

13.2.1 Equilibrium in various charge-driven structures

Of all natural examples, the underwater adhesive produced by the sandcastle worm is perhaps closest to a true complex coacervate.[2] The glue is secreted as a fully mixed dispersion of proteins, which acquire opposite charges when the pH changes from 5 in the worm's secretory system to above 7 in the ocean environment. In addition, the mixture contains curing agents with a high concentration of 3,4-dihydroxyphenylalanine (dopa) residues that convert into an unstable *o*-quinone at high pH and form cross-links. As the glue is secreted, the change in pH leads to an instantaneous electrostatic attraction between the fully mixed, charged proteins, giving rise to a structure that is similar to the semidilute networks we found in Chapter 7. At the same time however, the curing agents start cross-linking different components of the glue and within minutes to hours, the glue has become a leathery solid, unable to further rearrange. If only the complex coacervation process would play a role, we would expect the newly formed complex to expel or take up water, depending on its binodal composition, and some macroions to dissolve in the dilute phase. The latter would, however, be detrimental to the small volume of secreted glue, because eventually all proteins would dissolve in the vast ocean. Clearly, curing is essential for this adhesive. After curing, the structure of the glue appears porous. Possibly, these pores arise from a combination of the processes described above: the glue adheres to the solid particles, complex coacervation drives densification of the glue, leading to concentration gradients, and some of the proteins that are not cross-linked yet in the most dilute regions dissolve in the surrounding ocean.

In pectin-stabilised milk drinks the pectins form a tightly adsorbed layer around casein micelles that prevents flocculation by a combination of electrostatic and steric repulsion.[3] Apparently, the attractive electrostatic interactions between casein and pectin are so strong that virtually no relaxation of pectin layers takes place. Other-

wise, bridging and macroscopic phase separation into a complex coacervate phase and a dilute phase containing excess pectin might take place, analogous to the complex coacervation in mixtures of classical amphiphilic micelles and oppositely charged polyelectrolytes.[4]

In DNA/histon complexes, interactions between specifically recognised DNA sequences, histons and other DNA-binding proteins lead to a highly ordered folding of DNA around histon octamers instead of random mixing.[5,6] Apparently, the folding process leads to a state of lower free energy, as a result of these highly specific interactions. Also in the bacterial nucleoid, DNA, RNA and many different proteins all interact specifically with each other to form a highly organised structure.[7,8]

In layer-by-layer assemblies,[9,10] polyelectrolyte complexes and capsules[11,12] and membranes,[13] the various polyelectrolytes are aggregated in a kinetically frozen state, in which virtually no relaxation takes place and the polymers are immobile. Otherwise, layers would have to mix and possibly dissolve,[11,14] which they sometimes do,[15] capsules would collapse because of the interfacial tension acting on the boundaries and membranes would fold or collapse.

Summarising the above, the structures arising from attractive electrostatic interactions in natural systems and man-made materials are not the same as what we believe to be the equilibrium structure and composition of complex coacervates, because of anchoring of the interacting molecules, slow relaxation in kinetically frozen aggregates or additional interactions that overpower the attractions between opposite charges. This raises two important questions. First of all, what is the equilibrium state and structure of complex coacervates? This question relates to our experiments in Chapters 3, 7, 8, 9 and 10 and to the driving forces for complex coacervation, based on our discussion in Chapters 2 and 3. We address this question hereafter and in Section 13.3. Secondly, what is the relevance of our study of complex coacervates for the understanding of charge-driven complexation in practical situations? We address this question in Sections 13.5 and 13.6.

13.2.2 Equilibrium in the complex coacervates in this thesis

In Chapters 3 and 7 we argued that complex coacervates are phase separated from a coexisting dilute phase. The dilute phase contains a non-negligible polymer concentration. The complex coacervate is essentially a semidilute polymer solution in which both polycations and polyanions adopt an ideal-chain conformation. They form ionic bonds between single pairs or small sequences of opposite charges, which continuously break and reform. Our conviction that the complex coacervates we have studied in this thesis have reached an equilibrium composition and structure is based on experimental evidence from a combination of measurements. We mention four key observations.

First of all, we find identical compositions of the dilute phase and the complex coacervate when we change the order of mixing of polycation and polyanion. Moreover, the rheological behaviour of these complex coacervates remains unchanged. Most combinations of polyelectrolytes from Chapter 4 form very similar, transparent, liquid-like phases at sufficiently high salt concentrations, irrespective of the way they are prepared.

Secondly, if we add salt to an already phase separated mixture of polycations and polyanions, we find that the composition of the coexisting phases changes according to our experimental phase diagram (Figure 3.7). Moreover, the rheological behaviour of these complex coacervates changes accordingly.

Thirdly, the rheological behaviour of the complex coacervates indicates that they are viscoelastic *liquids* with a terminal relaxation time that increases with decreasing salt concentration (Chapter 8 and 9). Eventually, they flow and all stresses in the complex coacervate networks are dissipated. We find terminal relaxation times of $\mathcal{O}$ $(10^3 - 10^4$ s) for our complex coacervates at the lowest experimental salt concentrations. On the other hand, we typically let our samples equilibrate for $\mathcal{O}$ $(10^6 - 10^7$ s), which suggests that all relaxation processes must have run to completion.

Finally, the phase separated mixtures share many phenomenological characteristics with classical liquid-liquid phase separated systems, such as oil-water mixtures. At sufficiently high salt concentration the separated phases can be mixed by shaking to form complex coacervate droplets (see Figure 1.3), which will settle as a macroscopically separated phase again in time. In addition, they exhibit an interfacial tension, which we have quantified in Chapter 10.

13.3 The structure of complex coacervates: cohesion in simulations

Our understanding of the structure of complex coacervates from the size of individual monomers up to several micrometres comes predominantly from scattering experiments, as discussed in Chapter 7. Simulations offer a promising way to obtain more insight into the results from scattering experiments by combining fine control over the interactions between the various components and the possibility to analyse the resulting structures in great detail. Here we discuss the challenges in simulations of complex coacervates by considering the driving forces for the actual complex coacervate phase formation.

The cohesive interactions in complex coacervates must originate from correlations between charges if electrostatic interactions compose the only attraction between oppositely charged macroions, that is, if there are no additional hydrophobic interactions, hydrogen bonds or other specific interactions. If we reconsider the two opposite

charges from Section 1.4, we realise that Coulomb's law predicts that they will be attracted to each other until they have reached the exact same point, because their finite size is not taken into account. In reality, ions do have a finite size and salt solutions will eventually crystallise in well-defined lattices, because of a combination of electrostatic attractions and 'steric' repulsions due to overlap of orbitals. [16] Already in dilute electrolyte solutions the ensuing correlations between ions are apparent.

In the Voorn-Overbeek theory these correlations are explicitly taken into account at a Debye-Hückel level. The first term in Equation 3.4 is essentially the Debye-Hückel correlation free energy of an electrolyte solution. [17] As we have discussed in Chapter 3, the result is an effective cohesive interaction between charged species. Unlimited densification of the charges is prevented by the second term, the translational entropy. Since the polymers have a much smaller translational entropy than monovalent salt ions, they become much more concentrated and thus form a complex coacervate phase. Interestingly, monovalent salt ions are also expected to accumulate in the complex coacervate phase, because the charge density there is higher than in the coexisting dilute phase. Despite the success of this mean-field theory in predicting the occurrence of complex coacervation, it cannot be used to study the structural properties of complex coacervates, because the connectivity of polymeric charges is not taken into account.

In simulations of complex coacervates, aimed at resolving their equilibrium structure, the correlations between charges play a crucial role as well. Classical mean-field theories that do not explicitly include ion correlations are not capable of predicting the formation of complex coacervate phases at all. [18] Because actual potential energy fields are replaced by a mean-field potential that averages beyond single segments, two oppositely charged polymers will end up at exactly the same (average) position, and their combined mean-field potential equals zero. As a result, there is no cohesive interaction between several of these 'pairs'. In reality however, the finite size of monomers prevents two oppositely charged monomers from coming too close and the actual positions of two oppositely charged polymers will continuously fluctuate around an average identical position, giving rise to continuously changing dipoles. Clearly, these fluctuations are crucial for the formation of complex coacervate phases.

In the Random Phase Approximation (RPA) Gaussian fluctuations of concentrations around the mean-field average are taken into account via a one-loop correction of the mean-field potential. [19–21] Both chain connectivity and ion-ion correlations can be taken into account. The fluctuations induce a decrease of the structure factor at larger wave vectors, due to local inhomogeneities in the concentration, whereas at the mean-field level it is constant. [20] Using this one-loop approximation, the formation of polyelectrolyte complexes has been predicted theoretically. [20,21] The assumption that polymer chains are Gaussian at all length scales limits this approach to weakly charged chains at relatively high densities.

In Field-Theoretic Simulations (FTS) all fluctuations of the potential energy can be taken into account by extending the potential fields to the complex plane and adapting a complex Langevin (CL) stochastic simulation method to evaluate ensemble averages of observable quantities.[18,22,23] Using this approach, the full numeric simulation of polymer field theories becomes possible. As we described in Chapter 10, this approach has been used to simulate complex coacervate phases and complex coacervate core micelles and to calculate the interfacial tension between a complex coacervate phase and its coexisting dilute phase. So far however, this approach seems to be limited to Gaussian chains.[23]

In Molecular Dynamics (MD) simulations the finite size of ions and atoms can be taken into account at the level of individual ions and atoms.[24] In these simulations, the correlations between charges are not explicitly included, as in the theory of Voorn and Overbeek, but they follow from the pair potentials between various atoms. Usually however, MD simulations are carried out at a coarse-grained level, where monomers are represented by spheres that interact with a combination of the Lennard-Jones and Coulomb potential and a potential for the finite extension of chemical bonds in the backbone.[25,26] So far, these simulations can only include a limited number of polymer chains and the long and large simulations that are required to study the structure of complex coacervates are not feasible yet.

We finally return to the mean-field level to discuss an alternative possibility for studying complex coacervation in simulations. We have implemented a Monte Carlo (MC) algorithm that explores the translational degrees of freedom of polymer chains, while a self-consistent field routine evaluates the polymer chain conformations for a given position of the polymers (MC-SCF).[27] To allow for Monte Carlo moves, one segment in each polymer is anchored to a specific location: either a single grid point or a limited range of grid points. Equilibrium thermodynamic parameters are evaluated in the same way as for conventional Monte Carlo simulations, after sufficient sampling around an average total energy.

The advantages of this approach are twofold. First of all, anchoring of the chains by one of their segments gives rise to excluded volume effects and leads to swelling of the polymer chains ($R \propto N^{0.6}$ in dilute solutions with a good solvent).[27] In other words, the chains are no longer necessarily Gaussian. Secondly, and perhaps more importantly, the excluded volume effects prevent two oppositely charged polymer chains from occupying the exact same position in each Monte Carlo step. This gives rise to strongly correlated oppositely charged polyelectrolytes with a nonzero mean-field potential, analogous to dipoles on a molecular level. The nonzero mean potentials allow for the formation of bridges between two anchors by oppositely charged polymer chains, which gives an entropic contribution to the cohesion of the complex coacervates that are thus formed.

In Figure 13.1 we show some preliminary results of this approach. The snapshots

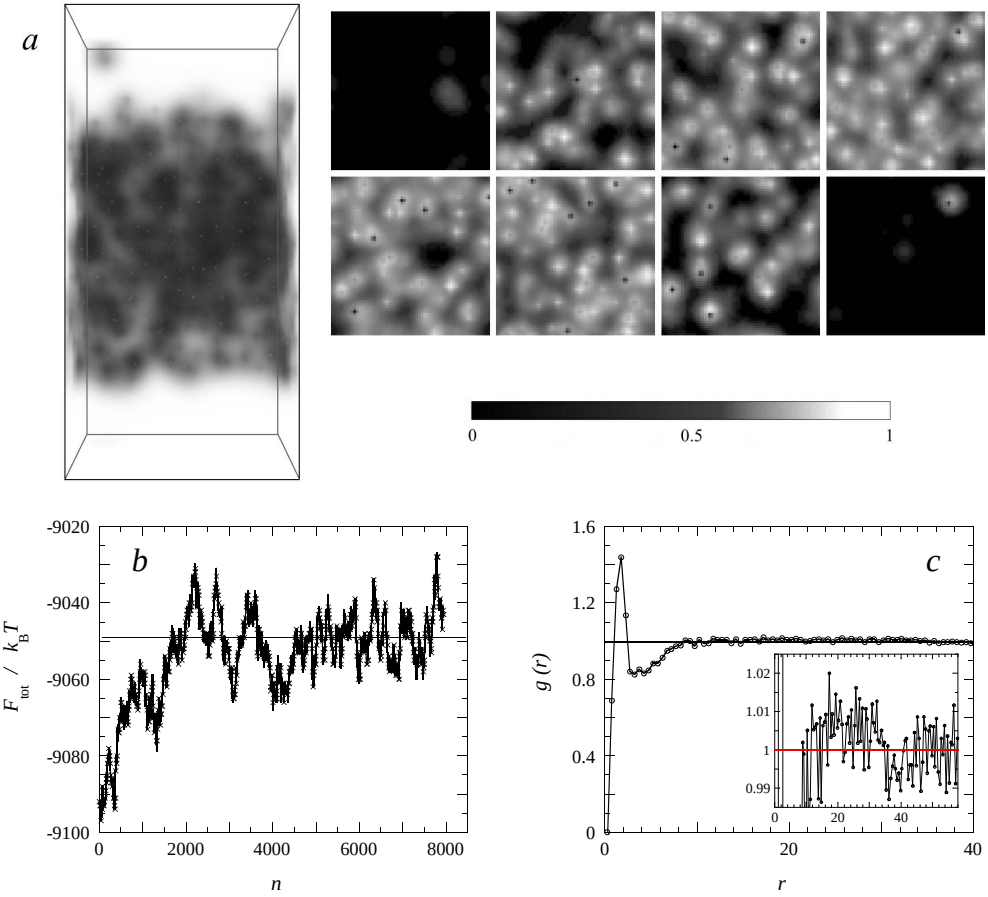

Figure 13.1: Preliminary MC-SCF results. (a) Snapshots of a simulation with 250 polycations and 250 polyanions of length 51 and a charge density of 0.5, in a box of $50 \times 50 \times 100$ with a salt volume fraction $\phi_s = 0.01$. The non-electrostatic interactions between monomers and solvent are given by $\chi = 0.5$. A 3-D view is shown on the left, 2-D slices in xy direction (50×50) are shown on the right, from left to right: $z = 15, 25, 35, 45$ (top row) and $z = 55, 65, 75, 85$ (bottom row). (b) Free energy trace of a simulation with the same number of chains in a box of $49 \times 49 \times 49$, which forms a homogeneous complex coacervate. (c) Pair correlation function of the MC segments in (b), averaged over the last 6000 MC steps.

clearly show the presence of a complex coacervate phase with a diffuse interface. The pair correlation function of the anchored (MC) polymer segments, shown in Figure 13.1c, exhibits a strong correlation peak at very short separations, corresponding to the close association of oppositely charged polymer chains. More importantly, a second weak correlation peak is found at much larger separations, close to the expected

radius of gyration of these polymers (see inset in Figure 13.1c). This correlation peak represents the cohesive interaction due to density fluctuations, between pairs of oppositely charged polyelectrolytes that are neutral on average.

Interestingly, these correlations are extremely weak, suggesting that the cohesion is weak as well and the interfacial tension, for instance, is low. We have made a rough estimate of the magnitude of the interfacial tension by comparing two simulations at slightly different box sizes and evaluating the free energy of both. We found that the interfacial tension is of $\mathcal{O}$ (1 mN/m) in our simulations at low salt concentrations, in good agreement with experimental results (Chapter 10) and the results obtained in field-theoretic simulations.[23]

Possibly, the weak cohesion is also related to the large-scale density fluctuations we found experimentally. The snapshots displayed in Figure 13.1a do show domains with higher and lower polymer density, thus supporting this hypothesis. Longer simulations of much larger complex coacervates are needed to establish the structure and possible existence of large-scale density fluctuations in complex coacervates with more certainty and to further investigate the properties of complex coacervates.

In summary, complex coacervation can be predicted and studied in simulations, either using RPA, FTS or a hybrid MC-SCF technique. These simulation methods offer a promising way to study many structural properties of complex coacervates in detail, as a function of parameters that are not easily adapted systematically in experiments, such as chain length, chain length mismatch, charge density and chain flexibility. An important question is which method is the most realistic for complex coacervates. At this point, we cannot give a definite answer. A detailed comparison of results from both FTS and MC-SCF and experimental data is needed to identify the strengths and weaknesses of these simulation techniques.

13.4 Generic electrostatics or specific chemistry

Bungenberg-de Jong and Kruyt originally discovered the phenomenon of complex coacervation for a combination of weakly charged polyelectrolytes. Since that discovery more and more types of macroions, including strong polyelectrolytes, micelles, proteins and rigid disk-like particles, have been found to form complex coacervates. This suggests that the interaction that are common to all these combinations, that is, the electrostatic attraction between opposite charges, predominates in the process of complex coacervation. In fact, we have also used theoretical arguments in Chapters 3, 5, 8, 9, 10 and 11 that are based on generic electrostatic interactions, rather than specific chemical interactions, to rationalise some of our findings. Here, we discuss to what extent this is justified and what the limitations of these theoretical arguments are.

In Chapter 4 we have studied various flexible polyelectrolytes. We found complex coacervation for most combinations in a range of salt concentrations up to a critical point. By definition, these complex coacervates were liquid phases containing a significant amount of hydration water. However, these complex coacervates had more similarities. The amount of hydration water seemed to be fixed to high values between 60 and 85%. Also complex coacervates that are formed by globular proteins, weakly charged polysaccharides and colloidal particles have a similarly high water content (see Chapter 3). Moreover, all complex coacervates we studied seemed to have a so-called preferred composition, corresponding to this 1 : 1 ratio. If the polyelectrolytes were mixed at a different ratio, excess polycations or polyanions ended up in the dilute phase. This preference was already suggested by Voorn to be a general characteristic of complex coacervates,[17] and implies again that electrostatic attractions predominate in the process of complex coacervation. We note that this preference would lead to a different shape of the phase diagram of complex coacervates than predicted by the theory of Voorn and Overbeek and we will discuss this in the following Section.

Of particular interest is our finding that both weak polyelectrolytes, such as PDMAEMA/PAA, and strong polyelectrolytes, such as PTMAEMA/PSPMA, form complex coacervates under nearly identical conditions. This disproves the suggestion made previously that strong polyelectrolytes or polyelectrolytes with high charge densities would always form precipitates.[28,29] It is worth considering this suggestion in some more detail.

We believe that there is no fundamental difference between weak polyelectrolytes and strong polyelectrolytes with similar densities of chargeable groups with respect to complex coacervation at sufficiently high salt concentration. As discussed in Chapter 2 and elsewhere by Biesheuvel et al.,[30] weak acidic or basic groups give rise to surfaces with charge-regulating characteristics. At sufficiently high salt concentrations and a solution pH well separated from the pK_a of the chargeable groups, most groups will be charged. Moreover, when two surfaces, be it planar, cylindrical or spherical, with chargeable groups of opposite sign are brought in close proximity, charging of both groups occurs. The resulting interactions between weak or strong polyelectrolytes in dense complex coacervates are therefore similar at sufficiently high salt concentrations. Only at very low or zero salt concentrations, we can point out a subtle difference. Strong polyelectrolytes always carry counterions, which are mostly bound to the charged polymeric groups at low salt concentrations. Upon complexation with an oppositely charged polyelectrolyte, the release of these counterions contributes favourably to the free energy. Weak polyelectrolytes on the other hand, may be dissolved without counterions. Upon complexation, the acidic and basic groups become charged, without counterions being released. This may lead to a smaller decrease in free energy, depending on the type of charged groups. Possibly, this partly explains the observation of precipitation of strong polyelectrolytes at very low salt concentrations.

The precipitates are thus trapped in a kinetically frozen state of aggregation that is not capable of retaining much hydration water, which further decreases the probability of ionic bond rearrangements (see Chapter 8). However, at sufficiently high salt concentrations, we expect no difference between complex coacervation of weak and strong polyelectrolytes based on generic electrostatic interactions.

Also the density of chargeable groups does not change the complexation behaviour fundamentally. Polyelectrolytes with both low and high charge densities are capable of forming complex coacervates, as is apparent from Chapters 3 and 4 and the work by Bungenberg-de Jong[31,32] and Weinbreck et al.[33] These complex coacervates merely differ in the critical salt concentration beyond which phase separation is suppressed. Polyelectrolytes with low charge densities have lower critical salt concentrations than polyelectrolytes with high charge densities, although exceptions exist, as shown in Chapter 4 (see hereafter). Nevertheless, there seems to be no discrete or fundamental difference between complex coacervates of polyelectrolytes with low and high charge densities.

Despite all similarities between different combinations of polyelectrolytes, we also found some striking differences. We found widely varying critical salt concentrations for different combinations of polyelectrolytes, even though they had approximately equal lengths, flexibilities and charge densities (see Chapter 4). In the theory of Voorn and Overbeek such differences can partly be explained by a different size of the monomeric groups l (Equation 3.4) and, consequently, a different contact distance of an ionic bond d (Equation 8.3). However, the fact that we also find greatly different critical salt concentrations for apparently similar charged groups (e.g., PTMAEMA/PSPMA and PTMAEMA/PSS), suggests that specific interactions related to the chemical nature of the backbone, the side group and the actual charge on the polymers, play an important role as well. The understanding of these effects would benefit from detailed quantum mechanical calculations of the interactions between two such individual charged groups, combined with molecular dynamics or Monte Carlo simulations that take into account the relative size of the charged groups along a polymer backbone.

Summarising the above, generic electrostatic interactions seem to play a predominant role in complex coacervation. As a result, complex coacervates will usually have a composition close to a 1 : 1 ratio of chargeable groups. The critical salt concentration beyond which no complexation occurs does vary with the combination of polyelectrolytes, because additional attractive or repulsive interactions, such as hydrophobic interactions, hydrogen bonds or steric repulsions can either strengthen or weaken the complexes. Moreover, some combinations of oppositely charged chemical groups seem to form stronger ionic bonds or associations than others, suggesting that specific interactions cannot be neglected.

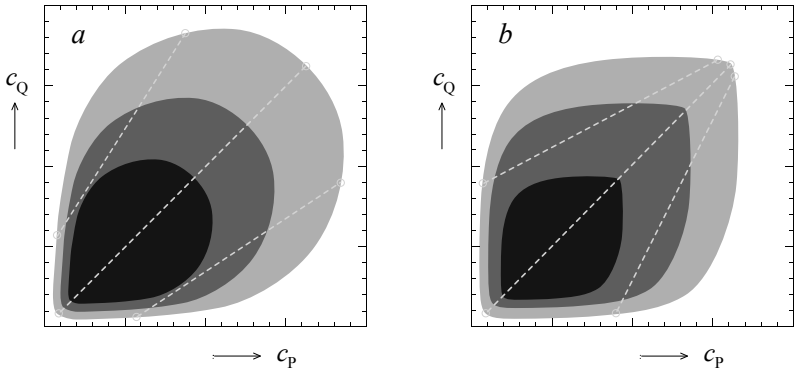

Figure 13.2: Schematic phase diagrams of complex coacervation for the case of (a) strong deviations from stoichiometry in the complex coacervate and (b) a preferred stoichiometric composition of the complex coacervate.

13.4.1 Preferred compositions of complex coacervates

Our observation of a preferred charge composition and an apparent constant water content in complex coacervates finally raise the question about the applicability of the mean-field theory of Voorn and Overbeek. Although Voorn recognised that complex coacervates seem to have a preferred composition close to a 1 : 1 ratio of chargeable groups and that excess amounts of either component would end up in the dilute phase, as schematically depicted in Figure 13.2b,[17] his model does not follow these predictions. On the contrary, the 3-D phase diagram shown in Figure 3.5 is extremely broad and allows for strong deviations from a 1 : 1 composition of the complex coacervate phase, like in the schematic diagram in Figure 13.2a. Moreover, our choice of parameters in the Voorn-Overbeek theory in Chapter 3 yields a correct prediction of the water content of roughly 70%, but similar complex coacervates with a charge density α of 0.01 could not be formed or would have a very different water content with the same parameters. However, experiments indicate that these complex coacervates actually have similar water contents. Clearly, the simple ingredients in Equation 3.4 cannot account for all of these aspects.

Here we give another tentative explanation for the constant water content of complex coacervates, which relates to our preliminary simulation results in Figure 13.1. We noted that correlations between oppositely charged polyelectrolytes beyond the first correlation peak must account for the cohesion of complex coacervates (see Figure 13.1c). These complex coacervates may be seen as weakly cohesive phases of neutral polycation-polyanion pairs. As these pairs still contain swollen coils, a large part of the volume in the complex coacervate will be taken up by water. We expect the correlations that account for the cohesion of complex coacervates to depend only weakly on chain length and charge density, because they originate from thermal

fluctuations of the charged groups. As a result, the cohesive interaction of all complex coacervates is very similar, as is the water content.

Finally, it is worth mentioning that some complex coacervates do allow significant deviations from a 1 : 1 ratio of chargeable groups. In Chapter 4 we already noted that the complex coacervates with living polymers containing metal-coordination bonds seem to reach different compositions when excess polycation is added or excess polyanion is added. Recent experiments in which the composition of the dilute and complex coacervate phase of PDMAEMA/L_2EO_4+Zn mixtures were quantified by NMR indicate that the phase diagram is actually strongly asymmetric, with one side resembling the diagram in Figure 13.2a and the other side resembling the diagram in Figure 13.2b.[34] This can be explained by the fact that the polyanion can easily adjust its charge by forming dimers or trimers with only one or two Zn^{2+} ions, thereby increasing its negative charge by up to -2 per dimer. Obviously, the polycations in this example cannot do the same.

13.4.2 Theoretical limitations

In our attempts to quantify the generic electrostatic interactions in complex coacervates we have made use of a Debye-Hückel approximation for the correlation energy of electrolyte solutions, both in Chapter 3 and in Chapters 8, 9, 10 and 11. We have discussed its validity within the framework of the Voorn-Overbeek theory in Chapter 3. Here we give some additional general considerations.

In deriving the Debye-Hückel approximation of the free energy of electrolyte solutions, it is assumed that the Poisson-Boltzmann equation can be linearised, that is, the potentials must be low ($ze\psi/k_BT \ll 1$). This assumption may indeed be justified in many studies on complex coacervates. On the one hand, polyelectrolytes with low charge densities form complex coacervates already at low salt concentrations, but they never reach high surface potentials.[32] On the other hand, strongly charged polyelectrolytes are studied at high salt concentrations, where high surface potentials are strongly screened.

A second assumption is that the concentrations of the ions are sufficiently low. In writing a Boltzmann distribution for the charge densities, local activity coefficients of the ions are neglected. In addition, in evaluating the electrostatic work of charging an electrolyte solution of certain concentration it is assumed that $\ln\gamma \propto \kappa \propto \sqrt{c_s}$, with γ the activity coefficient of a single ionic species.[35] In any case, this assumption will only be valid at sufficiently low concentrations. At high concentrations, both effects due to the discrete size of ions, which is not accounted for in the Boltzmann distribution, and higher-order corrections to the activity coefficients of electrolytes in solution, which are neglected in calculating the electrostatic work of charging, will lead to deviations of the Debye-Hückel approximation we applied. Especially for complex

coacervates of strong polyelectrolytes, for which we used salt concentrations of 1 M or more, the condition of low concentrations is not met.

A number of approaches exist to correct for deviations from the Debye-Hückel theory. Perhaps most frequently used are the Pitzer equations,[36] for which empirical coefficients have been tabulated for a wide range of electrolytes.[37] Interestingly, for many monovalent strong electrolytes the corrections for activities are modest up to concentrations of the order of 2 M, and even become smaller again for some at higher concentrations.[37,38]

We believe that our use of a Debye-Hückel theory in the context of complex coacervates of strong polyelectrolytes to estimate the energy related to electrolyte solutions is justified to at least qualitatively explain general trends we observe. The mean potentials in these complex coacervates are low and only monovalent electrolytes are considered. A quantitative agreement would require corrections for the activity of ions at higher concentrations. Nevertheless, the corrections for monovalent strong electrolytes are modest. At the same time, our choice of the various fitting parameters A (Equation 3.4) and a_s and b_s (Equation 8.3) could well have had the same effect of correcting for some over- and underestimations.

13.5 Formation of complexes

We believe our study of complex coacervates as phase separated liquids provides useful insights that help to understand some fundamental aspects of natural and man-made charge-driven materials. However, we have argued above that most of these materials never reach the same equilibrium state or structure because of additional interactions, anchoring of the chains, a simultaneous drying process, or because of slow relaxation in kinetically frozen aggregates. Depending on the actual relaxation rate an interesting balance between these opposing trends may arise. To better understand these effects, systematic studies on the formation kinetics of complexes between oppositely charged macroions, ultimately leading to the formation of complex coacervates, are needed. Such studies require a method to bring two oppositely charged macroions together in a controlled way, and initiate the complexation with a trigger. By varying the strength of the interactions, which is easily achieved by changing the salt concentration, the balance between complex coacervation and kinetic arrest can then be shifted to either side.

In Figure 13.3 we show some preliminary results of an experiment aimed at studying the formation of complexes. We prepared picolitre droplets of both polycationic PTMAEMA and polyanionic PSPMA (see Chapter 4) in a perfluorinated oil using a microfluidic PDMS device.[39] The droplets can be trapped in pairs or triplets and fused by electrocoalescence, allowing the study of complex formation at the interface

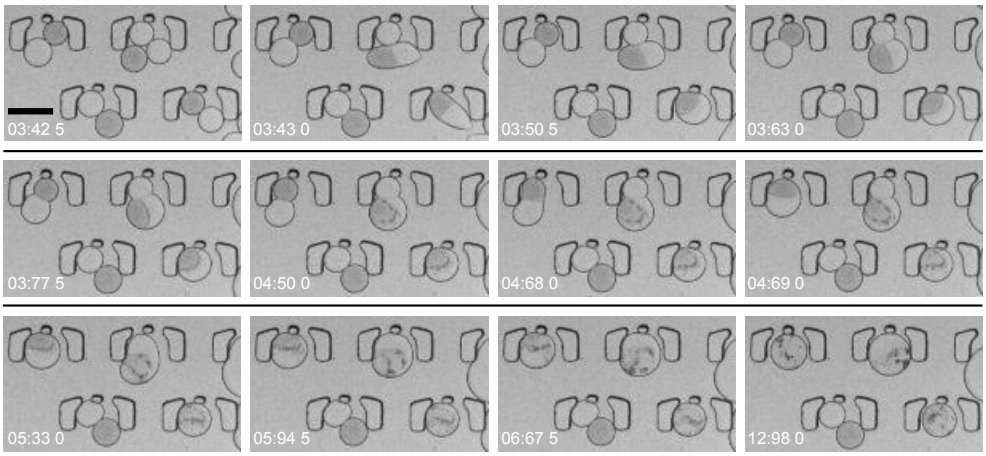

Figure 13.3: Preliminary results of electrocoalescence study of droplets containing oppositely charged polyelectrolytes. The oil phase consists of HFE-7500 (3-ethoxy-perfluoro-2-methylhexane). A PFPE-PEO-PFPE fluorinated triblock copolymer was used as a surfactant. The droplets contain a 10 g/L solution of $PTMAEMA_{96}$ or $PSPMA_{94}$ (see Chapter 4). The PSPMA-containing droplets are stained with Fast Green FCF, a water-soluble dye (E-number 143). The scale bar represents 50 µm. Time is shown in each frame as ss : fff. The electrocoalescence was achieved by applying electric field pulses with an amplitude of 5500 V/m, a pulse width of 100 µs and a frequency of 8 Hz.

between the contents of the original droplets by optical microscopy, fluorescence microscopy or coherent anti-Stokes Raman spectroscopy (CARS).

The coalescence of droplets can be monitored with millisecond time resolution.[39] As can be seen in Figure 13.3, the complexation in this experiment does not affect the coalescence of the droplets significantly. Within a millisecond, two droplets containing oppositely charged polyelectrolytes coalesce into a single, spherical droplet. The contents of these droplets are, however, not fully mixed yet. At the interface of the two solutions, complexation takes place. Because of the low concentration of polyelectrolytes, complexation at this interface does not prevent further mixing of the two solutions, as for the sacs formed from hyaluronic acid and peptide amphiphiles.[13] At higher concentrations of polyelectrolytes, we expect that the complexation will affect the process of coalescence by opposing the interfacial tension between the oil and water, which acts to minimise the interfacial area of the fused droplet. Quantification of the droplet deformation would then allow studying changes in relaxation dynamics of the complexes as they grow. By changing the salt concentration from zero to above the critical salt concentration, the various stages between complex coacervation and kinetic arrest can be investigated.

13.6 From ionic bonds to stability

We hope some aspects of the research described in this thesis contribute to a better understanding of complex coacervates and other charge-driven materials, both in nature and in laboratories. The ultimate goal of some of the measurements we presented would be to predict the structure and stability of any charge-driven material *a priori*. We imagine that knowledge of the bonds strength of ion pairs between the oppositely charged groups (Chapters 9 and 11) and of the interfacial tensions between the corresponding macroscopic complex coacervates and dilute aqueous solutions (Chapter 10), could lead to predictions of the stability of a macromolecular complex, both against disintegration by salt and against disruption by external forces. This seems impossible at first sight, but it may already be more than fiction.

As an example, we consider the micellar structures discussed in Chapter 5 (C3Ms). To assess their stability against mechanical deformation or external forces, we could measure the forces required to disrupt such a micelle using the setup and strategy described in Chapter 11 (see Figure 13.4a). To prevent adsorption of these micelles onto either the tip or the silica surface, both surfaces would have to be carefully coated with a dense layer of noninteracting polymers. Besides that, the actual disruption forces are probably very low, making it difficult to measure them accurately. We can, however, use the findings described in this thesis to estimate the magnitude of such disruption forces.

The tip-bound block copolymer in Figure 13.4a could unbind from the micellar core by breaking a number of ionic bonds. An alternative pathway with a much lower energy barrier is a division of the micelle into two neutral micellar objects. The energy barrier then amounts to $\gamma \Delta A$, with γ the interfacial tension of the core-solvent interface and ΔA the difference in total surface area between one big and two small micelles. For a symmetric division $\Delta A = (2 \times (2\pi/3)^{2/3} - 1) \times 4\pi {R_c}^2 \approx 8 {R_c}^2$, whereas for a division into two micelles with a 20 : 1 ratio of volumes (single block copolymer with an oppositely charged homopolyelectrolyte) $\Delta A \approx 1.2 {R_c}^2$, where R_c the radius of the initial micellar core. Taking a typical $R_c = 5$ nm,[40] $\gamma = 1$ mN/m at low salt (Chapter 10) and the force spectroscopy parameters from Chapter 11, we find an energy barrier of 8 $k_B T$ and an estimated rupture force of 300 pN. This indicates that the disruption of C3Ms could be measured, at least at very low salt concentrations, and that such micelles are reasonably stable in solution.

As a second example, we consider zipper brushes of block copolymers, anchored to a surface with grafted oppositely charged polymer chains (see Figure 13.4b).[41] These brushes are thought to effectively prevent adsorption of many types of particles. Here we assess the stability of these coatings against wear by a strongly attached particle in a laminar flow (see Figure 13.4b). The force exerted by the particle on a single chain of the zipper brush is $f = 6\pi\eta R v$ where η is the solvent viscosity, R is the

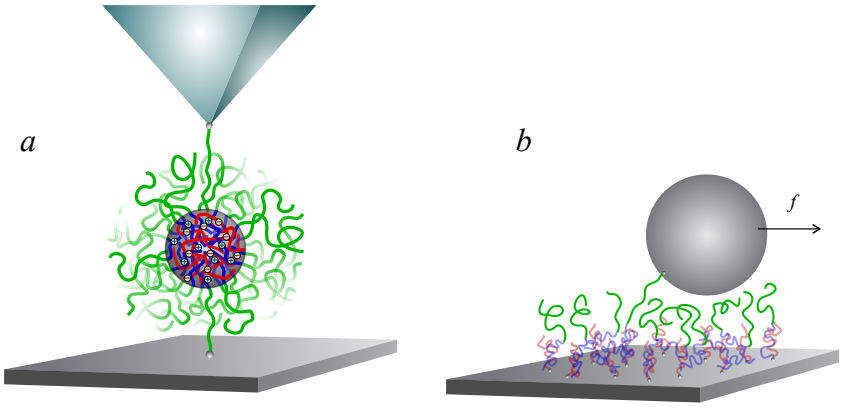

Figure 13.4: Schematic drawing of a hypothetical experiment to assess the stability of charge-driven structures. (a) Disrupting a C3M using an AFM setup. (b) Exerting a force on a zipper brush using an attached nanoparticle.

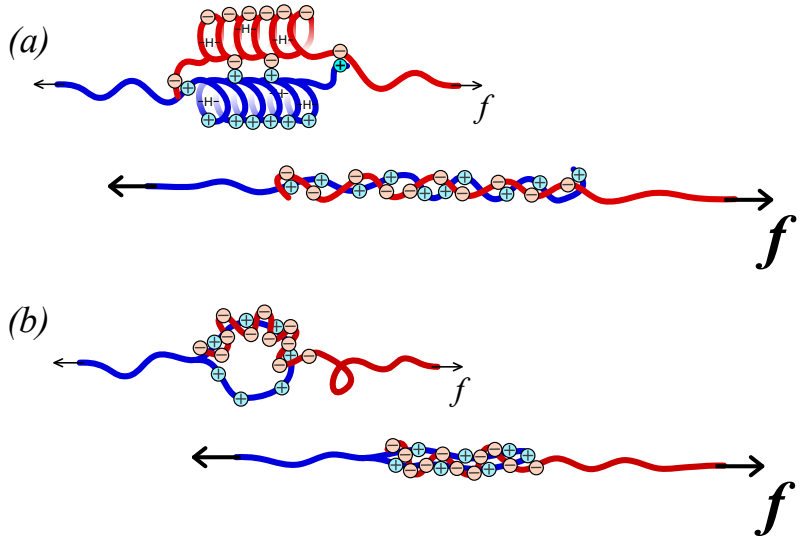

Figure 13.5: Schematic drawing of two hypothetical designs of ionic catch bonds. (a) A helix-based ionic catch bond. The helices unfold upon loading and expose more ionic groups. (b) A rigid-ring-based ionic catch bond. The rigid ring deforms upon loading, allowing the formation of more ionic bonds.

particle radius and v is the velocity of the flowing solvent. This force is typically small. For a 10 nm particle in water that flows at 1 m/s, $f \approx 200$ pN. On the other hand, the block copolymer is typically attached via 20 or more ionic bonds to the oppositely charged polymers on the surface,[41] giving rise to an unperturbed overall energy barrier of the order of 100 $k_{\mathrm{B}}T$ at low salt concentration. Here, it depends on the arrangement of the individual bonds (see Chapter 11: zipper or shear) what the expected rupture force is, but even the weaker zipper arrangements are not expected to fail at sufficiently low salt concentrations.

Finally, we note that the lifetimes of the ionic bonds we have studied in this thesis diminish when a force is applied to them, like almost all mechanical bonds. There is, however, a class of bonds that exhibit an opposite effect: they become more stronger when subjected to mechanical force. These 'catch' bonds were first discovered at the cell wall of bacteria and in leukocytes.[42] They are thought to help bacteria and eukaryotic cells to adhere to surfaces and to other cells in shear flows, which are present in many natural environments. A conformational change of the protein responsible for adhesion, induced at low to intermediate forces, underlies the strengthening of these adhesion bonds. After this conformational change, the strengthened adhesion bonds behave as conventional 'slip' bonds again, and weaken upon further increase of the force, until they eventually fail.

Incorporating similar catch bonds in complex coacervates or other charge-driven assemblies would open a range of new opportunities for stabilising these materials. After formation at zero or low shear force, the complexes would be highly stable against external deformation. Liquid coacervate droplets might, for instance, become more elastic when they are deformed, completely opposite to our findings for classical complex coacervates (see Chapter 8). One possible way to incorporate ionic catch bonds in complex coacervates would be to use designer protein polymers,[43] containing protein sequences with many charged groups, and sequences that fold into compact domains, such as helices, which can easily unfold under load, as shown in Figure 13.5a. Another possible design of ionic catch bonds is shown in Figure 13.5b. The charges on one of the polyelectrolytes are located on a rigid ring. Upon loading this complex, the ring may deform, thereby allowing more ionic bonds to be formed and thus strengthening the complex as a whole. We hope that a more detailed investigation of catch bond coacervates will prove useful for applications where complex coacervates are subject to strong external forces.

13.7 Outlook

In this Chapter we have discussed some apparent generalities of complex coacervates and some important open questions. Of these open questions, the partially unresolved structure of complex coacervates is one of the most pertinent to understanding com-

plex coacervation. We believe that a fundamental understanding of the driving forces for complex coacervation and their relation to the structure of complex coacervates, from the level of single ionic bonds to the level of macroscopic liquid phases, will be of most value for applications of complex coacervation in soft matter. It will not only aid predictions about strength and stability, such as those in Section 13.6, but also provide a basis for a better understanding of the stability of charged lyophilic colloids in general. We hope the ideas put forward in this thesis will partly inspire some of these developments.

References

[1] P. L. Dubin, *Adv. Coll. Int. Sci.*, 2011, **167**, 1.

[2] R. J. Stewart, C. S. Wang, and Hui Shao, *Adv. Coll. Int. Sci.*, 2011, **167**, 85–93.

[3] B. L. H. M. Sperber, *Ph.D. thesis*, Wageningen University, 2010.

[4] E. Kizilay, A. B. Kayitmazer, and P. L. Dubin, *Adv. Coll. Int. Sci.*, 2011, **167**, 24–37.

[5] J. M. Gottesfeld and K. Luger, *Biochemistry*, 2001, **40**, 10927–10933.

[6] A. Perico, G. La Penna, and L. Arcesi, *Biopolymers*, 2006, **81**, 20–28.

[7] K. Kleppe, S. Övrebö, and I. Lossius, *J. General Microbiol.*, 1979, **112**, 1–13.

[8] M. Thanbichler, S. C. Wang, and L. Shapiro, *J. Cell. Biochem.*, 2005, **96**, 506–521.

[9] G. Decher, *Science*, 1997, **277**, 1232–1237.

[10] R. von Klitzing, *Phys. Chem. Chem. Phys.*, 2006, **8**, 5012–5033.

[11] C. Ankerfors, *Ph.D. thesis*, KTH Stockholm, 2008.

[12] P. M. Biesheuvel, T. Mauser, G. B. Sukhorukov, and H. Möhwald, *Macromolecules*, 2006, **39**, 8480–8486.

[13] R. M. Capito, H. S. Azevedo, Y. S. Velichko, A. Mata, and S. I. Stupp, *Science*, 2008, **319**, 1812–1816.

[14] S. Sukhishvili, *Curr. Opin. Coll. Int. Sci.*, 2005, **10**, 37–44.

[15] D. Kovacevic, S. van der Burgh, A. de Keizer, and M. A. Cohen Stuart, *Langmuir*, 2002, **18**, 5607–5612.

[16] P. Atkins and J. de Paula, *Physical chemistry*, Oxford University Press, 2002.

[17] M. J. Voorn, *Ph.D. thesis*, University Utrecht, 1956.

[18] G. H. Fredrickson, *Soft Matter*, 2007, **3**, 1329–1334.

[19] P. G. de Gennes, *Scaling Concepts in Polymer Physics*, Cornell University Press, 1979.

[20] M. Castelnovo and J.-F. Joanny, *Eur. Phys. J. E*, 2001, **6**, 377–386.

[21] A. Kudlay and M. Olvera de la Cruz, *J. Chem. Phys.*, 2004, **120**, 404–412.

[22] Y. O. Popov, Y. Lee, and G. H. Fredrickson, *J. Pol. Sci. B*, 2007, **45**, 3223–3230.

[23] R. A. Riggleman, R. Kumar, and G. H. Fredrickson, *J. Chem. Phys.*, 2012, **136**, 024903.

[24] B. Qiao, J. J. Cerdà, and C. Holm, *Macromolecules*, 2010, **43**, 7828–7838.

[25] J. Jeon and A. V. Dobrynin, *Macromolecules*, 2005, **38**, 5300–5312.

[26] M. A. Trejo-Ramos, F. Tristán, J.-L. Menchaca, E. Pérez, and M. Chávez-Páez, *J. Chem. Phys.*, 2007, **126**, 014901.

[27] M. Charlaganov, *Ph.D. thesis*, Wageningen University, 2009.

[28] C. G. de Kruif, F. Weinbreck, and R. de Vries, *Curr. Opin. Coll. Int. Sci.*, 2004, **9**, 340–349.

[29] S. Lindhoud, *Ph.D. thesis*, Wageningen University, 2009.

[30] P. M. Biesheuvel and M. A. Cohen Stuart, *Langmuir*, 2004, **20**, 2785–2791.

[31] H. G. Bungenberg-de Jong and H. R. Kruyt, *Proc. KNAW*, 1929, **32**, 849–856.
[32] L. de Ruiter and H. G. Bungenberg-de Jong, *Proc. KNAW*, 1947, **50**, 836–848.
[33] F. Weinbreck, R. H. Tromp, and C. G. de Kruif, *Biomacromolecules*, 2004, **5**, 1437–1445.
[34] J. Wang, *Ph.D. thesis*, Wageningen University, 2012.
[35] T. L. Hill, *An introduction to statistical thermodynamics*, Dover Publications Inc., 1986.
[36] K. S. Pitzer and G. Mayorga, *J. Phys. Chem.*, 1973, **77**, 2300–2308.
[37] H.-T. Kim and W. J. Frederick Jr., *J. Chem. Eng. Data*, 1988, **33**, 177–184.
[38] E. Moggia and B. Bianco, *J. Phys. Chem. B*, 2007, **111**, 3183–3191.
[39] A. M. Huebner, C. Abell, W. T. S. Huck, C. N. Baroud, and F. Hollfelder, *Anal. Chem.*, 2011, **83**, 1462–1468.
[40] I. K. Voets, *Ph.D. thesis*, Wageningen University, 2008.
[41] W. M. de Vos, J. M. Kleijn, A. de Keizer, and M. A. Cohen Stuart, *Angew. Chem. Int. Ed.*, 2009, **48**, 5369–5371.
[42] W. E. Thomas, E. Trintchina, M. Forero, V. Vogel, and E. V. Sokurenko, *Cell*, 2002, **109**, 913–923.
[43] P. J. Skrzeszewska, *Ph.D. thesis*, Wageningen University, 2011.

Summary

Complex coacervates are dense phases of oppositely charged hydrophilic polymers, proteins or colloids that contain a significant amount of 'hydration' water, or another solvent. They form by associative phase separation of a mixture of the oppositely charged species and are essentially liquids ("tropfbare Flüssigkeiten"). Complex coacervates and the underlying aggregation by association of opposite charges are ubiquitous in natural and man-made materials. The natural underwater glue of the sandcastle worm, the bacterial nucleoid and the pectin-coated caseins in yogurt drinks are but a few examples of complex-coacervate-like structures and materials. In new applications, the same attractive interactions can drive the formation of capsules, membranes and gels and the coating of surfaces.

Despite the biological, industrial and fundamental scientific importance of complex coacervates, many questions about their formation, structure and stability remain unanswered. It is the aim of the research described in this thesis to investigate model systems for complex coacervation and to get more insight in their strength, structure and stability.

Stability

In the first part of this thesis we focus mainly on macrocsopic complex coacervates.

In Chapter 2 we consider the thermodynamic driving forces for complexation of oppositely charged colloids. We solve the Poisson-Boltzmann equation for oppositely charged plates, cylindrical polymers and sperical particles and explicitly evaluate the contributions of field energy and counterion entropy to the free energy of interaction. For planar surfaces both contributions can be calculated analytically and at low surface charge they are equal. At high surface charge, the free energy of interaction is dominated by the entropy gain due to counterion release. This classical result changes significantly for cylindrical polymers or spherical colloidall particles. For highly charged surfaces the free energy of interaction is still dominated by counterion entropy, regardless the number of interacting species. However, for low or intermediate surface charges it can become strongly dominated by a decrease of the field energy between the cylinders or spheres. Here, the balance between field energy and counterion entropy is governed by the curvature of the electrical double layer (κa). A lower κa implies a more curved double layer and an energy-dominated complexation. At high κa we find the limiting case of planar surfaces again. In most practical situations complexation is driven by a combination of energetic and entropic terms, and neither can be neglected.

In Chapter 3 we investigate how these driving forces are translated experimentally into the phase behaviour of mixtures of oppositely charged polyelectrolytes. We use poly(N, N-dimethylaminoethyl methacrylate) (PDMAEMA) and poly(acrylic acid)

(PAA) as a model system for polyelectrolyte complex coacervates. These polyelectrolytes phase separate into a dense, highly viscous, liquid phase that contains almost all polymers, and a dilute phase that contains a low concentration of both polymers. We construct the experimental salt-polymer phase diagrams of this complex coacervation process for varying chain lengths using fluorescently labelled PAA to quantify the concentrations. The complex coacervates contain about 70% water by weight, practically independent of chain length and salt concentration, and have a preferred composition where the ratio of chargeable groups on the polyelectrolytes is close to 1:1. Above a certain critical salt concentration, phase separation no longer occurs. We can quantify all results using the mean-field model for complex coacervation of Voorn and Overbeek. Alternatively, we can map the salt-dependent attraction between the polyelectrolytes onto a classical interaction parameter used in segregative demixing. The applicability of this strategy suggests that there is a strong similarity between complex coacervation and segregative demixing, with salt concentration playing the role of an effective temperature.

In Chapter 4 we investigate various other combinations of flexible polyelectrolytes with similar lengths and backbone structure. We try to establish which properties of complex coacervates are generic and which depend on the specific chemical structure of the components. For each combination we measure the critical salt concentration, water content and preferred composition. Most combinations form complex coacervates at sufficiently high salt concentrations. All complex coacervates have a very similar water content, between 60 and 85% and a preferred composition corresponding to a 1:1 ratio of chargeable groups. The critical salt concentrations on the other hand, vary strongly, from almost zero to more than the typical monovalent salt solubility in water. Moreover, the stability of complex coacervates, measured in terms of the critical salt concentration, depends on the type of monovalent salt, following the Hofmeister series. Large ions with smaller hydration shells are more effective in destabilising the phase separated complex coacervates. Probably, strongly hydrated ions dehydrate the complex coacervate, thereby strengthening the ionic bonds. Hydration is therefore an important characteristic of complex coacervates. Finally, increasing the temperature leads more strongly separated phases, analogous to the behaviour observed for classical polymer solutions with a lower critical solution temperature.

In the remaining Chapters of this part on stability, we investigate two cases in which complex coacervation is used as a driving force for the formation of self-assembled structures. In Chapter 5 we use a combination of polyelectrolytes we have also studied in Chapter 4, but with a neutral, water-soluble block attached to the polycation. This combination of PAA and poly(ethylene oxide)-*b*-poly(*N*-methyl-2-vinylpyridine) (PEO-*b*-PM2VP) gives rise to complex coacervation that is confined to a nanometre-sized volume in the core of a micelle. These complex coacervate core

micelles (C3Ms) are dynamic structures. Many aspects of their stability are equivalent to the stability of macroscopic complex coacervate phases. We measure the critical salt concentrations as a function of chain length of the homopolymer and the block copolymer. The critical salt concentration increases with both chain lengths in a way that is in agreement with the mean-field model we used in Chapter 3, but is always lower than the corresponding critical salt concentration for macroscopic complex coacervates. Another remarkable difference with macroscopic complex coacervates is the fact that these C3Ms can undergo morphological changes close to the critical salt concentration. We use polarised and depolarised static and dynamic light scattering, and small angle X-ray scattering to show that worm-like micelles with contour lengths up to 400 nm are formed close to the critical salt concentration. However, this transition is only possible if the length of the homopolymer does not exceed that of the cationic block. A critical review of existing literature on other C3Ms reveals that this transition is a more general, but so far overlooked, phenomenon.

If the polyelectrolyte chains are grafted tot the surface of a colloidal particle, the attractive interactions can drive the association of these colloidal particles into ordered arrangements (Chapter 6). We use monodisperse polystyrene (PS) colloidal particles with either polycationic or polyanionic chains grafted to their surface and different fluorescent dyes in their cores to distinguish them. The association occurs in a way that is very similar to complex coacervation. Above a critical salt concentration no aggregation occurs and already formed aggregates fall apart spontaneously into individual particles. This approach thus allows for the completely reversible assembly of oppositely charged colloidal particles in water. The aggregates form fractal-like gels, because the attractive interactions grow stronger in time to a level where interacting particles can no longer rearrange to find more favourable orientations. At an early stage, rearrangements do occur and this persists longer close to the critical salt concentration. Strongly asymmetric mixing ratios lead to raspberry-like heteroaggregates, in which a core particle of one charge is surrounded by particles of opposite charge. They are stable against further aggregation even below the critical salt concentration. At the end of this Chapter, we propose an improved design for colloidal particles that aggregate reversibly into equilibrium crystalline structures in water.

Structure

In the second part of this thesis we zoom in on the complex coacervates to investigate their structure.

We address the static structure of complex coacervates of PDMAEMA and PAA using scattering of neutrons, X-rays and light in Chapter 7. Both the polycation and the polyanion have a nearly Gaussian conformation in the complex coacervate. Together they form a two-component, semidilute polymer solution of overlapping chains with a characteristic mesh size that increases with decreasing salt concentration, in

agreement with our phase diagram in Chapter 3. At length scales larger than the mesh size, we find density fluctuations that give rise to a power law in the scattering of neutrons, X-rays and light. These large-scale density fluctuations probably arise from the weak correlations inside the complex coacervates. Both characteristics, the mesh size and the density fluctuations, are recovered in dynamic light scattering. We find two relaxation modes. A fast mode corresponds to mesh fluctuations and occurs on a time scale of 10 ms. A slow mode corresponds to large scale density fluctuations and occurs on a time scale of 10 s. The overall static structure of the complex coacervates hardly depends on salt concentration.

In Chapter 8 and 9 we study the dynamic structure of complex coacervates in more detail using rheology. In contrast to the static structure, we find that salt does have a pronounced effect on the dynamics of complex coacervates, changing them from mostly elastic gels, to highly viscous fluids and eventually causing the complex coacervate phase to become unstable and miscible with the dilute phase. The role of salt in this process is generic. In Chapter 8 we describe how the underlying microscopic relaxation processes, in which ionic bonds are broken and reformed elsewhere, leads to a salt-enhanced energy barrier. We use this relation between salt concentration and relaxation time to rescale linear and nonlinear rheological measurements at different salt concentrations onto a single mastercurve. This time-salt superposition principle is predicted to be general and allows studying rheological behaviour of charge-driven materials at time scales and frequencies that would otherwise be inaccessible by rheology.

In Chapter 9 we apply this time-salt superposition to study the relaxation processes in complex coacervates of PDMAEMA and PAA in more detail. We reconstruct the relaxation time spectra for complex coacervates of different chain lengths. The ionic bonds between oppositely charged groups act as sticky points in the semidilute complex coacervates and slow down relaxation of an applied stress or strain. The stress relaxation eventually occurs via Rouse modes of the polymer chains. Relaxation times, moduli and viscosities exhibit a scaling with salt concentration and chain length that agrees well with the sticky Rouse model.

Strength

In the third part of this thesis we zoom in on the complex coacervates even further. We investigate the strength of the two different interactions between pairs of oppositely charged polyelectrolytes. First of all, there is a strong correlation between two oppositely charged polyelectrolytes at very short distances, due to the ionic bonds that are formed between the oppositely charged groups. At the scale of the radius of gyration of the polyelectrolytes, there is a weak correlation, similar to the correlations in electrolyte solutions, which accounts for the cohesion of the complex coacervates and is related to their interfacial tension.

In Chapter 10 we measure the interfacial tension between a poly(N, N, N-trimethylaminoethyl methacrylate) (PTMAEMA) / poly(3-sulphopropyl methacrylate) (PSPMA) complex coacervate and its coexisting dilute aqueous phase by colloidal probe atomic force microscopy (CP-AFM). In the dilute phase a complex coacervate condenses as a capillary bridge in the confined space between the colloidal probe and a flat surface in close proximity. The force needed to disrupt this capillary bridge is directly proportional to the interfacial tension. The interfacial tension is low, approximately 100 µN/m, and decreases with increasing salt concentration, following a critical scaling that is also found for classical segregative demixing. At the critical salt concentration the interfacial tension vanishes and the phases become indistinguishable.

In Chapter 11 we address the strong short-range attractive interactions between opposite hydrated charges – commonly called ionic bonds. We measure the strength of these bonds directly using single molecule force spectroscopy on an atomic force microscope. We attach a low density of PEO-PM2VP (see Chapter 5) to the tip of an AFM cantilever and a PSPMA brush to a flat silica surface. The force-distance curves of approach and retract of the tip involve almost exclusively interactions between a single PEO-PM2VP block copolymer with the brush. The characteristic forces come in two distinct types. The 'zipper' mode corresponds to the rupture of ionic bonds, one at a time, and originates from parallel binding of two oppositely charged polyelectrolytes. The 'snapper' mode corresponds to rupture of a complex of multiple ionic bonds at once and originates from antiparallel binding of the oppositely charged polyelectrolytes. The ionic bonds weaken when the salt concentration is increased, following our model for the energy barrier from Chapter 8. Finally, we investigate how the formation of polyelectrolyte multilayers affects the attractive interaction between the same tip-bound block copolymer and a surface containing one, two, three or more polyelectrolytes layers. We find a strong decrease of the attractive interaction, because fewer ionic bonds need to be broken upon separation of the tip from the multilayered surface.

In Chapter 12 we extend our investigation of ionic bonds to the disruption of a complex of many ionic bonds between two oppositely charged polyelectrolyte brushes. We use CP-AFM to measure the rupture forces that also play an important role in the interactions between the oppositely charged hairy colloids we used in Chapter 6. Here, we find only one mode of rupture, representing an average of all ionic bonds between the brushes. By varying the compression time and the rate at which the brushes are separated we find that the complexation occurs essentially in a 'zipper' arrangement. The growth of these complexes is a linear, but slow process that does not reach a steady state in our AFM measurements.

Outlook

We hope the research described in this thesis contributes to a better understanding of complex coacervates. The generic electrostatic interactions seem to dominate their formation and dictate their structure and stability to a large extent. As a result, complex coacervates with a wide variety of components have many features in common. We have identified but a few and described useful experimental techniques to investigate them.

We believe recent advances in computer simulations combined with more systematic experiments on polyelectrolyte complex coacervates with varying chain lengths and charge densities will extend our understanding of this intriguing phenomenon. In particular, they should aim at understanding the connections between its driving forces, the correlations between oppositely charged species in complex coacervates and some of the observed generalities in their properties. At the same time, many natural structures and new materials based on complex coacervation exhibit phase separation, which is slightly different from the one studied in this thesis, because of additional nonelectrostatic interactions, slow relaxation in kinetically frozen assemblies or simultaneous drying processes. An investigation of the initial stages in the formation of complex coacervates and the consequences of intervening processes, such as drying and curing, should lead to a better understanding of those structure and materials.

Samenvatting

De titel van dit proefschrift luidt 'Stabiliteit, structuur en sterkte van complex coacervaten van polyelektrolieten'. Een complex coacervaat is een geconcentreerde vloeibare fase die gevormd wordt door fasescheiding van een mengsel van tegengesteld geladen colloïdale deeltjes. Complex coacervaten bevatten een grote hoeveelheid hydratiewater, of volumes van een ander oplosmiddel, in tegenstelling tot aggregaten van instabiele lyofobe colloïden (zie daarvoor Hoofdstuk 1). De term complex coacervatie is afgeleid van het voorvoegsel *co* (samen) en het Latijnse woord *acervus* (hoop) en betekent, vrij vertaald, samenhopen van ongelijke ladingen in een complex. Dit samenhopingsproces is chemisch gezien een fasescheiding waarbij een complex coacervaat ontstaat als geconcentreerde fase, met daarin vrijwel alle geladen colloïdale deeltjes. Daarnaast ontstaat een sterk verdunde fase waarin slechts kleine hoeveelheiden geladen colloïdale deeltjes aanwezig zijn (zie Figuur 1.3).

Een verscheidenheid aan colloïdale deeltjes kan een complex coacervaat vormen: voor onder meer eiwitten, polysacchariden, synthetische polyelektrolieten, discusvormige minerale deeltjes, micellen, multivalente ionen en virussen is dit in experimenten waargenomen. De aantrekking tussen dergelijke tegengesteld geladen colloïden die de drijvende kracht achter complex coacervatie vormt, is terug te vinden op veel plaatsen in de natuur en wordt in onderzoek en toepassingen vaak gebruikt om nieuwe structuren en materialen te ontwikkelen. Een voorbeeld uit de natuur is de lijm die de zandkasteelworm (*Phragmatopoma californica*) procudeert om zandkorrels en andere minerale deeltjes aan elkaar te plakken tot een bouwwerk dat hem moet beschermen tegen uitdroging en tegen roofdieren. Een ander voorbeeld vindt men in bacteriën, waar DNA gecondenseerd is in een gebied dat sterk lijkt op een complex coacervaat: de nucleoïde. Tot slot worden in zuiveldrankjes met fruitsmaak caseïnemicellen gestabiliseerd met pectine, dat op een vergelijkbare manier aan de caseïnemicellen gebonden is als de colloïden in een complex coacervaat.

Ondanks de relevantie van complex coacervaten en de onderliggende aantrekkingskrachten voor biologische systemen en industriële toepassingen en de interesse vanuit fundamenteel wetenschappelijk oogpunt, zijn nog veel vragen over de manier waarop complex coacervaten gevormd worden, hun stabiliteit en hun structuur onbeantwoord. Het doel van het onderzoek dat in dit proefschrift beschreven wordt, is het vinden van een deel van deze antwoorden door een modelsysteem voor complex coacervaten, bestaande uit geladen polyelektrolieten, te bestuderen.

Stabiliteit

Het eerste deel van dit proefschrift gaat over de stabiliteit van voornamelijk macroscopische complex coacervaten.

In Hoofdstuk 2 zoeken we antwoord op de vraag welke drijvende krachten binnen de thermodynamica kunnen leiden tot complexvorming van tegengesteld geladen colloïden. We maken hierbij onderscheid tussen vlakke, geladen oppervlakken, zoals sommige kleideeltjes in water, cylindervormige polymeren en bolvormige eiwitten en nanodeeltjes. We lossen de Poisson-Boltzmannvergelijking op voor verschillende combinaties van deze deeltjes. Met behulp van de elektrostatische potentiaal die hieruit volgt berekenen we hoe de veldenergie en de entropie van de ionen bijdragen aan de totale vrije energie van interactie. Voor zwak geladen vlakken zijn energie en entropie gelijk, terwijl voor sterk geladen oppervlakken de entropie altijd de overhand heeft. Complexatie wordt bij sterk geladen oppervlakken dus gedreven door een verhoging van de entropie van de tegenionen die vrijkomen uit de overlappende elektrische dubbellagen. Voor zwak geladen cylinders en bollen heeft juist de veldenergie de overhand en wordt complexatie eigenlijk gedreven door een verlaging van de elektrische energie wanneer de tegengesteld geladen oppervlakken elkaar dicht naderen. De overgang tussen beide situaties hangt af van de kromming van de elektrische dubbellaag (κa). Hoe kleiner deze parameter, hoe krommer de dubbellagen en hoe meer de elektrische energie bijdraagt aan de verlaging van de vrije energie van interactie. In de meeste in de praktijk voorkomende situaties geldt dat elektrische energie en entropie beide een niet te verwaarlozen bijdrage leveren aan de complexatie van tegengesteld geladen deeltjes.

In Hoofdstuk 3 onderzoeken we hoe deze drijvende krachten zich manifesteren in een experimenteel modelsysteem voor complex coacervaten. We gebruiken hiervoor positief geladen poly(N,N-dimethylaminoethylmethacrylaat) (PDMAEMA) en negatief geladen poly(acrylzuur) (PAA) van verschillende lengtes (zie Figuur 1.9 voor structuurformules). Mengen van oplossingen van deze polyelektrolieten leidt tot het soort fasescheiding dat karakteristiek is voor complex coacervatie (zie foto's in Figuur 1.3). De complex coacervaten bevatten een constante hoeveelheid water van 70% en een $1:1$ verhouding van ioniseerbare polymeergroepen. Door het poly(acrylzuur) te merken met een fluorescent molecuul kunnen we de polymeerconcentraties in zowel de verdunde fase als de complex coacervaat fase meten bij verschillende zoutconcentraties. We verwerken deze metingen tot een fasediagram dat de stabiliteit van deze complex coacervaten samenvat. Alle complex coacervaten van deze polyelektrolieten kunnen worden opgelost bij voldoende hoge zoutconcentraties. Het punt waar dit gebeurt heet de kritische zoutconcentratie. Voor kortere polymeerketens wordt de kritische zoutconcentratie eerder bereikt dan voor lange polymeerketens. Met het model van Voorn en Overbeek, dat de complex coacervaten benadert als mengsel van monovalente ionen volgens de theorie van Debye en Hückel, kunnen we al onze resultaten beschrijven en verklaren.

In Hoofdstuk 4 onderzoeken we achttien andere combinaties van polyelektrolieten die ook complex coacervaten vormen. We proberen een antwoord te vinden op de

vraag welke eigenschappen van complex coacervaten generiek zijn en welke afhangen van de specifieke chemische structuur van hun bestanddelen. Voor iedere combinatie meten we de kritische zoutconcentratie, het watergehalte en de verhouding van geladen polymeergroepen. Bovendien onderzoeken we voor twee van deze combinaties of het type zout en de temperatuur invloed hebben op de stabiliteit van de complex coacervaten. We vinden dat alle complex coacervaten ongeveer dezelfde compositie hebben, met 60 tot 85% water en een 1:1 verhouding van ioniseerbare polymeergroepen. De kritische zoutconcentraties daarentegen variëren sterk, omdat we vermoeden dat sommige geladen groepen veel hechtere en sterkere ionparen kunnen vormen. Bovendien heeft het type zout een grote invloed op de stabiliteit. Grote ionen die weinig gehydrateerd zijn, zijn in staat al bij lagere concentraties een complex coacervaat op te lossen. Kleine, sterk gehydrateerde ionen dehydrateren de complex coacervaten en dat leidt tot hechtere ionparen tussen de polyelektrolieten. Tot slot heeft ook de temperatuur invloed op de stabiliteit. Verhoging van de temperatuur leidt tot meer stabiele complex coacervaten.

In de overige Hoofdstukken van dit deel besteden we aandacht aan twee systemen waarin de drijvende krachten achter complex coacervatie gebruikt worden voor structuurvorming. In Hoofdstuk 5 gebruiken we een combinatie van polyelektrolieten die ook in Hoofdstuk 4 onderzocht is. In plaats van de homopolyelektrolieten gebruiken we nu een blokcopolymeer met een positief geladen blok en een neutraal, wateroplosbaar blok. Bij toevoeging van een negatief geladen homopolyelektroliet aan dit blokcopolymeer treedt een ruimtelijk begrensde complexatie op en worden micellen gevormd met een grootte van enkele tientallen nanometers (zie Figuur 1.6). Deze complex coacervaat-kern micellen (Engels: C3Ms) hebben veel overeenkomsten met de macroscopische complex coacervaten uit Hoofdstuk 3 en 4. Boven een kritische zoutconcentratie, die afhangt van de lengte van de polymeren, vallen de micellen uit elkaar. Deze kritische zoutconcentratie is altijd lager dan de kritische zoutconcentratie die we voorspellen voor macroscopische complex coacervaten, omdat de neutrale polymeerblokken voor bijkomende afstoting tussen de polymeerketens in het micel zorgen. Dicht bij de kritische zoutconcentratie kunnen sommige micellen wormvormige structuren vormen met een lengte van enkele honderden nanometers. We verklaren deze overgang met behulp van de pakkingsparameter die dicht bij de kritische zoutconcentratie groter wordt. Eenzelfde soort overgang komt in de bestaande literatuur veel vaker voor, maar is steeds onopgemerkt gebleven.

Wanneer de polyelektrolieten met een uiteinde aan een colloïdaal deeltje worden bevestigd, kan hun onderlinge aantrekking ervoor zorgen dat de deeltjes in ordelijke structuren gerangschikt worden. In Hoofdstuk 6 onderzoeken we of dit mogelijk is voor polystyreen deeltjes van ongeveer 1 micrometer. We maken twee soorten deeltjes met verschillende lading die van elkaar te onderscheiden zijn door de fluorescente kleurstof in hun kern (zie Figuur 6.1). We vinden wederom veel overeenkomsten met de complex

coacervaten in Hoofdstuk 3 en 4. Boven een kritische zoutconcentratie vallen deeltjes, die aan elkaar waren gebonden, spontaan uit elkaar. Dit is de eerste strategie die het mogelijk maakt om tegengesteld geladen colloïdale deeltjes in een waterige oplossing reversibel aan elkaar te laten plakken en weer uit elkaar te laten gaan. Beneden de kritische zoutconcentratie vormen mengsels van tegengesteld geladen deeltjes fractale gelen en geen ordelijke structuren, omdat de aantrekking tussen twee deeltjes die met elkaar in contact zijn gekomen langzaam sterker wordt in de loop der tijd. Herschikking van eenmaal vastgeplakte deeltjes is vaak niet mogelijk. Aan het eind van dit Hoofdstuk stellen we daarom een ontwerp voor een ander soort deeltje voor waarvoor de uiteindelijke reversibele rangschikking in een ordelijke structuur wel mogelijk zou moeten zijn.

Structuur

Het tweede deel van dit proefschrift gaat over de structuur van complex coacervaten.

In Hoofdstuk 7 onderzoeken we de statische structuur door analyse van de verstrooiing van neutronen, röntgenstraling en licht door complex coacervaten. We gebuiken hier hetzelfde modelsysteem als in Hoofdstuk 3. Zowel de positief geladen als de negatief geladen polyelektrolieten hebben een ideale Gaussische conformatie in de complex coacervaten. Samen vormen ze een semi-verdunde oplossing van overlappende polymeerketens, te vergelijken met een net met mazen van een karakteristieke grootte. Op lengteschalen die veel groter zijn dan de mazen van het netwerk wordt een complex coacervaat gekenmerkt door significante concentratieverschillen. Deze concentratieverschillen leiden tot verstrooiing van neutronen, röntgenstraling en licht volgens een machtswet. We stellen dat deze concentratieverschillen verklaard kunnen worden doordat slechts zwakke correlaties bestaan tussen geneutraliseerde paren van polyelektrolieten. De resultaten van dynamische lichtverstrooiing bevestigen ons beeld van de structuur. Beide structuurelementen, de mazen van het netwerk en de concentratieverschillen, verplaatsen via diffusie gedurende een karakteristieke tijd die overeenkomt met hun grootte. De structuur van complex coacervaten verandert slechts weinig met veranderende zoutconcentratie.

In Hoofdstuk 8 en 9 bestuderen we de dynamische structuur van complex coacervaten met behulp van reologie. In tegenstelling tot de statische structuur, heeft de zoutconcentratie wel een sterke invloed op de dynamica van complex coacervaten. Bij lage zoutconcentraties zijn het elastische gelen, terwijl het bij hoge zoutconcentraties viskeuze vloeistoffen zijn. De rol van zoutionen bij deze overgang is algemeen van aard. In Hoofdstuk 8 beschrijven we het moleculaire mechanisme achter de relaxatieprocessen in complex coacervaten en de bijbehorende energieniveaus. Ons model voorspelt dat de activeringsenergie van allerlei complexen afhangt van de zoutconcentratie en dat het mogelijk is om metingen bij verschillende zoutconcentraties te herijken zodat een unieke mastercurve voor een complex coacervaat ontstaat waarin het volledige re-

laxatiegedrag besloten ligt. We noemen deze herijking tijd-zout-superpositie (Engels: TSS).

In Hoofdstuk 9 passen we deze herijking toe op het modelsysteem uit Hoofdstuk 3 en 7. We reconstrueren de relaxatiespectra voor verschillende lengtes van de polyelektrolieten. De ionbindingen tussen de tegengesteld geladen polyelektrolieten bemoeilijken de beweging van de polymeerketens en kunnen worden gezien als punten van wrijving. Na verloop van voldoende tijd worden de ionbindingen vanzelf verbroken en kan een polymeerketen wel langs alle wrijvingspunten bewegen, volgens het relaxatiemodel van Rouse.

Sterkte

Het derde deel van dit proefschrift gaat over de sterkte van de ionbindingen tussen twee geladen polymeergroepen en de sterkte van de interactie die volgt uit de correlatie tussen twee geneutraliseerde paren van tegengesteld geladen polyelektrolieten. Deze laatste correlatie-interactie vormt de basis voor de cohesie van complex coacervaten en is verwant aan de grensvlakspanning tussen een complex coacervaat en zijn coëxisterende verdunde fase.

In Hoofdstuk 10 beschrijven we hoe de waarde van deze grensvlakspanning met een krachtmicroscoop kan worden gemeten. Aan het uiteinde van een V-vormige veer bevestigen we een colloïdaal deeltje van silica (zie Figuur 10.1). Tussen dit colloïdale deeltje en een dichtbij geplaatst vlak silica oppervlak in een oplossing van de verdunde fase treedt condensatie op van een complex coacervaat in de vorm van een capillaire brug (zie Figuur 10.2). De kracht die nodig is om deze capillaire brug te verbreken is recht evenredig met de grensvlakspanning. De grensvlakspanning is met ongeveer 100 µN/m laag, en neemt af met toenemende zoutconcentratie. Deze afname volgt hetzelfde kritische verband als de grensvlakspanning tussen segregatief ontmengde polymeerfasen.

In Hoofdstuk 11 gebruiken we de krachtmicroscoop om de sterkte van de veel sterkere ionbinding te meten. Hiervoor verankeren we de positief-neutrale blokcopolymeren uit Hoofdstuk 5 op het uiteinde van een V-vormige veer (zie Figuur 11.4). Daartegenover verankeren we negatief geladen polymeren als een borstel op een vlak silica oppervlak. Wanneer we deze veer herhaaldelijk in contact brengen met het silica oppervlak meten we voornamelijk interacties tussen een individueel blok copolymeer en de negatief geladen borstel. De bijbehorende krachten komen in twee verschillende categorieën. Het 'ritsmodel' is van toepassing op de eerste categorie waarin we de kracht meten die nodig is om de individuele ionbindingen een voor een te verbreken. Het 'plotsmodel' is van toepassing op de tweede categorie waarin we de kracht meten die nodig is om een groep van vijf à tien ionbindingen tegelijk te verbreken. Het kwalitatieve verschil tussen beide categorieën is afkomstig van de onderlinge oriëntatie van twee tegengesteld geladen polyelektrolieten: parallelle polymeren ritsen los en

antiparallelle polymeren komen plotsklaps, in een keer, los. Met het model voor de energiebarrière dat we in Hoofdstuk 8 hebben ontwikkeld, kunnen we de grootte van de gemeten krachten en hun afhankelijkheid van de zoutconcentratie beschrijven en verklaren.

In Hoofdstuk 12 blijft onze aandacht bij de ionbindingen tussen tegengesteld geladen polyelektrolieten. We onderzoeken hier niet de sterkte van individuele ionbindingen maar hun collectieve sterkte in de interacties tussen twee tegengesteld geladen polyelektrolietborstels, zoals tussen de colloïdale deeltjes in Hoofdstuk 6. We gebruiken de krachtmicroscoop met een veer waaraan eenzelfde colloïdaal deeltje als in Hoofdstuk 10 is bevestigd (zie Figuur 12.1). Wanneer we nu deze veer herhaaldelijk in contact brengen met het silica oppervlak waarop een tegengesteld geladen polyelektrolietborstel is verankerd, vinden we slechts een type kracht. Door de borstels langer te comprimeren en de scheiding met een hogere snelheid te meten, vinden we dat borstels steeds als ritsen in en uit elkaar gaan. De vorming van een complex tussen de tegengesteld geladen borstels is een langzaam proces dat gedurende onze metingen met constante snelheid plaatsvindt.

Vooruitblik

We hopen dat het onderzoek dat in dit proefschrift beschreven wordt heeft bijgedragen aan een beter inzicht in complex coacervaten. We vinden dat de algemene elektrostatische interacties de overhand hebben bij hun vorming en bepalend zijn voor hun structuur. Dit verklaart waarom complex coacervaten met zulke uiteenlopende componenten veel eigenschappen gemeen hebben. In dit proefschrift geven we een beschrijving van zinvolle methoden om ze te bestuderen aan de hand van modelsystemen.

In de nabije toekomst zouden simulaties met behulp van een computer, gecombineerd met systematische experimenten aan complex coacervaten van polyelektrolieten meer inzicht moeten kunnen geven in de verbanden tussen de drijfveren van de vorming van complex coacervaten, hun structuur en hun klaarblijkelijk onveranderlijke eigenschappen. Daarnaast erkennen we dat veel structuren in de natuur en veel materialen die zijn gebaseerd op dezelfde interacties niet dezelfde fasescheiding kennen die zo bepalend kan zijn voor complex coacervaten. Dit komt omdat meestal het proces van fasescheiding voortijdig wordt onderbroken of omdat bijkomende moleculaire interacties dat verhinderen. Voor een beter begrip van deze subtiele maar belangrijke verschillen stellen we voor om toekomstig onderzoek te richten op het proces van vorming van complex coacervaten en de manieren waarop daarin kan worden ingegrepen, bijvoorbeeld door simultane droging of uitharding. Desalniettemin blijven complex coacervaten hopelijk ook nog velen verwonderen.

Korte verklaring van veelgebruikte termen

Polymeer, homopolymeer, blokcopolymeer, polyelektroliet
Een polymeer is een lang molecuul, bestaande uit een groot aantal repeterende bouwstenen (monomeren), die via covalente chemische of niet-covalente fysische bindingen aan elkaar zijn verbonden, zoals de kralen in een kralenketting (Figuur 1.7). Polymeren die bestaan uit slechts een soort monomeren heten homopolymeren. Polymeren die bestaan uit twee, drie of meer soorten monomeren die in afzonderlijke groepen (blokken) gerangschikt zijn heten blokcopolymeren. Polymeren die een aantal elektrisch geladen monomeren bevatten heten polyelektrolieten.

Colloïde, colloïdaal deeltje, dispersie
Een colloïde is een stof die bestaat uit (colloïdale) deeltjes waarvan de afmetingen groter zijn dan die van atomen en moleculen (ongeveer 1 nanometer), maar kleiner dan wat wij met het blote oog kunnen zien (ongeveer 10 micrometer). Vanwege hun grootte hebben zowel de warmtebeweging als externe krachten, zoals de zwaartekracht en de elektrostatische kracht in een elektrisch veld, een belangrijk invloed op hun beweging. Soms gebruikt men de term colloïde om een enkel deeltje aan te duiden dat in dit bereik van groottes valt. Een dispersie is een colloïde waarin de deeltjes zich homogeen kunnen verdelen. Colloïden worden van oudsher ingedeeld in twee groepen: lyofobe en lyofiele colloïden. Lyofobe colloïden hebben gemeen dat hun deeltjes niet spontaan mengen met het oplosmiddel en de neiging hebben te vlokken. Vaak is een stabilisatie van de deeltjes via een elektrische lading nodig om vlokking te voorkomen. Lyofiele colloïden hebben gemeen dat hun deeltjes wel spontaan mengen met het oplosmiddel en dat de deeltjes een open structuur aannemen en geheel doorlaatbaar zijn voor het oplosmiddel.

Nanometer, micrometer
Een nanometer (nm) is 10^{-9} meter. Een micrometer (µm) is 10^{-6} meter. Ter vergelijking: de dikte van een menselijke haar varieert van 20 µm voor mensen met stijl blond haar tot 180 µm voor mensen met zwart haar. De dikte van een vel A4 papier van 80 g/m^2 is ongeveer 100 µm. Een rode bloedcel is bij benadering een discus met een diameter van 7.5 µm en een dikte van 2 µm. Een individueel griepvirus is gemiddeld 100 nm, maar varieert, afhankelijk van het type, tussen 10 nm en 300 nm. Een suikermolecuul (sucrose) is ongeveer 1 nm.

Thermodynamica, vrije energie, elektrische veldenergie, entropie
De thermodynamica is het onderdeel van de natuurwetenschap dat energiewisselingen en -omzettingen en de daarbij behorende natuurverschijnselen theoretisch onderzoekt. De thermodynamica gaat uit van thermodynamische systemen die, afhankelijk van

hun aard, arbeid kunnen uitoefenen op hun omgeving en warmte en materie kunnen uitwisselen met hun omgeving. Een klassiek voorbeeld van een thermodynamisch systeem is de ketel van een stoommachine. Centrale grootheden in de thermodynamica zijn de thermodynamische potentialen. Zij geven aan hoeveel energie in een systeem opgeslagen is. Bekende thermodynamicshe potentialen zijn de inwendige energie U, de (Helmholtz) vrije energie F, de (Gibbs) vrije enthalpie G, ook wel Gibbs vrije energie genoemd, en de (Landau) grootse potentiaal Ω. Bij elk soort thermodynamisch systeem hoort een karakteristieke thermodynamische potentiaal die een extreme waarde aanneemt wanneer dit systeem in evenwicht is met zijn omgeving.

De elektrische veldenergie is de inwendige energie U die geassocieerd is met een elektrisch veld rondom elektrisch geladen moleculen nabij elektrisch geladen oppervlakken. De entropie is een maat voor het aantal microscopische realiseringsmogelijkheden van een macroscopische toestand. Voor een begrip van deze omschrijving zou men de volgende analogie kunnen voorstellen. Men neme twee moleculen die slechts in één opzicht van elkaar verschillen: een van beiden kan twee vormen aannemen (een 'stoel'- en een 'boot'-vorm), terwijl de ander slechts een vorm kan aannemen. In het eerste molecuul kunnen beide vormen in elkaar overgaan via een knik in het midden van het molecuul, en er bestaan dus twee realiseringsmogelijkheden voor ieder molecuul. Ieder molecuul van de tweede soort kent daarentegen slechts een realiseringsmogelijkheid. Entropie is een belangrijke thermodynamische grootheid bij het bepalen in welke richting processen zullen verlopen. Voor spontane processen geldt dat de entropie van het systeem altijd moet toenemen.

Fasescheiding, fasediagram
Fasescheiding is de scheiding van een stof of een mengsel van stoffen in twee of meer fasen die blijvend naast elkaar kunnen bestaan. Klassieke fase-evenwichten in een zuivere stof zijn die tussen een gasfase en een vloeistoffase en tussen een vaste fase en een vloeistoffase. In mengsels van stoffen kunnen ook twee of meerdere vloeistoffasen naast elkaar bestaan, zoals bijvoorbeeld olie en water. Een fasediagram geeft aan onder welke omstandigheden van bijvoorbeeld temperatuur en druk, of temperatuur en zoutconcentratie, een stof of mengsel van stoffen als één, respectievelijk meerdere fasen bestaat.

Electrostatica
Elektrostatica is de leer van elektrische ladingen in rust. Elektrostatische verschijnselen zijn te herleiden tot de krachten die positieve en negatieve elektrische ladingen op elkaar uitoefenen. Bekende voorbeelden van zulke verschijnselen zijn de ontlading van bliksem, het vastplakken van cellofaan aan je hand wanneer je het van een tijdschrift haalt en het overbrengen van inktdeeltjes bij het maken van een kopie met een kopieerapparaat.

Fractaal
Een fractaal is een meetkundige figuur die zelf-gelijkend is, zodat men het kan opsplitsen in kleine stukjes die steeds gelijkvormig zijn aan het originele geheel. In het algemeen ontstaat zo'n figuur door het uitzetten van punten die de uitkomsten weergeven van een formule die vele malen op zijn eigen uitkomst wordt toegepast. Een van de bekendste fractalen is de kromme van Koch (hieronder weergegeven). Deze kromme kan worden gemaakt door herhaaldelijk een lijnstuk in drie gelijke stukken op te delen en het middelste stuk te vervangen door een gelijkzijdige driehoek zonder basis. Voorbeelden van natuurlijke fractalen zijn een broccoli romanesco, een varen, onze longen en sommige sneeuwvlokken.

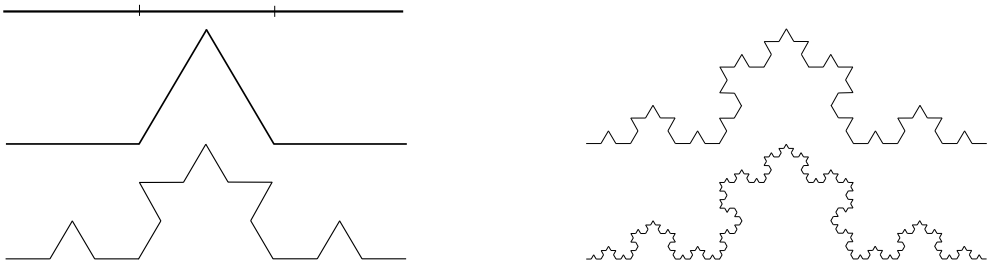

Neutronen, röntgenstraling
Een neutron is een subatomair deeltje dat voorkomt in vrijwel alle atoomkernen. Het heeft geen elektrische lading en ongeveer dezelfde massa als een proton. Neutronenstraling bestaat uit neutronen die met een bepaalde snelheid bewegen. De neutronen die in kleine-hoek neutronenverstrooiingsexperimenten worden gebruikt hebben een gemiddelde snelheid van 600 m/s en een typische golflengte van 0.6 nm. Röntgenstraling (X-rays) is kortgolvige elektromagnetische straling, bestaande uit fotonen, met een golflengte tussen 0.01 nm en 5 nm.

Micel
Een micel is een structuur bestaande uit een aantal amfifiele moleculen die spontaan gevormd wordt boven een zekere kritische micelconcentratie. Veel micel-vormende moleculen bestaan uit een wateroplosbaar en een wateronoplosbaar gedeelte. In water komen de wateronoplosbare delen bij elkaar en worden afgeschermd van het omringende water door een schil van de wateroplosbare delen (zie Figuur 1.6). Vanwege hun amfifiele karakter spelen micellen een belangrijke rol in de vetoplossende werking van zeep.

Krachtmicroscoop (AFM)
De krachtmicroscoop, in het Engels atomic force microscope genoemd, is een meetopstelling waarmee een oppervlak met een minuscule naald (tip) afgetast kan worden. De naald zit aan het uiteinde van een bladveer (zie Figuur 10.1) en via de reflectie van een laser vanaf de bovenkant van deze veer kan zijn verbuiging worden bepaald. De verbuiging van de veer is evenredig met de kracht die door het oppervlak op de naald wordt uitgeoefend. AFM wordt voornamelijk gebuikt om het hoogteprofiel van een oppervlak te bepalen met een resolutie van minder dan 1 nanometer, waarbij de tip al tappend of schuivend het gehele oppervlak 'bevoeld'. Aangezien kracht tussen tip en oppervlak rechtstreeks af te leiden is uit de verbuiging van de veer, kan AFM ook worden gebruikt om de kracht tussen aan het oppervlak verankerde moleculen en de tip te meten.

Reologie
Reologie is de leer van de stroming en vervorming van materialen. Stroming en vervorming treedt op door een kracht uit te oefenen op het materiaal, bijvoorbeeld via een ronddraaiende cylinder of een trillende naald.

Capillaire condensatie, capillaire brug
Een capillair is een kanaalvormige ruimte met een kleine binnendiameter, waar sommige vloeistoffen spontaan in kunnen stromen, tegen de richting van een externe kracht, zoals de zwaartekracht, in. De oorsprong van het woord capillair is Latijn: *capillus* betekent 'haar op het hoofd'. Capillairen worden daarom ook wel haarvaten genoemd. Capillaire condensatie is het condenseren van een stof in de gasfase in nauwe ruimtes, zoals in capillairen en tussen zandkorrels. Een capillaire brug is de vloeistofbrug die ontstaan is via capillaire consensatie. Zo'n brug verbindt twee oppervlakken die dicht op elkaar zitten, of de wanden van een capillair met elkaar (zie Figuur 10.2). De aanwezigheid van een capillaire brug tussen twee oppervlakken geeft aanleiding tot een aantrekkingskracht tussen beide oppervlakken, die voelbaar wordt wanneer je beide oppervlakken weer van elkaar wilt scheiden.

2

List of publications

This thesis

- E. Spruijt, J. Sprakel, M. A. Cohen Stuart and J. van der Gucht, Interfacial tension between a complex coacervate phase and its coexisting aqueous phase, *Soft Matter* **6** (2010), 172–178, doi 10.1039/b911541b (Chapter 10).
- E. Spruijt, M. A. Cohen Stuart and J. van der Gucht, Dynamic force spectroscopy of oppositely charged polyelectrolyte brushes, *Macromolecules* **43** (2010), 1543–1550, doi 10.1021/ma902403a (Chapter 12).
- E. Spruijt, A. H. Westphal, J. W. Borst, M. A. Cohen Stuart and J. van der Gucht, Binodal compositions of polyelectrolyte complexes, *Macromolecules* **43** (2010), 6476–6484, doi 10.21/ma10131t (Chapter 3).
- E. Spruijt, J. Sprakel, M. Lemmers, M. A. Cohen Stuart and J. van der Gucht, Relaxation dynamics at different time scales in electrostatic complexes: time-salt superposition, *Physical Review Letters* **105** (2010), 208301, doi 10.1103/PhysRevLett.105.208301 (open access) (Chapter 8).
- J. van der Gucht, E. Spruijt, M. Lemmers and M. A. Cohen Stuart, Polyelectrolyte complexes: bulk phases and colloidal systems, *Journal of Colloid and Interface Science* **361** (2011), 407–422, doi 10.1016/j.jcis.2011.05.080 (Chapter 4).
- E. Spruijt, H. E. Bakker, T. E. Kodger, J. Sprakel, M. A. Cohen Stuart and J. van der Gucht, Reversible assembly of oppositely charged hairy colloids in water, *Soft Matter* **7** (2011), 8281–8290, doi 10.1039/c1sm05881a (Chapter 6).
- E. Spruijt, S. A. van den Berg, M. A. Cohen Stuart and J. van der Gucht, Direct measurement of the strength of single ionic bonds between hydrated charges, *ACS Nano* **6** (2012), 5297–5303, doi 10.1021/nn301097y (Chapter 11).
- E. Spruijt, M. A. Cohen Stuart and J. van der Gucht, Linear viscoelasticity of polyelectrolyte complex coacervates, *Submitted to Macromolecules* (2012) (Chapter 9).
- E. Spruijt, A. A. van Well, R. Schweins, H. B. Bohidar, R. Fokkink, F. A. M. Leermakers, M. A. Cohen Stuart and J. van der Gucht, Structure of polyelectrolyte complex coacervates as measured by scattering of neutrons, X-rays and light, *In preparation* (2012) (Chapter 7).
- H. M. van der Kooij, E. Spruijt, I. K. Voets, R. Fokkink, M. A. Cohen Stuart and J. van der Gucht, On the stability and morphology of complex coacervate core micelles: from spherical to worm-like micelles, *Langmuir* (2012), doi 10.1021/la303211b (Chapter 5).

Other work

- J. Sprakel, E. Spruijt, M. A. Cohen Stuart, N. A. M. Besseling, M. P. Lettinga and J. van der Gucht, Shear banding and rheochaos in associative polymer networks, *Soft Matter* **4** (2008), 1696–1705, doi 10.1039/b803085e.
- E. Spruijt, E.-Y. Choi and W. T. S. Huck, Reversible electrochemical switching of polyelectrolyte brush surface energy using electroactive counterions, *Langmuir* **24** (2008), 11253–11360, doi 10.1021/la801994b.
- M. Rosso-Vasic, E. Spruijt, B. van Lagen, L. De Cola and H. Zuilhof, Alkyl-functionalized oxide-free silicon nanoparticles: synthesis and optical properties, *Small* **4** (2008), 1835–1841, doi 10.1002/smll.200800066.
- J. Sprakel, E. Spruijt, M. A. Cohen Stuart, M. A. J. Michels and J. van der Gucht, Intermittent dynamics in transient polymer networks under shear: signs of self-organized criticality, *Physical Review E* **79** (2009), 056306, doi 10.1103/PhysRevE.79.056306.
- M. Rosso-Vasic, E. Spruijt, Z. Popović, K. Overgaag, B. van Lagen, B. Grandidier, D. Vanmaekelbergh, F. Domínguez-Gutiérrez, L. De Cola and H. Zuilhof, Amine-terminated silicon nanoparticles: synthesis, optical properties and their use in bioimaging, *Journal of Materials Chemistry* **19** (2009), 5926–5933, doi 10.1039/b902671a.
- J. Sprakel, E. Spruijt, J. van der Gucht, J. T. Padding and W. J. Briels, Failure-mode transition in transient polymer networks with particle-based simulations, *Soft Matter* **5** (2009), 4748–4756, doi 10.1039/b910425a.
- A. M. Brzozowska, E. Spruijt, A. de Keizer, M. A. Cohen Stuart and W. Norde, On the stability of the polymer brushes formed by adsorption of ionomer complexes on hydrophilic and hydrophobic surfaces, *Journal of Colloid and Interface Science* **353** (2011), 380–391, doi 10.1016/j.jcis.2010.09.074.
- M. Lemmers, E. Spruijt, L. Beun, R. Fokkink, F. A. M. Leermakers, G. Portale, M. A. Cohen Stuart and J. van der Gucht, The influence of charge-ratio on transient networks of polyelectrolyte complex micelles, *Soft Matter* **8** (2012), 104–117, doi 10.1039/c1sm06281f.
- M. Lemmers, E. Spruijt, S. Akerboom, I. K. Voets, A. C. van Aelst, M. A. Cohen Stuart and J. van der Gucht, Physical gels based on charge-driven bridging of nanoparticles by triblock copolymers, *Langmuir* **28** (2012), 12311–12318, doi 10.1021/la301917e.

Dankwoord

Ik val
en denk al vallend na.
Zal ik nog iets roepen,
iets van het allergrootst belang,
dat onweerstaanbaar zal weerkaatsen
tegen een overkant?

Toon Tellegen

Dit dankwoord is voor iedereen die mij de afgelopen jaren heeft geholpen, op welke manier dan ook. Ik wil graag een aantal van hen in het bijzonder noemen, waarbij de volgorde niet noodzakelijkerwijs gerelateerd is aan mijn dankbaarheid.

Ik heb mijn onderzoek uitgevoerd in een groep waar ik me echt thuis heb gevoeld. De sfeer werd voor een gedeelte bepaald door de mensen die ook inhoudelijk hebben bijgedragen aan dit proefschrift, maar minstens net zo belangrijk waren alle anderen met wie ik koffiepauzes, lunches en borrels lang heb gepraat en gelachen, op aio-reis ben geweest en leuke labuitjes heb beleefd. Like the atmosphere in the group as a whole, the atmosphere in 0018 was always good. Serious when needed, social, lively and fun when possible. Marc and Yuan, thank you for all the discussions we had, the help you offered and the fun we had together, with and without sunglasses. I wish you both good luck with your scientific work in the Netherlands and in China. Mara, Anita, Josie, jullie leveren een onmisbare bijdrage aan de sfeer in en het draaiend houden van de groep. Bedankt voor alle hulp en gezelligheid. Lennart, Soumi and Thao, I think we have organised a great PhD trip that will not easily be forgotten. Thank you for the whole 'journey' of planning, organising and carrying our plans into effect.

Prettig werken lukt uiteindelijk alleen wanneer ook de inhoudelijke begeleiding prettig is. Jasper, ik had me geen betere begeleider kunnen wensen dan jij. Je stond altijd voor me klaar, je bent kritisch, nauwkeurig en snel, en je hebt me veel geleerd over alles wat we in de loop van dit onderzoek zijn tegengekomen.

Martien, ik ben blij dat ik bij Fysko mocht komen. Je hebt een groot talent om mensen ongedwongen te motiveren en te begeleiden. Je stimuleert creativiteit en kan als geen ander inspirerende presentaties geven. Bedankt voor alles wat je mij geleerd hebt.

Frans, jij bent in alle opzichten een bijzondere wetenschapper. Je bent altijd enthousiast en bereid om ergens over mee te denken, maar je bent bovenal gelukkig heel erg eigenwijs en een goed pleitbezorger voor de principes van de wetenschappelijke vrijheid. Ik zal jouw allereerste college over schaken nooit vergeten.

Joris, jij hebt voor mij een belangrijke rol gespeeld in veel van de afgelopen jaren, beginnend bij mijn afstudeervak tot aan het eind van mijn promotie. Je motiveerde me om steeds een stapje verder te gaan. Ik heb bewondering voor het schijnbare gemak waarmee je met nieuwe ideeën komt en de diepgang die je daarin steeds weet te bereiken.

Maarten, ik vond het leuk dat je steeds belangstelling hebt getoond in mijn onderzoek. Tegen het eind van deze promotie heb je me bovendien in zeer korte tijd met veel enthousiasme en oog voor detail veel geleerd over elektrostatica en celmodellen. Hoofdstuk 2 had zonder jouw hulp niet bestaan.

Sabine, Henriëtte, Bas en Hanne, ik ben blij dat ik bij jullie afstudeeronderzoeken betrokken mocht zijn. Jullie waren allevier zeer gemotiveerde onderzoekers. Sabine, ik hoop dat je talent voor presenteren nog vaak van pas zal komen in je eigen promotieonderzoek. Henriëtte, jouw veelzijdigheid is heel bijzonder en ik wens je veel succes met je eigen onderzoek in Utrecht. Bas, jouw handigheid, zelfstandigheid en doorzettingsvermogen vormen een ijzersterke combinatie, die je hopelijk nog ver zal brengen. Hanne, ik wil jou speciaal bedanken voor je hulp bij het afronden van Hoofdstuk 5 onder grote tijdsdruk. Ik ken weinig mensen die zorgvuldiger zijn dan jij. Ik hoop dat je zelf een leuk en uitdagend promotieonderzoek zult vinden.

The neutron scattering measurements in Chapter 7 were carried out at the ILL in Grenoble, with the help of a team of experts. Ralf and David, thank you for your kind support and helpful comments on site. Ad, bedankt voor je hulp bij onze pogingen om contrast matching te doen in Delft. Frans en Jasper, bedankt voor jullie hulp bij alle metingen. Remco, ik wil jou niet alleen bedanken voor je hulp in Grenoble, maar ook voor je bereidheid altijd mee te denken over allerlei andere vragen en problemen met betrekking tot verstrooiing, luchtdruk en andere technische kwesties.

De FCS metingen in Hoofdstuk 3 zijn uitgevoerd bij het Laboratorium voor Biochemie in Wageningen. Adrie en Jan-Willem, bedankt voor jullie hulp.

Ik ben verschillende mensen nog dankbaar voor hun hulp en advies ‘op verzoek’. Ilja, bedankt dat ik je altijd kon benaderen voor vragen over verstrooiing. Hans, bedankt voor je belangstelling in mijn onderzoek en de suggesties voor aanvullingen op de bestaande theorie en experimenten. Renko, bedankt voor je heldere en praktische suggesties voor Hoofdstuk 2. Dmitry, thank you for your help with photography and programming. Wilhelm, van jou heb ik geleerd wat het belang is van doelen, prioriteiten en samenwerken. Bedankt voor je inspiratie. Venkat, thank you for your help with the fusion experiments described in Chapter 13. I am looking forward to seeing you more often in Nijmegen.

Ten slotte, lezer, die nu een eerste indruk van dit proefschrift heeft gekregen, u wens ik veel plezier met het lezen van de rest.

Evan

About the author

Evan Spruijt was born on 28 June 1986 in Gouda, the Netherlands. He obtained his vwo diploma (secondary education) from the Coornhert Gymnasium in 2003 and then moved to Wageningen to start his studies of Molecular Sciences. As part of his MSc, he carried out two research projects of six months each. At the Laboratory of Organic Chemistry (prof. Han Zuilhof), he worked on the synthesis and fluorescent properties of oxide-free silicon quantum dots. At the Laboratory of Physical Chemistry and Colloid Science (prof. Martien Cohen Stuart), he studied the linear and nonlinear rheology of telechelic polymers with hydrophobic stickers. After finishing these projects, he spent five months at the Melville Laboratory for Polymer Synthesis (prof. Wilhelm Huck) at the University of Cambridge doing a research internship on responsive polymer brushes and hydrogels. In August 2008 he graduated from Wageningen University with an MSc in Molecular Sciences (*cum laude*). In September, he started his PhD research on a Toptalent grant from NWO (Netherlands Organisation for Scientific Research) at the Laboratory of Physical Chemistry and Colloid Science at Wageningen University, under supervision of prof. Martien Cohen Stuart and dr. Jasper van der Gucht. This thesis is the result of that research project.

Overview of completed training activities

General courses

- Mediatraining, NWO, Utrecht, 2008.
- Teaching and supervising thesis students, WUR, Wageningen, 2009.
- Write it right, NWO, The Hague, 2010.
- Negotiating, NWO, The Hague, 2010.
- Visualising science, VLAG, Wageningen, 2011.

Discipline-specific courses and conferences

- Han-sur-Lesse Winterschool, Han-sur-Lesse (Belgium), 2009 and 2010.
- Physics@FOM, Veldhoven, 2009, 2010 and 2011.
- Single molecule techniques, Linz (Austria), 2009.
- Gordon Research Conference, Chemistry of supramolecules and assemblies, Waterville, ME (USA), 2009. †
- Jülich Soft Matter Days, Bonn (Germany), 2009. †
- 241st ACS National Meeting, San Fransisco, CA (USA), 2010. ⋆
- 8th Dutch Soft Matter Meeting, Wageningen, 2010.
- Dutch Polymer Days, Veldhoven, 2011. ⋆†
- 10th Dutch Soft Matter Meeting, Utrecht, 2011.
- Gordon Research Conference, Chemistry of supramolecules and assemblies, Barga (Italy), 2011. †
- 11th Dutch Soft Matter Meeting, Eindhoven, 2011. ‡
- School on Rheology, Leuven (Belgium), 2011.
- Jülich Soft Matter Days, Bonn (Germany), 2011. †
- Chemistry as innovating science, Maarssen, 2011. ⋆
- 243rd ACS National Meeting, San Diego, CA (USA), 2012. ⋆

Other activities

- Group meetings and colloquia 2005–2009. ⋆
- PhD trip, Switzerland and Paris, 2009. ⋆⋆
- PhD trip, Southeast Asia, 2011. ⋆⋆
- Lab training, Weitz group, Harvard University, Cambridge, MA (USA), 2010.⋆

Notes: ⋆ oral presentation, † poster, ‡ soundbite

Cover: design by the author, photography by Dmitry Ershov.
Printing: GVO drukkers en vormgevers B.V. | Ponsen en Looijen, Ede.

This research was financially supported by the Netherlands Organisation for Scientific Research (NWO).